

This item was submitted to Loughborough University as a PhD thesis by the author and is made available in the Institutional Repository (<https://dspace.lboro.ac.uk/>) under the following Creative Commons Licence conditions.



For the full text of this licence, please go to:
<http://creativecommons.org/licenses/by-nc-nd/2.5/>

The high strain-rate behaviour of polymers and nanocomposites for lightweight armour applications

by Foz Hughes
Department of Physics
Loughborough University
Loughborough
Leicestershire
LE11 3TU
United Kingdom

©Foz Hughes 2013

A Doctoral Thesis submitted in partial fulfilment of the requirements for the award of the degree of Doctor of Philosophy of Loughborough University

Supervisor:
Dr. G. M. Swallowe
Department of Physics

Acknowledgments

My thanks and eternal respect go to my project supervisor, Dr. Gerry Swallowe, for his continuing help and enthusiasm. To my partner, Tracy, and her daughter Allie, your constant help, advice and encouragement has made this so much easier than it would have been without you. I would also like to thank my parents, Jill and Glynne for their support throughout my academic career. My co-conspirator Andy Prudom, who aided and abetted in a huge amount of seemingly ridiculous experiments, which yielded fascinating results on many occasions. Finally, a special thank you to all of the administrative and technical staff at Loughborough University who have responded admirably to my numerous unreasonable demands.

Abstract

The need for efficient, lightweight armour solutions has never been so great as it is today. Increasing numbers of personnel, both military and civilian are being placed in an expanding variety of life-threatening situations, and we must recognise the responsibility to maximise their *combat survivability*. One way to help protect these people is to provide them with some form of armour. Advanced polymeric materials are finding an increasing range of industrial and defence applications. These materials have the potential to improve the performance of current armour systems, whilst also reducing their cost and weight.

Polymers may be reinforced with the addition of nanofillers such as carbon nanotubes or graphene, to produce nanocomposites, an exciting emerging polymer technology. Nanomaterials have been shown to exhibit extraordinary strength, far higher than that of traditional armour materials. Nanocomposites have the possibility of being remarkable materials, with high strength and light weight. The work detailed in this report is an investigation into the mechanical properties of nanocomposites along with some novel blended polymer composites.

Two compressive testing techniques have been used to carry out this investigation. The intermediate strain-rate Optical Drop-Weight, and the high strain-rate Split-Hopkinson Pressure Bar. The latter required some significant modifications in order to optimise it for use with low-density polymers.

Ultimately, nanocomposites were found to behave virtually indistinguishably from the monolithic polymer matrices. Yield strengths and energy absorption characteristics remained inside the ordinary experimental scatter. Blended composites, in which a long chain length polymer is combined with a chemically similar polymer with a shorter chain length, proved to be more interesting. Yield strengths of these novel materials were increased over that of either constituent material, although energy absorption remained low.

Contents

Acknowledgments	iii
Abstract	v
Contents	vii
List of Figures	xiii
I Project background	1
1 Introduction	3
1.1 Armour	3
1.1.1 A historical perspective	3
1.1.1.1 The rise and fall of traditional armour	4
1.1.1.2 Lessons from history	7
1.1.2 Firearms and fire power	7
1.1.2.1 Firearms	7
1.1.2.2 Explosives	11
1.1.3 The aetiology of injury	13
1.1.3.1 Firearm trauma	13
1.1.3.2 Explosive trauma	14
1.1.4 The development of modern armour	14
1.1.4.1 World War I (1914 - 1918).	14
1.1.4.2 World War II (1939 - 1945).	16
1.1.4.3 The Cold War (approx. 1947 - 1991)	18
1.1.5 Modern threats	19
1.1.5.1 Threats to vehicles	20
1.1.5.2 Threats to personnel	22
1.1.6 The future of warfare	25
1.1.7 Designing the ideal armour	26
1.1.7.1 Personnel armour	27
1.1.7.2 Vehicle armour	28
1.2 Polymers, composites and nanocomposites	30
1.2.1 Polymers	30
1.2.1.1 Polyethylene	31
1.2.1.1.1 Low Density Polyethylene (LDPE)	31
1.2.1.1.2 Linear Low Density Polyethylene (LLDPE)	32
1.2.1.1.3 High Density Polyethylene (HDPE)	32

1.2.1.1.4	Ultra-High Molecular Weight Polyethylene (UHMWPE)	32
1.2.1.1.5	Dyneema® and Spectra®	32
1.2.1.2	Polyurea	33
1.2.2	Composites	33
1.2.3	Nanomaterials	34
1.2.3.1	Graphene	34
1.2.3.2	Carbon nanotubes	35
1.2.3.3	Buckminsterfullerene	36
1.2.4	Nanocomposites	36
1.2.4.1	Intercalated/exfoliated nanoclay	36
1.2.4.2	Carbon black	37
1.2.4.3	Titanium dioxide	37
1.3	The role of polymers in armour	39
1.3.1	Spall liners	39
1.3.2	Trauma attenuating backings	39
1.3.3	Laminate structures	40
1.4	The mechanical behaviour of solids	41
1.4.1	Stress and Strain	41
1.4.2	Mechanical properties	42
1.4.2.1	Young's modulus	43
1.4.2.2	Yield strength	43
1.4.2.3	Flow stress	43
1.4.2.4	Ultimate strength	44
1.4.3	Stress-strain curves	44
1.4.4	Strain rate	45
1.5	Mechanical Testing Techniques	47
1.6	Research description	48
1.7	About this report	49

II Mechanical testing techniques 51

2	Split-Hopkinson pressure bar	53
2.1	The modern SHPB	56
2.1.1	SHPB theory	57
2.2	Constructing an SHPB	59
2.2.1	Pressure bar configuration	59
2.2.2	Bar material considerations	61
2.2.2.1	Acoustic impedance.	61
2.2.3	Projectile design	63
2.2.4	Pulse shaping	63
2.2.5	Gas gun	64
2.2.6	Pressure bar support & alignment.	66
2.3	Specimen design	66
2.3.1	Inertia effects in specimens	68
2.3.2	Stress equilibrium in specimens	69
2.3.3	Friction in specimens	69
2.4	Supplementary equipment	70

2.4.1	Strain gauges.	70
2.4.1.1	The potential divider.	71
2.4.1.2	The Wheatstone bridge.	73
2.4.1.3	Power supply	73
2.4.1.4	Wiring considerations	74
2.4.1.5	Oscilloscopes	74
2.5	SHPB Operation	74
2.5.1	Smoothing & Filtering data.	75
2.5.1.1	Pre-process smoothing.	76
2.5.1.1.1	In-line filters	76
2.5.1.1.2	n-point rolling average.	78
2.5.1.2	Post-process smoothing.	79
2.5.1.2.1	Bézier smoothing.	79
2.5.1.2.2	Polynomial curve fitting.	80
2.5.1.3	Smoothing and filtering overview.	81
2.5.1.3.1	Comparing pre-process smoothing techniques.	81
2.5.1.3.2	Comparing post-process smoothing techniques.	82
2.5.1.3.3	Choosing the best smoothing method.	82
2.5.2	Analysing data.	84
2.5.2.1	Normalising data.	84
2.5.2.2	Pulse extraction.	85
2.5.2.3	Producing stress-strain curves.	85
2.5.3	Understanding stress-strain curves.	86
2.5.3.1	Finding the yield stress.	86
2.5.3.2	Estimating Young's modulus.	87
2.5.3.3	Finding the strain rate.	88
2.5.4	Measuring energy absorption	89
2.6	Alternative SHPB configurations	89
2.6.1	Tensile SHPB	89
2.6.2	Brazilian technique.	90
3	Optical Dropweight	93
3.1	Operational theory	93
3.2	The hardware	95
3.2.1	The dropweight, optical path and lower anvil	95
3.2.2	Anti-vibration block	95
3.2.3	Triggering system	96
3.2.4	Accelerometer	97
3.2.5	High-speed photography	97
3.2.5.1	AWRE C4 camera	98
3.2.5.2	Shimadzu HPV-1	99
3.2.5.3	Flash unit	100
3.3	Specimen design	100
3.4	ODW analysis	101
3.4.1	Smoothing and filtering data	101
3.4.2	Dropweight stress-strain curves	102

III Experimental	105
4 Understanding armour	107
4.1 Scaling down	108
4.2 The experiment	109
4.3 Observations	110
4.4 Improvements	111
4.5 Further experimentation	114
4.5.1 Improved production techniques	114
4.5.2 Additional materials	115
4.6 Scaling up	115
5 Split-Hopkinson pressure bar	117
5.1 SHPB Modifications	117
5.1.1 Alternative pressure bar materials	117
5.1.1.1 Experimental validation	120
5.1.1.1.1 Volume conservation	121
5.1.1.1.2 Strain gauge signal dependability	122
5.1.2 Tubular pressure bars	124
5.1.3 Pressure bar ‘necking’	126
5.1.4 Strain gauge attachment	128
5.2 High-speed photography	129
5.2.1 Camera alignment and lens considerations	130
5.2.2 Lighting	131
5.2.3 Increasing contrast	131
5.2.4 Triggering	132
5.3 High-speed photography analysis	133
5.3.1 Understanding digital images	134
5.3.2 Otsu’s method	135
5.3.3 Computational measurement of high-speed photographs	139
5.4 Measurement of specimen temperature	140
5.4.1 Theoretical	141
5.4.2 Experimental	142
6 Optical dropweight	145
6.1 High-speed photography analysis	145
7 Results & Discussion	147
7.1 Split-Hopkinson pressure bar	147
7.1.1 Polyethylene	147
7.1.1.1 Benchmark	147
7.1.1.2 LLDPE nanocomposites	150
7.1.1.3 HDPE nanocomposites	153
7.1.1.4 UHMWPE nanocomposites	156
7.1.1.5 PE blends and nanocomposites	158
7.1.2 Polyurea	161
7.2 Optical Dropweight	164
7.2.1 Polyethylene	164
7.2.1.1 LLDPE nanocomposites	166
7.2.1.2 HDPE nanocomposites	168

7.2.1.3	UHMWPE nanocomposites	170
7.2.1.4	PE blends and nanocomposites	172
7.3	Strain rate dependence	174
7.3.1	Yield strength	174
7.3.2	Energy absorption	177
8	Conclusions	181
8.1	Recommendations for further investigation	183
IV	Bibliography	185
	Bibliography	187
V	Publications	193
1	The high strain-rate behaviour of three molecular weights of polyethylene examined with a magnesium alloy split-Hopkinson pressure bar	195
2	Analysis of the high strain-rate behaviour of polyethylene based nanocomposites	205
3	Experimental and numerical analysis of stress wave propagation in polymers and the role of interfaces in armour systems	213
VI	Appendices	221
A	Low-pass filter GNU Octave code	223
B	Bézier smoothing C++ code	225
C	Polynomial fitting GNU Octave code	229
D	Normalisation C++ code	231
E	Pulse extraction C++ code	235
F	SHPB analysis C++ code	243
G	Yield Strength GNU Octave code	255
H	Young's Modulus C++ code	257
I	Otsu thresholding C++ code	261
J	Barfinder C++ code	265
K	Optical drop weight C++ code	273
L	Full page graphs	279
L.1	Split-Hopkinson Pressure Bar	279
L.2	Optical Dropweight	295

M Free Software

311

List of Figures

1.1	A pair of articulated sabatons circa 1610	5
1.2	Helmet worn by Ned Kelly	6
1.3	British Army Land Pattern service musket	7
1.4	Firing mechanism of the Land Pattern service musket	8
1.5	A musket charge.	9
1.6	Graph showing idealised projectile motion for a firearm	10
1.7	Cross-section of a modern conical, hollow bottomed bullet.	11
1.8	The Brewster body shield.	15
1.9	A British Mark I tank at the Somme.	15
1.10	An armour piercing bullet penetrating armour.	16
1.11	A shaped charge.	17
1.12	Explosive reactive armour.	19
1.13	Cross-section of an RPG-7 HEAT projectile.	21
1.14	Armour Piercing, Fin Stabilised, Discarding Sabot projectile.	21
1.15	A British Army Challenger 2 main battle tank in operation in Iraq.	22
1.16	A British Army sniper in Afghanistan.	24
1.17	The survivability onion.	26
1.18	Failure modes in impacted plates [Zukas, 1980].	28
1.19	Structure of a glucose molecule.	30
1.20	Structure of a cellulose chain.	30
1.21	Structure of a polyethylene chain.	31
1.22	The branched structure of LDPE.	32
1.23	The repeating unit of polyurea, with the urea sub-unit hilighted.	33
1.24	A woven mat for use as composite reinforcement.	34
1.25	The structure of graphene.	35
1.26	Dispersal, intercalation and full exfoliation of a layered mineral in a polymer matrix.	36
1.27	TEM image of nanoclay dispersed in a PE matrix.	37
1.28	SEM image of carbon black dispersed in a PE matrix.	38
1.29	Armour impact resulting in spall.	39
1.30	A body undergoing tensile strain.	41
1.31	A body undergoing compressive strain.	41
1.32	Typical tensile engineering stress-strain curve for a range of materials.	44
1.33	Strain rate regimes	46
2.1	A ballistic pendulum.	53
2.2	A pressure wave travelling along a metal rod.	54
2.3	Reflection of a pressure pulse at a free boundary.	55
2.4	Davies' parallel-plate capacitor.	56

2.5	A simple SHPB system.	56
2.6	Raw SHPB data of a copper specimen.	57
2.7	The strain pulses and consequent movement of the SHPB pressure bars.	57
2.8	A traditional three-bar SHPB configuration.	60
2.9	Pochhammer-Chree oscillations.	60
2.10	Wave motion along media of changing density.	62
2.11	A Tubular SHPB.	62
2.12	A shaped pulse.	64
2.13	A simple gas gun.	64
2.14	The compact gas gun used at Loughborough University.	65
2.15	A range of SHPB specimens	67
2.16	The mould used at Loughborough University for producing polymer specimens.	67
2.17	LLDPE specimens as extracted from the mould.	68
2.18	Close-up of a single LLDPE specimen.	68
2.19	Specimen barrelling due to inadequate lubrication.	69
2.20	A typical foil strain gauge.	70
2.21	A simple twin potential divider circuit.	71
2.22	A twin wheatstone bridge circuit.	74
2.23	Raw SHPB data of a copper specimen.	75
2.24	SHPB true stress-strain curve of a copper specimen.	75
2.25	Fourier transformation of the incident bar data from Figure 2.23.	77
2.26	The frequency response for a range of orders of Butterworth low-pass filters with a cut-off frequency of $f_c = 100$ kHz.	77
2.27	SHPB incident bar data filtered with a 7 th order Butterworth low-pass filter with a cut-off frequency of $f_c = 100$ kHz.	78
2.28	SHPB incident bar data smoothed with a 20-point rolling average.	79
2.29	A three point dataset.	79
2.30	The production of a Bézier curve for a three point dataset.	80
2.31	The production of a Bézier curve for a four point dataset.	80
2.32	SHPB incident bar data smoothed with a Bézier curve.	81
2.33	Comparison of different pre-process smoothing techniques.	82
2.34	Close-up of yield point in pre-process smoothing techniques.	82
2.35	Comparison of different post-process smoothing techniques.	83
2.36	Close-up of yield point in post-process smoothing techniques.	83
2.37	SHPB data showing significant electrical noise on the incident bar.	84
2.38	Normalised SHPB true stress-strain curve for copper and LLDPE.	87
2.39	A specimen with poor face parallelism.	87
2.40	Strain rate of a copper specimen in an SHPB.	88
2.41	Strain rate of an LLDPE specimen in an SHPB.	89
2.42	Tensile SHPB system.	90
2.43	Alternative tensile SHPB system.	90
2.44	The dynamic Brazilian technique performed with the SHPB.	91
3.1	Optical dropweight system.	94
3.2	Vibrations in the dropweight system.	96
3.3	The ODW trigger.	96
3.4	Simplified model of an accelerometer [Serridge and Licht, 1987].	97
3.5	The AWRE C4 Camera.	98

3.6	Images taken with the AWRE C4 camera.	99
3.7	The Shimadzu HPV-1 high-speed camera.	99
3.8	Images taken with the Shimadzu HPV-1 camera.	100
3.9	Unfiltered ODW data of an LLDPE specimen.	101
3.10	Filtered ODW data of an LLDPE specimen.	102
3.11	ODW Young's modulus history of an LLDPE specimen.	103
4.1	Experimental setup for testing armour simulants with an air rifle.	108
4.2	300 g monolithic gypsum plaster slab after impact, front view.	109
4.3	300 g monolithic gypsum plaster slab after impact, rear view.	109
4.4	250 g monolithic gypsum plaster slab after impact.	110
4.5	Progress of air rifle pellet through monolithic gypsum plaster slab.	111
4.6	Gypsum plaster slab with a layer of latex rubber on the reverse.	112
4.7	250 g gypsum slab with a 15 ml layer of latex rubber after impact.	112
4.8	Latex layer helping to arrest a pellet.	113
4.9	A sandwich simulant after impact.	113
4.10	A four-layer laminate after impact.	114
5.1	LLDPE specimen in maraging steel SHPB.	118
5.2	LLDPE specimen in pure Mg SHPB.	119
5.3	LLDPE specimen in ZK60 SHPB.	120
5.4	Comparison of stress-strain curves of LLDPE specimen in steel and ZK60 SHPBs.	120
5.5	High-speed photography of LLDPE specimen in ZK60A SHPB	121
5.6	Dynamic height and diameter of an SHPB specimen.	122
5.7	Dynamic volume of an SHPB specimen.	122
5.8	Photographic strain of an LLDPE SHPB specimen.	123
5.9	Photographic strain of a UHMWPE SHPB specimen.	123
5.10	Drilled section of SHPB transmitter bar.	124
5.11	Data collected from tubular SHPB system.	125
5.12	Superimposed pulses from tubular SHPB.	125
5.13	Pulses from tubular SHPB normalised and superimposed.	126
5.14	A necked pressure bar.	127
5.15	The movement of waves within a necked pressure bar.	127
5.16	Theoretical gain for a range of diameter reductions on a necked SHPB.	128
5.17	Original strain gauge attachment technique.	129
5.18	New strain gauge attachment technique.	129
5.19	Positioning and alignment of the camera.	130
5.20	The lighting configuration used in SHPB experiments.	132
5.21	A single video frame from an SHPB experiment.	132
5.22	Improved contrast SHPB.	133
5.23	SHPB photography triggering system.	133
5.24	A bitmap image.	134
5.25	Zoomed in area of SHPB photograph.	135
5.26	Three levels of thresholding.	135
5.27	A 50 × 50 pixel 8-bit greyscale image converted to 3-bit greyscale.	136
5.28	A frame from the high-speed photography after thresholding using Otsu's method.	139
5.29	Theoretical temperature increase of LLDPE in SHPB.	141
5.30	Thermal imagery of LLDPE in SHPB.	143

5.31	Temperature in thermal imagery of LLDPE in SHPB.	143
5.33	Temperature across the specimen face.	144
5.32	Close up of specimen in thermal image at 52 ms.	144
7.1	SHPB true stress/strain curves for LLDPE, HDPE and UHMWPE. . . .	147
7.2	SHPB Young's modulus evolution for LLDPE, HDPE and UHMWPE. .	148
7.3	SHPB energy absorption for LLDPE, HDPE and UHMWPE.	148
7.4	SHPB yield strengths of LLDPE, HDPE and UHMWPE.	149
7.5	SHPB energy absorption at 50% strain of LLDPE, HDPE and UHMWPE.	149
7.6	SHPB true stress/strain curves for LLDPE nanocomposites.	150
7.7	SHPB Young's modulus evolution for LLDPE nanocomposites.	151
7.8	SHPB energy absorption for LLDPE nanocomposites.	151
7.9	SHPB yield strengths of LLDPE nanocomposites.	151
7.10	SHPB energy absorption at 50% strain of LLDPE nanocomposites. . . .	152
7.11	SHPB true stress/strain curves for HDPE nanocomposites.	153
7.12	SHPB Young's modulus evolution for HDPE nanocomposites.	154
7.13	SHPB energy absorption for HDPE nanocomposites.	154
7.14	SHPB yield strengths of HDPE nanocomposites.	154
7.15	SHPB energy absorption at 50% strain of HDPE nanocomposites.	155
7.16	SHPB true stress/strain curves for UHMWPE nanocomposites.	156
7.17	SHPB Young's modulus evolution for UHMWPE nanocomposites. . . .	156
7.18	SHPB energy absorption for UHMWPE nanocomposites.	157
7.19	SHPB yield strengths of UHMWPE nanocomposites.	157
7.20	SHPB energy absorption at 50% strain of UHMWPE nanocomposites. .	157
7.21	SHPB true stress/strain curves for PE blends and nanocomposites. . . .	158
7.22	SHPB Young's modulus evolution for PE blends and nanocomposites. .	159
7.23	SHPB energy absorption for PE blends and nanocomposites.	159
7.24	SHPB yield strengths of PE blends and nanocomposites.	159
7.25	SHPB energy absorption at 50% strain of PE blends and nanocomposites.	160
7.26	SHPB true stress/strain curves for polyurea and nanocomposites. . . .	161
7.27	SHPB Young's modulus evolution for polyurea and nanocomposites. . .	162
7.28	SHPB energy absorption for polyurea and nanocomposites.	162
7.29	SHPB yield strengths of polyurea and nanocomposites.	162
7.30	SHPB energy absorption at 50% strain of polyurea and nanocomposites.	163
7.31	ODW true stress/strain curves for LLDPE, HDPE and UHMWPE. . . .	164
7.32	ODW Young's modulus evolution for LLDPE, HDPE and UHMWPE. .	164
7.33	ODW energy absorption for LLDPE, HDPE and UHMWPE.	165
7.34	ODW yield strengths of LLDPE, HDPE and UHMWPE.	165
7.35	ODW energy absorption at 50% strain of LLDPE, HDPE and UHMWPE.	165
7.36	ODW true stress/strain curves for LLDPE nanocomposites.	166
7.37	ODW Young's modulus evolution for LLDPE nanocomposites.	166
7.38	ODW energy absorption for LLDPE nanocomposites.	167
7.39	ODW yield strengths of LLDPE nanocomposites.	167
7.40	ODW energy absorption at 50% strain of LLDPE nanocomposites. . . .	167
7.41	ODW true stress/strain curves for HDPE nanocomposites.	168
7.42	ODW Young's modulus evolution for HDPE nanocomposites.	168
7.43	ODW energy absorption for HDPE nanocomposites.	169
7.44	ODW yield strengths of HDPE nanocomposites.	169
7.45	ODW energy absorption at 50% strain of HDPE nanocomposites.	169

7.46	ODW true stress/strain curves for UHMWPE nanocomposites.	170
7.47	ODW Young's modulus evolution for UHMWPE nanocomposites.	170
7.48	ODW energy absorption for UHMWPE nanocomposites.	171
7.49	ODW yield strengths of UHMWPE nanocomposites.	171
7.50	ODW energy absorption at 50% strain of UHMWPE nanocomposites.	171
7.51	ODW true stress/strain curves for PE blends and nanocomposites.	172
7.52	ODW Young's modulus evolution for PE blends and nanocomposites.	172
7.53	ODW energy absorption for PE blends and nanocomposites.	173
7.54	ODW yield strengths of PE blends and nanocomposites.	173
7.55	ODW energy absorption at 50% strain of PE blends and nanocomposites.	173
7.56	Yield strength by strain rate for pure PE matrices.	174
7.57	Yield strength by strain rate for LLDPE nanocomposites.	175
7.58	Yield strength by strain rate for HDPE nanocomposites.	175
7.59	Yield strength by strain rate for UHMWPE nanocomposites.	175
7.60	Yield strength by strain rate for PE blends and nanocomposites.	176
7.61	Energy absorption by strain rate for pure PE matrices.	177
7.62	Energy absorption by strain rate for LLDPE nanocomposites.	178
7.63	Energy absorption by strain rate for HDPE nanocomposites.	178
7.64	Energy absorption by strain rate for UHMWPE nanocomposites.	178
7.65	Energy absorption by strain rate for PE blends and nanocomposites.	179
L.1	SHPB true stress/strain curves for LLDPE, HDPE and UHMWPE.	280
L.2	SHPB Young's modulus evolution for LLDPE, HDPE and UHMWPE.	281
L.3	SHPB energy absorption for LLDPE, HDPE and UHMWPE.	282
L.4	SHPB true stress/strain curves for LLDPE nanocomposites.	283
L.5	SHPB Young's modulus evolution for LLDPE nanocomposites.	284
L.6	SHPB energy absorption for LLDPE nanocomposites.	285
L.7	SHPB true stress/strain curves for HDPE nanocomposites.	286
L.8	SHPB Young's modulus evolution for HDPE nanocomposites.	287
L.9	SHPB energy absorption for HDPE nanocomposites.	288
L.10	SHPB true stress/strain curves for UHMWPE nanocomposites.	289
L.11	SHPB Young's modulus evolution for UHMWPE nanocomposites.	290
L.12	SHPB energy absorption for UHMWPE nanocomposites.	291
L.13	SHPB true stress/strain curves for PE blends and nanocomposites.	292
L.14	SHPB Young's modulus evolution for PE blends and nanocomposites.	293
L.15	SHPB energy absorption for PE blends and nanocomposites.	294
L.16	ODW true stress/strain curves for LLDPE, HDPE and UHMWPE.	296
L.17	ODW Young's modulus evolution for LLDPE, HDPE and UHMWPE.	297
L.18	ODW energy absorption for LLDPE, HDPE and UHMWPE.	298
L.19	ODW true stress/strain curves for LLDPE nanocomposites.	299
L.20	ODW Young's modulus evolution for LLDPE nanocomposites.	300
L.21	ODW energy absorption for LLDPE nanocomposites.	301
L.22	ODW true stress/strain curves for HDPE nanocomposites.	302
L.23	ODW Young's modulus evolution for HDPE nanocomposites.	303
L.24	ODW energy absorption for HDPE nanocomposites.	304
L.25	ODW true stress/strain curves for UHMWPE nanocomposites.	305
L.26	ODW Young's modulus evolution for UHMWPE nanocomposites.	306
L.27	ODW energy absorption for UHMWPE nanocomposites.	307
L.28	ODW true stress/strain curves for PE blends and nanocomposites.	308

L.29 ODW Young's modulus evolution for PE blends and nanocomposites. . 309
L.30 ODW energy absorption for PE blends and nanocomposites. 310

Part I

Project background

Introduction

“In the beginning the Universe was created. This has made a lot of people very angry and been widely regarded as a bad move.”

—DOUGLAS ADAMS
THE HITCHHIKER’S GUIDE TO THE GALAXY

1.1 Armour

The need for efficient, lightweight armour solutions has never been so great as it is today. Increasing numbers of personnel, both military and civilian, are being placed in an expanding variety of life-threatening situations. Whether it be a news media team documenting soldiers in battle, humanitarian aid workers transporting crucial supplies to war stricken areas, or a military squad travelling through areas abound with IEDs^a, we must recognise the responsibility to maximise their *combat survivability*. One way to help protect these people is to provide them with some form of armour.

1.1.1 A historical perspective

The first recorded use of body armour may be seen on the Stele of the Vultures (circa 2500 B.C.E.) which shows the Sumerian king Eannatum’s soldiers wearing leather cloaks onto which a number of metal disks have been sewn [Gabriel, 2007]. Although it is not entirely clear when or to whom the invention of armour may be attributed, what is clear is that its ability to protect the wearer from injury has been central in defining the outcome of warfare.

In antiquity the weapons of war consisted primarily of striking weapons which could be either blunt or bladed (swords, clubs etc.) and low-velocity projectiles (arrows, spears.) To afford some level of protection from these weapons, untold different types of armour were developed across the world, with three materials providing the foundation for them all.

Leather The inventors of leather armour perhaps gained their inspiration from the animal kingdom, where a tough outer-skin was adequate to provide

^aImprovised Explosive Devices.

defence against most forms of attack. Leather armour is, as the name implies, constructed primarily of thick animal hides, and provided the mainstay of personnel armour. Animal hides are of course readily available, and given their relative toughness^b, flexibility, low weight, simple manufacturing and easy maintenance, leather could provide a firm foundation.

Mail Sometimes referred to as *chainmail*, this material consists of interlocking metal rings, linked together to form a mesh. By its nature, it is strong and flexible, however its manufacture is both time consuming and highly skill intensive. In addition to what we traditionally consider to be mail armour, garments such as the brigandine and jack of plates in which iron plates were sandwiched between layers of leather or canvas fabric were also used. The manufacture of these items was significantly simpler than 'ordinary' mail armour, making them much more affordable.

Plate The top-of-the-range armour solution available in that time was undoubtedly the full plate suit of armour, made from sheets of steel which were often carburised or case hardened [Williams, 2003]. The fit of a suit of plate armour was critical, with each suit being designed specifically for one person, although it wasn't uncommon for armour to be modified to fit another person. The construction of a suit was a highly specialised process, and so full suits of plate armour were typically only available to the very wealthiest.

Most traditional armour was made up from combinations of two or more components from the above list. For example, a 17th century English Harquebusier^c, requiring a large degree of flexibility, would wear light armour consisting of a plate helmet and a plate breast piece providing protection to the vital organs, worn over a leather coat, safeguarding the arms from at least glancing blows.

1.1.1.1 The rise and fall of traditional armour

Perhaps the greatest misconception about traditional armour may be attributed, at least in part, to Mark Twain who, in *A Connecticut Yankee in King Arthur's Court* (1889) wrote

'You don't get on your horse yourself; no, if you tried it you would get disappointed. They carry you out, just as they carry a sun-struck man to the drug store, and put you on...'

This was pushed further into cultural myth by Laurence Olivier's 1944 film adaptation of Shakespeare's *Henry V*. In the film, one scene depicts a fully armoured knight being lifted onto his horse by use of a winch, implying that his armour was so heavy that he could not lift his own weight onto his horse. In actual fact, a complete suit of plate armour made from well-tempered steel would only weigh around 20kg [James, 2003]. As testament to this, an anonymous biography of Jean Le Maingre, a 15th century marshal of France, claimed that he

^bAt least compared to human skin.

^cA common form of cavalryman, carrying a harquebus or carbine, a firearm with a shorter barrel than a rifle or musket.



FIGURE 1.1: A pair of articulated sabatons circa 1610, ©Board of Trustees of the Armouries.

was capable of performing cartwheels and even jumping onto his war horse fully armoured [Nicholson, 2003].

Neither was armour restrictive; it is worth remembering that since mankind had been working metals since the Bronze Age, metal workers would have been very highly skilled craftsmen, perfectly able to produce articulated garments of the most exceptional quality. A good example of this is shown in Figure 1.1.

The protection provided by armour was also quite remarkable. The impact resistance of good quality armour is graphically illustrated in Richard Atkyn's account of his personal duel with parliamentarian Sir Arthur Haselrigge at the battle of Roundway Down in 1643, as written in *The Vindication of Richard Atkins* [sic],

'Twas my fortune in a direct line to charge their General of Horse which I supposed to be so by his place. He discharged his carbine first but at a distance not to hurt us, and afterwards one of his pistols, before I came up to him and missed with both. I then discharged mine; and I'm sure I hit him, for he staggered and presently wheeled off from his party and ran...

...in six score yards I came up to him, and discharged the other pistol at him and I am sure I hit his head for I touched it before I gave fire and it amazed him at that present, but he was too well armed all over for a pistol bullet to do him any harm, having a coat of mail over his arms and a headpiece (I am confident) musket proof.' [Blackmore, 1990]

So, if the armour of antiquity was so good, why did it fall from favour?

The development of firearms, discussed in greater detail in Section 1.1.2.1 below, was ultimately to blame for the steady decline in the use of armour on the battlefield. Early firearms were inaccurate, not especially powerful and particularly slow to load, so their arrival did not have an immediate effect on the use of



FIGURE 1.2: *Helmet worn by Ned Kelly, ©State Library of Victoria, Australia.*

armour in the field. However, as the power and accuracy of firearms increased, the usefulness of armour declined. There became little point in providing armour for front-line troops as it afforded them little protection, and only slowed them down. There is no evidence for the manufacture of Pikeman's armour after the early 1640s and by the formation of Cromwell's New Model Arms in 1645, no armour whatsoever was issued to Pikemen [Blackmore, 1990].

There is, perhaps, only one notable use of armour to defend against firearms between the end of the English civil wars and the beginning of the 20th century. Edward 'Ned' Kelly was an Australian bushranger, notorious outlaw and murderer. In 1880 Kelly and his gang took on a special force of police dispatched to bring Kelly to justice. Kelly had constructed a number of suits of armour for himself and his gang, made from iron plough blades around 6.35mm (0.25 inch) thick. The suits consisted of a breastplate and backplate, a pair of shoulder plates and a helmet and visor. During the inevitable confrontation it was reported that Kelly survived several direct hits from the police (as may be seen from the dents in his helmet as shown in Figure 1.2) before they realised that only his upper body and head were invulnerable to their bullets, and turned their weapons on his legs. Kelly was badly wounded but survived to be tried, was convicted of murder and executed.



FIGURE 1.3: A British Army Land Pattern service musket or 'Brown Bess' dated 1731, ©Board of Trustees of the Armouries.

1.1.1.2 Lessons from history

It is easy to think of our ancestors as simple people with a poor understanding of technology, relying on little more than strength and blood lust to succeed in battle. This is, of course, wrong. Their ability to develop armour solutions without the use of the high-technology materials and manufacturing techniques that are available to us today was nothing short of amazing. Since the development of firearms and the decline in the use of armour, much has been forgotten about the design and construction of armour which had steadily improved over the course of a few thousand years.

1.1.2 Firearms and fire power

Before discussing the development of modern armour, it is useful to gain an understanding of the sort of threat it has been designed to protect a user from.

1.1.2.1 Firearms

Early muskets were muzzle-loading^d, single-shot, smoothbore^e weapons, firing either one or a number of lead balls or *shot*.

Accuracy. The manufacture of muskets was a highly skilled process. Barrels were made by passing sheets of steel through rollers until they formed tubes, the seams of which were then fire welded to create an air-tight cylinder. Using this technique must have made it particularly difficult to produce perfect specimens. Other components, such as the trigger mechanism and hammer assembly, also required extremely precise manufacture or the gun simply wouldn't work.

Not only was the accurate manufacture of musket barrels a difficult task, the casting of the shot itself was hardly an exact science with the musketeers themselves making much of their own ammunition in iron moulds which produced irregularly shaped shot. It was therefore necessary for the shot to be loose fitting in the barrel of the musket.

Badly fitting shot allows some of the expanding gases to pass around it, not only decreasing the efficiency of the burning gun powder but also causing *windage*^f where the gases passing around the shot would cause it to bounce around inside

^dLoaded from the muzzle (the dangerous end) rather than the breech, where the firing mechanism is located.

^eThe inside surface of the barrel being smooth.

^fNot to be confused with the modern meaning of 'windage' which refers to adjustments to the rifle sights to account for projectile drift caused by a side wind.

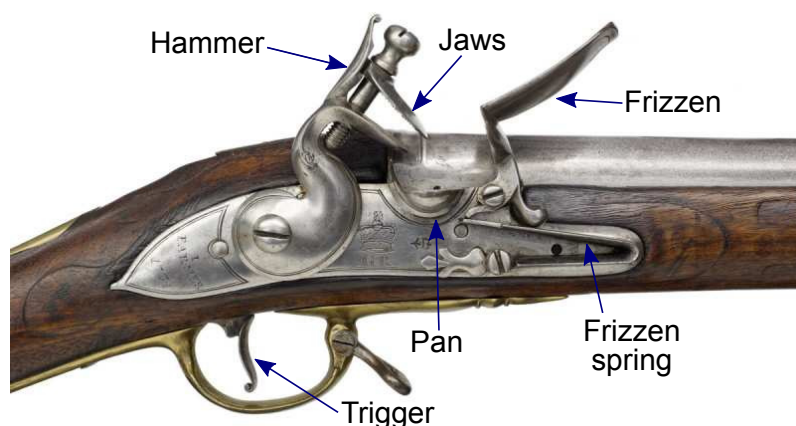


FIGURE 1.4: Close-up of the firing mechanism of the Land Pattern service musket, ©Board of Trustees of the Armouries.

the barrel [Tennent, 1864]. The result was a fairly slow moving, inaccurate projectile which would have had a useful range of only 50 - 75 metres.

One answer to this inaccuracy was often to load the musket with a lot of smaller shot. Propelling a large number of small shot did nothing to increase the accuracy of the weapon, but did improve the likelihood of a hit simply because of the number of projectiles was higher. Clearly though, the smaller projectiles carried less momentum than a single shot, reducing the effective range of the firearm and lessening the wounding potential of the individual shot.

These slow, imprecise projectiles fired from weapons that could only be fired a few times every minute were, at least to begin with, not much of a challenge to armour. As manufacturing techniques improved however, barrels and shot started to become more uniform in size, significantly increasing the efficiency of the powder burning in the barrel, converting much more of the powder's chemical energy into kinetic energy in the shot.

Rate of fire. Figure 1.3 shows one of the most famous muskets, the British Army's famous Land Pattern service flint lock musket or '*Brown Bess*' in service between 1722 and 1838, which could, perhaps, be considered the pinnacle of smoothbore firearms. Figure 1.4 shows a close-up of the firing mechanism[§].

The loading sequence for the Brown Bess was as follows:

- The trigger is pulled back to '*half cock*', providing access to the pan.
- A musket '*charge*' (Figure 1.5) is picked up, the top of which, including the shot, is bitten off and held in the shooter's mouth.
- A small quantity of gun powder is poured into the pan. In Figure 1.4 a small hole is just visible behind the pan; this leads from the pan into the rear of the barrel.

[§]In this and other flintlocks, the hammer jaws would hold a piece of flint providing a source of ignition, a much safer mechanism than earlier '*matchlocks*' where a constantly lit, slow burning cord or '*match*' was used to ignite the powder.

- The frizzen is closed, completely covering the pan and preventing the small amount of gun powder from spilling.
- The rifle butt is placed on the ground with the barrel pointing upwards. The remaining powder is poured into the barrel, along with the remains of the greased paper cartridge to act as wadding.
- The shooter spits the shot into the barrel.
- The shot and wadding are pushed down to the rear of the barrel with a ram rod, and then pressed down tight.
- The hammer is then pulled to full cock, making the rifle ready to fire.

The shooter then takes aim and pulls the trigger. The trigger releases the hammer, which (powered by a spring) strikes the flint onto the frizzen, simultaneously causing it to open, revealing the pan, and creating sparks which fall onto the powder held in the pan. The powder in the pan ignites, carried via the small hole into the rear of the barrel, igniting the compressed powder therein. Clearly, this whole process is time-consuming, with a well-trained soldier being able to fire around four rounds per minute.

Effective range. The effective range of firearms is chiefly a function of two properties, the muzzle velocity^h and the ballistic coefficient of the shotⁱ.

The muzzle velocity is affected very strongly by the windage discussed above, as well as the amount of gun powder in the barrel. Since the loading of a musket required a small amount of powder to be poured into the pan before loading the barrel, the *precise* amount of gun powder propelling the shot would vary widely from shot to shot. Considering Figure 1.6, which shows just how much of a difference muzzle velocity makes to the effective range of a projectile, knowing exactly where to aim the musket in order to hit a target more than a few tens of metres away would have been nothing more than guess work.

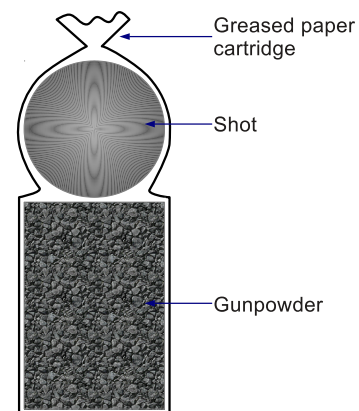


FIGURE 1.5: A musket charge.

In describing the demise of the Brown Bess service musket, Sir James Emerson Tennent wrote:

‘Although officially said to be effective at a range of 200 yards [183 m], it was the working rule of the soldier to reserve his shot *till he saw the whites of his enemy’s eyes*, and even then it was said that before he could bring down his man, he must fire a full weight of his body in lead...

...The French admit that during the Crimean war they fired away upwards of 25,000,000 cartridges, and certainly did not hit 25,000 men nor kill one-half

^hThe velocity of the projectile at the point where it leaves the barrel.

ⁱA measure of the effect of wind resistance on the leading surface of the projectile.

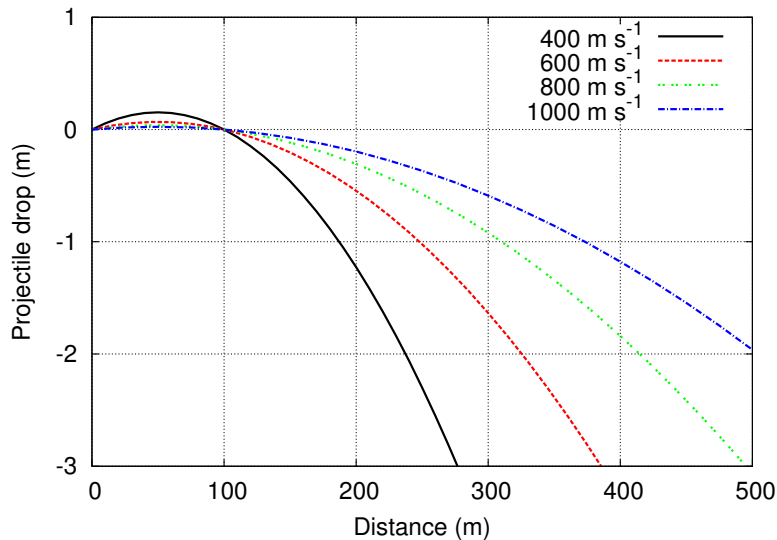


FIGURE 1.6: Graph showing idealised (i.e. ignoring the effect of all external stimuli except gravity) projectile motion for a firearm with sights zeroed at 100 m, over a range of muzzle velocities.

that number by musketry fire. “We believe,” says the *Times* writing about that period, that “the calculation used to be that one bullet in 250 carried death; and that estimate is probably not far from the truth.” ’

In 1838, a team of British Army Royal Engineers performed a series of tests to ascertain the accuracy capabilities of the Brown Bess. Reporting the results, the *Edinburgh Review* said:

‘The target first employed was 3 feet [0.9 m] wide and 11 feet 6 inches [3.5 m] high, which was struck by about three fourths the balls at 150 yards [137 m], fired with full charges - with reduced charges only above one half hit. Above this distance, the difficulty of hitting was so great, that the width of the target had to be increased to six feet; and, at 250 yards [229 m], of ten shots fired with full charges, not one hit the target: at 300 yards [274 m] shot after shot was fired without one hitting the object aimed at, or its whereabouts being ascertained. After various expedients in vain resorted to hit such an object at such a range, the officers gave it up in despair; and proceeded to calculate a table of “instructions for soldiers,” in firing with the musket, some of which will appear strange at the present day. The soldier was told in firing at a man at 600 yards [549 m], *to fire 130 feet [40 m] above him!* or in other words, if you wish to hit a church-door aim at the weather cock.’ [Tennent, 1864]

In the late 15th century rifling, the cutting of spiral grooves into a barrel, was developed. As the projectile was pushed along the barrel, it contacted the grooves which imparted spin onto it. This helped stabilise the projectile in flight, however its use was impractical in military use since it made it necessary to produce extremely accurate shot which was difficult to load into a barrel which was already fouled from previous firings.

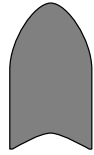


FIGURE 1.7: *Cross-section of a modern conical, hollow bottomed bullet.*

In 1823 Captain John Norton of the British army developed a conical bullet which had a hollow bottom. As the gunpowder ignited, the expanding gases forced the bottom of the bullet to expand 1. , forming an *obduration ring* which prevent the gases from escaping and engage the barrel's rifling. This design was initially rejected by the British Board of Ordnance, reportedly because spherical bullets had been in use for the last three hundred years and

had been adequate thus far. Over time, the conical, hollow-bottomed bullet was accepted and has become the norm for firearms [Shelke et al., 2010].

Figure 1.7 shows a cross-section of a typical modern bullet. This development has dramatically increased the effective range and accuracy of firearms. It was, perhaps, the invention of the revolver by Samuel Colt in 1835, the first firearm which was capable of being fired repeatedly without reloading, and subsequently the semi-automatic and fully automatic weapon which made firearms the threat that they are today.

1.1.2.2 Explosives

Explosives have been a battlefield threat for countless years; the Chinese famously used their invention of gunpowder to propel explosive rockets toward their foes. Early explosive devices were nothing more than gunpowder ignited inside a sealed container. When ignited in open space, gunpowder burns relatively slowly, giving off large quantities of hot gases. When contained, on the other hand, since there is nowhere for the heat to go, a burning grain of gunpowder will tend to ignite all the grains nearby, leading to much more rapid burning of the powder and bringing on an explosion.

Broadly speaking, explosives may be categorised in two ways; by their sensitivity or by their rate of decomposition. The sensitivity classifications are:

Primary explosives are extremely sensitive to external stimuli such as impact, friction, heat and static electricity. This makes them particularly dangerous to handle as they can ignite unexpectedly. Examples of primary explosives include the infamous nitroglycerin and 'Armstrong's mixture'^j.

Secondary explosives such as trinitrotoluene (TNT) and RDX (an initialism for Research Department Explosive) require significantly more energy to initiate than primary explosives, making them far safer to handle. A secondary explosive will usually need to be initiated with the use of a blasting cap, a small primary explosive charge which may be triggered by a variety of means, most commonly electrically.

Tertiary explosives or *blasting agents* are extremely insensitive and cannot ordinarily be triggered with a primary explosive. AN/FO (a mixture of *Ammonium Nitrate* fertiliser and a *Fuel Oil* such as diesel) is so insensitive that it can

^jA highly sensitive mixture of red phosphorous and an oxidiser such as potassium chlorate, chemicals which may be obtained from the strikers and heads respectively of ordinary household 'safety' matches.

only be detonated by a secondary explosive such as TNT, which in turn must be initiated with a primary explosive. Dual media blasting caps, in which a primary explosive is triggered, initiating a secondary explosive charge, are required to ignite tertiary explosives.

When classified by their decomposition rate, explosives fall into two subcategories:

Low explosives have a rate of decomposition (i.e. the rate at which they burn) which is lower than the speed of sound. Gunpowder is a low explosive.

High explosives such as TNT, detonate with an explosive shock wave that travels through the material at a supersonic speed. Explosive velocities for high explosives are typically in the range $3000 - 9000 \text{ m s}^{-1}$. The high explosive velocity gives high explosives a much larger destructive power than low explosives.

Nitroglycerin is one of the most famous explosive materials ever made. Being a primary explosive, it is highly sensitive to shocks and can easily be ignited by vibrations. It is also a high explosive, having a decomposition rate of around 7700 m s^{-1} . This makes it extremely difficult to handle. In the mid 19th century, Alfred Nobel famously discovered that, by absorbing nitroglycerin into a range of organic materials such as sawdust or diatomaceous earth^k, a far less sensitive explosive could be made. This discovery revolutionised safety, particularly within the mining industry, and assured Nobel's fortune.

Of course, military uses for stable high explosives are manifold. Explosive devices have always been popular in war theatres, initially because their explosive blasts were omnidirectional, that is the shock wave from the explosion travels in all directions. This means that, given a large enough explosion, large numbers of personnel can be immobilised with the use of a single explosive device.

Although there are a plethora of different types of explosive devices, they can, broadly speaking, be put into three categories.

Grenade. A small, light, hand-held device which may be thrown towards the intended target. Usually triggered by a timer.

Mine. A stationary device which may be buried or placed on a surface, often triggered mechanically via trip wire or pressure switch.

Mortar & Rocket. An explosive mounted on an external propellant device which may be 'fired' at a target. Triggering often performed by impact sensitive pressure switch.

^kA naturally forming silica based rock which easily crumbles to a fine powder.

The end result of explosive devices is usually the same. When initiated, huge amounts of gases are produced which expand rapidly; so rapidly in fact that, as they expand they pressurise the atmospheric air surrounding the explosive. The pressurised air is then forced to move away from the explosion faster than the speed of sound. This is known as a *blast wave*. As the blast wave is incident with a surface, energy is transferred into the body which then propagates through as a high velocity shock wave. The explosion will also violently throw the shattered remains of its container out as *shrapnel* or *fragmentation* which can travel at velocities measured in km s^{-1} . When these fragments hit other objects, these in turn may fragment and be thrown out as *secondary fragmentation*. In most cases, all of this will be accompanied by a large increase in temperature.

1.1.3 The aetiology of injury

1.1.3.1 Firearm trauma

The use of firearms by law enforcement and military personnel today is based upon the concept of *immediate incapacitation*, that is, the person being fired upon should be wounded to the extent that they instantaneously cease to be any threat [Patrick, 1989]. In the heat of a fire fight, heightened adrenalin levels may enable a severely, even mortally wounded aggressor to continue to pose a serious threat for some time after receiving the injury. In fact the only truly reliable way of immediately incapacitating an attacker is to damage the brain or upper spinal cord. Since armed personnel rarely have the opportunity to take carefully-aimed shots, this is not always achievable, and for this reason bullets are designed to impart horrific injuries on their targets. There are three basic components of projectile wounding:

Penetration. The tissue through which the projectile passes, and which it disrupts or destroys.

Permanent cavitation. The volume of space once occupied by tissue that has been destroyed by the passage of the projectile. This is a function of penetration and the frontal area of the bullet. Quite simply, it is the hole left by the passage of the bullet.

Temporary cavitation. The expansion of the permanent cavity by stretching due to the transfer of kinetic energy during the projectile's passage [Patrick, 1989].

The probability of immediate incapacitation is greatly increased by improving any of the three above factors. If penetration is increased, the bullet travels further through the body, increasing the possibility of damaging critical organs. Likewise, a bullet with a larger diameter, causing greater permanent cavitation will also be more likely to critically wound. Projectiles designed to transfer their kinetic energy reliably on impact will induce a substantial temporary cavity, potentially causing the fatal tearing of body tissues.

Penetration is primarily a function of fluid dynamics and streamlining, and bullets are already designed to be streamlined in order to increase their effective range. Larger diameter bullets are, by their very definition, heavier than their thinner counterparts, exacerbated by the need for larger amounts of propellant

to accelerate them to a useful velocity, and effectively decreasing the quantity of ammunition that may be carried by personnel. Hence, the only way of reliably increasing the damage from a bullet is to increase the efficiency of transfer of kinetic energy to the body.

This is commonly achieved by either designing frangible bullets that fragment shortly after penetration, with the fragments deviating from the projectile's initial path, or bullets which, when impacting at high velocity, tend to yaw in tissue, increasing their frontal surface area.

As discomfiting as the concepts discussed in this section may be, it is important to understand them since it may be possible to use these designs to our advantage in the design of suitable armour.

1.1.3.2 Explosive trauma

Explosives can have a devastating affect on humans. The cause of damage may be broadly categorised into four areas:

Blast wave. Being hit by a blast wave would be comparable to being hit with a hammer. Large explosives can produce blast waves which are capable of tearing off limbs.

High-speed shock wave. As the energy of the blast wave is transferred into the body, a high-speed shock wave is generated which travels through. It can be strong enough to tear tissues and rupture organs.

Fragmentation. Trauma from fragmentation is in many ways very similar to being stuck by a bullet. The key differences are *a)* unlike the precision manufactured bullets, fragmentation comes in all shapes and sizes, and *b)* fragmentation can be moving many times faster than a bullet. This means that penetration, temporary cavitation and permanent cavitation can all be significantly larger than for a bullet, and hence even more catastrophic.

Heat. The effect of high temperatures on the human body is quite obvious. Explosions can readily create temperatures in excess of 1000 °C [Cashdollar and Zlochower, 2007], which can cause rapid and significant burning.

Perhaps the greatest difficulty with explosives is their unpredictable nature. Two seemingly identical explosives will eject fragmentation of different sizes, moving at different speeds. This makes it particularly difficult to design explosive-resistant armour.

1.1.4 The development of modern armour

1.1.4.1 World War I (1914 - 1918).

Perhaps it was the change in the machinery of warfare that made military commanders re-investigate the use of personnel armour during the first World War. By this time rifles had become both accurate over long ranges and fast to fire and reload. The British Army had adopted the iconic Short, Magazine Lee Enfield Mk III (SMLE) rifle in 1907. With its supremely reliable bolt action and five-round magazine, the SMLE allowed a rifleman to take 15 well-aimed shots every minute, with a reasonably competent marksman being able to hit a 4 inch target at 100 yards [Miller, 2003].



FIGURE 1.8: *The Brewster body shield.*

The machine gun had also become an important part of the battlefield. The British Army used Vickers and Lewis machine guns, which had rates of fire of up to 600 rounds per minute and were fed by belts or large magazines. Machine guns such as these were able to apply sustained fire on relatively large areas a considerable distance away, and were easily capable of pinning down for extended periods, or even slaughtering entire companies of soldiers.

Military strategies had not evolved at the same rate as the technology however. Reports of men marching at a slow walk into machine gun fire were commonplace¹, and the excruciating stalemates during battles such as the Somme and Passchendaele, with an estimated 625,000 and 245,000 allied casualties respectively and somewhere around two million casualties in total, proved to both sides that something new was needed to swing the balance in their favour.

Plate armour was developed, such as the Brewster Body Shield from the United States, Figure 1.8. Constructed from chrome nickel steel and consisting of a helmet and breast plate, it was capable of withstanding Lewis gun bullets travelling at 820 m s^{-1} . It weighed 18 kg and was extremely cumbersome, and made it difficult to operate a weapon, so its practicality was limited [Bashford, 2008]. All of the other attempts to produce body armour suffered from the same problems, and so it was rarely seen on the field.

To provide an indication of the effectiveness of armour, the military helmets used in the first World War, typically having a very simple pressed steel construction, is estimated to have prevented between 2 and 5 per cent of the total casualties. This represents approximately 700,000 to 1,875,000 dead and wounded [Dunstan and Volstad, 1984]. For such a simple device, this figure is nothing short of remarkable.

World War I also saw the introduction of the tank, developed independently and simultaneously by the British and the French. These were the first real armoured war vehicles and, although they were not initially entirely effective, over time they certainly accelerated the end of the war. At this stage in their development, they were little more complex than a gun and an engine, fitted with tracks and surrounded by hardened steel.



FIGURE 1.9: *A British Mark I tank at the Somme.*

Tank crews during World War I were far from invulnerable. While the 8mm side armour was, for the most part, impenetrable to small arms fire, there was still

¹It should be noted that this was not in itself a military tactic, but was far too often the result of a combination of unreliable communications and a do-or-die attitude among the officer class.

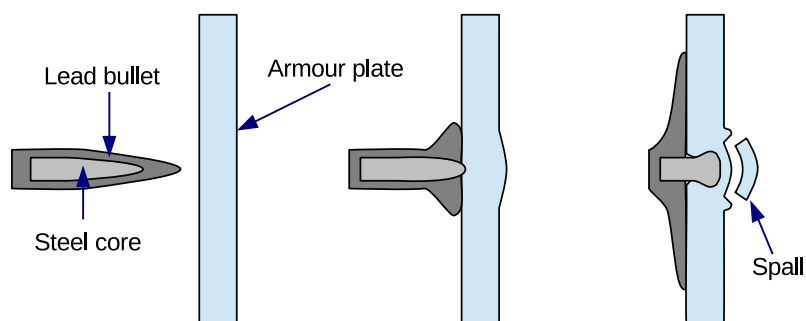


FIGURE 1.10: An armour piercing bullet penetrating armour.

considerable danger from mortars, grenades and the recently developed armour-piercing round, having a core constructed from tool steel. It is the hardness of the steel core within an armour-piercing bullet which enables it to perform its function. As shown in Figure 1.10, upon impact the lead outer of the bullet will peel away, but the hard steel core is still moving fast enough, and is hard enough, to impart considerable damage on the armour plate. During penetration the steel core deforms, becoming blunt which tends to cause the section of armour directly in front of the impact to detach and fly off as spall. Explosives have a similar effect.

Spall was acknowledged as a threat, and British crews of the iconic Mark I tank, shown in Figure 1.9, were issued with leather and chainmail masks and leather helmets to help protect them from it.

1.1.4.2 World War II (1939 - 1945).

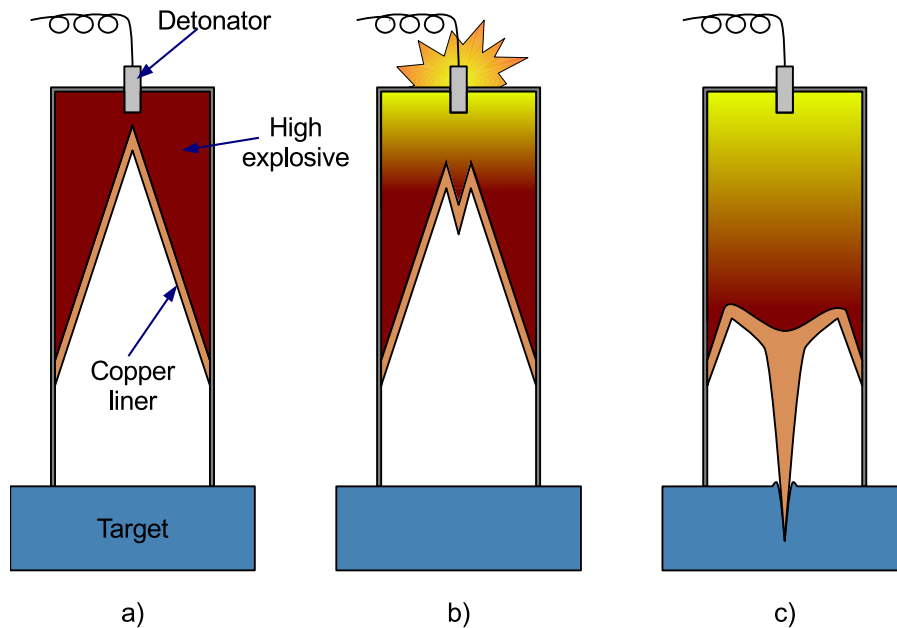
The second World War saw significant improvements in both body and vehicle armour.

During missions over Nazi-occupied Europe, possibly the most serious threat to allied bomber crews was that of *flak* (named after the German *Fliegerabwehrkanone*^m anti-aircraft cannon, which fired altitude triggered, explosive rounds which peppered aircraft with shrapnel). In an analysis of the wounds received by bomber crews, the US Eighth Air Force found that as many as 70% were caused by flak [GlobalSecurity.org, 2011].

The *flak jacket* was developed to help protect aircraft crews. It was constructed using woven strands of ballistic nylon, and proved to be good at defeating shrapnel and low-velocity projectiles, but was ineffective in the defence against bullets.

While there are reports of the occasional use of plate armour, it is thought that developments in firearms, particularly machine guns, made the use of plate armour practically futile. The infamous German MG-42 machine gun was not only supremely accurate, and with its 7.92×57 mm Mauser cartridge, firing a 12 g bullet at a velocity of around 800 m s^{-1} with a muzzle energy of approximately 4,000 J and a firing rate of 1,200 rounds per minute, it was also devastating. Personnel armour would prove to be ineffective against a sustained barrage of heavy, high-velocity bullets, and the accepted tactic when faced with the MG-42 was to take cover and

^mLiterally *Flyer defence cannon*, known as *Flak* for short.

FIGURE 1.11: A *shaped charge*.

attempt to attack the enemy machine gun crew only when the gun was being reloaded or having an overheating barrel changed.

Throughout the second World War, the only form of personnel armour in common use was the humble pressed steel helmet, which really only provided protection against glancing impacts and slow moving projectiles.

Armoured vehicles, on the other hand, had become commonplace. Not only were main battle tanks a regular sight on the battlefield, there were scores of additional armoured vehicles, from personnel carriers to mobile artillery. They all relied on hardened armour steel for their protection. The American M4 Sherman tank, for example, used armour plate with a thickness of up to 76 mm on the front of the turret and 45 mm on the sides of the hull. This made them all but impervious to rifle fire, and even to high explosives.

In 1888 Charles Monroe, a civilian chemist working with the United States Navy, had noticed that when a block of explosives with the manufacturer's name stamped into it was detonated next to a metal plate, the lettering from the stamp was cut into the plate. Now known as the *Monroe effect*, it is possible to focus explosive power by forming the explosive into certain shapes. These are typically referred to as *shaped charges*.

Figure 1.11 a) shows a simple shaped charge, in which a high explosive charge is packed around a conical copper liner. As the detonator initiates the charge, b), the explosive nearest the detonator ignites first. This starts deforming the copper liner into an inverted cone. As the detonation continues, c), the copper liner becomes a jet of copper travelling towards the target at or above the speed at which the explosive material detonatesⁿ. Whereas an ordinary explosive charge

ⁿThe detonation speed of PE4, the plastic explosive commonly used by the British military, is around 8200 ms^{-1} .

may barely dent the surface of armour plating, the copper jet is moving so quickly, it is able to force its way through a target which is far thicker.

This was used to great effect in such weapons as the German Panzerfaust (literally *armour fist* or *tank fist*) which fired a rocket propelled projectile which had a 400 g shaped charge warhead containing a 50:50 mixture of TNT and trihexogen. This weapon was capable of penetrating any of the armoured vehicles in use at that time.

1.1.4.3 The Cold War (approx. 1947 - 1991)

This period was, perhaps, the pinnacle of military development, at least in terms of the number and rate of new technologies being introduced. With the global superpowers preparing themselves for an all-out war, with the possibility that nuclear weapons may be employed, military spending on the development of new technology reached a crescendo. The expectation was that, should international relations break, battles would be held between highly technically advanced enemies.

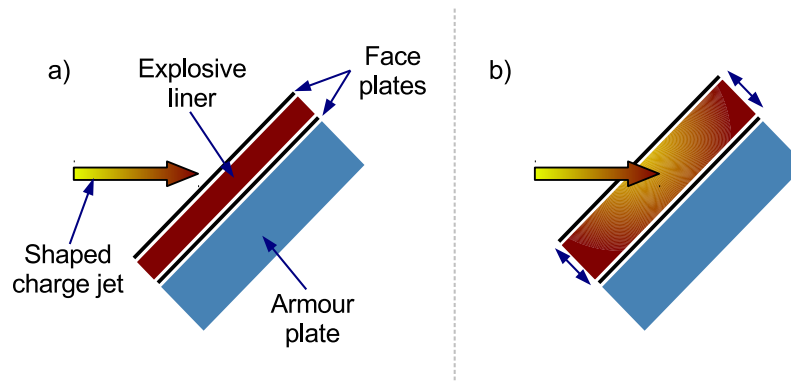
In 1966, whilst developing a new high strength fibre to act as a replacement for the steel used in tyres, Stephanie Kwolek created poly-paraphenylene terephthalamide, better known today as Kevlar[®]. It is a polymer which can be spun^o to produce fibres with an extremely high tensile strength, 3,600 MPa according to the manufacturers [DuPont, 2013]. Kevlar fibres can be woven into sheets, producing a material which is highly resistant to tearing. This property makes it particularly useful in armour, as a relatively small amount of Kevlar is capable of stopping bullets.

Kevlar was used to great effect in the Improved Northern Ireland Body Armour (INIBA) which was originally developed to protect British troops from small arms fire. The body armour was a vest which was worn underneath the soldier's smock, and incorporated an unspecified number of Kevlar layers. Due to the flexible nature of Kevlar fabric, it moves when struck by a projectile which can lead to significant blunt trauma underneath the impact site. The INIBA therefore had pockets in which hard armour panels, normally made of a hard ceramic like alumina (Al_2O_3), which enabled the assembly to protect the wearer from 7.62 mm bullets.

Developments in vehicle armour came in a variety of forms, from the simple to the highly technical. At the former end of the scale, one simple but very effective improvement was the use of angled armour plates. A projectile incident with an armoured surface which is normal to its direction of motion will obviously impart all of its energy onto the armour. By angling a surface, not only is the effective thickness of the armour increased, but there is a probability that the projectile will simply be deflected. The steeper the angle, the greater the probability of deflection.

Composite armour, consisting of several layers of different materials such as metals, plastics and ceramics, proved to be an effective method of defeating high explosive anti tank weapons.

^oThe spinning process is discussed further in Section 1.2.1.1.5 on page 32.

FIGURE 1.12: *Explosive reactive armour.*

Explosive reactive armour (ERA) is possibly the most counter-intuitive concept in armour development. Shown in Figure 1.12, it consists of a high explosive liner sandwiched between two face plates, normally of metal construction. A shaped charge penetrating the outer face plate causes the explosive liner to detonate which results in rapid expansion of the ERA. This can disrupt the passage of the shaped charge jet and can shatter kinetic energy projectiles. Since the explosion is not shaped, it causes little damage to the armour plate beneath. ERA, although effective, provides protection for a single impact, leaving the area underneath the exploded ERA vulnerable to additional strikes.

In order to overcome ERA, dual-warhead weapons have been developed. The BILL 2 anti-tank guided weapon produced by Saab and used by the Swedish Army since 1998, carries two separate warheads. When fired at a vehicle, the projectile senses when it is directly above an armoured target (the top often being relatively weakly armoured) and initiates its first explosive charge. This causes any ERA on the vehicle to be detonated, leaving the vehicle vulnerable to attack from above. Moments later, the projectile triggers its second warhead, a shaped charge which penetrates the now unprotected armour.

1.1.5 Modern threats

Conflict today is actually rather different than was envisaged during the Cold War years. Instead of fighting a highly technically advanced foe in carefully staged theatres, recent wars, such as those in Iraq and Afghanistan, have been fought against a relatively poorly equipped, but highly motivated enemy in what is known as *asymmetric warfare*. Fighting regularly takes place in urban environments, which adds an additional level of difficulty.

Increasing media coverage has resulted in a never-before-seen level of public awareness of the way conflict is performed. This has prompted in the development of ever more accurate weapons in an attempt to minimise the possibility of *collateral damage*, the incidental destruction of civilian property and non-combatant casualties.

Table 1.1 shows the mechanism of combat deaths for US military forces in the recent conflicts in Iraq and Afghanistan up to 2006 [Holcomb et al., 2007]. The overwhelming cause of death, almost three-quarters of the total, come from either explosions or gunshot wounds, with the former being accountable for more than half of all deaths according to documentation available to the public.

Mechanism	Deaths	Percentage
All explosions	2030	55
IED	1201	32
RPG	466	12
Rocket/mortar attack	337	9
Other explosions	26	1
Aircraft crash	33	1
Fall	353	9
Gunshot wound	712	19
Motor vehicle crash	579	15
Total	3707	100

TABLE 1.1: *Mechanisms of combat deaths of US Special Operations Forces up to 2006 during Operation Iraqi Freedom (Iraq) and Operation Enduring Freedom (Afghanistan) [Holcomb et al., 2007].*

1.1.5.1 Threats to vehicles

In modern times, two explosive threats are particularly prevalent, the improvised explosive device (IED) and the rocket propelled grenade (RPG).

IEDs may be constructed using entirely improvised explosive materials or with surplus explosive shells. They can be triggered using simple wire-and-battery systems, remotely using radios or mobile telephones, with simple timer systems, or by a wide variety of alternatives. The particular problem with this type of explosive is that they can be constructed by anyone with a suitable level of training, or access to the Internet or even book shops, where instructions are easy to find [U.S. Department of the Army, 2012]. They can range in size from small hand held devices through to entire cars or trucks packed with explosives.

Probably the most common use of IEDs today is as a means to disable armoured vehicles. Once disabled, all of the surviving vehicle occupants must exit the vehicle where they are vulnerable to more conventional attacks. When used in a staged attack, this can be a very effective offensive technique.

IEDs are typically omnidirectional explosives using traditional high explosives^P and so they are most effective when employed against light armoured vehicles and personnel. Their primary mechanisms for injury are through the explosive blast wave they generate and primary and secondary fragmentation. Heavily armoured vehicles such as main battle tanks are not easily penetrated by all but the largest IEDs.

The most common rocket propelled grenade system is the Russian made RPG-7. It can fire a number of different projectiles, with the high explosive anti tank (HEAT) being the most effective against armour. A cross-section of the RPG-7 HEAT round is shown in Figure 1.13. It is fired from a shoulder-mounted launcher and propelled by a rocket motor to a maximum range of around 920 m. Upon impact, the piezoelectric trigger causes the primary explosive detonator to ignite the high explosive charge. It uses a conical liner to give a shaped charge effect which enables it to penetrate armour quite effectively.

^Pi.e. they do not use shaped charges.

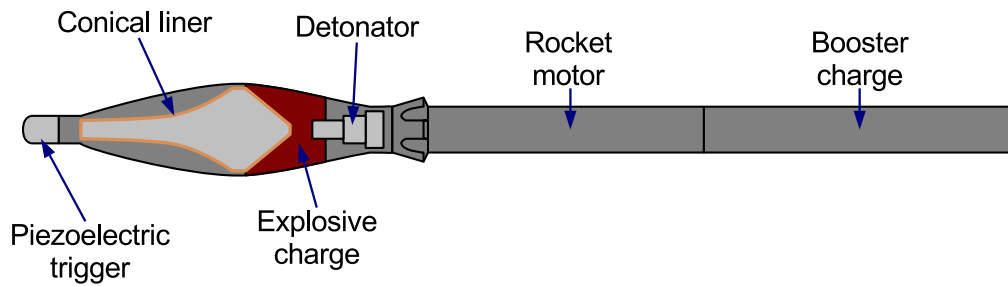


FIGURE 1.13: Cross-section of an RPG-7 HEAT projectile.

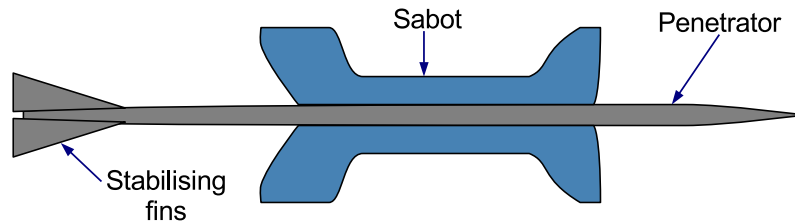


FIGURE 1.14: Armour Piercing, Fin Stabilised, Discarding Sabot projectile.

A modern threat to highly armoured vehicles is the kinetic energy penetrator. More accurately known as the Armour-Piercing Fin-Stabilised Discarding Sabot or APFSDS round, the projectile consists of two components as shown in Figure 1.14. The penetrator itself resembles an arrow and is held in an aluminium sabot which allows the slim projectile to fit snugly within a barrel. Upon firing, the sabot falls away from the penetrator, allowing the extremely streamlined shape of the penetrator to give it exceptional accuracy and range. With a projectile of this shape, it is not necessary to impart spin upon it to keep it pointing in the right direction in flight. Kinetic energy penetrators may be fired from smoothbore barrels which have a lower internal friction than their rifled counterparts, increasing the projectile velocity further.

The key to the kinetic energy penetrator lies in a delicate balance between having a low enough mass to achieve high muzzle velocities of upwards of 1500 m s^{-1} , whilst being heavy enough to carry a large amount of kinetic energy. This is achieved by constructing slim projectiles ($\approx 2 \text{ cm}$ diameter) using extremely high density material such as tungsten or depleted uranium [Zaloga and Sarson, 1993]. The slim, pointed design allows all of the energy carried by the penetrator to be imparted on a small area, and the elongated length ensures that it can continue to apply a penetrative force, even if the leading edge of the penetrator is eroded by armour.

After impact, as the kinetic energy penetrator passes through armour plate, it tends to break up into small shards. These shards, still moving at a reasonably high velocity, deliver their remaining energy to the internal components (including the ammunition and the crew) of the vehicle.

Modern armoured vehicles, such as the British Army Challenger 2 main battle tank shown in Figure 1.15 use a range of different methods to protect their occupants, including angled armour plating and explosive reactive armour, which is visible in Figure 1.15 on the side of the vehicle, and is particularly effective against both shaped charges and kinetic energy weapons. The Challenger 2 also carries countermeasures such as flares to confuse thermally guided projectiles.



FIGURE 1.15: A British Army Challenger 2 main battle tank in operation in Iraq. ©Crown copyright 2003.

Firearm	Cartridge	Bullet mass (kg)	Velocity (m s ⁻¹)	Energy (J)
Pistols				
S & W Model 10	.38 Special	0.0084	247	257
Colt M1911	.45 ACP	0.0120	373	836
Glock 17	9×19mm	0.0075	396	585
Colt Python	.357 Magnum	0.0084	430	778
S & W Model 29	.44 Magnum	0.0156	457	1625
IMI Desert Eagle	.50 Action Express	0.0211	427	1917
Assault rifles				
AK-47	7.62×39mm	0.0080	732	2133
SA80 L85A2	5.56×45mm NATO	0.0041	936	1787
M4A1 Carbine	5.56×45mm NATO	0.0041	936	1787
Sniper rifles				
Barrett M82	.50 BMG	0.0454	908	18686
L115A3	.338 Lapua Magnum	0.0162	914	6773
Dragonov SVD	7.62×54mm	0.0113	796	3568

TABLE 1.2: Energies produced by a range of firearms.

1.1.5.2 Threats to personnel

The threat to individual personnel from firearms is greater today than ever before. The precision of modern manufacturing techniques is easily capable of producing exceedingly accurate weapons which can fire bullets along a very predictably defined path. This has allowed manufacturers to produce increasingly powerful weapons, extending their range further and further.

Table 1.2 shows a number of firearms which are commonly used today. The range of energies produced by these weapons is extremely broad, and ideally, armour should be chosen based on the type of threat faced.

The ballistic threat imposed by a bullet depends on many factors including its mass, composition, shape and velocity. Since the use of different materials in the construction of an armour panel directly affects the level of protection it provides, the ballistic performance of an individual panel may be classified into one of several categories, based upon the type of ammunition the vest is designed to withstand. Detailed below are the categories as defined by the United States National Institute of Justice (USNIJ) [USNIJ, 2000].

Type I This armour protects against .22 calibre Long Rifle Lead Round Nose (LR LRN) bullets, with nominal masses of 2.6 g (40 gr⁹) impacting at a minimum velocity of 320 m s⁻¹ or less, and 380 ACP Full Metal Jacketed Round Nose (FMJ RN) bullets, with nominal masses of 6.2 g (95 gr) impacting at a minimum velocity of 312 m s⁻¹ or less.

Type IIA This armour protects against 9 mm Full Metal Jacketed Round Nose (FMJ RN) bullets, with nominal masses of 8.0 g (124 gr) impacting at a minimum velocity of 332 m s⁻¹ or less, and 40 S&W calibre Full Metal Jacketed (FMJ) bullets, with nominal masses of 11.7 g (180 gr) impacting at a minimum velocity of 312 m s⁻¹ or less.

Type II This armour protects against 9 mm Full Metal Jacketed Round Nose (FMJ RN) bullets, with nominal masses of 8.0 g (124 gr) impacting at a minimum velocity of 358 m s⁻¹ or less, and 357 Magnum Jacketed Soft Point (JSP) bullets, with nominal masses of 10.2 g (158 gr) impacting at a minimum velocity of 427 m s⁻¹ or less.

Type IIIA This armour protects against 9 mm Full Metal Jacketed Round Nose (FMJ RN) bullets, with nominal masses of 8.0 g (124 gr) impacting at a minimum velocity of 427 m s⁻¹ or less, and 44 Magnum Jacketed Hollow Point (JHP) bullets, with nominal masses of 15.6 g (240 gr) impacting at a minimum velocity of 427 m s⁻¹ or less.

Type III (Rifles) This armour protects against 7.62 mm Full Metal Jacketed (FMJ) bullets, with nominal masses of 9.6 g (148 gr) impacting at a minimum velocity of 838 m s⁻¹ or less.

Type IV (Armour Piercing Rifle) This armour protects against .30 calibre armour piercing (AP) bullets, with nominal masses of 10.8 g (166 gr) impacting at a minimum velocity of 869 m s⁻¹ or less.

The USNIJ (or NIJ for short) classifications are the most commonly used performance standards for bullet resistant clothing. The British police force also publish their own classifications known as HOSDB [Croft and Longhurst, 2007]. Broadly speaking, the HOSBD standard defines levels of protection which correspond to the NIJ classifications. Since NIJ is the more universal standard, HOSBD will not be discussed further in this work.

Recent theatres, including *The Troubles* in Northern Ireland as well as those in Iraq and Afghanistan, have taken place in urban environments. Narrow streets

⁹The grain, from the avoirdupois system of weights, is the traditional unit for the mass of bullets. 1 gr \approx 65 mg.



FIGURE 1.16: A British Army sniper in Afghanistan. ©Crown copyright 2008.

overlooked by buildings provide ideal conditions for snipers. Personnel are forced into tight formations making them easy targets, and buildings give good hiding places which are difficult to search. Snipers typically carry large calibre rifles which fire a heavy bullet at high velocity. The high kinetic energy of such a bullet present significant problems for body armour (see Table 1.2). In 1971 and 1972 in Northern Ireland, more deaths of British soldiers were attributed to snipers than to any other cause [Taylor, 1998].

Ballistic protection for today's British armed forces comes in the form of the Osprey modular body armour system. Osprey is, in its most basic configuration, a vest containing soft armour panels with additional pockets in which hard armour plates may be inserted. Additional components may be added to the vest to add protection to the shoulders and upper arms, neck and upper pelvic area [DE & S Joint Supply Chain, 2013]. Figure 1.16 shows a British Army sniper in operation in Afghanistan, wearing the Osprey body armour. A pocket containing a hard armour plate is clearly visible on his back. Exact details of the construction of the Osprey body armour system and its soft and hard armour components are, for obvious reasons, classified. It is thought, though, that the soft armour panels in the Osprey vest are classified as USNIJ Type IIIA (9 mm FMJ, .44 Magnum JHP) with the hard armour inserts being USNIJ Type III (Rifles) (7.62 mm FMJ) [Stirling, 2012].

There are commercially available ballistic vests and hard inserts available. AR500 Armor produce an armour insert made from 1/4 inch (≈ 6 mm) thick abrasive resistant steel with a Brinell hardness of 500 or greater which is rated to NIJ level III (Rifle) and weighs approximately 3.4 kg per panel [AR500 Armor, 2013]. Armored Mobility Inc. build ceramic based armour plates which incorporate a Dyneema® backing which also weighs approximately 3.4 kg per panel and is rated to NIJ level III (Rifle) [Armored Mobility Inc., 2013]. Another option is the MASS III produced by Midwest Armor & Strategic Solutions [Midwest Armor & Strategic Solutions, 2013]. Also rated at NIJ level III (Rifle), the armour component

in this panel is constructed solely from Dyneema® and weighs only 1.5 kg but is significantly thicker than the previous two examples.

Clearly, the act of skinning a cat may be performed using a variety of techniques. It is likely that different armed forces around the world will use a diverse range of body armour constructions.

1.1.6 The future of warfare

The present financial climate has seen a reduction in military spending, both operationally and in the development of new technologies. In a reversal to previous trends, modern high technology solutions are today being driven by low-cost, low-power consumer electronics. The components used to build today's 'smart' mobile telephones are in such wide demand that their construction has become remarkably cheap. Mobile phone central processing units (CPUs) are powerful enough to control a wealth of new technologies, such as automatic guidance systems for missiles, unmanned air vehicles (UAVs) and robotics can all be driven using cheap, off-the-shelf electronics.

It is expected that these technologies will be used to induce a dramatic increase in accuracy. This will help, not only with the protection of civilians and their property, but also reduces the cost involved in eliminating a target.

An example of this is the Automatic Target Engagement system for small arms, currently being developed. This is a device which is designed to retro-fit onto existing small arms. It uses an infra-red sensor to identify potential targets and a laser to measure the distance. It then augments the users view through the telescopic sight with the projection of an ideal aiming point. When the user pulls the trigger, the rifle waits until it is pointing at exactly the right place before firing a bullet [Corriveau et al., 2013].

The penetration of vehicle armour, a role traditionally taken by high energy explosives, appears to be moving towards kinetic energy (KE) projectiles. Long, thin, light and arrow-like, KE projectiles fly at extremely high velocities and are constructed from very dense materials such as tungsten or depleted uranium.

With the development of weapons offering pinpoint accuracy, traditional armour systems are likely to become less useful. With rifles all-but guaranteeing a head shot, the head generally being the most weakly armoured point, the focus on personnel armour is likely to shift slightly towards providing 100% coverage of the head. Improvements in and increasingly comprehensive use of armour piercing ammunition will possibly make existing armour solutions ineffective, necessitating the development of new materials.

The key to extending combat survivability for as long as possible may be held in the so called *survivability onion* shown in Figure 1.17. It shows a layered system in which being further away from the centre increases the possibility of survival.

Don't be seen. By keeping troops and vehicles a significant distance away from an enemy force, they will be unable to detect from which direction they are being attacked. This can be done with the use of unmanned vehicles, remotely controlled by an operator situated several kilometres from harm.

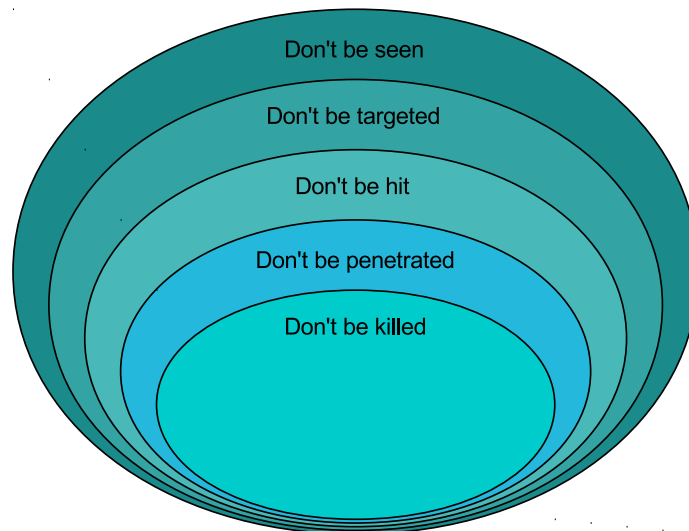


FIGURE 1.17: *The survivability onion.*

Don't be targeted. Improvements in radar jamming and *stealth* technologies will make it considerably more difficult for autonomously guided weapons to lock onto a target.

Don't be hit. Active protection systems for armoured vehicles such as tanks have been in use for some time, as well as decoy flares on aircraft. Improvements in sensor technologies and processing techniques to identify a threat are likely to drive the development of future countermeasures.

Don't be penetrated. Should vehicles or personnel find themselves in a position where each of the above layers has been overcome, it is necessary to prevent the penetration of any impactors. Armour systems should really be considered the last line of defence.

Don't be killed. Should all of the above fail, the only hope for personnel is rapid extraction from the combat zone and immediate, comprehensive medical care.

From the survivability onion, the most effective method of protecting tomorrow's military personnel, will be to keep them as far away from the battle as possible. The further development of unmanned vehicles, particularly those capable of operating autonomously, may be the ultimate goal for military powers at the present time. Although this may sound a bit like science fiction, it is likely to be only a few decades before autonomous fighting robots make their entrance in theatres of war.

1.1.7 Designing the ideal armour

Designing an 'ideal' armour is far from a trivial undertaking. While one material may provide a reasonable level of protection from a specific threat, it may be completely unable to protect from another. It is important to consider all of the main causes of injury in a design.

1.1.7.1 Personnel armour

On the face of it, arresting a projectile is a relatively straightforward task. This can be achieved using a suitably thick plate of an extremely hard material such as the ceramics alumina and boron carbide, or hardened armour steel. This is, however, only the first stage of protection.

‘It is a false assumption that eliminating the penetration of a projectile into the body by using a personal armour system absolves the wearer from serious injury or death. The kinetic energy of the projectile must be dissipated; the key is to ensure that the proportion of this energy which is coupled into the body is minimised, or is transferred over an extended time-scale or surface area. However, the design of a trauma attenuating backing placed between an armour plate and the body to enable this re-distribution of energy, must also ensure that the ballistic performance of the plate is not compromised.’ [Cannon, 2001]

In order to provide adequate protection for the wearer, it is first necessary to build a detailed picture of how injury may be inflicted on armoured personnel. Once a projectile has been arrested, there are three main potential injurious causes:

High-speed stress wave. The impact of the projectile on the hard face of the armour generates a very short duration stress wave within the armour plate, travelling at the plate’s sound speed. Assuming that the armour plate is in direct contact with the body, the stress wave can propagate from the armour into the body. Although there is very little gross movement of the armour panel with this event, the stress wave alone is capable of tearing tissue and damaging internal organs.

Movement of armour plate. The bullet impact imparts all of its kinetic energy onto the armour plate, resulting in a gross movement of the plate. This energy is then passed to the body, spread over the entire area of the plate. Although a bullet is light weight and an impacted armour panel is relatively heavy, since the bullet moves very fast, the corresponding plate velocity can be surprisingly high^r. This can lead to a large blunt force trauma.

Plate deformation. Whatever the composition of the armour plate, and assuming it is not stressed to failure by the impact, the armour plate will undergo some deformation. This is normally in the form of a bulge in the rear of the plate. The plate deformation will also result in blunt force trauma.

Dealing with each of these causes of injury individually can be relatively simple. Attaching a material to the rear of the armour plate which has a considerably different density to the plate itself will effectively trap the high-speed stress wave in the plate (see Section 2.2.2.1: Acoustic impedance). A soft material positioned between the body and the armour plate can provide a degree of cushioning which

^rA 5.56×45 mm NATO bullet having mass $m = 4 \text{ g}$ and velocity 940 m s^{-1} has a kinetic energy of $E_k = 1/2 mv^2 = 1767 \text{ J}$. If this energy is imparted in its entirety onto a non-deformable plate of mass 1000 g, it will be accelerated to a velocity of around 4 m s^{-1} .

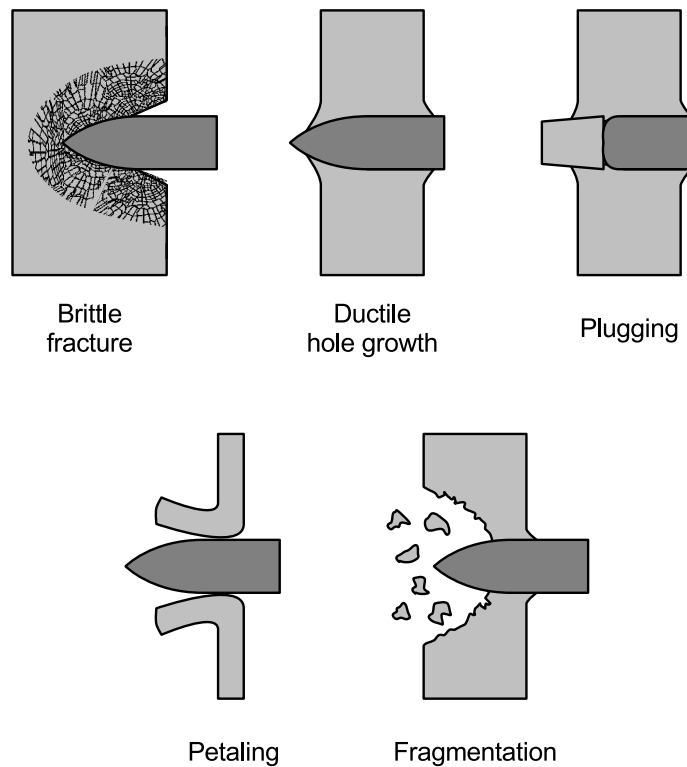


FIGURE 1.18: *Failure modes in impacted plates [Zukas, 1980].*

will reduce the effects of the gross plate movement and deformation. These solutions rely on the addition of materials onto the rear of armour, increasing both its size and weight, neither of which are at all desirable.

Military personnel are expected to carry a significant amount of equipment with them, including their weapon, ammunition, rations and hydration. Their lives depend on the ability to react and move quickly, so additional weight or bulk could be disastrous.

Modern ceramics such as alumina and boron carbide have proven to be successful in defeating rifle ammunition. It could even be said that, at the present time, armour has the edge over firearms, but this is not likely to remain true for long. A simple increase in the production and use of armour piercing ammunition could render current armour solutions ineffective. It is likely that there will be new developments in ammunition technologies in the not-too-distant future, which may make it possible to produce armour piercing rounds more cost effectively, with them becoming ubiquitous on the battlefield.

Current armour materials will need to become thicker and heavier if they are to withstand armour piercing ammunition which, as already discussed, could be detrimental to the effectiveness of combatants. It is necessary, therefore, to develop and investigate the use of new materials, composites and laminates in armour solutions in order to maintain the level of protection required by personnel.

1.1.7.2 Vehicle armour

Impacted plates tend to fail in a variety of ways, known as *failure modes*, which are dependant on a range of variables including material properties, impact velocity

and projectile shape. Some of the more dominant failure modes are shown in Figure 1.18.

Brittle fracture occurs when the target is constructed from a material with an extremely high compressive strength. Fragments of the target tend to be ejected from the impacted face as spall. Because of the large number of small, sharp fragments, brittle fracture can be useful in eroding a projectile.

Ductile hole growth can be caused when a relatively soft, ductile material is impacted by an ogival projectile. The impactor simply forces the target material out of the way as it passes through. This is accentuated by a fast moving projectile.

Plugging is the result of an extremely fast moving blunt or hemispherically nosed projectile. The generally accepted mechanism behind plugging is the work of plastic deformation local to the impactor being converted almost entirely into heat. Due to the high rate of deformation, the heat is unable to propagate away from the plastic region. The hot region around the projectile encourages further plastic flow in front of the projectile.

Petaling is mostly evident in thin targets, where an ogival impactor initially forces its way through the target and then imparts a bending moment onto the surrounding material.

Fragmentation occurs when the target material has a relatively low tensile strength. As the impactor passes into the target, the displaced material forces the rear of the target into tensile failure, ejecting material from the rear face as spall.

Monolithic armour plates will tend to exhibit one of the above failure modes depending on the speed and composition of the impactor. The future of vehicle armour will most likely concentrate on the use of laminate structures; layers of different materials, each exhibiting a unique failure mode, in order to provide a combination of properties.

For example, as discussed in more detail in Chapter 4 (page 107), a material which fragments under impact can be given an improved ballistic performance with the application of a thin elastomer layer on the rear face. Different combinations of materials will affect the progress of a specific projectile in different ways.

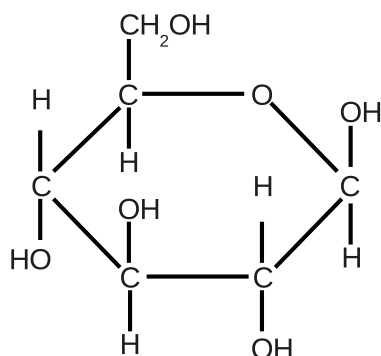


FIGURE 1.19: Structure of a glucose molecule.

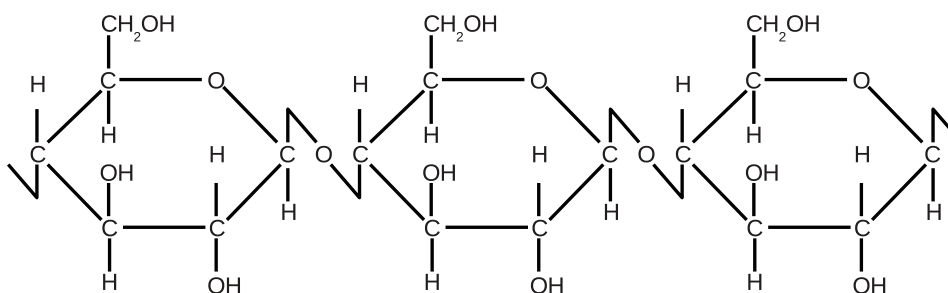


FIGURE 1.20: Structure of a cellulose chain.

1.2 Polymers, composites and nanocomposites

1.2.1 Polymers

Polymers^s are large molecules which are composed of repeating structural units.

Cellulose, the structural component found in the cell walls of green plants, is a naturally occurring form of polymer. It is constructed from long chains of the glucose molecule shown in Figure 1.19. In polymerisation, the outlying HO and OH groups in the glucose unit lose their hydrogen atom and join to oxygen atoms. Oxygen, having a valency of two, allows glucose units to join together to form long chains, between several hundred and several thousand units long. This is shown in Figure 1.20.

In the 1830s, Henri Braconnot discovered that by reacting concentrated nitric acid with wood or cotton fibres, he could obtain a highly flammable material which he named *Xyloidine*. What he had discovered was a precursor of nitrocellulose, and may be considered to be the first artificially engineered polymer.

Of course today, polymers are among the most commonly used materials. Unlike many organic materials, wood for example, polymers can be constructed to have very predictable and homogeneous mechanical properties. They can also be produced without the need for large amounts of heat, as would be required in the smelting of metals. Many polymers can also be formed into complex shapes by moulding them. These reasons may explain why polymers have become so common in this day and age.

^sFrom the Greek *poly* (many) and *meros* (parts).

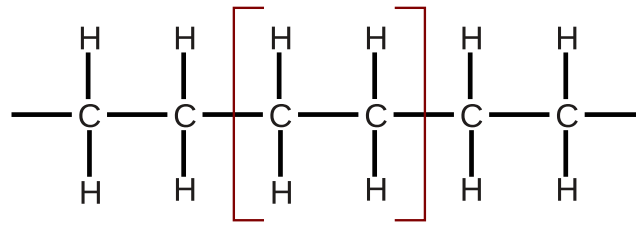


FIGURE 1.21: Structure of a polyethylene chain.

The term *plastic* is commonly used these days as a generic name for many types of polymers. Plastic can be used to describe artificially produced polymers, whereas the numerous naturally forming polymers are not generally considered to be plastics. This term could be considered apocryphal as polymers fall into three major classes:

Elastomer. Elastomers are rubbery materials in which the polymer chains are in a very disordered state, that is their entropy is high. Upon deformation the polymer chains tend to stretch out, becoming increasingly parallel to each other, which causes the entropy to decrease. Upon release, the entropy will return to a higher value, pulling the elastomer back to its original shape.

Thermoplastic. A thermoplastic polymer will soften upon heating to a critical temperature, and will then re-harden upon cooling. This is a repeatable process, which is ideal for the production of recyclable materials.

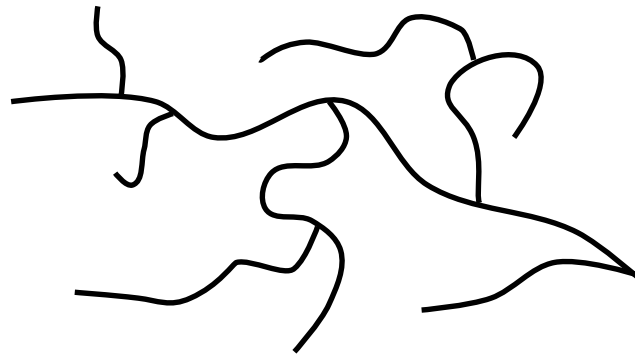
Thermosetting polymer. Sometimes called *thermosets*, these materials will soften upon heating to a certain temperature, but unlike thermoplastics, the heating causes a chemical change to take place, so when the material cools, known as *curing*, it will no longer soften under heating. This is useful for materials which are subjected to higher temperature environments.

1.2.1.1 Polyethylene

The most commonly produced polymer is polyethylene, PE. It has manifold uses, but is most commonly seen in the form of the ubiquitous plastic carrier bag. It is produced by the polymerisation of the gaseous molecule ethylene, C_2H_4 , into long chains as shown in Figure 1.21, where the repeating ethylene molecule is shown inside the red brackets.

PE is a thermoplastic with a melting point around $240^\circ C$. It has a number of different structural configurations, some of which are discussed in the following sections. All PE types show quite good resistance to corrosion from a wide range of chemicals and solvents, and their relatively high strength and simple moulding results in them having a wide variety of applications. In addition to the PEs described below, there are also a number of intermediate materials, such as Medium Density Polyethylene (MDPE), however these will not be discussed in this work.

1.2.1.1.1 Low Density Polyethylene (LDPE) LDPE has a relatively small number of ethylene molecules in its chains, in which branching is common. Branching occurs when, at certain points along the chain a carbon atom becomes covalently

FIGURE 1.22: *The branched structure of LDPE.*

bonded to another PE chain, instead of the usual hydrogen atom. This is shown in Figure 1.22. This results in LDPE having a lower density than other PEs since the branches prevent the chains from packing in well together. Its density is around 920 kg m^{-3} and it has a tensile strength of 10 MPa [A to Z of Materials, 2001c].

1.2.1.1.2 Linear Low Density Polyethylene (LLDPE) LLDPE retains a degree of the branching structure seen in LDPE, however the branches tend to be much shorter providing for a substantially linear molecule. Since, because of this linearity, multiple chains are able to exist closer together, the density of LLDPE is slightly higher, at around 925 kg m^{-3} . This also substantially increases the tensile strength to around 20 MPa [A to Z of Materials, 2001b].

1.2.1.1.3 High Density Polyethylene (HDPE) With a density of 960 kg m^{-3} , HDPE has a much smaller degree of branching than its lower density counterparts. This allows intermolecular forces to be much stronger and increases the tensile strength further to around 32 MPa [A to Z of Materials, 2001a]. The increased strength means that HDPE has applications which are unsuited to the lighter materials, such as hard hats and underground water pipes.

1.2.1.1.4 Ultra-High Molecular Weight Polyethylene (UHMWPE) UHMWPE has extremely long PE chains, and usually has a molecular weight of $2 - 6 \times 10^6$. It has a density of 945 kg m^{-3} , making it less dense than HDPE, and a tensile strength of 35 MPa being the strongest PE structure, at least in tension [A to Z of Materials, 2001d]. With the high strength of UHMWPE, its applications include such things as components for hip replacements.

1.2.1.1.5 Dyneema® and Spectra® Two variations of UHMWPE, Dyneema® from DSM and Honeywell's Spectra® alter the structure by passing UHMWPE which has previously been dissolved in a strong solvent, through a spinneret which forms thin fibres in which the PE chains predominantly line up, in the same way that spiders produce silk. This produces a material which has an exceptionally high tensile strength. These materials, which have been referred to as "The world's strongest fibre", are finding applications in a wide variety of situations, perhaps most interestingly in the form of armour, where woven mats of spun UHMWPE are layered on top of one another to produce an extraordinarily tear-resistant fabric.

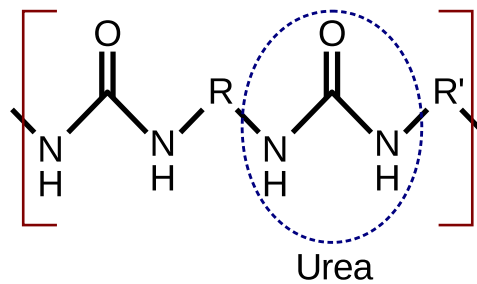


FIGURE 1.23: The repeating unit of polyurea, with the urea sub-unit highlighted.

The production of these materials is, however, particularly expensive. Whilst dissolved in the solvent, the UHMWPE solution is still quite viscous and requires a significant amount of energy to force it through the spinneret. The solvent itself is completely lost as the fibre dries.

1.2.1.2 Polyurea

Unlike PE, polyurea (PUr) is an elastomer. It is polymerised by the reaction of an isocyanate with a synthetic resin. The reaction of the two constituents can be particularly fast, with the resulting PUr curing in a matter of seconds. This property makes it particularly suited to use as a spray-on coating, being sprayed from a twin-nozzle gun and curing almost immediately on impact with the substrate.

The most common use of PUr is as a spray-on coating to protect the beds of pick-up trucks. It is tough, hard wearing, resistant to most chemicals and adheres well to many surfaces with little prior treatment necessary. It has also seen some use as a spall liner for blast mitigation on buildings, where it is sprayed onto the inner and outer faces of traditionally constructed walls [LINE-X.com, 2010]. Since the PUr adheres well to the wall and is highly elastic, a wall which would normally be destroyed by a blast may be held together by the coating.

The polyurea tested in this work was produced and supplied by Line-X UK[†], who produce a variety of different types of PUr for use as protective coatings. The variety of PUr tested carries the name PX3350. The precise chemical composition of PX3350 is a trade secret.

1.2.2 Composites

A composite is a material which is made up from two or more constituent materials, each having different mechanical properties. When the ingredients are combined, the resulting composite will inherit some of the properties from each constituent.

A classic example of a composite, and one of the earliest ever produced, is the *adobe* brick which is typically made from a mixture of straw and clay. The clay, when dried, has a decent strength under compression, making it an excellent building material. However, it has poor strength when enduring tensile or shear stresses, and buildings constructed solely of clay could crumble when subjected to high winds or impacts. To increase the strength of the clay, it is reinforced with straw. Straw has a poor compressive strength, but is much stronger under tension.

[†]<http://www.line-x.co.uk/>

The combination of these two materials results in a composite which is strong in all situations.

The basic components of composites are the *matrix* and the *reinforcement*, the clay and the straw respectively in the case of adobe bricks. More modern composites include the likes of glass-reinforced plastic, or fibreglass as it is more usually known, in which a hard polymer matrix, commonly epoxy, is reinforced with extremely fine glass fibres. Glass has a particularly high tensile strength, which combines with the high compressive strength of the matrix to create an extremely useful material.

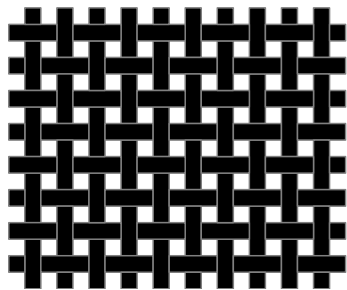


FIGURE 1.24: A woven mat for use as composite reinforcement.

In recent years, carbon fibre reinforced polymers have become particularly prominent. They are made in the same way as fibreglass, but use fine carbon fibres instead of glass, which has a significantly higher tensile strength. The resulting composite can have a strength which is, weight-for-weight, much higher than that of steel. This makes carbon fibre reinforced polymers especially popular in the automotive and aeronautical industries, where high strength and low weight are crucial.

Such composites can be expressed as having *dimensional strength*, that is, the strength it inherits from the reinforcement only applies when the force is exerted in a direction parallel to the fibres. In order

to maintain a high tensile strength in directions other than along the fibres, matrices often come in the form of a woven mat, as shown in Figure 1.24. This provides a high level of tensile strength in two directions, and by constructing a composite with multiple layers of reinforcing mats in different directions, it is possible to produce a material with high strength along all of its axes.

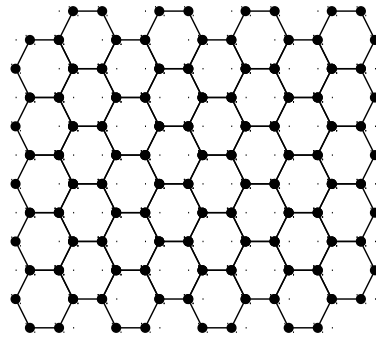
1.2.3 Nanomaterials

One of the most exciting developments in recent years has been that of nanomaterials. As the name implies, nanomaterials have physical dimensions measured in the order of nanometres (nm, 10^{-9} m), and are usually constructed from carbon.

There are numerous allotropes of carbon, many of which form naturally, and the range of properties exhibited by them extend to the extremes. For example, diamond is the hardest naturally forming material known, it is often used for its abrasive properties and is an excellent electrical insulator. On the other hand, graphite is one of the softest materials known, makes a superb lubricant and conducts electricity very well. These examples provide a hint that carbon, in different structural configurations, can form a remarkably diverse range of materials. Carbon-carbon bonds are strong and stable, so compounds which are made up entirely of carbon can be extremely tough.

1.2.3.1 Graphene

Graphene is a single layer of carbon atoms, having atoms arranged in a regular hexagonal pattern, as shown in Figure 1.25. Since it is only a single atom

FIGURE 1.25: *The structure of graphene.*

thick, graphene is the first truly two-dimensional material. Naturally forming graphite actually comprises layers of graphene stacked on top of each other, and considering that graphite is one of the softest materials known, it may appear counter-intuitive that graphene is, at the time of writing, the very strongest material known. Having a breaking strength of 42 N m^{-1} , where a hypothetical steel film of the same thickness would have a breaking strength of 0.4 N m^{-1} , graphene is more than 100 times stronger than steel [The Royal Swedish Academy of Sciences, 2010].

While graphene may be a truly remarkable material, its production in anything greater than tiny quantities is extremely difficult [Raza, 2012]. The most common technique, and that used by Andre Geim and Konstantin Novoselov who won the 2010 Nobel Prize in Physics for their work with graphene, is to take a graphite monolith and attach to it a piece of adhesive tape. When peeled off, the tape will pull away a few layers of the graphite along with it. This may then be pressed onto a substrate and, as long as the adhesion between the substrate and the graphite layer is stronger than the inter-layer bonding, a single layer of graphite, i.e. graphene, will be deposited [Novoselov, 2011].

There are, clearly, two problems with this technique, known as the *Scotch-tape method*. Firstly, very high quality graphite monoliths are required, and secondly, it is only possible to produce very small quantities.

While in recent years a variety of methods have been developed to isolate single layers of graphene (a good, recent review of which can be read in [Song and Cai, 2012]), producing it in significant quantities remains elusive.

1.2.3.2 Carbon nanotubes

A carbon nanotube (CNT) is effectively a sheet of graphene which has been rolled up to form a tubular shape. Being constructed from the same material as graphene, it shares its high strength. The tube formations can have an extremely small diameter of as little as around $0.4 \text{ nm}^{\text{u}}$. CNTs as long as 18.5 cm have been produced [Wang et al., 2009]. They can either be single-walled, i.e. a single tube, or multi-walled, being CNTs within larger diameter CNTs, with the multi-walled varieties showing a higher strength than the single. Being so small, CNTs can be considered to be one-dimensional.

^uCompared to carbon fibres which have a typical diameter of around 4000 nm.

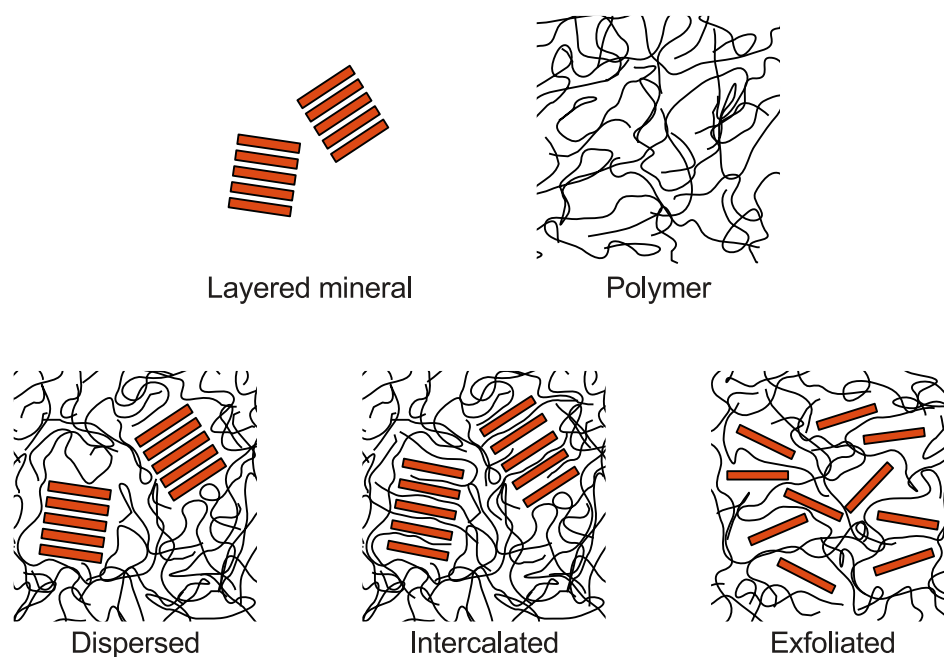


FIGURE 1.26: *Dispersal, intercalation and full exfoliation of a layered mineral in a polymer matrix.*

1.2.3.3 Buckminsterfullerene

The Buckminsterfullerene or *bucky ball* is a sphere constructed from a section of graphene, having a chemical formula C_{60} . It takes the shape of a truncated icosahedron, similar to a football, made of twenty hexagons and twelve pentagons and has a diameter of around 1 nm.

1.2.4 Nanocomposites

The strength of the nanomaterials discussed above is very closely related to their size. If nanomaterials are allowed to come in contact with one another, much of their inherent strength is lost, only to be replaced by the weak intermolecular bonds which make graphite so weak. In order to fully exploit their strength, they must be kept apart. One possible way in which this may be achieved is by using them as the reinforcing component in a composite material. In order help prevent the nanofillers from clumping together within a matrix, they must be used in very small quantities, typically a maximum of 5% by weight of nanofillers will be used.

True nanomaterials are, of course, complex and expensive to produce. Within this research project, a range of alternative materials were also experimented with.

1.2.4.1 Intercalated/exfoliated nanoclay

The idea of using organic clays as a composite reinforcement are a relatively recent development which has attracted some attention in recent years. The process, shown in Figure 1.26, involves first dispersing a layered mineral in a molten polymer matrix. By agitating the mixture (e.g. by forcing it through a screw extruder) the clay layers begin to separate, allowing strands of the polymer to intercalate the clay. Further agitation may cause the clay to exfoliate entirely. If a suitable organic

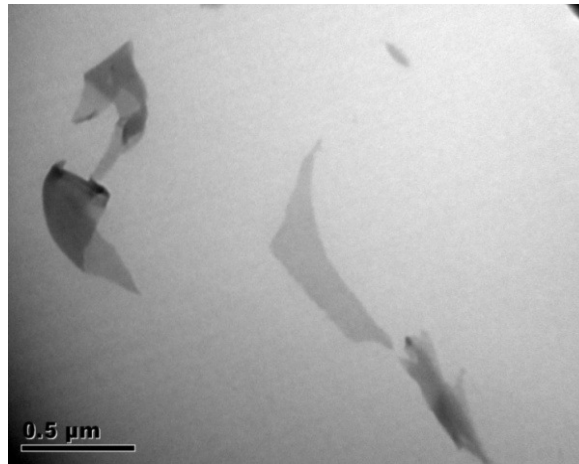


FIGURE 1.27: TEM image of nanoclay dispersed in a PE matrix.

clay is chosen, this method can be used to produce a nanocomposite without the need to first obtain the nanomaterial.

This technique has been used by a variety of experimenters, for example [Durmuş et al., 2007] who observed a >30% increase in yield strength for an LLDPE matrix containing 5%/wt organic clay over that of the unfilled polymer.

Figure 1.27 shows a transmission electron microscope (TEM) image of nanoclay dispersed in a PE matrix. This nanocomposite was produced by the Loughborough University Department of Materials as part of this research project.

1.2.4.2 Carbon black

Carbon black (CB) is one of the most commonly produced carbon materials today. It is produced by the incomplete combustion of heavy aromatic oils or natural gas in an oxygen free environment. The resulting carbon particles agglomerate into an aciniform^v of around 97% pure carbon. It sees common use as a reinforcement in rubber products such as automotive tyres, and as an industrial pigment [Mitsubishi Chemical Corporation, 2006]. CB is not normally considered a true nanomaterial as the agglomerated aciniforms typically have diameters of 100-1000 nm.

Perhaps the greatest attraction of CB over the truly nano Buckminsterfullerene is cost. At the time of writing, chemicals supplier Sigma-Aldrich offer CB with aciniforms <500 nm in diameter for under £20 per gram, whereas Buckminsterfullerenes cost over £300 for the same quantity [Sigma-Aldrich Co., 2013].

Figure 1.28 shows a scanning electron microscope (SEM) image of a PE matrix containing 2%/wt carbon black. As can be clearly seen in this image, the CB particles are clumped together in aciniforms.

1.2.4.3 Titanium dioxide

Titanium dioxide, TiO_2 , is a naturally occurring compound which is mainly used as a white pigment. Having an average particle diameter of around 190 nm, TiO_2 has been shown to provide increases in both yield stress and Young's modulus when used as a reinforcement in some nanocomposites [Selvin et al., 2003].

^vA shape which is similar to a bunch of grapes.

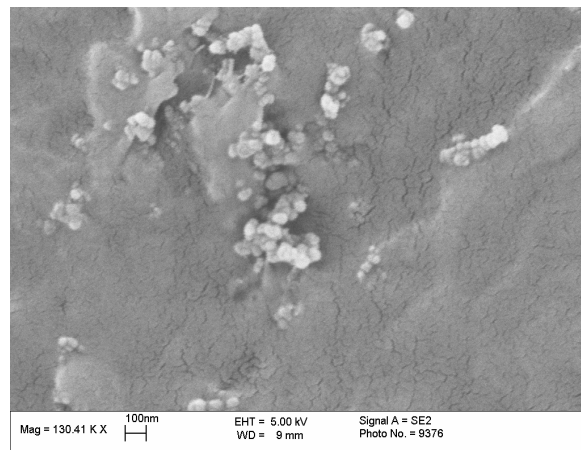


FIGURE 1.28: *SEM image of carbon black dispersed in a PE matrix.*

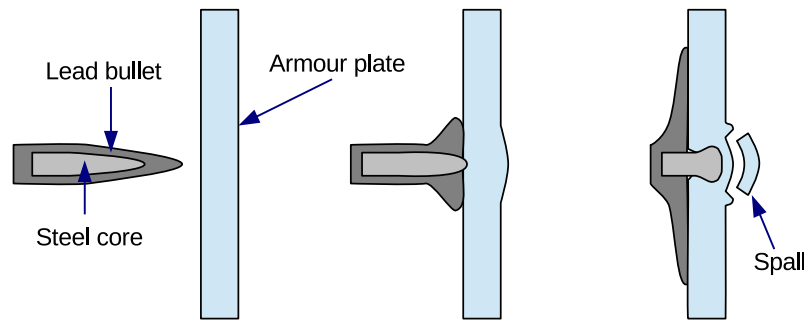


FIGURE 1.29: *Armour impact resulting in spall.*

1.3 The role of polymers in armour

As discussed in Section 1.1.7.2 (page 28), armour can fail in a variety of ways. While preventing the failure is difficult - normally leading to thicker, heavier armour plating - it may be possible to continue to protect personnel, even in the event of failure.

1.3.1 Spall liners

For penetrated vehicle armour, the most significant danger to the occupants comes in the form of spall. A typical impact resulting in spall is shown in Figure 1.29. When a projectile impacts, a significant amount of the energy carried by the impactor is lost in deforming the armour plate, and hence spall tends to move at a relatively low - albeit still potentially deadly - velocity. Vehicle spall liners often take the form of a polymeric or elastomeric layer adhered to the rear face of armour plate. This deforms plastically and/or elastically, absorbing the remaining momentum carried by the spall, ultimately arresting it. Perhaps the key to the effectiveness of a spall liner is its adhesion with the armour itself. Poorly adhered liners may simply move out of the way upon impact, whereas a liner with good adhesion will be forced to deform, absorbing kinetic energy as intended.

In the case of body armour, particularly that constructed from ceramic plates, protection from spall is still very important. An ceramic plate impacted by a high-velocity projectile will tend to fracture, ejecting many small, sharp, fast-moving fragments from the rear face, and presenting a considerable threat to the wearer^w. In order to capture the spall from ceramic armour, the liner should be capable of defeating at least low-velocity pistol bullets.

1.3.2 Trauma attenuating backings

In circumstances where armour is not completely perforated by an impact, especially where a ductile armour material is used, there is likely to be a significant amount of deformation to the rear armour face. This is likely to impart a blunt force trauma on the wearer, which in itself could easily be life threatening [Canon, 2001]. It is necessary to provide some form of padding between the armour and the wearer in the form of a *Trauma Attenuating Backing* (TAB).

Similar to spall liners, TABs can be constructed from polymeric or elastomeric layers, adhered to the rear face of the armour. The material they are constructed

^wThis failure mode is discussed in greater detail in Chapter 4 - *Understanding armour* on page 105.

from should be capable of absorbing the energy of the armour deformation in order to protect the wearer.

1.3.3 Laminate structures

The use of *bullet-resistant glass* has been in regular use in military vehicles since World War II. They are typically laminates, constructed from multiple layers of tempered glass and a clear polymer such as polycarbonate. The tempered glass layers, being relatively hard, perform the function of flattening and eroding the projectile. The softer polycarbonate layers absorb impact energy. By using multiple layers, the bullet erosion and energy absorption can happen multiple times, arresting the projectile rapidly.

Laminates may also be used as armour plating, using hardened armour steel or ceramic layers, separated by polymeric or elastomeric layers.

For all of the polymeric armour enhancements, the key property of the material being used is the amount of energy it can absorb during deformation - its toughness.

1.4 The mechanical behaviour of solids

Whether it is a bicycle wheel or a highly stressed building member, for countless inventions it is vital to understand the mechanical properties of the materials it is to be constructed from. The mechanical properties enable a designer to predict exactly how their component will react to different types and strengths of forces. As an example, consider the design of a simple golf club. It is important to minimise the weight of the club's shaft, whilst ensuring it has just the right amount of flexibility to dampen impact shocks. Knowing the mechanical properties of potential shaft materials allows a designer to make educated decisions without the need for trial-and-error testing of prototypes.

In order to quantify these properties, a sample of the material is forced to deform. To do this, we subject it to stress.

1.4.1 Stress and Strain

Stress, σ , is the measurement of the average force per unit area of an imaginary surface inside a deformable body. When the body undergoes a force which acts to deform the body, internal forces within the material resist any changes in its dimensions. These forces are referred to as *stress*, and are defined as the force acting on the body, F , divided by its cross-sectional area, A , i.e.

$$\sigma = \frac{F}{A} \quad (1.1)$$

In practice, this relation only works for non-deformed specimens, as during deformation the cross-sectional area of the body will change (see below) and so this stress is more usually referred to as the engineering stress, σ_E . It has the same units as pressure, $N m^{-2}$ or commonly the Pascal, Pa in SI units.

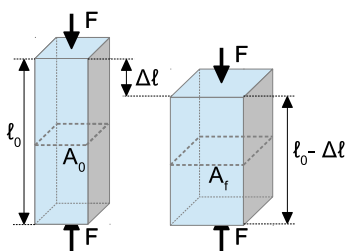


FIGURE 1.31: A body undergoing compressive strain.

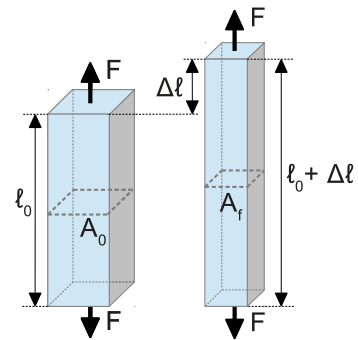


FIGURE 1.30: A body undergoing tensile strain.

As a body is subjected to stresses, it will begin to deform. As shown in Figures 1.30 and 1.31, tensile strain results in the elongation of the body parallel with the force, and a contraction perpendicular to it, whereas compressive strain has the opposite effect.

The term given to the measure of the deformation is *strain*. Its simplest form, the engineering strain, ε_E , is expressed as the ratio

$$\varepsilon_E = \frac{\ell}{\ell_0} \quad (1.2)$$

where ℓ_0 is the initial length of the specimen and the change in length $\ell = \ell_0 \pm \Delta \ell^x$. Since both ℓ_0 and ℓ have the same units which cancel out in the fraction, ε_E is a dimensionless value, although it is often expressed as a percentage.

^xFor tensile strain $\ell = \ell_0 + \Delta \ell$ and for compressive strain $\ell = \ell_0 - \Delta \ell$. See Figures 1.30 and 1.31.

This value provides a reasonable approximation when the change in length of the body is much smaller than the initial length (i.e. where $\ell \ll \ell_0$). To take larger strains into account, it is necessary to rewrite Equation 1.2 and consider the *strain path* for a body under deformation by using the infinitesimal change in length, $\delta\ell$. By doing this, the values of strain more accurately relate to larger strains, and so is usually referred to as the true strain, ε_T . Equation 1.2 becomes

$$\delta\varepsilon_T = \frac{\delta\ell}{\ell} \quad (1.3)$$

where ℓ is the instantaneous length of the body. It stands to reason then that

$$\int \delta\varepsilon_T = \int_{\ell_0}^{\ell_f} \frac{\delta\ell}{\ell} \quad (1.4)$$

where ℓ_f is the final length, and so

$$\varepsilon_T = \ln\left(\frac{\ell}{\ell_0}\right) \quad (1.5)$$

$$= \ln(1 + \varepsilon_E) \quad (1.6)$$

Making the stress calculation more accurate at larger strains is simple, as long as we assume that the volume of the specimen is conserved throughout deformation. That is

$$A(t) \cdot \ell(t) = A_0 \cdot \ell_0 \quad (1.7)$$

where $A(t)$ and $\ell(t)$ are the area and length of a specimen at any time during the deformation. If this assumption hold true, then we can change Equation 1.1 thus

$$\sigma_E = \frac{P}{A} \quad (1.8)$$

$$\sigma_T = \frac{P}{A_0} \cdot \frac{\ell}{\ell_0} \quad (1.9)$$

$$= \sigma_E (1 + \varepsilon_E) \quad (1.10)$$

where σ_T is the true stress [Prudom, 2012].

The engineering stress and strain provide adequate approximations at low strains. As the strain increases, however, it becomes much more important to use the true stress and strain. In compressive strain the surface area of a specimen increases, whereas tensile strain decreases the surface area. This change in surface area affects the stress, necessitating compensation.

1.4.2 Mechanical properties

It is quite obvious that, before attempting to construct something using a particular material, it is necessary to have a clear understanding of how that material will behave during operation. It is possible to quantify this behaviour by inducing the deformation of a material.

1.4.2.1 Young's modulus

From Hooke's law, when a spring or other elastic material is stretched, the force, F , required to stretch it is proportional to the extension thus:

$$F = kx \quad (1.11)$$

where x is the extension of the spring, and k is the *stiffness* of the material, known as the spring constant. An important point to note about this relationship is that it is reversible. When the force is removed, x will return to zero. In other words, by undergoing a deformation in which Hooke's law applies, the deformation to the material is not permanent.

The stiffness defined by k is only partly a function of the material; it is also influenced by the shape of the material. For example, a straight piece of wire will have a different value of k from the same material coiled up in a spring, as the coiled version will exhibit a much larger extension for the same force.

In order to understand a stiffness which is purely a property of the material, it is necessary to normalise Hooke's law by the cross-sectional area of the specimen. This is done by replacing the force with the stress as defined in Equation 1.1, and the extension with the strain from Equation 1.2.

Hooke's law now becomes

$$\frac{F}{A} = E \frac{\ell}{\ell_0} \quad (1.12)$$

or

$$\sigma = E\varepsilon \quad (1.13)$$

where E is the constant of proportionality known as Young's modulus or the modulus of elasticity. Since strain is unitless, E has the same units as stress, the Pascal.

1.4.2.2 Yield strength

Perhaps the most critical of all mechanical properties, the yield strength of a material is a measure of the stress applied to it before it begins to deform plastically. The terms *yield strength*, *yield stress* and simply *yield* all have the same meaning in this context. It is important to note, therefore, that they are used interchangeably throughout this work.

As a material is subjected to stress and begins to undergo strain, the deformation will initially be elastic in nature, that is it will not be permanent with Hooke's law being obeyed. As the material strains further, a critical amount of stress will be reached where the strain becomes plastic, i.e. permanent. This critical point is known as the yield stress, σ_Y . Simply put, σ_Y is the strength of the material, applying a stress greater than this will result in permanent deformation.

1.4.2.3 Flow stress

Flow stress may be defined as the amount of stress required in order to cause a material to continue deforming. The flow stress is ordinarily most visible in low strain rate experiments (see Section 1.4.4) where the deformation continues over a relatively long period of time.

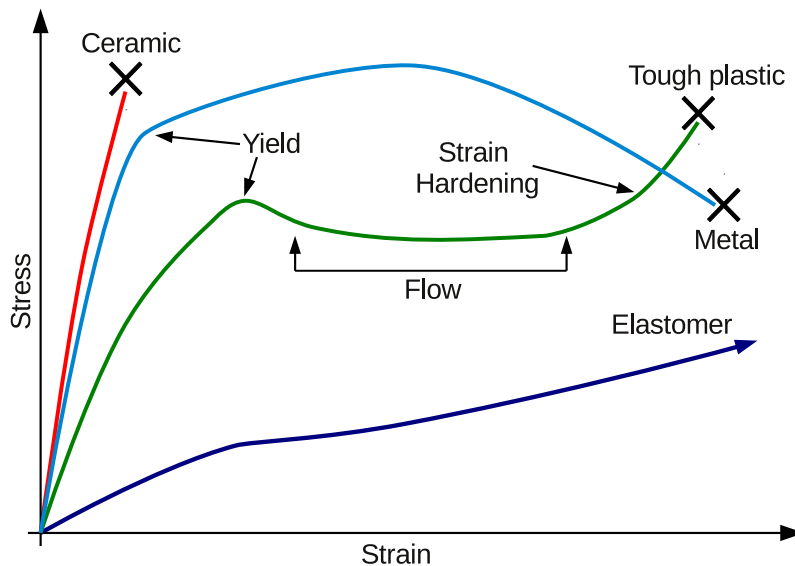


FIGURE 1.32: Typical tensile engineering stress-strain curve for a range of materials.

1.4.2.4 Ultimate strength

The ultimate strength of a material is the maximum stress which it can withstand. After yield, the stress will typically continue to increase up to the point of ultimate strength. At this point, the material begins to fail and its strength gets increasingly weaker.

1.4.3 Stress-strain curves

The qualities described above can be measured with the use of a stress-strain curve. Different types of material will have markedly different stress-strain relationships, some simplified examples of which are shown in Figure 1.32^y [Sperling, 2005].

Ceramic. Ceramics are particularly hard, brittle materials. The result of this is that ceramics are unable to undergo a significant strain before they fail. The red coloured curve in Figure 1.32 shows that a typical ceramic will absorb a fairly considerable amount of stress, strain remaining relatively low, until failure denoted by \times . Ceramics, therefore, don't really have a yield strength, but rather a stress-to-failure.

Metal. The light-blue curve in Figure 1.32, being significantly more ductile than ceramics, a metal will deform quite elastically up to yield, and then continue to deform right up to failure. The ultimate strength is the point of greatest stress within the curve.

Tough plastic. The behaviour of tough plastic materials is somewhat different. Rather than the smooth transition from elastic to plastic behaviour, upon yield a plastic will typically begin to flow, with a flow stress being a little lower than yield. Another important plastic behaviour is strain hardening,

^yN.B. These curves are representative of typical tensile stress-strain curve shapes only and are not meant to indicate the relative strengths of the materials shown.

where as the strain increases, the material becomes stiffer. Finally, the gradient of the stress-strain curve prior to yield is significantly non-linear, so Young's modulus is not constant for plastic materials. See Section 2.5.3.2 (page 87) for more information on estimating Young's modulus for plastic materials.

Elastomer. An ideal elastic would be defined by a purely linear stress-strain graph, showing no signs of yield or strain hardening. Real elastomers will, however, have a stress-strain curve more similar to a plastic material.

1.4.4 Strain rate

Materials have an intrinsic strain dependency on stress, in other words, applying a certain stress to a particular material will cause it to strain by a specific amount. It is, however important to consider the rate of strain, $\dot{\epsilon}$,

$$\dot{\epsilon} = \frac{d\epsilon}{dt} \quad (1.14)$$

Many materials have a range of responses within different strain rate regimes. Take, for example, a shear thickening fluid such as oobleck^z, a non-Newtonian fluid in which the viscosity increases with the rate of strain. While it is a thick, viscous liquid to the gentle touch, hitting it, such as with the slap of a hand, causes it to become so viscous, it feels almost solid. This peculiar property means that, while it would be impossible to stand in a body of oobleck, one could conceivably run across it.

Materials don't just become more viscous at higher strain rates, some become thinner. Tomato ketchup is an example of a shear thinning fluid. In its usual state it has a relatively high viscosity which is why it is often so difficult to get out of the bottle. Shaking the bottle rarely helps expel the ketchup, whereas holding the bottle vertically and tapping the side sends waves of shear stress through it, making it significantly thinner on a momentary basis, allowing it to flow.

The examples of oobleck and ketchup here were chosen to show relatively extreme examples of material behaviour at high strain rates. Most materials have a much smaller response to changes in strain rate, however at extremely high rates, this small response will be magnified, making a considerable difference to the observed results.

The strain rate

$$\dot{\epsilon} = \frac{d\epsilon}{dt} \quad (1.15)$$

is the rate of change of strain, ϵ , with respect to time, t . Since strain is a dimensionless quantity, $\dot{\epsilon}$ is expressed in units of s^{-1} .

Quasi-static mechanical tests are typically performed at strain rates of around $10^{-3} s^{-1}$, which induces a strain of 50% in 500 seconds. Such tests are commonly performed using universal test machines and may be compressive or tensile in nature. At quasi-static strain rates, since specimen deformation is performed so slowly, there is no need to take into consideration the effects of inertia or stress wave propagation, and the deformation may be assumed to be isothermal, as any temperature increase within the specimen has time to be transferred to the surrounding environment. As the strain rate increases these factors become increasingly important.

^zA suspension of starch, typically cornstarch, in water.

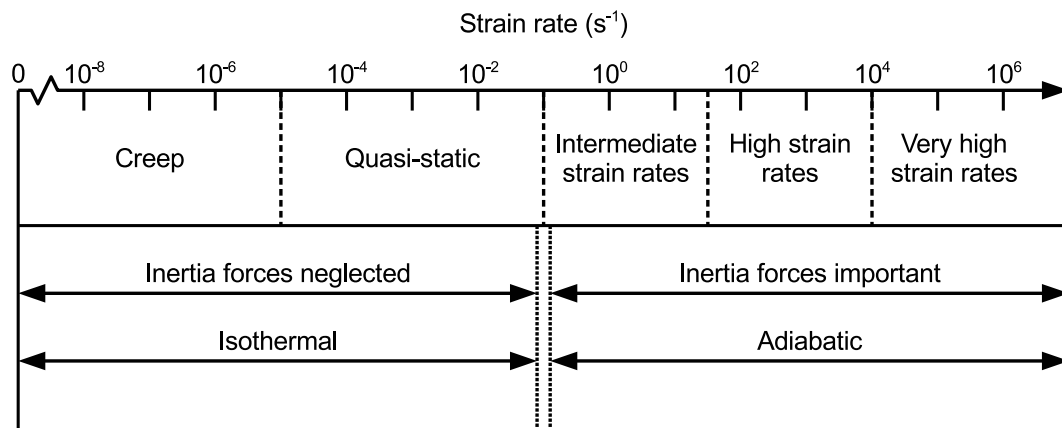


FIGURE 1.33: *Strain rate regimes. Adapted from [Nemat-Nasser, 2000].*

1.5 Mechanical Testing Techniques

In order to understand the mechanical behaviour of materials there are a range of testing techniques available. The methods are categorised by the way in which they cause a material to deform, and the speed of deformation. A few examples of mechanical testing techniques are detailed below.

Quasi-static strain rates. Perhaps the most common quasi-static technique is performed using a universal testing machine. As its name implies, this is a particularly versatile piece of equipment, capable of performing a wide variety of mechanical tests, across a wide range of quasi-static strain rates. Specimens tend to be small cylinders for compressive, and flat dog-bone shapes for tensile tests.

Intermediate strain rates. Universal testing machines are also often capable of deforming a material at intermediate strain rates. Dropweight systems, where a falling weight provides a compressive or tensile impulse at strain rates typically around a few hundred per second are also common. See Chapter 3.

High strain rates. The most common high strain rate experiment is the split-Hopkinson pressure bar (Chapter 2) which is primarily used for compressive tests, although tensile testing at a slightly reduced strain rate is possible with some modifications. Expanding ring techniques, where an explosion causes the dynamic expansion of a ring of material, and flying wedge systems, in which a pair of anvils gripping the specimen are forced apart by an incident wedge, are examples of high strain rate tensile tests.

Very high strain rates. At very high strain rates, the impulse must be driven by an extremely violent event such as an explosion.

1.6 Research description

The purpose of this research project is to construct a range of composite materials, in which the reinforcement is some form of nanomaterial or a different polymer, gain an understanding of their mechanical properties, and to develop numerical simulations which may be used to provide a thorough description of how they will respond in realistic scenarios. The information gleaned from this research will be used to develop an understanding of how high technology polymers and their nanocomposites may be employed to improve the effectiveness of both vehicle and body armour.

The role of polymer nanocomposites in body armour would most likely fit in the rear of hard armour panels, where they can help to absorb some of the energy of the impactor and the deforming armour plate, whilst assisting in the arrest of any remaining mobile particles.

In vehicle armour, nanocomposites could be positioned on the impact face of armour plate to capture any shards of eroded projectile and possibly alter the shape of the impactor, or on the reverse face where they can act as a spall liner to help protect the vehicle's occupants from fragmentation following an impact.

This is a collaborative project, with five distinct teams performing research in the areas:

Department of Materials, Loughborough University Developing nanocomposites and techniques for mixing and dispersal of nanofillers in the polymer matrices.

Department of Physics, Loughborough University Mechanical testing of new materials developed to determine their high strain-rate properties.

Department of Engineering, Cambridge University Mechanical testing of materials in a simulated impact environment.

Wolfson School of Mechanical Engineering, Loughborough University Developing numerical simulations of the behaviour of nanocomposite materials.

The Defences Science and Technology Laboratory (Dstl) Providing guidance and support to the overall benefit of the project.

The research detailed in this report is on the high strain rate behaviour of the materials developed for this project.

1.7 About this report

This report is written with two purposes in mind. First, it is a Ph.D thesis, detailing the work done and conclusions made over the course of a project. Secondly, with so much literature in the form of academic papers on the split-Hopkinson pressure bar technique, for new researchers, such as the author, establishing what information will be helpful to their specific requirements can be a daunting task. This report is intended to act as a guide, explaining the principles, construction, operation and analysis of the technique, and as such it is written to be accessible in a way that academic reports are commonly not. For this reason the computer code contained within the appendices is complete, which will allow an interested party to simply type in the code out of this report and run it, without having to fully understand it first.

Part II

Mechanical testing techniques

Split-Hopkinson pressure bar

“The most exciting phrase to hear in science, the one that heralds new discoveries, is not ‘Eureka!’ but ‘That’s funny...’.”

—ISAAC ASIMOV

The split-Hopkinson pressure bar (SHPB) is undoubtedly one of the most popular techniques for the investigation of material properties in strain rate regimes of around $10^3 - 10^4 \text{ s}^{-1}$. Its popularity is probably due to a number of reasons, including its reliable, straight-forward operation, and the relative ease with which data may be analysed.

The roots behind the SHPB can be traced back to B. Robins’ ballistic pendulum [Robins, 1805], which was designed to measure the velocity of bullets. As shown in Figure 2.1, a projectile of mass m is fired at velocity u to impact with, and be captured by a heavy pendulum of mass M . The transfer of momentum from the projectile causes the pendulum to swing away at velocity v .

The velocity of the pendulum is obtained using its maximum height h ,

$$E_{\text{kinetic}} = E_{\text{potential}} \quad (2.1)$$

$$\frac{1}{2} (m + M) \cdot v^2 = (m + M) \cdot gh \quad (2.2)$$

$$\therefore v = \sqrt{2gh} \quad (2.3)$$

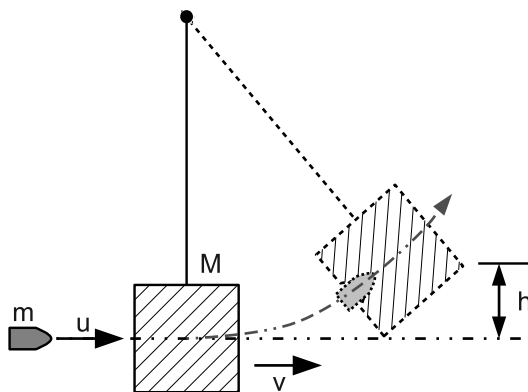


FIGURE 2.1: A ballistic pendulum.

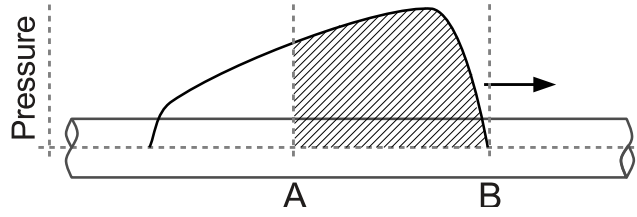


FIGURE 2.2: A pressure wave travelling along a metal rod.

where g is the acceleration due to gravity. We may now calculate the speed of the bullet using conservation of momentum, P ;

$$P_{\text{projectile}} = P_{(\text{projectile}+\text{pendulum})} \quad (2.4)$$

$$m \cdot u = (m + M) \cdot \sqrt{2gh} \quad (2.5)$$

$$u = \frac{(m + M) \cdot \sqrt{2gh}}{m} \quad (2.6)$$

$$= \left(1 + \frac{M}{m}\right) \cdot \sqrt{2gh} \quad (2.7)$$

The ballistic pendulum allowed the accurate measurement of the momentum of a projectile, being equal to the average pressure developed in an impact, multiplied by the time during which it acts. It was however incapable of measuring the instantaneous pressures created, or the exact time scales over which this happened since the energy of the projectile was imparted onto the pendulum so rapidly.

B. Hopkinson extended the ballistic pendulum with a view to overcoming this deficiency [Hopkinson, 1914]. Consider a projectile impacting with the end of a long metal rod; the momentum from the projectile is transferred into the rod and carried along its length as a wave of pressure, as shown in Figure 2.2, at a velocity equal to the speed of sound in the rod, $c_0 = \sqrt{E/\rho}$, where E is the Young's modulus and ρ the density of the rod material. If we further consider the area of the pressure curve represented by the length AB , which occurs over a time $t = AB/c_0$, the time integral of the pressure curve within this region, i.e. the shaded area, is equal to the momentum imparted into the bar by the projectile in time t . The pressure wave continues to travel along the rod until, as detailed in Figure 2.3, it reaches the free end, at which point it is reflected as a wave of tension.

Hopkinson utilised this with the addition of a split in his bar. A second, shorter bar called a *time-piece* was placed in contact with the end of the initial pressure bar. In what is now called the *Hopkinson pressure bar* the two bars have identical diameters, and the touching surfaces are carefully faced so that they are in almost perfect contact. The two rods are suspended in a horizontal position so that they are free to move. A projectile is fired at the at the pressure bar, creating a wave of pressure within the bar. The pressure wave travels along the bar, and at the split it is transmitted from the pressure bar into the time-piece practically unchanged. As with a solid bar, as the wave reaches the free end of the time-piece it is reflected as a wave of tension. As the tension wave reaches the split, the time-piece, unable to withstand any tension, flies away from the pressure bar, carrying with it the momentum imparted by the projectile in time $t = L/c_0$, where L is the length of the time-piece. The velocity of the time-piece, and hence its momentum, may be

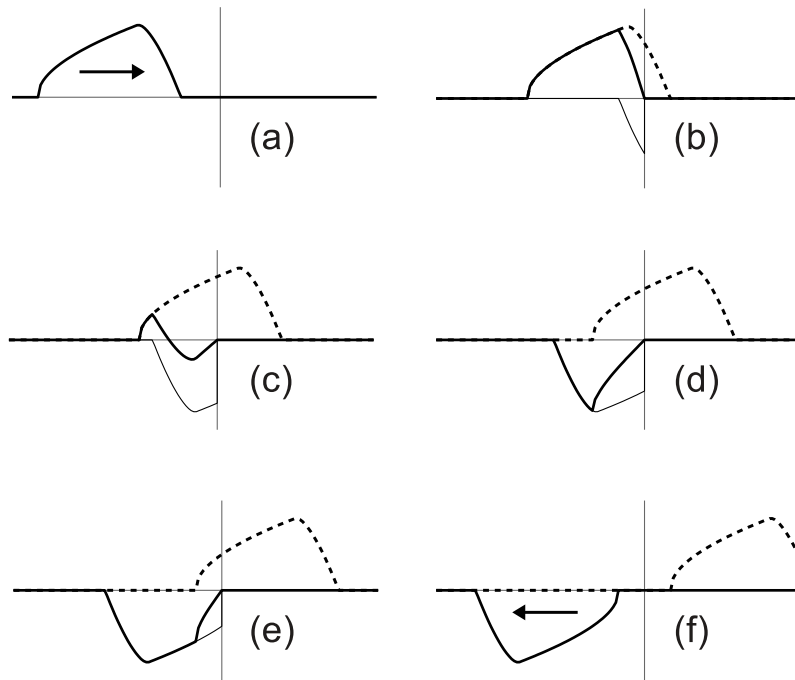


FIGURE 2.3: Reflection of a pressure pulse of arbitrary shape at a free boundary, represented by the vertical line. The dashed line shows the unimpeded progress of the pulse, P_u , as if there was no boundary, the thin line shows the magnitude of the pulse reflected, P_r , and the thick line shows the resultant stress in the medium, $P_u + P_r$.

measured by allowing it to be captured in a ballistic pendulum. If this experiment is repeated using time-pieces of differing lengths, it is possible to determine the areas of the pressure-time curves for different intervals.

The precise shape of the pressure curve, however, may not be deduced from such measurements.

In 1948 R. Davies devised a modification to the Hopkinson Pressure bar which utilised advances in modern electronic technology [Davies, 1948]. Instead of using a time-piece, Davies effectively turned the pressure bar into the earthed connector of a parallel-plate capacitor, as shown in Figure 2.4. This modification allowed measurements to be made electrically, and for the first time provided a continuous record of the longitudinal displacement, and hence strain, produced by the pressure pulse. The isolated conductor consisted of a brass disk held in an ebonite frame, attached close to the end of the pressure bar. The pressure wave induces a strain in the pressure bar, and hence it carries with it a longitudinal movement of the bar itself. The induced strain is dependent on the pressure bar's bulk modulus; its resistance to compression. As the pressure wave approaches the end of the bar, the small movement of the bar changes the capacitance between the bar end and the brass disk. If a potential difference is applied between pressure bar and brass disk, the movement of the bar can be recorded as a change in potential on an oscilloscope.

H. Kolsky may be attributed for the invention of what we today call the *split-Hopkinson pressure bar* (SHPB)^a [Kolsky, 1949]. He altered the focus of the experiment so that, instead of measuring the momentum of a projectile, the mechanical

^aAlso known as the *Kolsky bar* or *Kolsky's apparatus* in many circles.

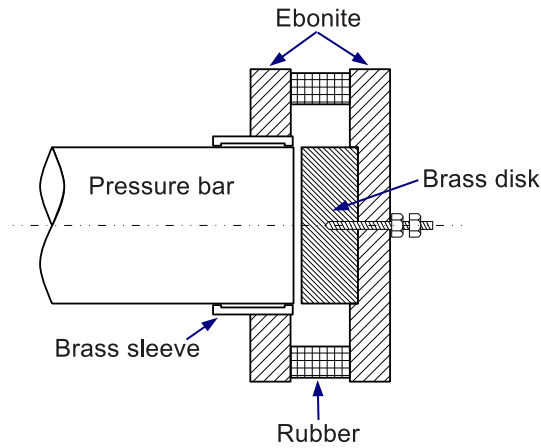


FIGURE 2.4: *Davies' modification to the Hopkinson pressure bar turned the free end of the pressure bar into the earthed conductor of a parallel-plate capacitor.*

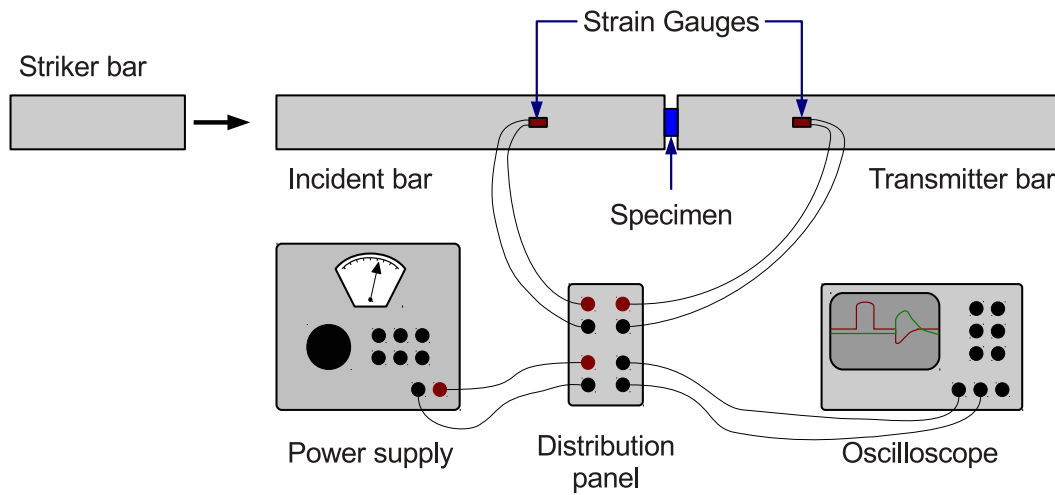


FIGURE 2.5: *A simple SHPB system.*

behaviour of a material undergoing rapid compression could be investigated. A projectile was propelled with the use of an explosive detonator, to collide with an incident pressure bar. The stress wave travelling along the bar, resulting in a strain in the bar, which was measured with a cylindrical condenser microphone placed around the pressure bar. At the end of the first pressure bar, the stress wave was incident with the specimen being examined, before being transferred into a second pressure bar connected to a parallel plate condenser similar to that used by Davies.

2.1 The modern SHPB

The developments made by Kolsky lead over time to the development of the modern SHPB. The fine tuning of the technique which has taken place over the last 60 years have made this one of the most versatile and universally trusted methods to investigate the mechanical properties of materials at high rates of strain.

A simplified version of the SHPB is shown in Figure 2.5. In use, a projectile or *striker bar* is propelled at speed to collide with the incident bar, creating an incident

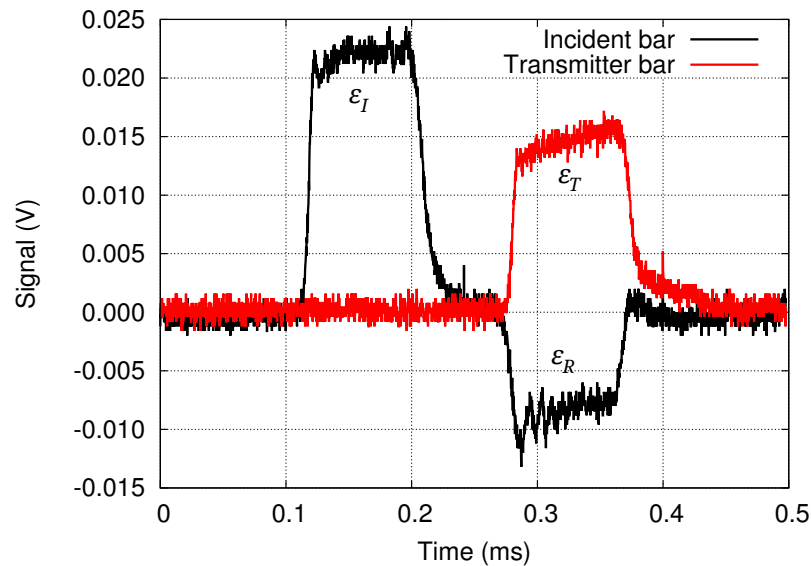


FIGURE 2.6: Raw SHPB data of a copper specimen.

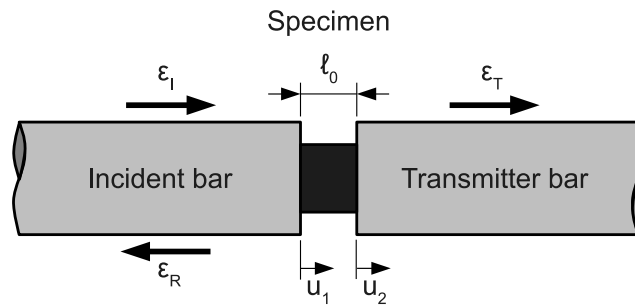


FIGURE 2.7: The strain pulses and consequent movement of the SHPB pressure bars.

strain pulse, ε_I of duration L/c_0 , where L is the projectile length and c_0 its sound speed, which propagates along the bar until it reaches the specimen. At this point, acoustic impedance mismatches between bar and specimen materials result in a portion of the pulse reflecting back down the incident bar, ε_R , while some of the pulse is transmitted through the specimen and into the transmitter bar, ε_T .

Figure 2.6 shows a typical oscilloscope recording from a modern SHPB system, in this case a copper specimen is used. The incident, reflected and transmitted pulses (ε_I , ε_R and ε_T respectively) are clearly visible. In the following sections it will be shown how such data could be analysed to produce a stress-strain curve.

2.1.1 SHPB theory

As the projectile impacts with the incident bar, the stress from the collision is effectively converted to elastic strain within the pressure bar. As shown in Figure 2.7 the pressure bar strain causes the incident bar to move by a distance u_1 . This puts stress on the specimen, causing it to deform and transferring some of the pressure onto the transmitter bar, which then moves by distance u_2 .

In a long rod, i.e. one with a length considerably greater than its diameter, it is reasonable to assume that the strain pulses take the form of a plane, one-dimensional wave. From the one-dimensional theory of elastic wave propagation,

the displacement, u of an arbitrary point in the bar at time t is

$$u = c_0 \int_0^t \varepsilon dt \quad (2.8)$$

where c_0 is the elastic wave velocity and ε is the strain. The displacement of the face of the incident bar, u_1 , is as a result of both the incident pulse, ε_I , travelling in the positive x direction, and the reflected pulse, ε_R , travelling in the negative x direction. It may be therefore defined as

$$u_1 = c_0 \int_0^t \varepsilon_I dt + (-c_0) \int_0^t \varepsilon_R dt \quad (2.9)$$

$$= c_0 \int_0^t (\varepsilon_I - \varepsilon_R) dt. \quad (2.10)$$

Similarly, the displacement of the transmitter bar, u_2 is caused by the transmitted pulse ε_T as

$$u_2 = c_0 \int_0^t \varepsilon_T dt. \quad (2.11)$$

The engineering strain in the specimen, ε_S is then

$$\varepsilon_S = \frac{u_1 - u_2}{\ell_0} = \frac{c_0}{\ell_0} \int_0^t (\varepsilon_I - \varepsilon_R - \varepsilon_T) dt \quad (2.12)$$

where ℓ_0 is the initial specimen length.

Assuming the stress across the compressive specimen is constant, an assumption which becomes more precise as ℓ_0 approaches zero, then

$$\varepsilon_R = \varepsilon_T - \varepsilon_I. \quad (2.13)$$

Substituting Equation 2.13 into Equation 2.12 gives

$$\varepsilon_S = \frac{-2c_0}{\ell_0} \int_0^t \varepsilon_R dt \quad (2.14)$$

with the engineering strain rate being

$$\frac{d\varepsilon}{dt} = \frac{-2c_0}{\ell_0} \cdot \varepsilon_R. \quad (2.15)$$

The applied loads, F_1 and F_2 , on each face of the specimen are

$$F_1 = EA(\varepsilon_I + \varepsilon_R) \quad (2.16)$$

$$F_2 = EA\varepsilon_T \quad (2.17)$$

where E is the modulus of elasticity (Young's modulus) and A is the cross-sectional area of the pressure bars. Hence, the average stress in the sample, σ_S , is given by

$$\sigma_S = \frac{F_1 + F_2}{2A_S} = \frac{1}{2} E \cdot \frac{A}{A_S} \cdot (\varepsilon_I + \varepsilon_R + \varepsilon_T) \quad (2.18)$$

where A_S is the cross-sectional area of the specimen. As before, Equation 2.13 may be substituted into Equation 5.1 to give

$$\sigma_S = \frac{E A}{A_S} \cdot \varepsilon_T. \quad (2.19)$$

The equations above show that the engineering stress is directly proportional to the transmitted pulse, ε_T , while the engineering strain is directly proportional to the reflected pulse, ε_R [Al-Maliky, 1997].

Both the engineering stress and strain fail to take into account the surface area of the specimen during deformation. For engineering applications this is an adequate representation of a material, as the deformation is very small. For situations in which specimen deformation is significant, it is necessary to calculate the value of true stress and strain, σ_{true} and $\varepsilon_{\text{true}}$ respectively.

This is done by using instantaneous values, so true stress becomes

$$\sigma_{\text{true}}(t) = \frac{F(t)}{A_S(t)} \quad (2.20)$$

and the true strain becomes

$$\varepsilon_{\text{true}} = \int_{\ell_0}^{\ell} \frac{d\ell}{\ell} \quad (2.21)$$

where the form $X(t)$ represents the instantaneous value of the property at time t .

In the case of SHPB work, instantaneous values of the length, ℓ , and surface area, A_S of the specimen are not normally known^b and so it is more convenient to represent the true stress and strain as a function of the engineering stresses and strains. In order to do this, we must assume that the volume of the specimen remains constant at all times, i.e.

$$A_S(t) \cdot \ell(t) = A_0 \cdot \ell_0 \quad (2.22)$$

A perfectly incompressible specimen such as this would exhibit a Poisson's ratio of 0.5.

2.2 Constructing an SHPB

This section discusses the construction of an SHPB system.

2.2.1 Pressure bar configuration

Probably the most common configuration of SHPB systems is the three-bar system shown in Figure 2.8. In this configuration, the incident and transmitter bars discussed earlier are combined with an additional *momentum bar*. During operation, as the strain pulse enters the momentum bar and is reflected back to the interface between momentum and transmitter bars, it is pulled away from the transmitter bar. This effectively traps the strain pulse within the momentum bar, preventing it from passing back into the rest of the pressure bar system. The energy in the momentum bar is attenuated by allowing it to move into a soft damping block constructed from modelling clay.

^bUnless the experiment is being recorded using high speed video.

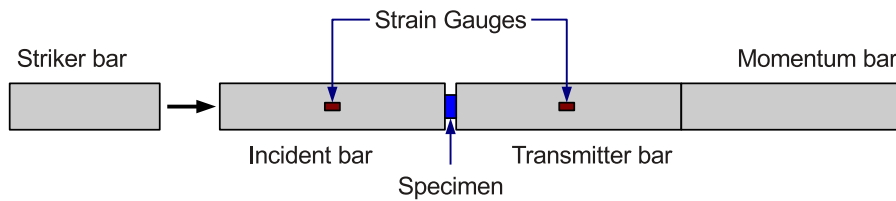


FIGURE 2.8: A traditional three-bar SHPB configuration.

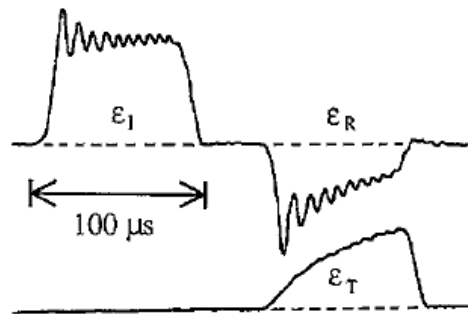


FIGURE 2.9: Pochhammer-Chree oscillations. Reproduced from [Parry et al., 1995].

An alternative configuration is the four-bar system, in which a *pre-loading bar* is installed between the striker and incident bars. This can be particularly useful to provide smoothing of the incident pulse. Shown in Figure 2.9, strain pulses which have a fast rise-time (which are normally desirable in an SHPB) are subject to so-called Pochhammer-Chree oscillations which are visible on the top of both the incident and reflected pulses. Rapidly rising strain pulses, similar to a square wave, are made up of a large number of Fourier components. Higher frequency components tend to travel slower than those of lower frequency. This dispersion results in the oscillations appearing to be superimposed on top of the incident pulse.

The addition of a pre-loading bar which is constructed of a material which has a lower yield strength than the incident pressure bar, can be extremely effective in damping the higher frequency Fourier components of the incident pulse. This can almost entirely remove the Pochhammer-Chree oscillations, and is not dependant on the length of the pre-loading bar [Parry et al., 1995].

Pressure bars must be of a length which allows pulses to pass over strain gauges without interfering, and sufficiently long enough to ensure one-dimensional wave propagation. Consider a system of steel bars, having a wave speed of 6000 m s^{-1} , onto which a strain pulse of duration $100 \mu\text{s}$ is imparted. Whilst travelling along a bar, the strain pulse will have a length of 0.6 m . Ideally, in order to maintain decent separation between incident and reflected pulses, pressure bars should be approximately double the length of the strain pulse. Practically, pressure bar lengths of 1.0 m are perfectly effective, which can make the location of materials much easier than for than for longer bars.

Clearly, strain gauges should also be positioned using similar rules. From experience, locating them on the incident and transmitter bars at a position 0.4 m away from the specimen is usually satisfactory. More information on strain gauges is given in Section 2.4.1 below.

Metal	ρ kg m ³	c_0 m s ⁻¹	σ_Y MPa	Z_0 kg m ⁻² s ⁻¹
Aluminium	2710	5119	80	13.9×10^6
Aluminium, 7068 alloy	2850	5061	550	14.4×10^6
Magnesium	1740	5029	95	8.8×10^6
Nickel	8900	4823	60	42.9×10^6
Nickel, strong alloy	8500	3597	1200	30.6×10^6
Steel, stainless	7930	5022	230	39.8×10^6
Steel, maraging	8100	5092	1800	41.2×10^6
Titanium	4540	5055	20	22.9×10^6

TABLE 2.1: *The density (ρ), wave speed (c_0), yield stress (σ_Y) and acoustic impedance (Z_0) of a range of metallic solids [Tennent, 1971].*

2.2.2 Bar material considerations

A primary consideration when designing an SHPB system is the material from which the pressure bars will be constructed. This choice will be dictated, in part, by the type of material which is to be tested.

Whatever material is to be tested, it is highly desirable that it undergoes a deformation which takes it beyond its yield stress. It should be quite conspicuous therefore that the pressure bars should be constructed from a material which has a significantly higher yield stress than the test material.

Consider, for example, that testing is planned for metallic materials. Many common metals have yield strengths ranging from 20 MPa (magnesium) through to around 1500 MPa (high-strength steel alloys). In order to test a wide range of metallic materials, it is clearly necessary to utilise pressure bars constructed from an extremely high strength material.

High strength, though, often carries with it high density, as shown in Table 2.1, which can lead to another complication.

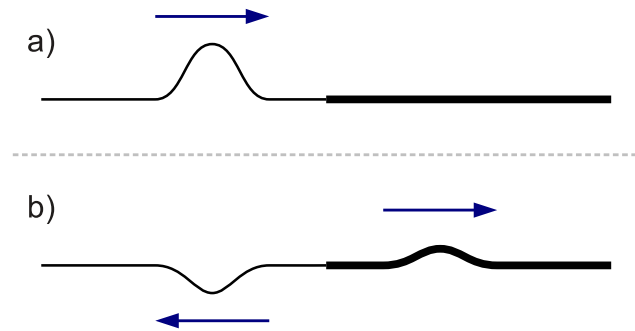
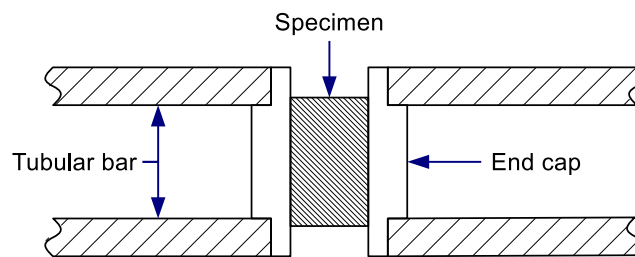
2.2.2.1 Acoustic impedance.

From ordinary wave dynamics, when a wave travelling along a medium reaches a point at which the medium's impedance changes, only a portion of the incident wave will be transmitted into the second medium, with the rest of the energy reflected back along the initial medium with a 180° phase shift. This is shown in Figure 2.10.

In terms of a wave travelling along a metal rod, it is the acoustic impedance, Z_0 , which defines this situation,

$$Z_0 = \rho c \quad (2.23)$$

where ρ is the density and c the wave speed in the material.

FIGURE 2.10: *Wave motion along media of changing density.*FIGURE 2.11: *A Tubular SHPB.*

It is this dependency on the density of the material which makes the acoustic impedance such an important consideration, particularly when it is desirable to measure the mechanical behaviour of low density, low impedance materials. An impedance mismatch will result in much of the incident pulse being reflected back along the incident bar. This leaves the transmitted pulse with such a low amplitude that any data obtained will have a signal-to-noise ratio which is too low to provide accurate, reliable measurements of the stresses involved in the experiment. A number of techniques are in common use as attempts to amend this problem.

The use of viscoelastic pressure bars is a popular technique employed to more closely match the impedances of specimen and pressure bar materials [Sawas et al., 1998], [Zhao et al., 1997]. Due to the viscoelastic nature of the bar material however, any wave input into the system will change as it travels along the pressure bars; the wave amplitude will attenuate, and the wave period will elongate. This makes it necessary to incorporate complex compensatory mathematical terms in the analysis of obtained data [Bacon, 1998]. Viscoelastic pressure bars require complete homogeneity of the bar material, and could be unreliable in environments of inconstant temperature and humidity. Additional techniques have been developed to minimise some of the difficulties associated with the nature of the viscoelastic bars, including the use of velocity gauges to replace the strain gauges [Casem et al., 2003]. This technique, however, remains a complicated one.

Another technique uses tubular pressure bars. The usual measurement of the engineering stress, σ_S within an SHPB experiment uses the relation

$$\sigma_S = \frac{EA}{A_S} \cdot \varepsilon_T \quad (2.24)$$

where E and A are the Young's modulus and surface area of the pressure bars, A_S is the surface area of the specimen and ε_T is the transmitted strain pulse. Rearranging for ε_T , it is clear that the amplitude of the transmitted wave is inversely proportional to the cross-sectional area of the pressure bar thus;

$$\varepsilon_T = \frac{\sigma_S A_S}{EA} \quad (2.25)$$

hence tubular pressure bars may be used to reduce the overall cross-sectional area of the bars, increasing the amplitude of the transmitted wave [Chen et al., 1999]. Whilst this is desirable, concern has been expressed by the author, [Hughes et al., 2013], that employing a tubular pressure bar system could be detrimental to the quality of recorded data.

With all SHPB systems it is necessary to have a flat surface in contact with the specimen, and so the bars employed in tubular systems must be *capped* at each end. As may be seen in Figure 2.11, an end cap introduces an additional interface between the bars and the specimen, resulting in wave reflections within the pressure bar cap. This makes it more difficult to deduce exactly what the specimen is experiencing. As the incident pulse is incident with the end cap, the energy will not be transferred uniformly into the cap, with the outer edge being loaded first, before propagating towards the centre. This can result in the non-uniform loading of the specimen, which may affect the reliability of any data obtained.

In terms of providing reliable, easily interpreted data, the simplest SHPB design uses solid, metallic pressure bars. The use of low-density metallic pressure bars can increase the amplitude of the transmitted signal. Previous studies have showed successful results from several low-density pressure bar materials including titanium [Gray et al., 1997] and alloys of magnesium [Shergold et al., 2006], [Hughes et al., 2013]. In this study a number of suitable, low impedance bar materials were examined to test their accuracy and reliability. Full details of this work is discussed in Section 5.1.1 (page 117).

2.2.3 Projectile design

The design of a striker bar or projectile is a fairly trivial task. The most common duration for an incident strain pulse is around $100 \mu s$, and so the appropriate length of the projectile may simply be calculated using the wave speed in the material it is constructed from.

It should be constructed of the same material as the pressure bars, and of the same diameter.

2.2.4 Pulse shaping

Some specimens, particularly those constructed from hard, brittle materials such as ceramics, benefit from a slow rise time of the incident pressure wave. This can be performed with the use of a pulse shaper. Figure 2.12 A shows an idealised representation of an ordinary incident pulse, with B being shaped to slow down the rise time.

Building a pulse shaper depends on the construction of the particular SHPB system in use. With the four-bar SHPB used at Loughborough university, where

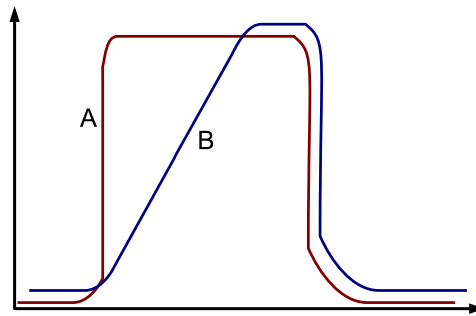


FIGURE 2.12: A shaped pulse.

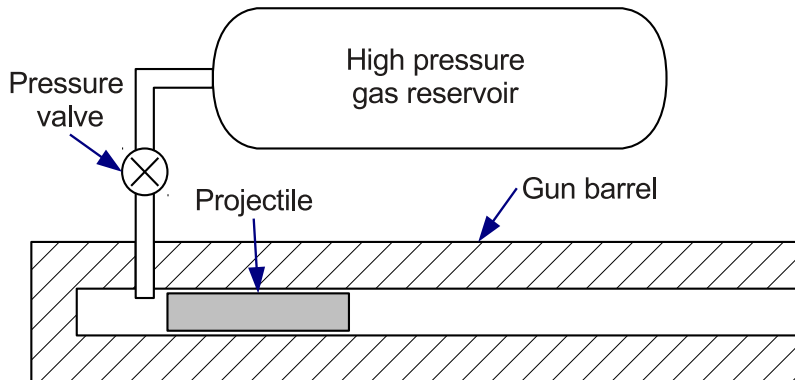


FIGURE 2.13: A simple gas gun.

an addition pre-loading pressure bar is inserted before the incident bar, a small section of a material softer than the pressure bars (e.g. copper) may be inserted between pre-loading and incident bars. The deformation of the copper section will cause the shape of the pulse which reaches the specimen to have a much slower rise time. Alternatively, constructing the projectile out of a softer material will also have the same end result, however, the projectile is likely to plastically deform during an experiment, limiting the number of experiments which may be performed using it.

2.2.5 Gas gun

The next consideration, and likely the most complex component of the whole system, is a means of accelerating the projectile.

In early experiments, such as those of Kolsky, projectiles were accelerated with the use of small explosive charges. In this day and age the use of explosives is highly regulated^c and so this is out of reach for many institutions. A more common method is the use of a gas gun. In simple terms, gas guns accelerate a projectile with the use of high pressure gases.

Figure 2.13 shows a simple design for a gas gun, which incorporates a high pressure reservoir which is filled with compressed gas. This is fed through pressure hoses, via a high pressure valve, into the rear of a gun barrel. When the pressure valve is opened, high pressure gas rushes into the barrel, accelerating the projectile towards the breach of the barrel. While this design may be simple, it is not without limitation.

^cAt least in the United Kingdom.

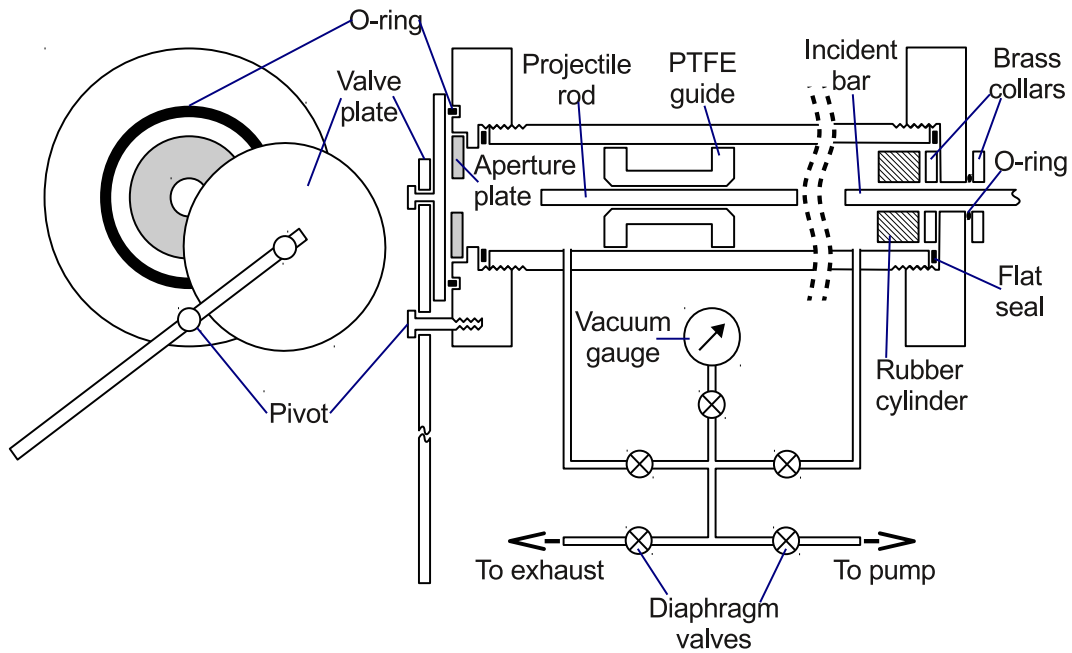


FIGURE 2.14: *The compact gas gun used at Loughborough University.*

- The pressure valve must be of a design which allows virtually instantaneous opening. If the valve is opened too slowly, low pressure gas will enter the gun barrel, pushing the projectile along the barrel. By the time the valve is fully opened, the projectile will have travelled part of the way along the barrel, limiting its maximum velocity. This function is normally performed by some form of bursting diaphragm.
- To ensure that the gas pressure doesn't drop significantly as the projectile moves along the barrel, the reservoir needs to have a volume several times that of the barrel.
- With the inside diameter of the barrel being only slightly greater than the projectile diameter, in order to achieve the desired projectile velocities of around 40 m s^{-1} it is necessary to have reservoir pressures of around 2 MPa (20 atm) with barrel lengths as long as 3 m [Parry and Griffiths, 1979].

In order to work around these limitations, a compact evacuated gas gun was designed at Loughborough University [Parry and Griffiths, 1979], shown in Figure 2.14. This device uses a wide-bore barrel, which significantly reduces the need for high pressure gases to accelerate the projectile, with atmospheric pressure being adequate. It is evacuated with the use of a simple roughing pump. Its operation is as follows:

1. The valve plate is opened and aperture plate removed.
2. The projectile is inserted, aperture plate replaced and valve plate closed.
3. The vacuum pump is turned on, exhaust valve closed and other valves opened.

4. When the internal pressure has dropped to around 1 KPa, the diaphragm valves are all closed. The system is now ready to fire.
5. To fire, the valve plate is rapidly opened by pulling the lever.

The projectile may be extracted by evacuating the gas gun again, then opening the exhaust valve and the valve leading to the far end of the barrel. Air will enter the barrel, pushing the projectile back towards the near end.

Although the design of the compact gas gun is fairly complex compared to a high pressure system, it presents a number of benefits over high pressure projectile propulsion systems:

- Since there is no requirement for high pressure gases or explosives to accelerate the projectile, the compact gas gun is inherently safe, with no requirement for the user to wear protective clothing. There is also no need to vent away any waste gases.
- Atmospheric pressure varies very little in a static location, so the projectile can be consistently accelerated to a predictable velocity.
- The system is very cheap to run since there is no need to purchase high pressure gas.
- It is significantly shorter than a high pressure gas system, having a barrel length of 1.32 m.

2.2.6 Pressure bar support & alignment.

Alignment of the pressure bar system is critical for reliable results. In order to maintain correct alignment along the length of the all of the pressure bars, they are supported on an optical rail using adjustable optical rail mounts.

The pressure bars rest on supports constructed from UHMWPE which are greased with a molybdenum based grease, to allow the pressure bars to move around with as little friction as possible. Accurate bar alignment is ensured with the use of a laser level.

Even more important than accurate pressure bar alignment, is the alignment of the bar faces. It is imperative that their faces are parallel as non-parallel faces will cause reflections of the pressure waves which could skew the data.

2.3 Specimen design

Specimens can be constructed from a diverse array of materials. Figure 2.15 shows a selection of just some of the materials which have been tested at Loughborough University in recent months. Construction methods for hard, metallic materials is relatively straightforward, as they can usually be machined out of larger pieces.

Producing polymer specimens can be a little more difficult. Many polymers begin to melt at quite low temperatures. When machining them, the heat build up underneath the cutting tool can easily increase the specimen temperature beyond

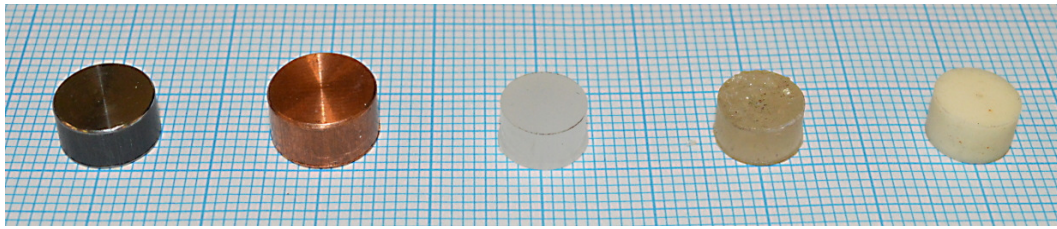


FIGURE 2.15: A range of SHPB specimens. Left to right: nickel-titanium, copper, LLDPE, polycarbonate and bovine femur.

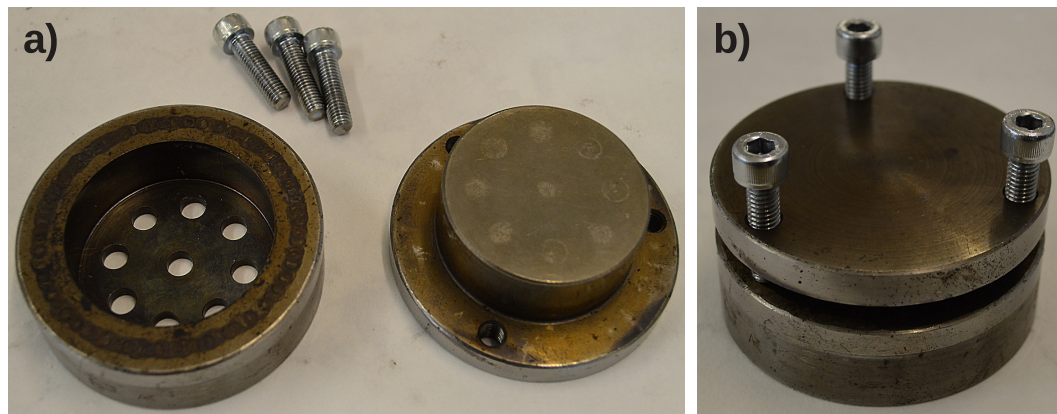


FIGURE 2.16: The mould used at Loughborough University for producing polymer specimens.

its melting point. This will, most likely, result in specimens which are inaccurately manufactured.

An alternative, and probably the simplest method of reliably producing accurate, reproducible specimens quickly, is to mould them in a hot press.

Figure 2.16 a) and b) show the mould in use at Loughborough University for the production of polymer specimens. Figure 2.16 a) shows the three components of the mould; the mould itself on the left, the mould lid on the right, and the extraction screws at the top of the picture. Its method of use is as follows:

- A measured quantity of the polymer to be tested in granulated form is added to the mould, and the mould lid is placed on top.
- The mould assembly is inserted into a hot press machine.
- The press is set to a predetermined temperature, a specific pressure is applied, and then left for a certain time to allow the moulding process to take place.
- While still under pressure in the hot press, the mould is cooled to approximately room temperature.
- Once removed from the press, the extraction screws are fitted and screwed in to prise the mould lid off, and the specimens removed.

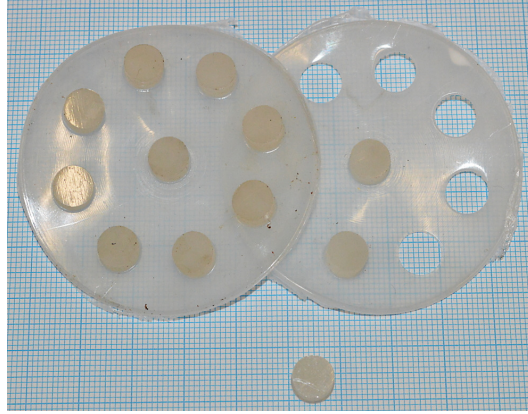


FIGURE 2.17: LLDPE specimens as extracted from the mould.

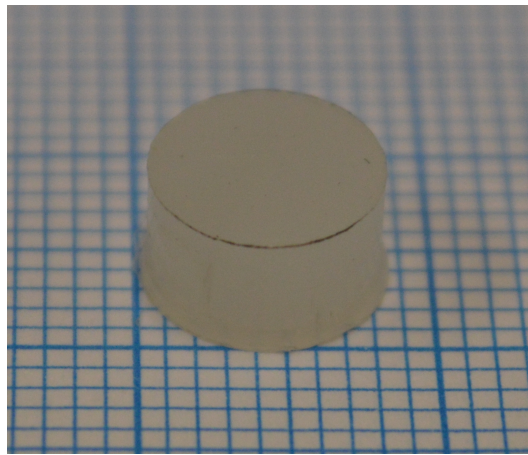


FIGURE 2.18: Close-up of a single LLDPE specimen.

Once removed from the mould, specimens take a form similar to that shown in Figure 2.17. From here, they can be removed from the backing sheet with the use of a punch. Due to the inevitable shrinkage of hot-moulded polymers, the punching out of specimens does tend to leave a small lip at one end, but it is typically so small it's effects can be ignored. The lip can be seen in the punched out LLDPE specimen shown in Figure 2.18.

In order to assume that the specimen is loaded in a uniform manner, it is vital to ensure that the specimens faces are as parallel as possible.

2.3.1 Inertia effects in specimens

Since the specimen is initially at rest and is expected to deform at a particular rate during an experiment, acceleration, and hence inertia, are associated with the change in strain rate. Inertia should be minimised in order to determine the intrinsic material properties.

While exploring the dynamic deformation of copper and aluminium, [Samanta, 1971] concluded that the specimen stress, σ , should be measured by the mean value of the stresses at both ends, with some additional inertia terms, and taking into account the rate of change of specimen energy, in the equation

$$\sigma = -\frac{1}{2}(\sigma_1 + \sigma_2) - \rho \left(\frac{\ell_0^2}{12} + \frac{a^2}{8} \right) \dot{\epsilon} - \rho \left(\frac{\ell_0^2}{12} + \frac{a^2}{16} \right) \dot{\epsilon}^2 \quad (2.26)$$

where σ_1 and σ_2 are the stresses at each end of the specimen, ρ is the specimen density, ℓ_0 is the initial specimen length, a its radius and $\dot{\epsilon}$ is the time rate of change of strain rate within the specimen. This analysis indicates that an initial length-to-diameter ratio of $\sqrt{3}/4$ for specimens can help minimise the effects of inertia within a specimen [Chen and Song, 2011]. In practical terms, $\sqrt{3}/4 \approx 0.5$, which can help make the construction of specimens a simpler process.

2.3.2 Stress equilibrium in specimens

One common assumption in experiments performed at any strain rate, is that the specimen is in a state of stress equilibrium, that is, the stress experienced by the specimen is uniform along its entire length. In high strain rate experiments, particularly those in which the specimen material has a low sound speed, that is not entirely true.

Mismatches in acoustic impedance between specimen and pressure bars will result in the incident pulse being reflected repeatedly within the specimen, known as *ringing*. It takes a few wave reflections (three or four), irrespective of the type of material, for a specimen to achieve effective stress equilibrium [Parry et al., 1994]. Since specimens are typically small, this happens very quickly; for example, a 5 mm long copper specimen with a sound speed of $3.9 \text{ mm } \mu\text{s}^{-1}$ will reach equilibrium in a little over $1 \mu\text{s}$.

This can be improved further by slowing down the rise time of the incident pulse with use of a pulse shaping technique. See Section 2.2.4.

2.3.3 Friction in specimens

As the specimen is deformed between the pressure bars and its diameter increases, it will be subjected to friction on the interfacial surfaces. Left unchecked, friction can result in barrelling of the specimen as shown in Figure 2.19, which causes non-uniform strain within the specimen and can lead to poor results from data.

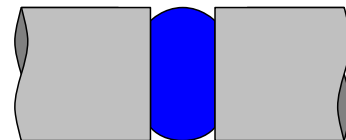


FIGURE 2.19: *Specimen barrelling due to inadequate lubrication.*

It is, however, quite simple to drastically reduce the effect of specimen friction, by covering the pressure bar ends with a small quantity of lubricant.

The exact lubricant used appears to be a question of personal taste, with some researchers favouring a petroleum gel, [Briscoe and Nosker, 1984], while at Loughborough university a MolyKote molybdenum disulphide-based grease has been chosen for its lower coefficient of friction.

Only a very small quantity of lubricant is required. Briscoe and Nosker recommend a grease thickness of $10 \mu\text{m}$, while in practical use, the author finds that a very thin smear tends to have a thickness of $50 \pm 20 \mu\text{m}$, and may be applied quickly without measurement. Too much grease should be avoided, mainly due to the mess it makes when it squirts out of the interface upon impact.

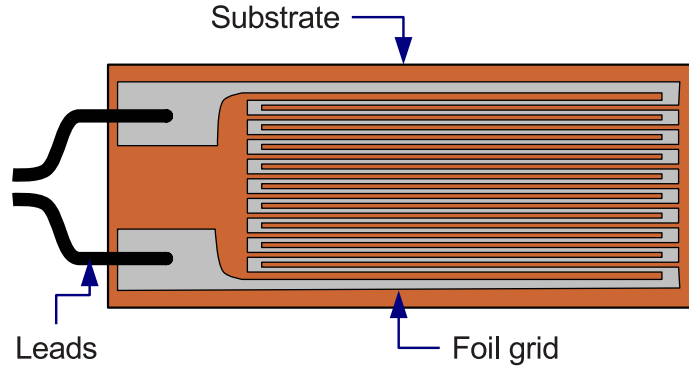


FIGURE 2.20: A typical foil strain gauge.

2.4 Supplementary equipment

2.4.1 Strain gauges.

Strain gauges work by taking advantage of the dependence of resistance of a material on its physical dimensions. Consider a conductor of length L , cross-sectional area A and resistivity ρ . The resistance, R , is given by

$$R = \rho \frac{L}{A} \quad (2.27)$$

If this conductor is subjected to a tensile force, it will stretch. As well as its length increasing, its cross-sectional area will decrease, resulting in a change in resistance, ΔR , given by

$$\Delta R = (\rho + \Delta\rho) \frac{L + \Delta L}{A + \Delta A} - \rho \frac{L}{A} \quad (2.28)$$

where Δ indicates a change in a quantity.

The gauge factor, K , essentially gives the sensitivity of a strain gauge and is defined by

$$K = \frac{dR_s/R_s}{\varepsilon} \quad (2.29)$$

where R_s is the resistance of the strain gauge [Ghosh, 2009]. The strain in the gauge is therefore

$$\varepsilon = \frac{dR_s}{R_s K} \quad (2.30)$$

There are a number of different types of strain gauge available, perhaps the most common of which are of foil (as shown in Figure 2.20) or semiconductor construction. Foil strain gauges consist of a grid formed from very thin sheets^d of a conducting material. This is attached to a thin electrically insulating polymer substrate, which allows the assembly to be attached, using a cyanoacrylate adhesive, to the material being measured. Foil strain gauges typically have gauge factors of around 2.

^dNormally less than $5 \mu\text{m}$ thick.

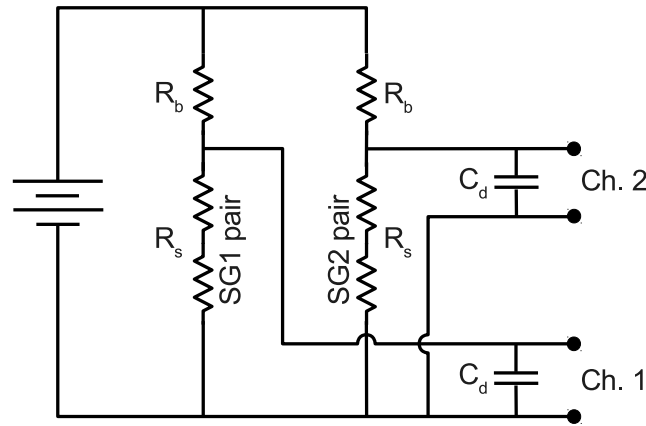


FIGURE 2.21: A simple twin potential divider circuit.

Semiconductor gauges use the piezoresistivity of doped silicon or germanium, which has a change in resistance when stressed. Semiconductor gauges are normally smaller than foil, and have a much higher gauge factor of around 100, making them much more sensitive. They are, however, rather delicate and significantly more expensive than foil gauges.

The strain gauges used on the SHPB at Loughborough University are the model FLA-1-11 foil gauges manufactured by TML [Tokyo Measuring Instruments Laboratory Co., 2013]. These have proven to be reliable, accurate and inexpensive for SHPB use.

They are fitted directly to the pressure bar in pairs, on opposite sides of the pressure bar which cancels out any strains caused by the bending of the pressure bar during use. They are wired in series and affixed with the use of a cyanoacrylate adhesive.

The resistance change in the strain gauge pairs is measured by using them as a component of either potential divider or Wheatstone bridge circuits.

2.4.1.1 The potential divider.

The potential divider or voltage divider circuit is perhaps the simplest method of measuring the resistance change of a strain gauge. Figure 2.21 shows a circuit diagram for a simple twin potential divider circuit, capable of supplying an input voltage to two independent sets of strain gauges, i.e. powering both the incident bar and the transmitter bar gauges. The two serially-connected strain gauges take the place of one resistor in each potential divider, R_s . Also in the circuit are a ballast resistor, R_b , and a decoupling capacitor, C_d .

The output voltage of the potential divider^e, V_{out} is given by

$$V_{out} = \frac{R_s}{R_s + R_b} \cdot V_{in} \quad (2.31)$$

^ei.e. The output from either of the points marked Ch.1 and Ch.2 in Figure 2.21.

where R_s is the combined resistance of each strain gauge pair. It is possible to simplify (2.31) by substituting

$$n = \frac{R_b}{R_s} \quad (2.32)$$

to leave

$$V_{out} = \frac{1}{n+1} \cdot V_{in} \quad (2.33)$$

Differentiating (2.33) with respect to n gives

$$\frac{dV_{out}}{dn} = -\frac{1}{(n+1)^2} \cdot V_{in} \quad (2.34)$$

and so

$$dV_{out} = -\frac{V_{in}}{(n+1)^2} \cdot dn \quad (2.35)$$

Differentiating (2.32) with respect to R_s yields

$$\frac{dn}{dR_s} = -\frac{R_b}{R_s^2} \quad (2.36)$$

hence

$$dn = -\frac{R_b}{R_s^2} \cdot dR_s \quad (2.37)$$

Substituting (2.37) into (2.35)

$$dV_{out} = \frac{dV_{in}}{(n+1)^2} \cdot \frac{R_b}{R_s^2} \cdot dR_s \quad (2.38)$$

Rearranging for dR_s

$$dR_s = \frac{R_s^2(n+1)^2}{R_b} \cdot \frac{dV_{out}}{V_{in}} \quad (2.39)$$

Substituting (2.39) into (2.30)

$$\varepsilon = \frac{R_s^2(n+1)^2}{R_b} \cdot \frac{dV_{out}}{V_{in}} \cdot \frac{1}{R_s K} \quad (2.40)$$

$$= \frac{(n+1)^2}{nK} \cdot \frac{dV_{out}}{V_{in}} \quad (2.41)$$

For convenience n may be expressed in terms of voltages as

$$n = \frac{R_b}{R_s} \quad (2.42)$$

$$= \frac{IR_b}{IR_s} \quad (2.43)$$

$$= \frac{(V_{in} - V_{out})}{V_{out}} \quad (2.44)$$

When designing a potential divider circuit, the resistance of R_b must be considered. From (2.31), the output voltage is highly dependent on the ratio $R_s/(R_b +$

R_s). When the strain gauge pair is deformed, the resistance changes to $R_s + dR_s$. Strain gauges such as the TML FLA-1-11, having a gauge factor of $K \approx 2.1$, a resistance of $R_s = 120 \Omega$, and a maximum strain limit of $\varepsilon = 5\%$, when deformed maximally will exhibit a resistance change of $dR_s \approx 12.6 \Omega$. Choosing a ballast resistor with a relatively high resistance will result in a poor response to these fairly small changes in resistance from the strain gauge.

By the very nature of potential divider circuits, the signal will be superimposed on top of a DC potential. This can be removed quite simply by capturing the strain gauge data on an oscilloscope capable of working in AC mode.

There are also a pair of decoupling capacitors, C_d , which have a very low capacitance (a few picofarads) and help remove any very high frequency noise that may be picked up.

2.4.1.2 The Wheatstone bridge.

A Wheatstone bridge, such as the quarter bridge circuit shown in Figure 2.22, may also be used. The output voltage of the Wheatstone bridge is calculated differently from that of the simple potential divider as

$$V_{out} = \left(\frac{R_3}{R_s + R_3} - \frac{R_2}{R_1 + R_2} \right) \cdot V_{in} \quad (2.45)$$

$$= \frac{R_3}{R_s + R_3} \cdot V_{in} - \frac{R_2}{R_1 + R_2} \cdot V_{in} \quad (2.46)$$

Similarly, this may be simplified with the use of (2.32)

$$V_{out} = \frac{1}{n+1} \cdot V_{in} - \frac{R_2}{R_1 + R_2} \cdot V_{in} \quad (2.47)$$

If we differentiate (2.47) with respect to n

$$\frac{dV_{out}}{dn} = -\frac{1}{(n+1)^2} \cdot V_{in} \quad (2.48)$$

and so

$$dV_{out} = -\frac{V_{in}}{(n+1)^2} \cdot dn \quad (2.49)$$

it is clear that this equations matches (2.35) for the potential divider circuit above, and so the analysis of the SHPB, whether using a potential divider or a Wheatstone bridge, may be performed in an identical manner.

The main benefit of using a Wheatstone bridge over a voltage divider is that, assuming ballast resistors are chosen carefully, the output will not be superimposed on a DC offset, making analysis marginally less complicated.

2.4.1.3 Power supply

In order to measure the resistance change in the strain gauges, it is necessary to pass a voltage across them, to be measured with an oscilloscope. Since the change in resistance is very small, it is absolutely vital that a good quality, stable, regulated power supply is used, such as the PLH120 linear regulated DC bench power supply from Thurlby Thandar Instruments^f. In practice, putting a 50 V potential difference across the strain gauges provides a decent return.

^f<http://www.tti-test.com/>

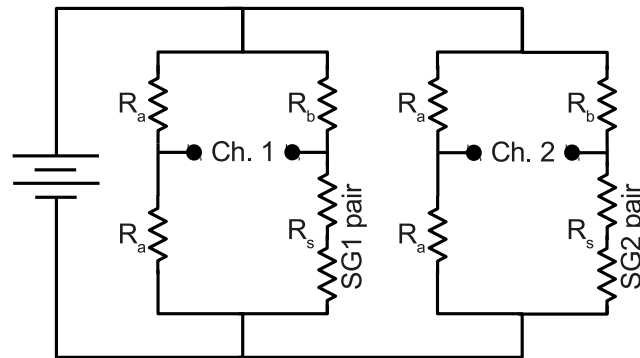


FIGURE 2.22: A twin wheatstone bridge circuit.

2.4.1.4 Wiring considerations

Although seemingly trivial, there are two important considerations to make before wiring the strain gauges. Firstly, during an experiment there will be a considerable amount of movement in the pressure bars which is violent in nature. It is therefore necessary to ensure any wires have plenty of free movement, but are firmly attached to the pressure bars so that they are not torn away from the strain gauges. Secondly, long wires make quite effective aerials for picking up RF interference from the surrounding environment. Using some form of shielded cable is recommended, with shielded mini-coaxial cable working particularly well.

2.4.1.5 Oscilloscopes

Just about any modern digital storage oscilloscope (DSO) will be easily capable of recording SHPB experiments. The key considerations when choosing a DSO are:

- **Voltage sensitivity.** The maximum amplitude of a recorded SHPB strain pulse is likely to be somewhere around 20 – 40 mV. In order to achieve decent resolution, a DSO should be sensitive to voltages as low as 0.1 mV.
- **Stored data memory.** DSOs have a limited memory in which to store data, and all data captured will be saved into the available memory. Say, for example, a particular DSO has enough memory to store 20,000 data points, if two channels are recorded, each will have 10,000 unique data points recorded. The greater the memory, the higher the resolution. In practice, 5,000 data points per channel are perfectly acceptable.

Should a DSO not have adequate voltage sensitivity, it is possible to amplify the signal prior to capture using a scope amplifier, several of which are commercially available. Should one be used, care must be taken as they often incorporate low- and high-pass filters which must be fully understood before employing. See Section 2.5.1 for further information.

2.5 SHPB Operation

Once data has been captured on the SHPB, it must be analysed. This section discusses options and methods for processing and examining data.

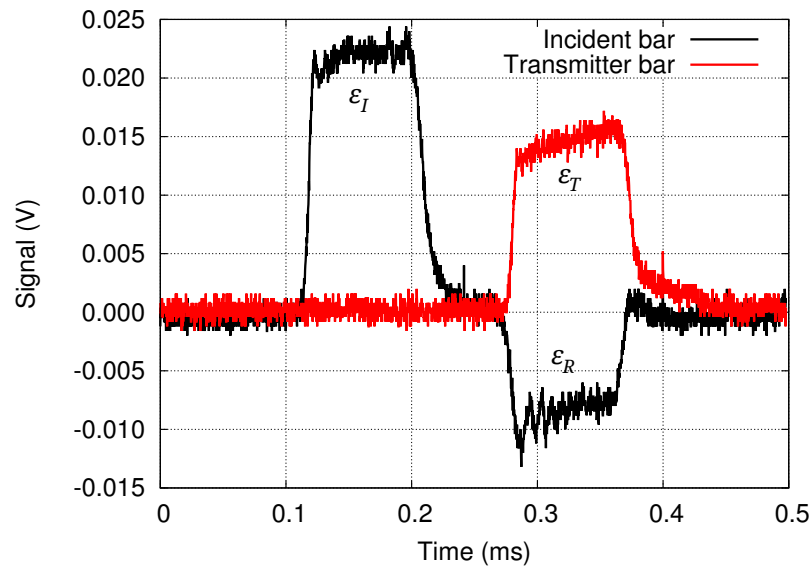


FIGURE 2.23: Raw SHPB data of a copper specimen.

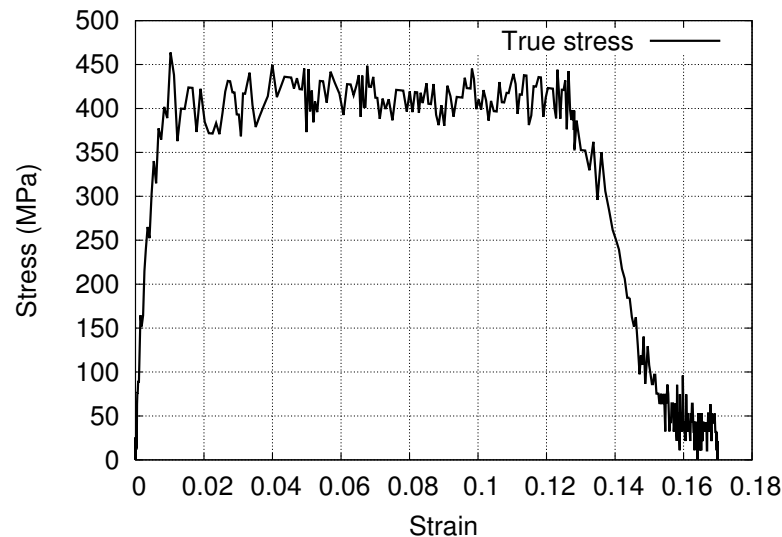


FIGURE 2.24: SHPB true stress-strain curve of a copper specimen.

2.5.1 Smoothing & Filtering data.

Considering the low voltages measured by an oscilloscope, there is likely to be some noise present in any collected data. Figure 2.23 shows raw, unfiltered data in which a copper specimen was crushed in a traditional SHPB system. Figure 2.24 shows the true stress-strain curve produced from this data. Clearly a notable amount of noise is visible in this data which can obscure the detail contained within, making it difficult to pick out distinct points of interest.

In order to increase the readability of the resulting stress-strain curve, it may be necessary to use some form of data smoothing or filtering technique. While it may appear that the most obvious thing to do would be to install some form of in-line electronic filtering system, it is important to understand any effect this will have on the resulting data.

In this section a number of different filtering and smoothing techniques are discussed, along with considerations for their application. A comparison of how each technique affects the resulting stress-strain curve is shown in Section 2.5.1.3 on page 81.

2.5.1.1 Pre-process smoothing.

Pre-process techniques involve the smoothing or filtering of data as it is gathered, i.e. prior to any analysis being performed.

2.5.1.1.1 In-line filters An in-line filter is a device positioned between the strain gauges and the oscilloscope. As the strain gauge signal passes through the filter, it removes any components of the signal which have a frequency outside of a pre-determined range. There are four fundamental types of in-line filter:

Low-pass. As the name implies, the low-pass filter allows frequencies lower than the cut-off frequency, f_c , to be passed.

High-pass. This is the opposite of the low-pass filter, passing only frequencies higher than f_c .

Band-pass. Passes only frequencies which are between lower and higher cut-off frequencies, f_L and f_H .

Band-stop. Passes only frequencies outside of the range f_L to f_H . This can be particularly useful when trying to eliminate noise with a regular frequency, such as the 50 or 60 Hz mains electricity hum.

When choosing an in-line filter, it is first necessary to ensure that it will remove no useful data, compromising the validity of the results. Performing a Fourier transformation on a sample set of data can help to indicate the frequency range in which the data lies. Figure 2.25 shows the power spectrum of a Fourier analysis of the incident bar data from the copper specimen shown in Figure 2.23. In this data set the majority of the data exists in the range 1 – 10 kHz, with none appearing above 50 kHz.

One of the most popular forms of in-line filter is the Butterworth filter [Butterworth, 1930], which is designed to have as flat a frequency response as possible in the passband, which then rolls off towards zero in the stopband. A first-order filter's response rolls off at -6 dB per octave (-20 dB per decade). A second-order filter rolls off at -12 dB per octave, a third-order at -18 dB per octave and so on. The frequency response for a range of orders of Butterworth low-pass filters for data sampled at $f_s = 5000$ kHz and a low-pass cut-off frequency of $f_c = 100$ kHz are shown in Figure 2.26. In each case the filter's response has rolled off by -3 dB at the point of the cut-off frequency. Since the lower ordered filters roll off more gradually, it is important to choose a filter order that ensures that no data is lost in the filtering process.

Since all of the data in Figure 2.23 resides below 50 kHz, in this particular case it should be possible to isolate the data from the noise by using a high-ordered Butterworth low-pass filter with a cut-off frequency of $f_c = 100$ kHz. Keeping the

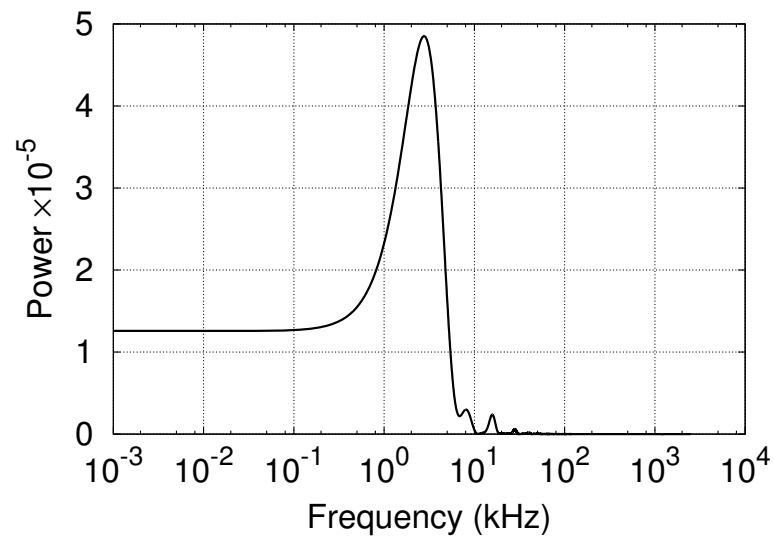


FIGURE 2.25: *Fourier transformation of the incident bar data from Figure 2.23.*

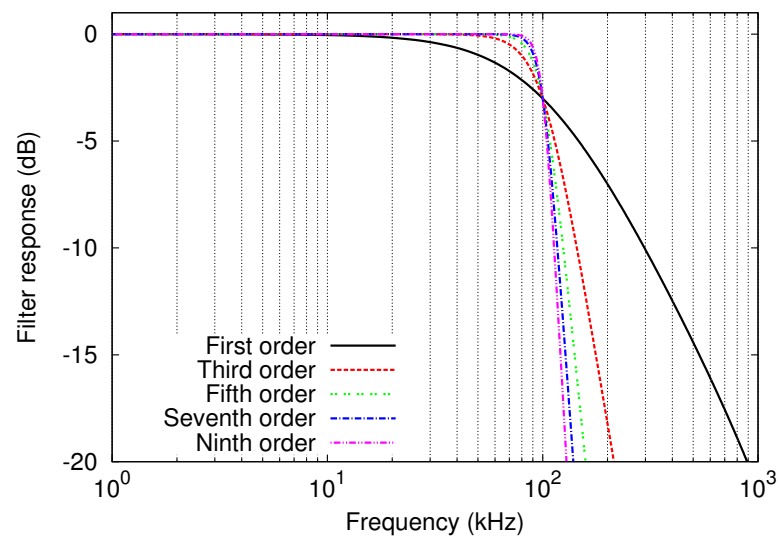


FIGURE 2.26: *The frequency response for a range of orders of Butterworth low-pass filters with a cut-off frequency of $f_c = 100$ kHz.*

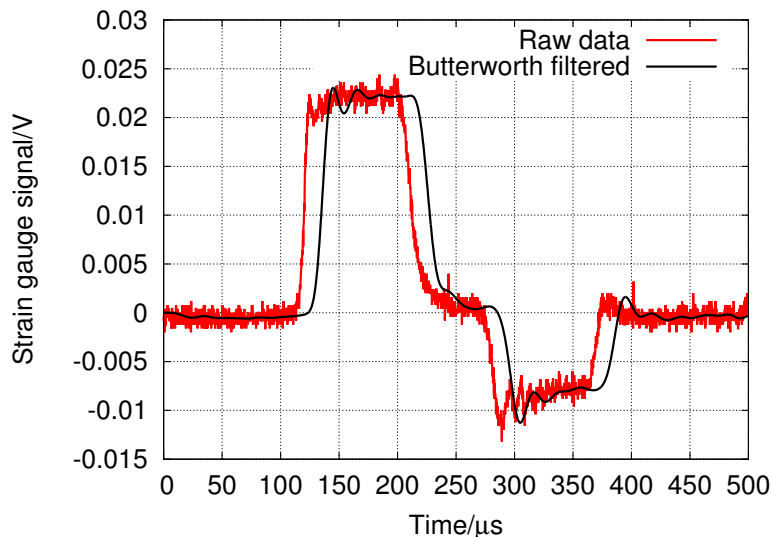


FIGURE 2.27: SHPB incident bar data filtered with a 7th order Butterworth low-pass filter with a cut-off frequency of $f_c = 100$ kHz.

values of f_c and the filter order high ensures that no data is removed during the filtering process.

Figure 2.27 shows the same data from Figure 2.23 after being processed by a 7th order Butterworth low-pass filter with a cut-off frequency of $f_c = 100$ kHz. The slight phase shift of the data has no impact on the resulting stress-strain curve.

There are actually two methods of implementing an in-line filter, either by using a physical filter, or by recording the data unfiltered, and processing it using a computer-based numerical filter. While neither of these methods is technically better than the other, it is the opinion of the author that computer-based filtering is preferable since it provides the operator with both filtered and unfiltered data, affording a choice of cut-off frequencies after the experiment has been performed. Appendix A contains a GNU Octave script[§] which will perform the low-pass filtering discussed in this section.

2.5.1.1.2 n-point rolling average. This is probably the most straight-forward method of smoothing data, and involves simply averaging the recorded data over a number of rows thus,

$$X_j = \frac{1}{n} \sum_{i=j}^n x_i \quad (2.50)$$

where X_j are the calculated averages, n is the number of rows the data is to be averaged over and x is the original recorded data. The performance of the calculation is trivial, whether it is performed in a spreadsheet or using any programming language, and hence is not discussed further here. An example of some data smoothed with a 20-point rolling average is shown in Figure 2.28.

[§]Although the script was written to be run in GNU Octave, due to their remarkably similar syntax, it may be converted to run in Mathworks MatLab quite simply.

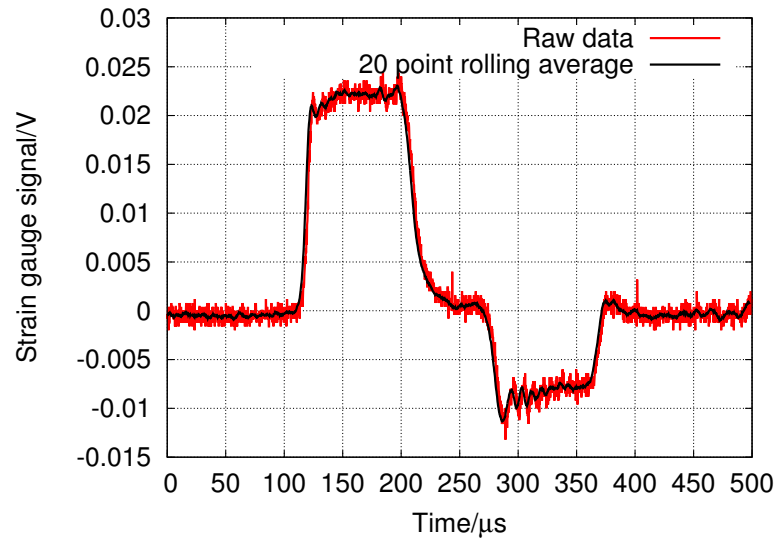


FIGURE 2.28: SHPB incident bar data smoothed with a 20-point rolling average.

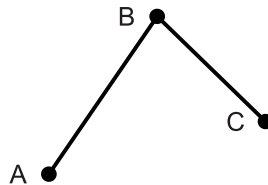


FIGURE 2.29: A three point dataset.

Of all the techniques discussed here, the rolling average produces a curve which has the greatest similarity to its raw dataset. It does, however, lack the aesthetic appeal of smoother curves.

It is, of course, possible to use a rolling average to smooth data both pre- and post-processing.

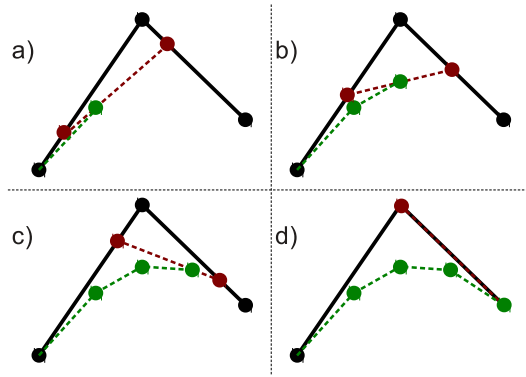
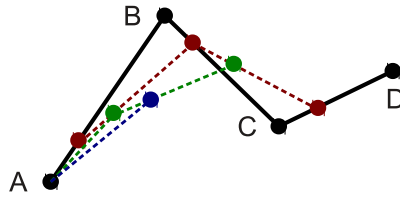
2.5.1.2 Post-process smoothing.

Due to the relative complexity of the data being analysed, some smoothing techniques are not suitable for cleaning the raw data. If, however, the data is fully analysed to produce an unfiltered stress-strain curve, this curve is less intricate, and so lends itself well to a range of post-process smoothing techniques.

2.5.1.2.1 Bézier smoothing. A smoothing technique used in a great deal of computer packages is the Bézier curve. In order to explain the production of Bézier curves, a simple example will be used. Consider a dataset of three points, *A*, *B* and *C* as shown in the example shown in Figure 2.29.

It is possible to create a Bézier curve representing this data. It is first necessary to decide the number of points, *N*, over which the curve is to be constructed^h. In the example shown in Figure 2.30, a value of *N* = 4 has been used.

^hIt may be interesting to note that changing *N* does not alter the shape of the Bézier curve, only its relative ‘smoothness’.

FIGURE 2.30: *The production of a Bézier curve for a three point dataset.*FIGURE 2.31: *The production of a Bézier curve for a four point dataset.*

The first step is to locate the point $\frac{1}{N}$ of the way along the vector \overline{AB} , along with the point $\frac{1}{N}$ along \overline{BC} . These points are then joined by a line and a third point $\frac{1}{N}$ along this line then becomes the first point of the Bézier curve. This is shown in part a) of Figure 2.30.

This is then repeated, choosing points $\frac{2}{N}$ along each of the vectors, then $\frac{3}{N}$ along, etc. until the final point is taken at $\frac{N}{N}$, i.e. the final point in the dataset. Figure 2.30 parts a) to d) show the complete process.

The fundamental principal of this technique is that it takes the initial three point dataset, reduces it to two points, shown in red, and then reduces it further to a single data point, in green.

Bézier smoothing at this level is relatively straightforward, but is made more complicated by additional points in the data set. The principal, however, remains the same. Keep finding points and reducing the number of data points until only one remains. An example of the initial steps for producing a Bézier curve for a four point dataset is shown in Figure 2.31. A program written in C++ is shown in Appendix B which is capable of producing a Bézier for any n-point dataset.

Since this method is perfectly capable of smoothing any form of data, it should also be suitable for use in pre-processing. As can be seen in Figure 2.32, however, it tends to produce a curve which is perhaps a little ‘too smooth’, which could then result in missing some of the finer details. Ergo, Bézier smoothing should be reserved for use in post-processing.

2.5.1.2.2 Polynomial curve fitting. An n^{th} order polynomial may be fitted to most curves. A first order polynomial,

$$y = ax + C \quad (2.51)$$

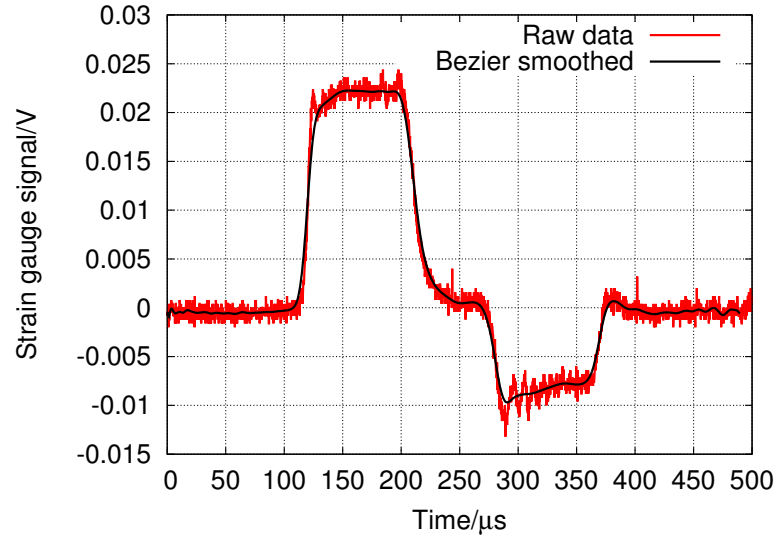


FIGURE 2.32: SHPB incident bar data smoothed with a Bézier curve.

where a is the slope and C defines the intercept, will exactly fit two points on a curve with distinct x coordinates. A polynomial of second order,

$$y = a_2x^2 + a_1x + C \quad (2.52)$$

will exactly fit three points on the curve. As we increase the order of the polynomial, it can be made to fit more points on any curve, as long as the x coordinates remain distinct.

A script designed to run in GNU Octave which will calculate an n^{th} order polynomial is shown in Appendix C.

The complexity of the raw data from an SHPB demands an extremely high-ordered polynomial to describe it which, for practical purposes, inhibits the use of fitted polynomials. On the other hand, the relative simplicity of the stress-strain curve lends itself well to this sort of description, as shown in Section 2.5.1.3.2 below.

2.5.1.3 Smoothing and filtering overview.

The purpose of this section is to examine the affects of using the different filtering and smoothing techniques discussed above.

2.5.1.3.1 Comparing pre-process smoothing techniques. Figure 2.33 shows a comparison of the pre-process smoothing techniques, with Figure 2.34 showing a close-up of the data around the point of yield. The Butterworth low-pass filter was performed computationally, and was of order 7, with a cut-off frequency of $f_c = 100$ kHz.

Both smoothing techniques produce a reasonable representation of the raw data. The Butterworth filter, however, produces a less representative curve than the rolling average. It may be possible to improve the response of the Butterworth filter by increasing the filter order and/or the cut-off frequency.

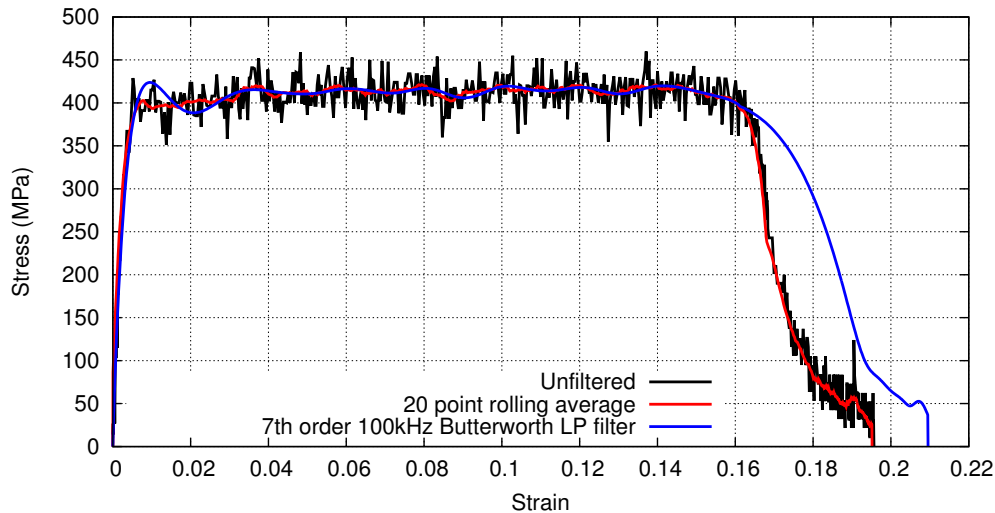


FIGURE 2.33: Comparison of different pre-process smoothing techniques.

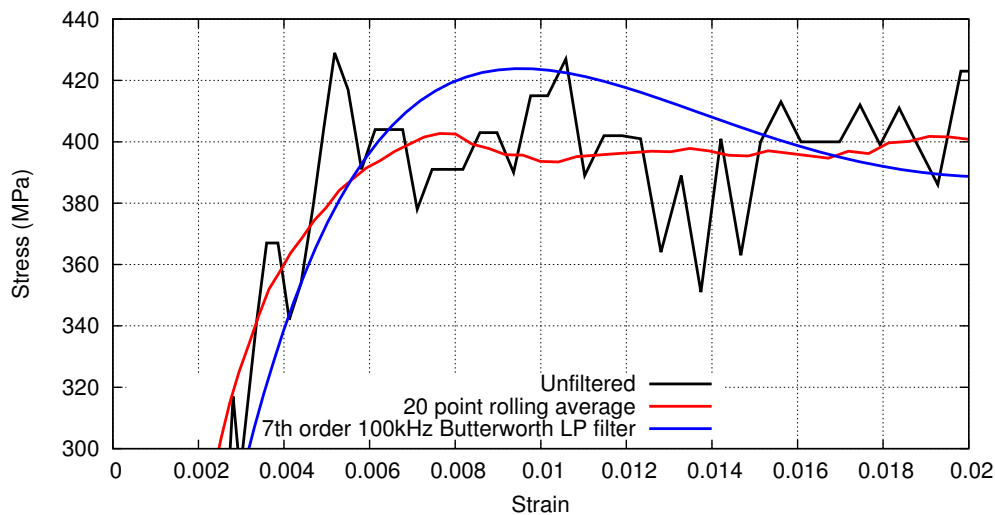


FIGURE 2.34: Close-up of yield point in pre-process smoothing techniques.

2.5.1.3.2 Comparing post-process smoothing techniques. A comparison of the post-process smoothing techniques is shown in Figure 2.35. Each of the curves shows a very reasonable fit with the raw experimental data. Figure 2.36 shows a close-up of the data around the point of yield.

These figures reveal that there is a small but noticeable difference between the three methods, with the fitted polynomial showing a marginally exaggerated yield stress.

2.5.1.3.3 Choosing the best smoothing method. Each of the smoothing techniques discussed here is quite capable of making data more straight forward to read, and the decision of which to use ultimately comes down to personal preference. In fact, since much SHPB work provides a comparison of material differences, the most important thing is consistency, i.e. whichever technique is chosen, that method should be used for every experiment. That is, for example, in a hypothetical study of two materials, it could be just as important to show that Material

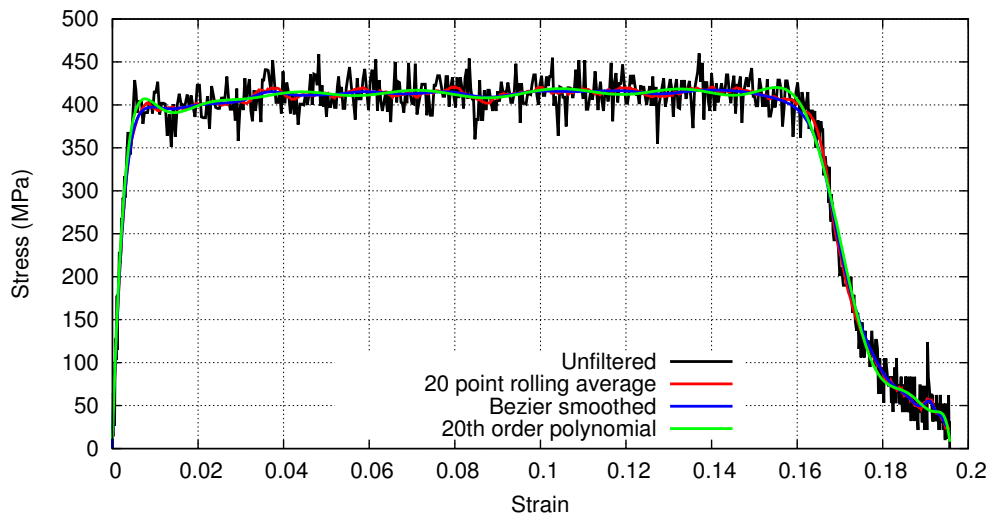


FIGURE 2.35: Comparison of different post-process smoothing techniques.

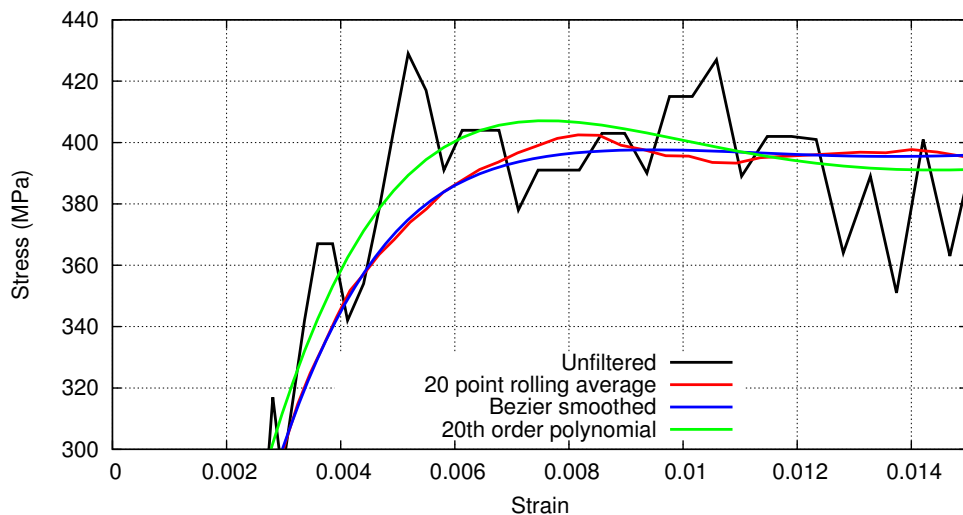


FIGURE 2.36: Close-up of yield point in post-process smoothing techniques.

A has a yield strength 10% higher than Material B, rather than their precise values. This can easily be evaluated whichever technique is used.

That is not to say, however, that the author does not have his own personal preference.

Electronic filters are thought to be generally of little use. Used in-line, they alter the data before it is recorded, making it impossible to 'undo' their affects. Since it is necessary to understand much about the filter, e.g. its precise frequency response, all but the most expensive commercially available filters should not be trusted, making it ordinarily preferable to construct bespoke units.

While the use of a rolling-average in either pre- or post-processing *probably* produces a curve which fits the stress-strain curve produced from raw data most accurately, the 'rough' nature of the curve does tend to make it more difficult to use the automated methods shown below in Sections 2.5.3.1, 2.5.3.2 and 2.5.3.3 to pick out the interesting points on the stress-strain curves.

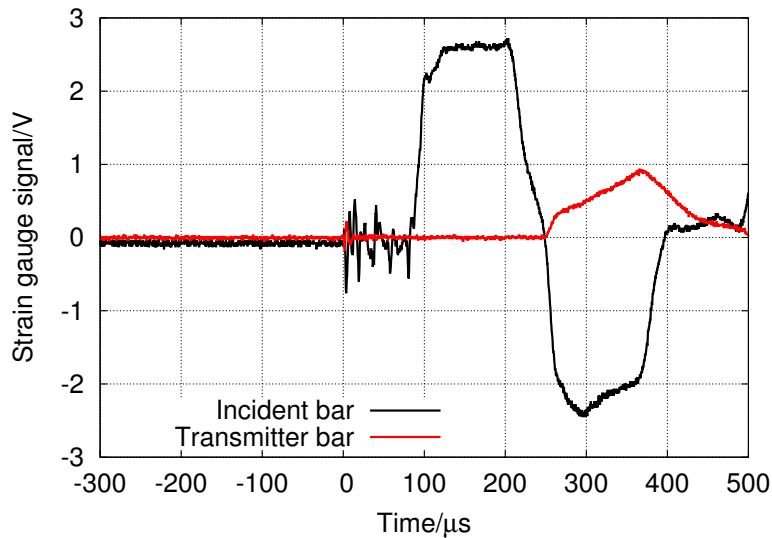


FIGURE 2.37: SHPB data showing significant electrical noise on the incident bar.

In the work presented here and elsewhere, smoothing has been performed in post-processing using a Bézier curve. This method was chosen because it tends to follow the unfiltered curve closely without over-emphasizing any point. The relative ‘smoothness’ of the curves it produces are aesthetically pleasing, which makes them suitable for both print and for use with the automated calculations detailed below.

2.5.2 Analysing data.

The analysis of recorded SHPB data can, of course, be performed manually although this can be a laborious process. Automating the process to computationally produce a stress-strain curve from a data set can save a significant amount of time. Computational analysis must be performed in a number of steps, which are discussed in detail in this section.

2.5.2.1 Normalising data.

In Section 2.4.1 the use of a potential divider or a Wheatstone bridge to provide power to, and measure any voltage change from strain gauges was discussed. Whichever of these methods is used, there is likely to be some DC offset applied to the resulting signal, and it is necessary to remove this before attempting analysis. This is best performed computationally.

Glancing back to Figure 2.23 on page 75, the oscilloscope trigger point has been set so that a small portion of the beginning of the recording contains no data. If the recording is started a reasonable time before the incident pulse begins, an accurate value of the offset may be obtained by simply calculating the average value of the data up to this point. This may then be subtracted from the data and the normalisation is complete.

Figure 2.37 shows some SHPB data which has a large amount of electrical noise occurring immediately prior to the incident strain pulse. This adds a complication to the normalisation process in that the noise, being significant, could artificially

alter the calculated DC offset. In any computational technique this must be considered.

Appendix D contains a program written in C++ which performs this function, calculating the average DC offset from the first five hundred rows in a dataset. To avoid the difficulty with noise, the program simply ignores points within the data the magnitude of which are greater than 5% of the maximum dataset amplitude.

2.5.2.2 Pulse extraction.

Since it is only necessary to have the transmitted and reflected pulses to produce a stress/strain curve, they can be extracted from the data set prior to analysis. Although this would appear to be a simple task to perform manually, ensuring that the point chosen as the start of the pulse is in precisely the right place can be tricky.

A simple method, which provides excellent consistency, is to choose the first point with a value greater than zero, and from which subsequent points remain above zero for an extended period. With a typical SHPB experiment, incident pulses will have a duration of around $100 \mu\text{s}$. Transmitted and reflected pulses, however, may be somewhat shorter than this.

Appendix E contains a C++ program which is capable of extracting all three pulses out of incident and transmitted data files. It searches for pulses which are (as default) greater in length than $75 \mu\text{s}$, but this value may be altered by changing the initial value of one variable in the program. See Appendix E for more details.

It also takes into account possibility that, depending on wiring, the orientation of the pulses can change. With the strain gauges wired one way, the incident pulse will be positive and the reflected negative. Changing the wires around will result in the incident pulse being negative and the reflected positive. The program looks for both positive and negative pulses, and forces them all to be positive in the resulting files.

2.5.2.3 Producing stress-strain curves.

From Equations 2.14 and 2.19 above (page 58), the engineering strain in a specimen is

$$\varepsilon_S = \frac{-2c_0}{\ell_0} \int_0^t \varepsilon_R dt \quad (2.53)$$

where ε_R is the reflected strain pulse.

The engineering stress experienced by a specimen is

$$\sigma_S = \frac{EA}{A_S} \cdot \varepsilon_T \quad (2.54)$$

where ε_T is the transmitted strain pulse.

Hence, it is possible to calculate the engineering stress and engineering strain in the specimen from the strain measured in the pressure bars.

From Equation 2.41 (page 72), the strain from the strain gauges is given by

$$\varepsilon = \frac{(n+1)^2}{nK} \cdot \frac{dV_{out}}{V_{in}} \quad (2.55)$$

where ε is the strain recorded by the strain gauge, n is the ratio of the ballast and strain gauge resistances, K is the gauge factor of the strain gauges, V_{in} is the voltage across the strain gauges, and dV_{out} is the change in voltage across the strain gauge pair.

For convenience, the ratio n can be expressed in terms of the input and output voltages, V_{in} and V_{out} thus

$$n = \frac{(V_{in} - V_{out})}{V_{out}} \quad (2.56)$$

Using these terms, calculating the stress and strain in the specimen from the strain in the pressure bars is a relatively trivial task which may be performed computationally quite simply.

Once calculated, the engineering strain can be converted to true strain using

$$\varepsilon_T = \ln(1 - \varepsilon_S) \quad (2.57)$$

and the true stress may be calculated using

$$\sigma_T = \sigma_S(1 - \varepsilon_T) \quad (2.58)$$

Appendix F contains a program written in C++ which calculates stress-strain data from a pair of comma-separated-value files containing the reflected pulse data and the transmitted pulse data. After producing the stress/strain data, it goes on to calculate the representative Bézier curve for the data, which is saved as a separate file.

2.5.3 Understanding stress-strain curves.

2.5.3.1 Finding the yield stress.

Defining the yield stress of a material from its stress-strain curve can be quite difficult, particularly for materials which do not display ideal elasticity, such as polymers. Figure 2.38 shows normalised true stress-strain curves for LLDPE and copper specimens from an SHPB experiment. From the figure, the yield strength of the copper is much more easy to pick out than that of the LLDPE, since the transition from elastic to plastic behaviour is much sharper.

Perhaps the simplest technique to locate the *turning point* of the stress-strain curve, defined as the maximum value of the second derivative of stress with respect to strain. This is not possible when the stress-strain curve being analysed contains any noise, as any deviation from the general shape of the curve may result in incorrect identification of the point of yield.

This can be overcome by producing an approximation of the stress-strain curve, making it as simple as possible without losing its general shape. In the work presented in this report, this has been performed using the following method:

1. The stress-strain data between the start and the point of maximum stress is selected. This allows for the approximation to be created more easily than for the full stress-strain curve.

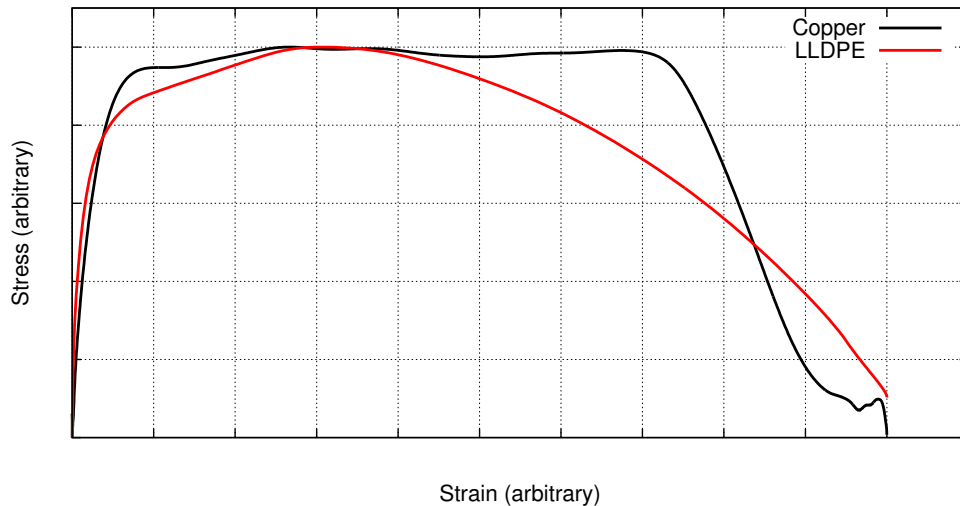


FIGURE 2.38: *Normalised SHPB true stress-strain curve for copper and LLDPE.*

2. A 20th order polynomial is fit to the reduced data set.
3. The first and second derivatives of stress with respect to strain are calculated.
4. The first point at which the second derivative is greater than or equal to zero, denotes the turning point of the stress-strain curve, and hence the point of yield.

This technique assumes that the point of yield occurs prior to the point of maximum stress, which has been appropriate to the work presented here, but should be considered for any other work. Appendix G contains a GNU Octave program which uses the technique discussed to find the yield strength of a stress-strain curve.

2.5.3.2 Estimating Young's modulus.

While it is perfectly possible to estimate values of Young's modulus, E , with split-Hopkinson pressure bar experiments, some considerations must be made in order to get reliable results.

As discussed in Section 2.1.1, the measurement of stress in SHPB experiments is defined by

$$\sigma_S = \frac{EA}{A_S} \cdot \varepsilon_T \quad (2.59)$$

where A is the cross-sectional area of the SHPB pressure bars, with E being their Young's modulus, A_S is the cross-sectional area of the specimen and ε_T is the amplitude of the transmitted strain pulse. The dependency of this measurement on the specimen cross-sectional area can have significant ramifications if the specimen construction and face parallelism, as well as that of the pressure bars

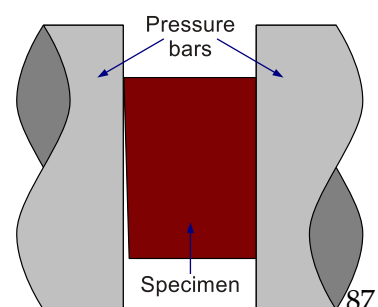


FIGURE 2.39: *A specimen with near face parallelism*

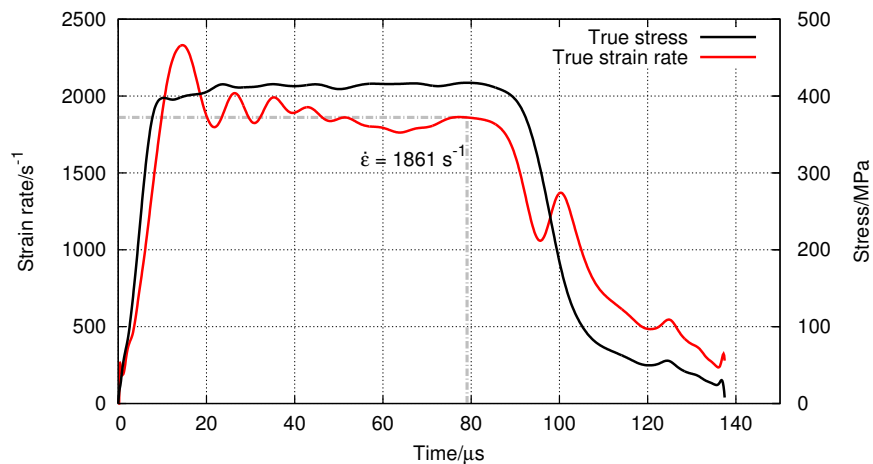


FIGURE 2.40: Strain rate of a copper specimen in an SHPB.

themselves, is anything less than perfect, an example of which is shown in Figure 2.39.

Accordingly, imperfect conditions will result in inaccurate measurements of E with the split-Hopkinson pressure bar. Since the world is, of course, an imperfect place, this is practically unavoidable. The most reliable course of action is to take a measurement of the stress-strain curve gradient slightly after the first moments of specimen compression. That way it can be reasonably assumed that the specimen has been compressed enough to have forced any gaps out of the system.

Stress-strain curves are, however, rarely ideal. While E should be calculated from the gradient of the curve prior to yield, this value is very unlikely to be constant. For this reason, E is presented in this report in the form of a graph showing the history of E with respect to specimen strain.

Appendix H contains a program written in C++ which extracts the history of Young's modulus between the start of the stress-strain pulse and the approximate point of specimen yield.

2.5.3.3 Finding the strain rate.

Strain rates are typically reasonably constant in SHPB experiments in which metals are being tested, but this is not so for softer specimens such as polymers. As the specimen starts to plastically deform, the majority of the energy is converted directly into specimen heat. With polymeric specimens, where the strain achieved in an SHPB experiment are typically very high, specimen heating can be rather high which softens the specimen significantly, ultimately leading to an increase in the strain rate.

Figures 2.40 and 2.41 show the difference in the strain rate evolution over the duration of an SHPB experiment for copper and LLDPE specimens. With the relative constancy of the copper strain rate, identifying the experimental strain rate is a trivial matter. The LLDPE on the other hand, requires a little more attention.

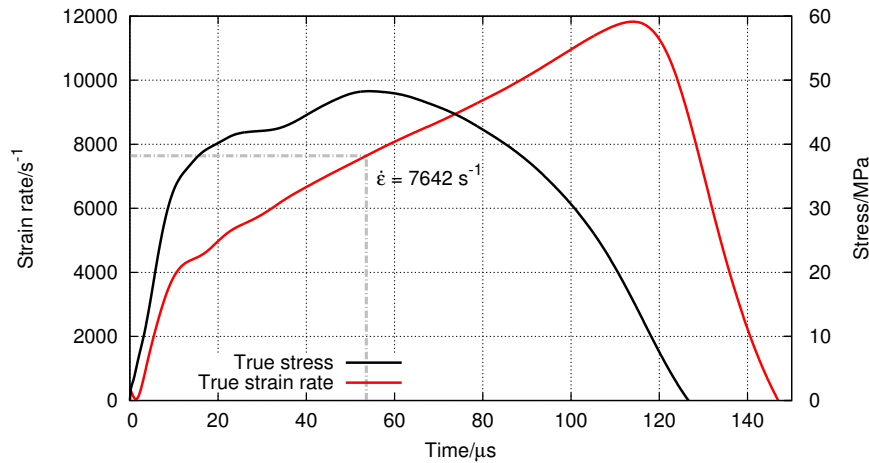


FIGURE 2.41: Strain rate of an LLDPE specimen in an SHPB.

While there is no one *correct* way of doing this, perhaps the simplest technique, and that used throughout this work, is to quote the strain rate at the point of maximum stress.

2.5.4 Measuring energy absorption

The energy absorption of a material shows the ability of a material to absorb energy without breaking apart. This can be quite a useful property to measure, especially for materials which are designed to absorb the energy of an impactor, such as armour or protective clothing for dangerous pursuits like skiing or motor-cycling.

The energy absorption, K , at a particular strain, ϵ_p , is defined as

$$K = \int_0^{\epsilon_p} \sigma d\epsilon \quad (2.60)$$

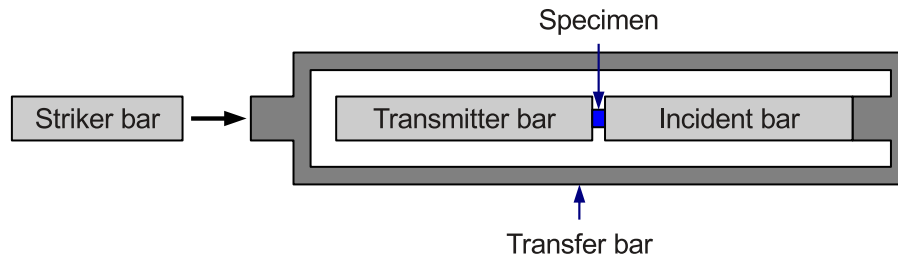
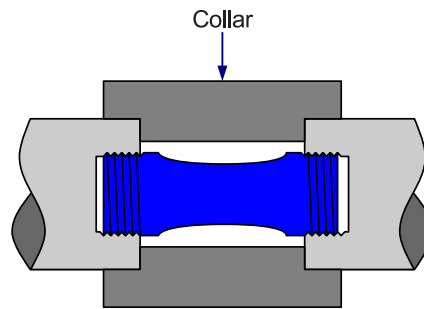
Calculating K is simply the integral of the area of the stress-strain curve up to the strain point. The strain point for brittle materials is ordinarily the point at which the specimen fractures. For ductile materials which do not fracture under compression, an arbitrary strain point must be chosen in order to compare the results of different materials. For the work presented here, a strain point of $\epsilon = 50\%$ was chosen.

2.6 Alternative SHPB configurations

2.6.1 Tensile SHPB

It is possible to perform direct tensile tests with an SHPB system, provided some modifications are made.

Figure 2.42 shows a tensile SHPB similar to that used by [Eskandari and Nemes, 2000], in which the striker bar is incident with a *transfer bar* which carries the energy of the impact to the rear of the system, where it is clamped to the incident pressure bar, so that the specimen is subjected to a wave of tension. Data suggests that a system of this type is capable of inducing strains at a rate of

FIGURE 2.42: *Tensile SHPB system.*FIGURE 2.43: *Alternative tensile SHPB system.*

around two or three hundred per second, an order of magnitude or so slower than a compressive SHPB system. It is thought that this reduction in strain rate is as a result of the high mass of the transfer bar.

An alternative tensile technique, shown in Figure 2.43, more closely resembles a traditional SHPB. A collar, constructed from the same material as the pressure bars, is fitted around (but not touching) the specimen. This allows the normal incident compressive pulse to pass directly from the incident bar to the transmitter bar with negligible effect on the specimen. When the pulse reaches the free end of the transmitter bar, it is reflected as a wave of tension with the same amplitude and duration. It is this wave which is used to load the specimen. This technique has been used to induce plastic strain rates of about 750 s^{-1} in specimens of type 321 stainless steel, only a little slower than with the compressive SHPB [Ellwood et al., 1982].

For both of the aforementioned methods, a different design of specimen is required. Obviously a specimen which is subjected to tensile strain cannot simply be placed between two barsⁱ, and so it must be secured. This can be done either by drilling and threading the ends of the pressure bars so that the specimen may be screwed into them, as with the example in Figure 2.43, or external clamps may be used to firmly hold the specimen.

2.6.2 Brazilian technique.

The Brazilian technique is an indirect tensile test originally designed for the analysis of the low strain rate behaviour of very hard materials such as rock. The test is quite easily adaptable for employment within a split-Hopkinson pressure bar, as shown in Figure 2.44.

ⁱIt would just fall out as soon as the tensile pulse reached it.

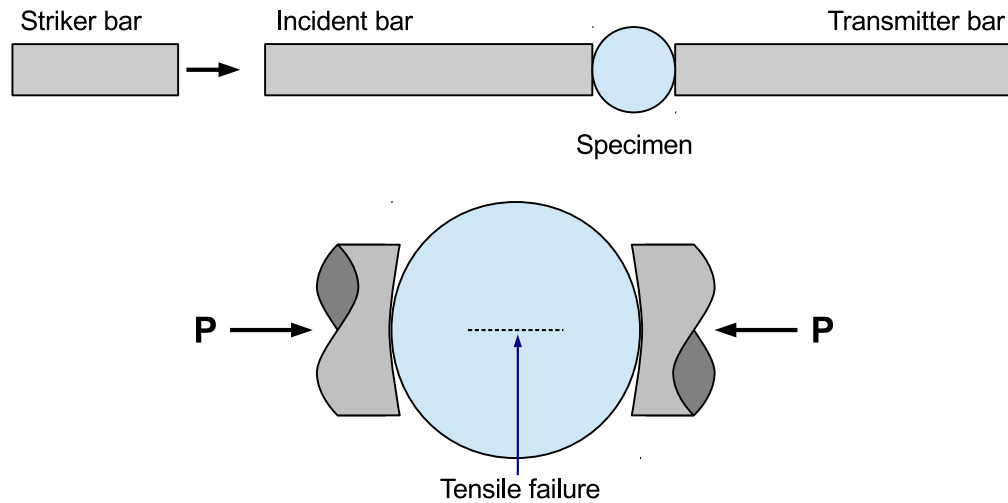


FIGURE 2.44: *The dynamic Brazilian technique performed with the SHPB.*

The force of the SHPB incident strain pulse is applied on the cylindrical specimen, within which a material element along the diameter coincident with the applied load is subjected to a compressive stress, σ_c ,

$$\sigma_c = \frac{2P}{\pi \ell D} \cdot \frac{D^2}{r(D-r)} \quad (2.61)$$

and to a tensile stress, σ_t , which at the centre of the specimen is defined by

$$\sigma_t = \frac{2P}{\pi \ell D} \quad (2.62)$$

where ℓ is the specimen height, D its diameter, and r is the distance from the element to the point where the load is applied. From Equation 2.62 it is possible to determine the tensile strength of the specimen in terms of the maximum force recorded, P_{max} , and the specimen geometry. It should be noted, though, that since the specimen is in a state of biaxial stress, with σ_c being higher than σ_t . This invalidates a direct comparison between the results obtained in a Brazilian test with those of a simple tensile test [Andreev, 1991], [Rodriguez et al., 1994], [Grantham et al., 2004].

Optical Dropweight

“If you try and take a cat apart to see how it works, the first thing you have on your hands is a non-working cat.”

—DOUGLAS ADAMS

The Optical Dropweight (ODW), a cross-section of which is shown in Figure 3.1, is an intermediate strain-rate compressive testing technique. A relatively simple technique which, as its name implies, compresses a specimen material by dropping a heavy weight on top of it. Strain-rate regimes with this experiment are typically in the region of a few hundred per second, around one order of magnitude slower than the split-Hopkinson pressure bar [Dawson, 1993], [Hamdan, 1994]. It is a useful experiment for testing specimens constructed of relatively soft, ductile materials such as polymers, but is not particularly suited to testing metals or ceramics.

An optical path which runs through the whole experiment allows high-speed photography to be used to produce images of the cross-section of the specimen as it is compressed.

3.1 Operational theory

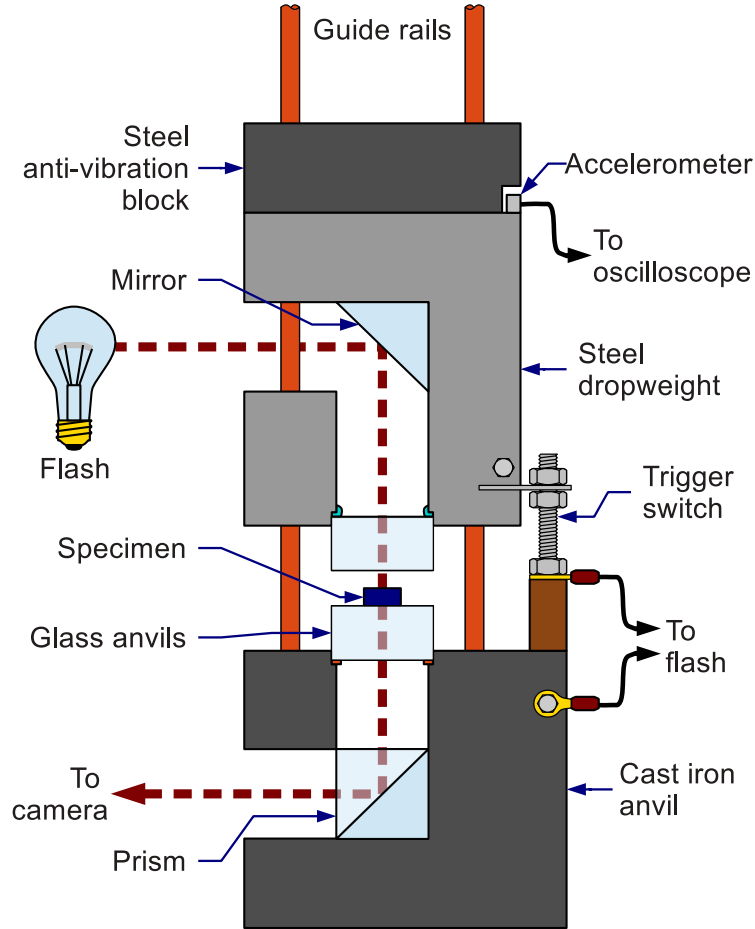
A heavy weight with a flat strike face, when dropped onto the flat face of a cylindrical specimen, will impart a compressive axial engineering stress, $\sigma_E(t)$, onto the specimen.

$$\sigma_E = \frac{F}{A} \quad (3.1)$$

where F is the force of the falling weight, and A is the area of specimen face. The force will cause the specimen to deform, which in turn reduces the speed of the weight.

If the dynamic area of the specimen is given by

$$A = \pi r^2 = \frac{\pi D(t)^2}{4} \quad (3.2)$$


 FIGURE 3.1: *Optical dropweight system.*

where $D(t)$ is the dynamic (i.e. growing) diameter of the specimen, then the engineering stress can be expressed as a function of time as

$$\sigma_E(t) = \frac{4F}{\pi D(t)^2} \quad (3.3)$$

The force applied to the specimen, F , is simply the mass of the falling weight, m , multiplied by its acceleration, a

$$F = ma \quad (3.4)$$

which is measured by an accelerometer attached directly to the dropweight.

The dynamic true strain, $\varepsilon_T(t)$, is usually expressed as a function of the initial and dynamic lengths of the specimen, ℓ_0 and $\ell(t)$ respectively, thus

$$\varepsilon_T(t) = -\ln \frac{\ell(t)}{\ell_0} \quad (3.5)$$

If it is assumed that the specimen is incompressible, it is possible to equate the initial volume, V , of the specimen with that at any time during the duration of the experiment as

$$V = \frac{\pi D^2}{4} \cdot \ell \quad (3.6)$$

$$\frac{\pi D_0^2}{4} \cdot \ell_0 = \frac{\pi D(t)^2}{4} \cdot \ell(t) \quad (3.7)$$

Rearranging for $\ell(t)$,

$$\ell(t) = \ell_0 \left(\frac{D_0^2}{D(t)^2} \right) \quad (3.8)$$

this can be inserted into Equation 3.5 to give

$$\varepsilon_T(t) = -\ln \left(\frac{D_0^2}{D(t)^2} \right) \quad (3.9)$$

This relation holds true with the additional assumption that barrelling and fracture within the specimen are insignificant for the duration of the experiment.

3.2 The hardware

As can be seen in Figure 3.1, the ODW is constructed from a number of elements, several of which deserve individual explanation.

3.2.1 The dropweight, optical path and lower anvil

The dropweight itself is a simple steel block of cylindrical shape. It measures 94 mm high with a diameter of 108 mm. It has three holes drilled vertically through it, through which it slides on three guide rails. It can be lifted, using a simple pulley system, to a maximum height of around 1 m.

A pair of holes with a diameter of 32 mm are drilled at right-angles into the dropweight. At the point at which the holes meet is positioned a 45 degree mirror, so that light shone into the dropweight hole from the side will be transmitted through to the bottom.

The specimen is crushed between a pair of glass anvils, the upper of which is held in place in the dropweight with a small quantity of "Blu-Tack". The lower is placed loosely onto the lower cast iron anvil, separated by a thin copper gasket. The relative softness of the copper provides a small amount of cushioning to the lower glass anvil, protecting it from shocks significant enough to break it.

The lower cast iron anvil has an optical path similar to the dropweight, but uses a prism instead of a mirror to channel the light out towards a high-speed camera.

3.2.2 Anti-vibration block

On top of the dropweight sits a 51 mm high steel anti-vibration block, also having a diameter of 108 mm. The purpose of this object is to reduce the vibrations received by the accelerometer. Although not rigidly attached to the dropweight, a thin layer of grease between them provides enough adhesion to ensure that, as the weight and the anti-vibration block fall, they stay in contact with each other.

As the dropweight impacts the specimen, a high-speed vibrational wave travels up the length of the dropweight. Figure 3.2 shows a graph representing the movement of this wave. Position *A* is the bottom of the dropweight, *B* is the

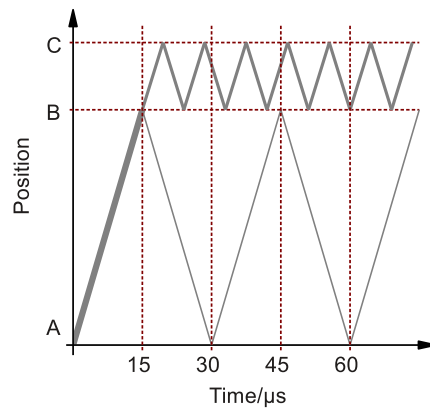


FIGURE 3.2: *Vibrations in the dropweight system.*

interface between dropweight and anti-vibration block, and C is the top of the anti-vibration block.

Upon incidence with the anti-vibration block, the majority of the wave is transmitted into the block, with a smaller amplitude wave reflecting into the dropweight due to imperfections in the dropweight - anti-vibration block interface. The relative amplitudes of the vibrational waves are illustrated with the thicknesses of the lines in Figure 3.2.

As the wave transmitted into the anti-vibration block reaches the top, it is reflected as a wave of tension. The tensile wave is incident with the interface, and is strong enough to separate the two components from each other, effectively trapping the majority of the vibrational wave inside it.

3.2.3 Triggering system

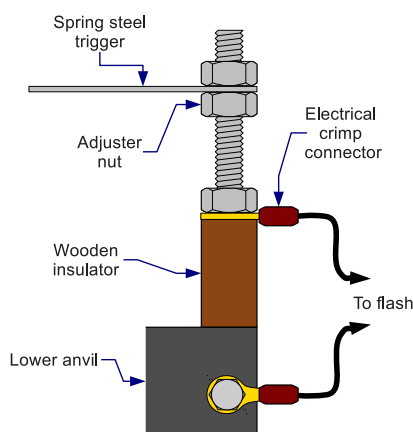


FIGURE 3.3: *The ODW trigger.*

The triggering system used on the ODW is of a rudimentary design. Its simplicity, however, is of great benefit in this instance as it provides for a great deal of extremely simple and rapid adjustment.

Its primary component is the trigger itself, which is simply a thin, flexible strip of spring steel. It is held on a threaded bar by means of a threaded rod and a pair of adjuster nuts. The vertical position of the trigger may be quickly adjusted by screwing the nuts up or down. The trigger on its threaded rod are kept electrically insulated from the lower anvil by means of a wooden insulator block.

As the dropweight falls, a bolt screwed into the weight itself (visible in Figure 3.1) touches the spring steel trigger. With the dropweight, lower anvil and guide rails being constructed entirely out of metal, this closes the electrical connection between the lower anvil and the trigger. This closed connection is used to trigger the flash, and in cases where a digital high-speed camera is used (see Section 3.2.5) the camera as well.

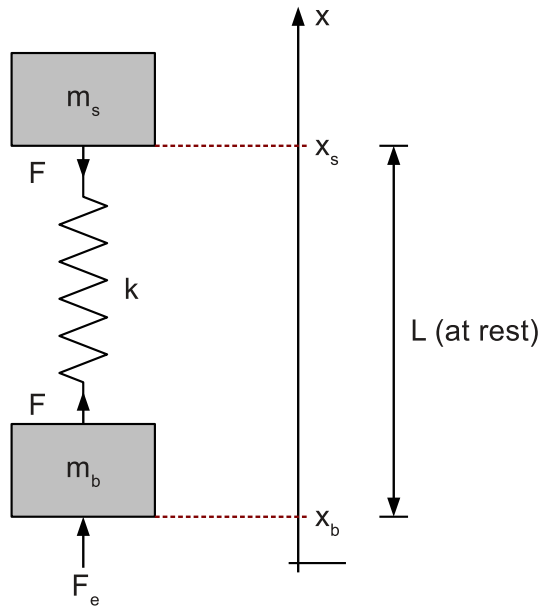


FIGURE 3.4: *Simplified model of an accelerometer [Serridge and Licht, 1987].*

3.2.4 Accelerometer

The accelerometer fitted to the ODW is a Brüer & Kjær type 4344 piezoelectric compression transducer which has a flat frequency response up to 30 kHz.

A simplified model of such an accelerometer is shown in Figure 3.4. The base of the accelerometer with mass m_b and position x_b is connected to a seismic mass, m_s , at position x_s by means of an ideal spring with a spring constant k . At rest, the two weights are separated by a distance L . When a seismic excitation force, F_e , causes the position of the accelerometer base to change, the distance L changes linearly with respect to the acceleration caused by F_e . By connecting the two weights to a piezoelectric transducer, it is possible to measure this change in distance, and hence calculate the acceleration undergone by the accelerometer.

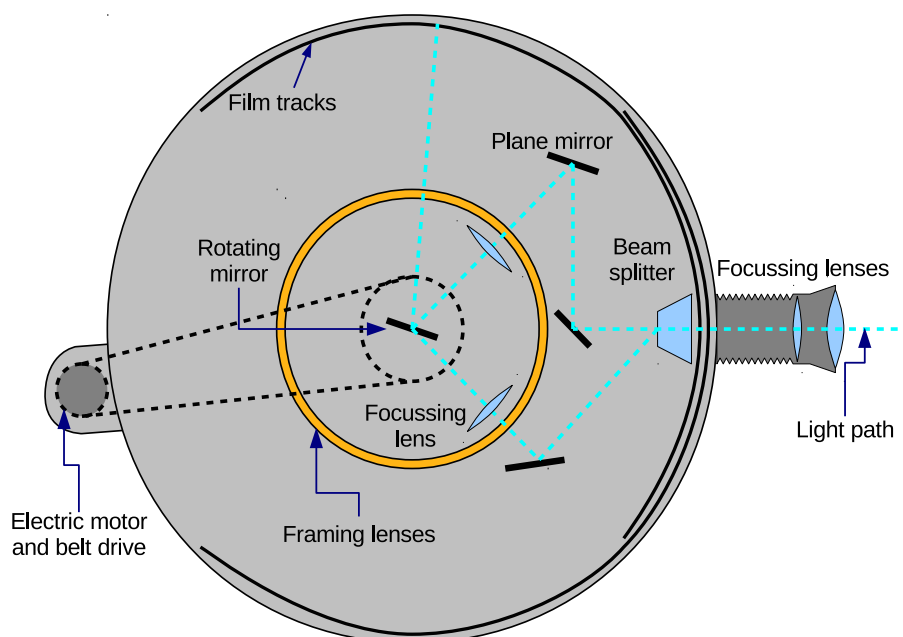
3.2.5 High-speed photography

There are two primary considerations for a high-speed camera in an ODW system; experimental duration and required resolution.

The duration of an experiment is very much dependant on the material being tested; a stiffer material will deform very little, so the experiment will be over quickly, whereas a softer material will exhibit more significant deformation over a longer time. With the polymeric specimens examined in this work, upon impact they would expand smoothly until they were larger than the field of vision. A typical duration for this experiment would be of the order of 1 ms.

High-speed cameras which are fast enough for this type of experiment, are typically only capable of storing a relatively small number of images at a time. For example, the Shimadzu HPV-1 discussed below is capable of recording a maximum of 100 frames at a time.

The experimental duration and the number of captured frames will dictate the desired frame rate, e.g. for an experiment lasting 1 ms with a camera capable of recording 100 images, the ideal inter-frame time is 0.01 ms making the frame rate 100,000 frames per second.

FIGURE 3.5: *The AWRE C4 Camera.*

3.2.5.1 AWRE C4 camera

The first camera that was used in this project was a C4 camera built by the Royal Armament Research and Development Establishment (RARDE) at Fort Halstead for the Atomic Weapons Research Establishment (AWRE) in Aldermaston, Berkshire, UK. Originally built some time in the 1950s or 1960s^a to record the initial moments of high explosive and nuclear detonations, the C4 is capable of recording at speeds of up to 200,000 frames per second (fps) if the camera is evacuated, or around 125,000 fps in atmospheric conditions, capturing a total of 140 frames.

A cross-section of the camera is shown in Figure 3.5 which illustrates its principal of operation. Light enters through a set of focussing lenses at the front of the camera, and is split into two separate light paths. Each path is reflected via plane mirrors onto the central rotating mirror. The rotating mirror points the light through one of 140 framing lenses held in a brass ring around the rotating mirror, and are finally focussed onto one of two slightly elliptical film tracks around the outside of the camera body.

Film for the C4 is not commercially available and must be prepared from large format aerographic film. The film used in this work was Kodak Double-X Aero-graphic (2405) film which is supplied in 75 m (250') long rolls of 241 mm (9.5") width. The film must be cut prior to use in order to fit into the C4 camera's film tracks. They are cut into arcs of around 3 m in length, with a radius of curvature of 5.3 m using a cutting table specifically designed for this purpose which is currently in the possession of the Department of Physics at Loughborough University.

The cut film is loaded into light-proof film cassettes, and must be manually drawn around the camera's film tracks. Since the film used is panchromatic, there

^aPrecise details of the design and construction of this camera are shrouded in the secrecy that would be normally expected from an organisation set up to build atomic weapons. The years quoted here come from anecdotal references.

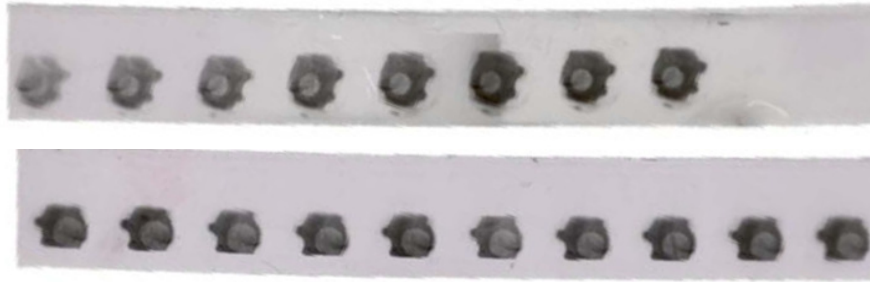


FIGURE 3.6: *Images taken with the AWRE C4 camera.*



FIGURE 3.7: *The Shimadzu HPV-1 high-speed camera.*

is no safe light and so any work performed with the film must be performed in total darkness [Skinner, 1962] [Prudom, 2012].

Using such a camera does present a number of difficulties. With the global acceptance of digital photography, camera film is becoming increasingly difficult to locate. Since it has a limited shelf life, much film that has been sat in a warehouse for a considerable time will have deteriorated beyond any practical use. Any film obtained will need to be kept in a freezer in order to extend its life as much as possible.

Getting film developed is also tricky. While some companies are still capable of developing film, this is limited to the more 'ordinary' formats such as 35 mm. It is most likely that any film will need to be developed manually in house, which is a rather time consuming business. Because of the need for manual film processing, it was found that using the C4 camera limited the number of experiments performed in a day to three or four.

Figure 3.6 shows some typical images of an LLDPE specimen being compressed in the ODW taken with the AWRE C4 camera.

3.2.5.2 Shimadzu HPV-1

Although using film cameras can be a laborious process, it is only in recent years that digital high-speed cameras have begun to catch up with film in terms of quality, speed and total recorded images. For this work a Shimadzu HPV-1 camera was loaned from the Engineering and Physical Sciences Research Council (EPSRC) engineering instrument loan pool.

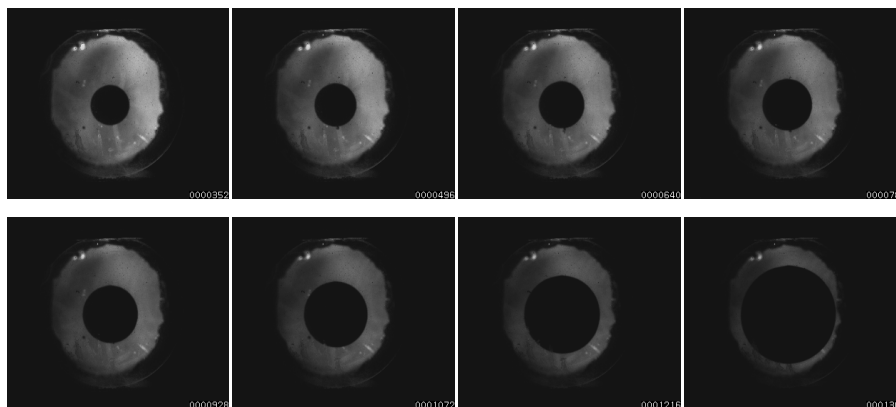


FIGURE 3.8: Images taken with the Shimadzu HPV-1 camera.

It is capable of recording at speeds of between 30 and 1,000,000 fps and captures a total of 100 greyscale images at a resolution of 312×260 pixels. It consists of a camera recording head to which any lens using the Nikon F-mount SLR format may be attached, and a separate Microsoft Windows XP computer which runs software to receive and store the images from the camera. The CCD^b is unique to Shimadzu, and has the capability to store 100 full size images on the chip itself, which are streamed to the computer post capture.

The HPV-1 can be triggered by a variety of methods including an electrical short or a 5 V TTL pulse, making it a versatile piece of equipment which can easily be used in a variety of experimental situations.

Figure 3.8 shows some sample ODW images of an LLDPE specimen taken on the Shimadzu HPV-1 camera.

3.2.5.3 Flash unit

The flash unit used with the ODW was a Bowens MonoGold 1500W studio flash. This is an ordinary studio flash unit and most flash units of a similar intensity should be able to perform the job perfectly well. Flash triggering is performed by connecting a $\frac{1}{4}$ " (6.35 mm) mono audio jack to the triggering system discussed in Section 3.2.3 (page 96) in parallel with the high-speed camera trigger cable.

3.3 Specimen design

The design of specimens for ODW experiments is relatively straightforward. They should be cylindrical in shape, with a volume small enough so that they do not expand beyond the area of the glass anvils too rapidly, yet large enough so that their expansion is easily measurable. They should not be too long so that, during compression, they do not bend visibly, and barrelling is insignificant.

Since in this work the ODW was used to produce data which was complimentary to the SHPB experiments, and since the SHPB specimens were of a suitable shape and size for use in the ODW, the same specimens were used for both experiments. See Section 2.3 (page 66) for full details of the design of specimens for SHPB experiments.

^bCharge-coupled device, the image sensor used in digital photography.

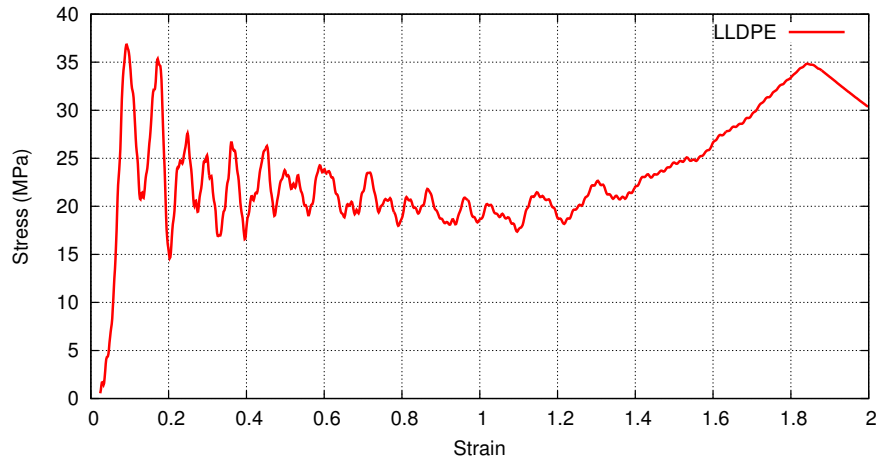


FIGURE 3.9: *Unfiltered ODW data of an LLDPE specimen.*

3.4 ODW analysis

From Equation 3.9, the true strain experienced by a specimen in an ODW experiment is

$$\varepsilon_T = -\ln \frac{D_0^2}{D(t)^2}$$

and from Equation 3.3, the engineering stress is

$$\sigma_E(t) = \frac{4F}{\pi D(t)^2}$$

which may be converted to true stress using the relation

$$\sigma_T = \sigma_E(t) \cdot (1 - \varepsilon_T)$$

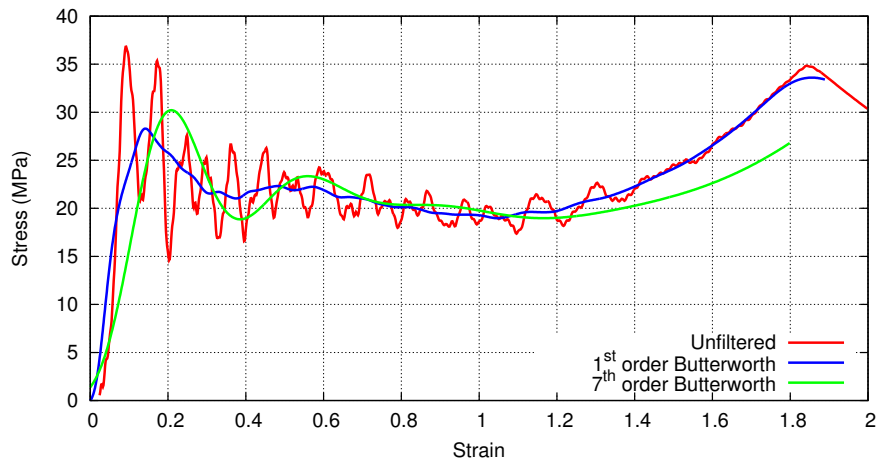
Analysis is, therefore, a relatively trivial task involving a comparison between the original specimen diameter D_0 , its dynamic diameter $D(t)$, and the force measured by the accelerometer, F .

3.4.1 Smoothing and filtering data

Despite the anti-vibration block, the ODW still produces a significant amount of noise in the form of ringing within the dropweight. Filtering, therefore, is especially important with this experiment. Figure 3.9 shows typical unfiltered data of a specimen compressed in the ODW.

A number of filtering and smoothing techniques are discussed in Section 2.5.1 (page 75) in relation to SHPB experiments, and for the most part, the same options apply to ODW experiments. The considerable amplitude of the noise, however, means that care must be taken when employing filters. High-order Butterworth filters, having a sharp tail-off of response at frequencies higher than the cut-off frequency^c, tend to be too harsh for use with ODW stress-strain curves, as may be seen in Figure 3.10.

^cSee Figure 2.26 on page 77 for a graph of the frequency response of various orders of Butterworth filter.

FIGURE 3.10: *Filtered ODW data of an LLDPE specimen.*

As with SHPB filtering, the ultimate choice of which technique to use comes down to personal preference. In the work presented here, the analysis has been performed with unfiltered data, and then smoothed post-process using a first order Butterworth filter with a cut off frequency of 10kHz. The data is given a final smoothing using a Bézier algorithm, which does little to the data, but makes it a little more presentable for publication.

3.4.2 Dropweight stress-strain curves

On the whole, ODW stress-strain curves may be analysed and interpreted in the same way as SHPB stress-strain curves. Section 2.5.3 (page 86) contains detailed explanations of how the analysis may be performed, and the C++ and GNU Octave programs in the associated appendices may easily be adapted to work with ODW data.

The heavy filtering required can have an effect on the measurement of Young's modulus. Figure 3.11 shows this effect, where Young's modulus should be highest at the start of the curve. In this case, the value becomes accurate as the curve reaches its initial peak. This has been deemed an acceptable compromise for the work presented here.

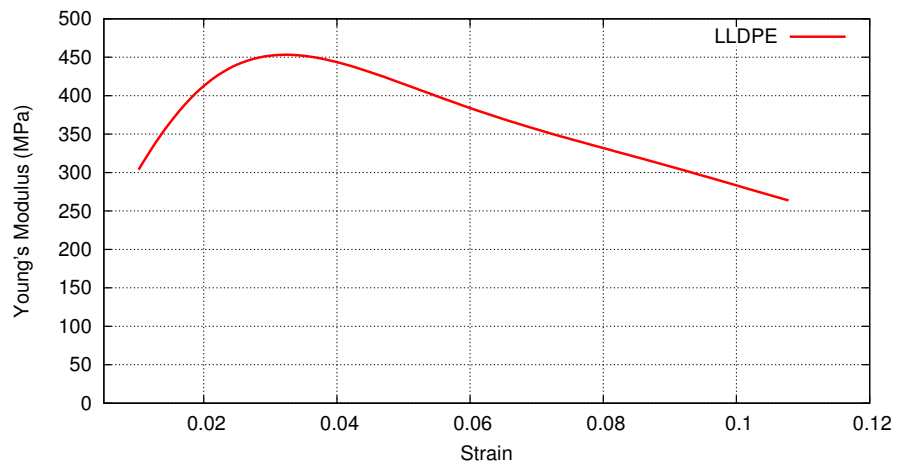


FIGURE 3.11: *ODW Young's modulus history of an LLDPE specimen.*

Part III

Experimental

Understanding armour

“There is nothing worse than a sharp image of a fuzzy concept.”

—ANSEL ADAMS

The main difficulty with developing materials for use in armour, is understanding exactly what it is that is needed to improve existing solutions. Considering that the majority of armour is developed with military use in mind, much of the information relating to their design and use has restricted availability. This means that the usual scientific research approach of scouring books and journal articles, often produces disappointing results, particularly in regards to modern, high technology solutions.

A theoretical approach is also rather complicated. According to Newton’s approximation for the impact depth of a high speed projectile, the depth of penetration, D , is

$$D \approx \ell_p \frac{\rho_P}{\rho_T} \quad (4.1)$$

where ℓ_p is the length of the projectile and ρ_P and ρ_T are the densities of the projectile and target respectively. This approximation only considers the momentum carried by the projectile, and it is assumed that the velocity of the projectile is high enough to ignore any cohesion in the body of the target, and that the target is infinitely deep. As the projectile moves into the target, it pushes away the target material directly in front of it, transferring some of its momentum into the separated material which then moves along at the same speed as the projectile. The further the projectile passes, the greater the mass of the separated material becomes. When the masses of the projectile and the dislocated material are equal, all of the projectile’s momentum will have been transferred into the target body and it will be arrested.

While this approximation can be informative, the assumptions made therein mean it can’t begin to describe the complexities of genuine armour.

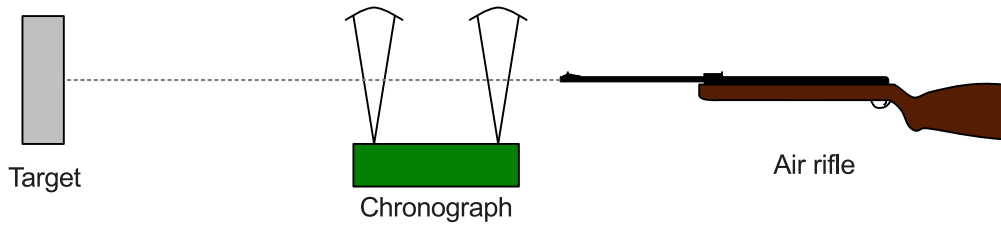


FIGURE 4.1: *Experimental setup for testing armour simulants with an air rifle.*

4.1 Scaling down

One possible way to supplement information gleaned through theory and research, is to attempt to construct something which is capable of reproducing a similar end result to the ‘real’ material. This *simulant* may not be able to give any information on the precise properties of the real material, but can provide valuable qualitative data which can help to explain how materials may be improved.

Of course, the material of interest in this work is armour, and that introduces additional complexities into this form of evaluation.

The ordinary method of testing armour materials is to subject them to the same sort of impacts they would have to contend with in real world use. This would typically involve shooting at them with high-powered rifles for body armour, or subjecting them to blast forces in the case of vehicle armour. Since access to firearms and explosives, not to mention locations safe enough to employ such experiments, is highly regulated, this form of testing is not within the grasp of many institutions.

The trick is to scale down both the simulant, by using weaker materials, thinner layers etc., *and* the testing methodology.

For this research a number of different materials were experimented with in order to produce a simulant of the ceramic armours normally found in military body armour. At the time of writing, possession and use of an air rifle with a muzzle energy of less than 12 foot-pounds (~ 16 J) is unlicensed and may be carried out, with due care, at any location. At this energy, a typical .22 calibre air rifle pellet, with a mass of 14.3 grains (~ 0.93 g) will be propelled to a maximum velocity of around 187 m s^{-1} . While this is hardly comparable to, say, the .338 calibre Lapua Magnum cartridge used in the L115A3 Long Range Rifle used by the British Armed Forces^a, it does provide for similar testing conditions.

Figure 4.1 shows the experimental configuration for these experiments. Before being incident with the simulant, the pellet passes through a chronograph in which its velocity is measured. The overall distance between the end of the air rifle and the simulant is approximately 3 m. It was assumed that, at this short distance, the projectile would lose very little velocity before impacting the target. One single type of pellets were chosen for this experiment in order to minimise differences in muzzle velocities and pellet mass & shape. The chronograph showed that the pellets used consistently travelled at $180 \pm 6 \text{ m s}^{-1}$.

^aBullet weight 200 grains (~ 13 g), muzzle energy 4967 foot-pounds (~ 6734 J), maximum velocity 1019 m s^{-1} .

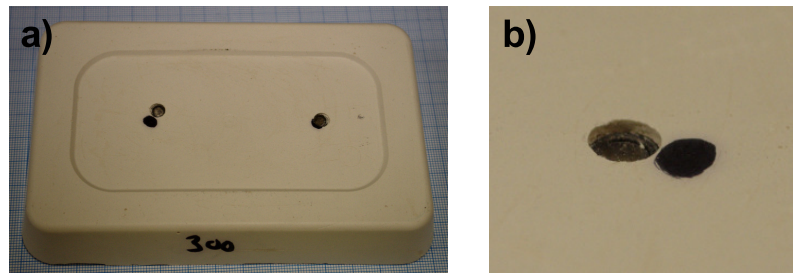


FIGURE 4.2: 300 g monolithic gypsum plaster slab after impact, front view.

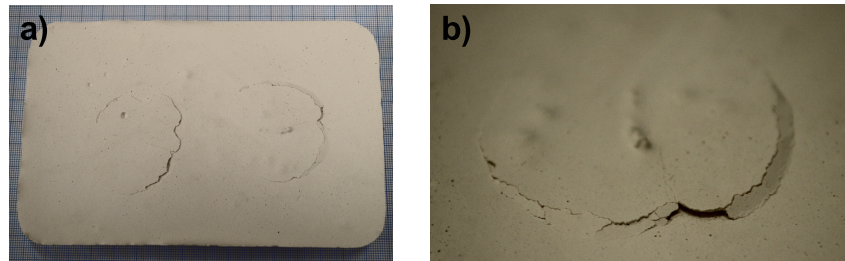


FIGURE 4.3: 300 g monolithic gypsum plaster slab after impact, rear view.

Of the simulant body armour materials tested, one stood out as particularly interesting. Common-or-garden gypsum plaster, *plaster of Paris*, was a particularly interesting material to be used for testing with an air rifle. Not only is it very cheap and easy to work with, but when fired upon, the damage received by the armour appeared precisely what would be expected from ceramic armour after an impact with a high-velocity rifle round.

4.2 The experiment

Simulants were moulded in disposable plastic food containers which ensured that each specimen was of a matching shape. Once the liquid plaster was poured into the mould, they were left to set for one week to allow them to dry adequately before use. Experiments revealed that a mixture of 300 g of dry plaster mixed with 150 ml of tap water produced a block of material which was just adequate to completely arrest an air rifle pellet. Using less plaster than this resulted in the pellet penetrating right through the simulant.

Figures 4.2 and 4.3 show a monolithic gypsum plaster slab constructed from 300 g plaster and 150 g water. On the front face of the slab, the rear side of the pellets may be seen^b with Figure 4.2 b) showing a close-up of one impact site. The rear side of the simulant shows that the penetration of the pellets have caused a large section of the gypsum to begin to break away from the bulk. Again, a close-up is shown in Figure 4.3 b).

Figure 4.4 shows a monolithic plaster block constructed from 250 g of dry plaster and 125 ml of tap water after impact, with a) showing the exit face and b) showing a cut through cross-section of the penetration fracture cone. The difference between this and the 300 g simulant are quite conspicuous.

^bEach slab was subjected to impact twice to help ensure that the results were not significantly affected by irregularities, such as air pockets, within the body.

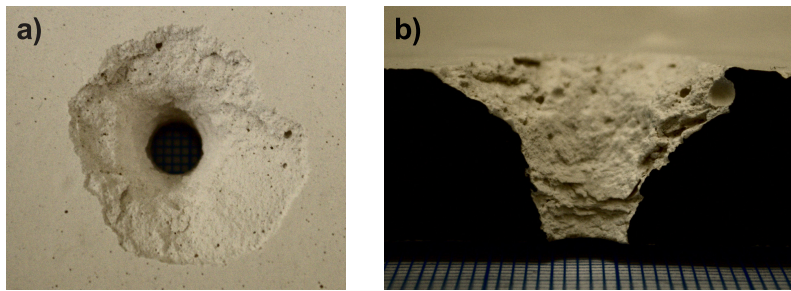


FIGURE 4.4: 250 g monolithic gypsum plaster slab after impact. The faces of the cutaway view in b) have been coloured black to increase the contrast.

This would provide a useful benchmark during experimentation with plaster slabs. The goal was the production of a slab which was capable of arresting a projectile, but which used a thinner (and therefore lighter) layer of gypsum plaster.

4.3 Observations

From the experiments performed with monolithic armour simulants, a number of observations were made in regard to the progress of a pellet as it passed through (or was arrested inside) the body of a simulant. These are shown in Figure 4.5 and discussed below.

- a) *Approach.* The air rifle pellet approaches the simulant.
- b) *Impact.* The initial impact results in spall being ejected from the front face of the simulant. The pellet begins to slow down and deform. The material directly in front of the pellet is compressed, at the pellet velocity, into the body of the simulant (shown in red).
- c) *Channelling.* Still retaining a significant velocity, the pellet is able to carve a channel into the body of the simulant. It continues to deform, with its leading edge being flattened and expanding, increasing the contact surface area. This, along with the increasing quantity of displaced material being compressed in front of the pellet, causes the pellet to slow at an increased rate. The displaced material, having significant thickness at this point, breaks away and compresses material further into the body. The slowing pellet means that simulant cohesion begins to affect the shape of the displaced material in front of the pellet, splaying it further into the body.
- d) *Fracture cone generation.* The slowing pellet, the increasing displaced material in front, and the growing effect of cohesion result in the development of a fracture cone. The shape of the cone accelerates the slowing of the pellet. If the pellet loses all of its momentum before the fracture cone reaches the rear face of the simulant, the pellet is arrested. If some momentum remains at this point, the body of the simulant will no longer present any hinderance to the pellet's progress.
- e) *Exit.* As the pellet exits the rear of the simulant, the material which was inside the channel and fracture cone is ejected as spall.

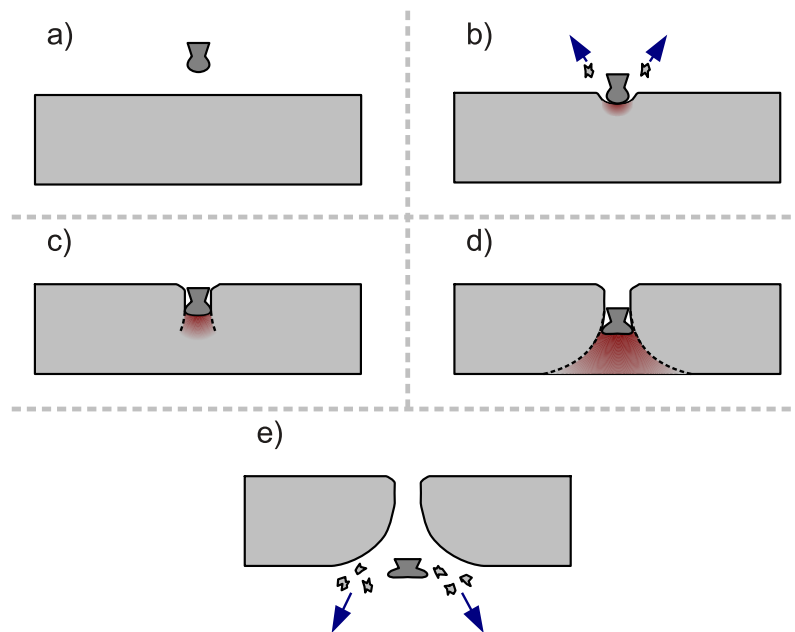


FIGURE 4.5: *Progress of air rifle pellet through monolithic gypsum plaster slab.*

Within this timeline, channelling and fracture cone generation are critical in terms of slowing down and ultimately arresting an impacting projectile.

During channelling the pellet is moving fast enough, at least initially, to limit the effect of cohesion within the body of the simulant, that is, Equation 4.1 provides a reasonable approximation for the progress of the projectile. Once the pellet passes a critical penetration depth, the additional mass of the simulant body material pushed in front reduces its speed sufficiently so that the cohesion within the simulant begins to take effect.

The result of cohesion is the generation of a fracture cone within the simulant body. The slower the pellet moves, the greater the effect of cohesion which causes the cross-section of the fracture cone to take on a curved shape similar to that shown in Figure 4.5 e) and which may be seen in a real target in Figure 4.4. It is important to note that, because of the generation of the fracture cone, the pellet does not need to carry enough energy to completely penetrate the simulant, as the fracture cone will reach the rear face while the pellet is only a fraction of the way through.

4.4 Improvements

In order to improve the behaviour of an object such as the armour simulants, it is worth considering the effect of employing materials with entirely different properties. As part of this research the monolithic slabs of gypsum were altered by the addition of layers of alternative materials both on the strike face and on the reverse.

Figure 4.6 shows a gypsum plaster simulant which has had 15 ml of latex applied onto the rear face. The latex was applied in liquid form onto pre-hardened plaster, and allowed to dry completely. Adhesion between the gypsum and the latex was insubstantial, with the rubber layer being quite simple to peel away from

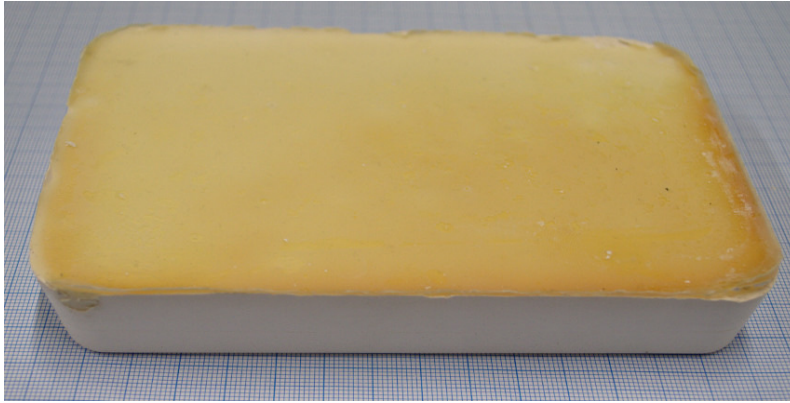


FIGURE 4.6: *Gypsum plaster slab with a layer of latex rubber on the reverse.*

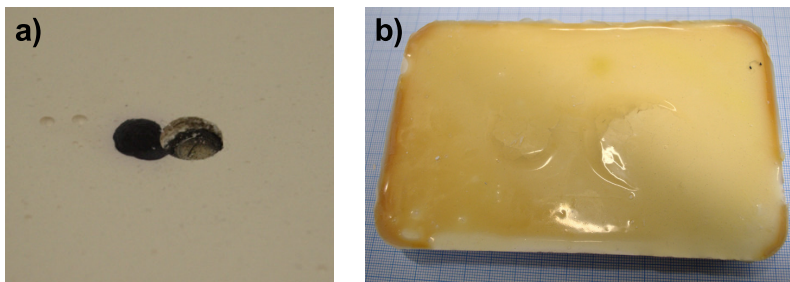


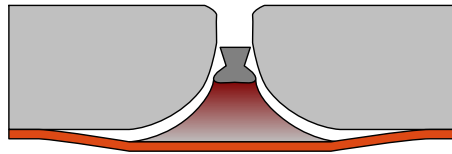
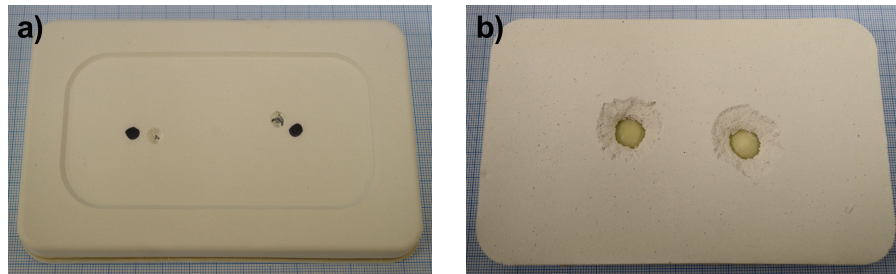
FIGURE 4.7: *250 g gypsum slab with a 15 ml layer of latex rubber after impact.*

the plaster, but was strong enough to stay in place during fairly rough handling. As liquid latex dries it contracts slightly, meaning it was impossible to deposit thick layers of it onto the plaster; volumes in excess of around 50 ml resulted in the thick latex layer delaminating from the plaster as it dried. For the purposes of this experimentation, latex layers produced from either 15 ml or 30 ml of liquid latex were used. 15 ml was just enough latex to barely cover the surface of the plaster, needing to be 'painted' on, while 30 ml was just enough to pour on and allow to settle into an even coating.

It was observed that the addition of a latex layer onto the front face of the plaster (the impact face) had no discernible affect on the progress of the air rifle pellet, although it did greatly reduce the amount of spall ejected from the impact site. Applying latex to the rear face, however, appeared to dramatically increase its ability to arrest a projectile.

Figure 4.7 shows a simulant constructed from 250 g gypsum and 15 ml latex on the reverse face. a) shows the impact point of the pellet, which is clearly visible just below the surface of the plaster, and b) shows the reverse on which it appears that the latex has prevented the detached material from the fracture cone from falling free of the body of the simulant, and brought about the arrest of the pellet. This is shown schematically in Figure 4.8.

It is thought that the key properties of the latex layer that enable it to do this are its adhesion with the surface of the simulant, and its elasticity. Although, as discussed above, adhesion is not substantial in this configuration, it is enough to prevent the fracture cone from being ejected from the rear face of the plaster slab. The elasticity of latex allows the fracture cone to move without tearing.

FIGURE 4.8: *Latex layer helping to arrest a pellet.*FIGURE 4.9: *A sandwich simulant after impact.*

With the monolithic simulants, a pellet had only to travel a short distance into the body of the plaster, before pushing the fracture cone away from the rear face and being allowed free passage through the rest of the material. The addition of a thin latex layer artificially increases the effective thickness of the plaster dramatically.

Several experiments were performed with a variety of thicknesses of plaster with both 15 ml and 30 ml of latex on the reverse face. It was found that as little as 225 g of plaster could arrest a pellet with the addition of a latex layer. Both 15 ml and 30 ml latex layers performed equally well.

Additional experiments were also attempted using sandwich structures. It was hypothesised that a three layer simulant made up of two layers of gypsum sandwiching an intermediate layer of latex would allow the pellet to form a channel in the upper gypsum section, without imparting significant amount of stress onto the lower gypsum section. The layer of elastic was positioned between gypsum slabs made of equal amounts of plaster, and were of approximately equal thickness. It was hoped that the latex layer would be roughly just after the point at which fracture cone generation began.

Figure 4.9 shows a typical sandwich structure, constructed from two layers of 125 g gypsum surrounding a single 15 ml latex layer. In a) the arrested pellets are barely visible, while b) shows that the fracture cone has been fully ejected from the rear of the simulant.

Since this structure successfully arrested the projectile, it would appear that this configuration improved the performance of the monolithic plaster. Considering that the earlier experiments with the latex on the rear face also showed a performance increase, it seemed reasonable to assume that a combination of the two configurations may be able to provide further improvements. A number of four-layer laminate structures were constructed. Figure 4.10 shows such a laminate structure after impact with a) showing the front face, b) the rear face, and c) a side-on view, revealing the construction of the simulant.

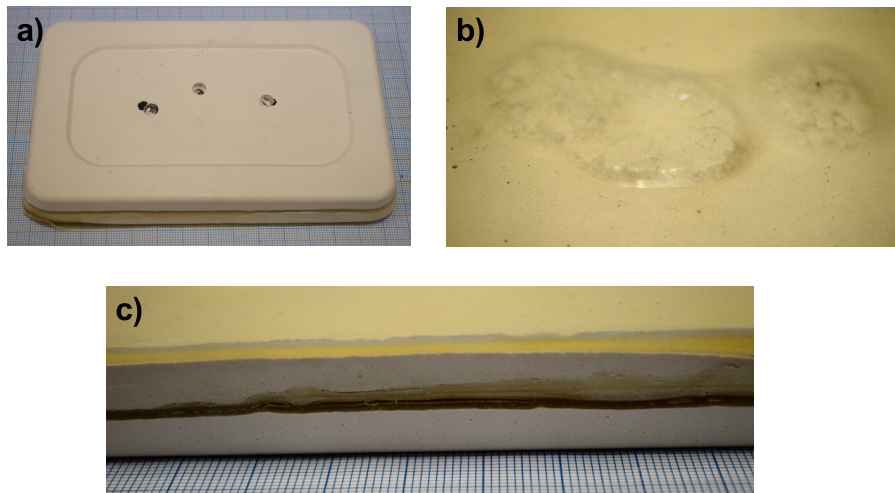


FIGURE 4.10: A four-layer laminate after impact.

This configuration had a dramatic effect on the performance of the simulant, and was repeated with a range of layer thicknesses. It was found that it was possible to produce a laminate consisting of two layers of 100 g gypsum/50 ml water and two layers of 15 ml latex, one in between the gypsum layers and another on the reverse face, shown in Figure 4.10^c. This simulant was capable of arresting the air rifle pellet, effectively performing the same function as a 300 g monolithic gypsum slab.

4.5 Further experimentation

4.5.1 Improved production techniques

Clearly the experiments performed here provide purely qualitative observations of how it may be possible to improve the properties of a hard ceramic armour with the addition of a number of elastomeric layers. In order to quantify the results, some modifications to the experimental method are necessary.

The moulds used were simple plastic food containers, which were chosen partly because they made it possible to reliably produce simulants of matching shape, but mainly because they were cheap. The overall shape of the resulting specimens was not ideal, having tapered sides and a non-flat bottom surface as may be seen in the preceding images. More precise moulds could be constructed quite easily.

Prior to mixing, the dry plaster was weighed using digital scales to a reasonable level of accuracy (± 1.0 g), but the water used was measured in a graduated beaker and was likely to have an uncertainty of $\pm 10\%$. Mixing was performed by hand, which may give rise to undissolved clumps of dry plaster, and certainly results in air bubbles within the plaster slab. These issues could be resolved by introducing a more precise method for measuring the water, using mechanical means to mix the plaster and water (e.g. a kitchen blender) and by drying the specimens in a partially evacuated environment, for example in a desiccator.

^cThis simulant was shot three times to ensure that the result of the first two shots were not a chance occurrence.

Although it seems clear that the addition of the elastic layer on the exit face improved its ability to arrest a projectile, what is not known is how much additional energy the projectile would need to penetrate. This is complicated to evaluate with the current experimental setup, since the air rifle is only capable of operating at a single muzzle energy. Many air rifles create high pressure air by rapidly pushing a piston along a barrel with a spring. It may be possible to lower the muzzle energy by drilling one or more small holes into the face of the piston, and hence create a variable energy air rifle.

4.5.2 Additional materials

Additional information could be gleaned by testing alternative materials. There are a range of different types of plaster available, from 'stone powder' which is claimed to be significantly harder than ordinary gypsum, to household plaster designed to repair cracks in walls. By performing experiments with these additional materials, it would be possible to gain an understanding of how the use of softer and harder materials affects the progress of a projectile. Of course it may be that a certain hardness of plaster works well on the impact face, while a different hardness improves the exit face, and these additional experiments would provide the opportunity to investigate this.

If the addition of an elastic layer within the body of the simulant improves its performance, then perhaps alternative materials could improve this further. Materials such as cotton fabric, thin copper or aluminium sheets, or wire mesh could be experimented with to evaluate their use.

4.6 Scaling up

Of course it is impossible at this stage to know how well, if at all, the configurations discussed in this section would work if they were scaled up to realistic armour ceramic materials impacted by high-energy projectiles. In order to understand this, it would be necessary to replace the materials used in the experiments performed here with realistic armour materials.

Replacing the gypsum plaster with armour ceramics such as alumina or boron carbide, or with armour steel would be appropriate. A replacement for the latex provides for some interesting questions. A highly elastic material with reasonable adhesion would be required. The polyurea discussed elsewhere in this report would seem an ideal candidate.

Split-Hopkinson pressure bar

“The truth knocks on your door and you say, ‘Go away, I’m looking for the truth,’ and so it goes away. Puzzling.”

—ROBERT M. PIRSIG
ZEN AND THE ART OF MOTORCYCLE MAINTENANCE

5.1 SHPB Modifications

A number of modifications were made to the SHPB in order to optimise it for the measurement of polymeric specimens.

5.1.1 Alternative pressure bar materials

The low density of many polymers results in them having a low acoustic impedance. To reduce the impedance mismatch between the specimen and the SHPB pressure bars, it was decided to replace the bars with new ones constructed of a different material which more closely matched the impedance of the specimens to be tested.

The SHPB system in use at Loughborough University was constructed using maraging steel pressure bars with an additional stainless steel pre-loading bar [Ellwood et al., 1982] and a 20 cm long stainless steel projectile fired from a compact, evacuated gas gun [Parry and Griffiths, 1979]. Pressure bars and projectile all have a diameter of 12.7 mm. Before any modifications were made to the system, a benchmark was obtained by testing a low impedance specimen with the SHPB in its original configuration. LLDPE was chosen as a test material, and cylindrical specimens measuring approximately 8 mm in diameter and 4 mm long were formed by compression moulding. To obtain a thorough illustration of specimen behaviour, it was decided that it should undergo a total strain of around 100%. Without modifications to the gas gun, the lowest projectile impact velocity achievable was $v \approx 10 \text{ m s}^{-1}$, which, in the standard SHPB configuration, caused the specimen to strain significantly more than this, although reducing the projectile velocity to limit specimen strain was deemed to be unnecessary.

Figure 5.1 shows the strain gauge data collected from this experiment. The amplitude of the transmitted pulse is very low with the percentage of the pulse

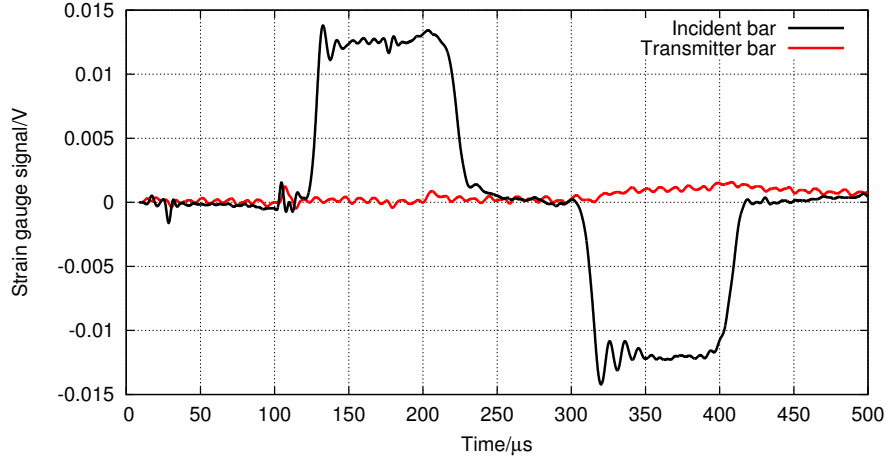


FIGURE 5.1: LLDPE specimen in maraging steel SHPB.

Metal	ρ kg m^3	c_0 m s^{-1}	σ_Y MPa	Z_0 $\text{kg m}^{-2}\text{s}^{-1}$
Aluminium	2710	5119	80	13.9×10^6
Aluminium, 7068 alloy	2850	5061	550	14.4×10^6
Magnesium	1740	5029	95	8.8×10^6
Nickel	8900	4823	60	42.9×10^6
Nickel, strong alloy	8500	3597	1200	30.6×10^6
Steel, stainless	7930	5022	230	39.8×10^6
Steel, maraging	8100	5092	1800	41.2×10^6
Titanium	4540	5055	20	22.9×10^6
LLDPE	920	442	25	0.4×10^6

TABLE 5.1: The density (ρ), wave speed (c_0), yield stress (σ_Y) and acoustic impedance (Z_0) of a range of metallic solids and LLDPE [Tennent, 1971].

transmitted being only around 10%. Although this data could be analysed to produce a stress-strain curve, any subtleties therein could be lost in the background noise.

Table 5.1 shows the acoustic impedance, Z_0 , of a range of pure metals along with LLDPE for comparison. Since the impedance is primarily a function of density, the lowest density metal also has the lowest Z_0 . Bars constructed of pure magnesium made for an obvious choice of which pressure bar material to test first. 12.7 mm diameter Mg bars were sourced and installed into the SHPB along with a 20 cm projectile of the same material.

The initial attempt to replace the pressure bars and projectile with those of pure Mg were partially successful, providing a noticeable improvement in the transmitted pulse amplitude. It was found, however, that the low mass of the Mg projectile resulted in a lower overall energy, reducing specimen strain to an

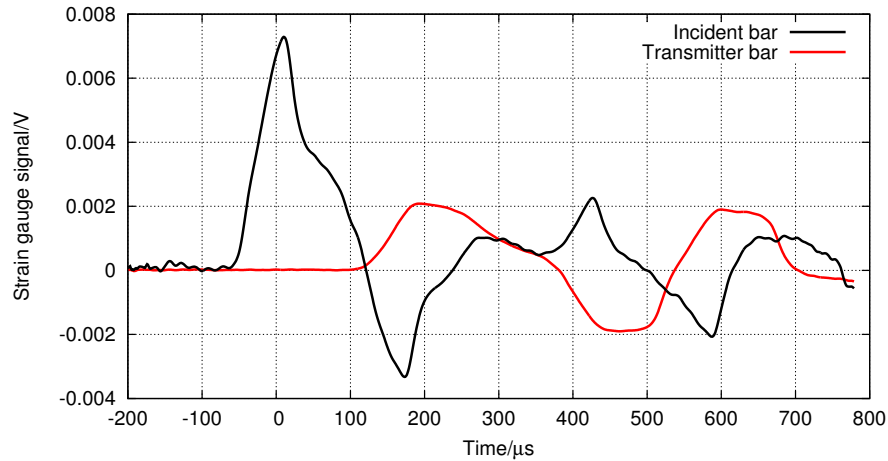


FIGURE 5.2: LLDPE specimen in pure Mg SHPB.

unsatisfactory level. The stress in an SHPB can be described [Dioh et al., 1995] using

$$\sigma = \rho c_0 v \quad (5.1)$$

where ρ is the density of the pressure bars, c_0 is the wave speed in the bars and v the projectile impact velocity. The total stress imparted by the impact of an Mg projectile travelling at $v \approx 10 \text{ m s}^{-1}$ is therefore $\sigma = 88 \text{ MPa}$, just within the yield stress of Mg. To increase the specimen strain it would be necessary to increase the projectile velocity, taking the pressure bar strain over the yield strength. Notwithstanding, the projectile impact velocity was increased to $v \approx 20 \text{ m s}^{-1}$ ($\sigma = 176 \text{ MPa}$). As expected the pressure bars began to deform plastically, which gave rise to a triangular-shaped incident pulse instead of the usual parallelogram, clearly visible in Figure 5.2. Specimen strain was improved, but still slightly less than desired.

A second attempt was made using the alloy ZK60 which was chosen for its higher claimed yield stress of 260 MPa. It has a chemical composition of 5.5% Zn, 0.5% Zr and 94% Mg. It has a density slightly greater than that of Mg ($\rho_{\text{ZK60}} = 1830 \text{ kg m}^{-3}$) and a lower wave speed ($c_0 = 4936 \text{ m s}^{-1}$), giving an acoustic impedance only marginally higher than pure Mg at $Z_0 = 9.0 \times 10^6 \text{ kg m}^{-2} \text{ s}^{-1}$. Pressure bars made from ZK60 were installed into the SHPB and a projectile was constructed with an increased length of 30 cm in order to extend the total strain duration. This was tested at projectile impact velocities of $v \approx 20 \text{ m s}^{-1}$. The strain gauge data from an experiment with this configuration is shown in Figure 5.3, which has proven to be quite acceptable. The transmitted pulse amplitude has increased agreeably, with over 25% of the incident pulse being transferred into the transmitter bar, making the resolution of the transmitted signal more than double that of the steel-based SHPB.

A comparison of the stress-strain curves generated with an LLDPE specimen in both steel and ZK60 based SHPB systems is shown in Figure 5.4. It is clear that the two curves show approximately the same data, but that taken with the ZK60 SHPB shows a dramatic improvement in readability.

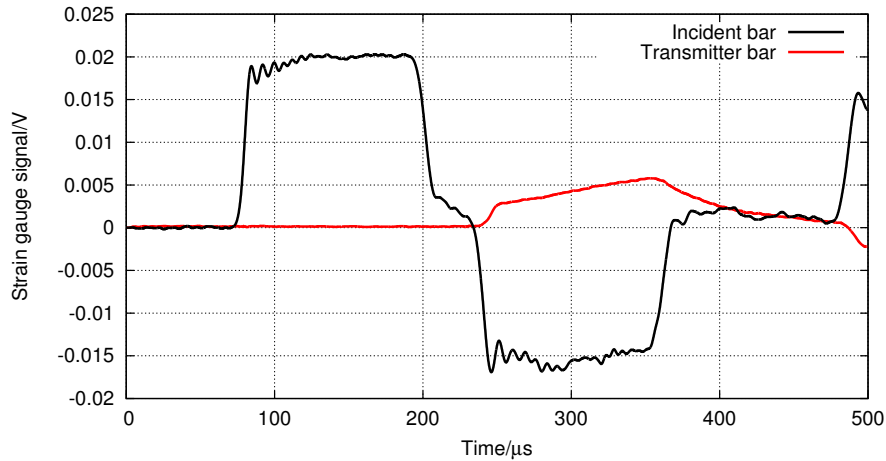


FIGURE 5.3: LLDPE specimen in ZK60 SHPB.

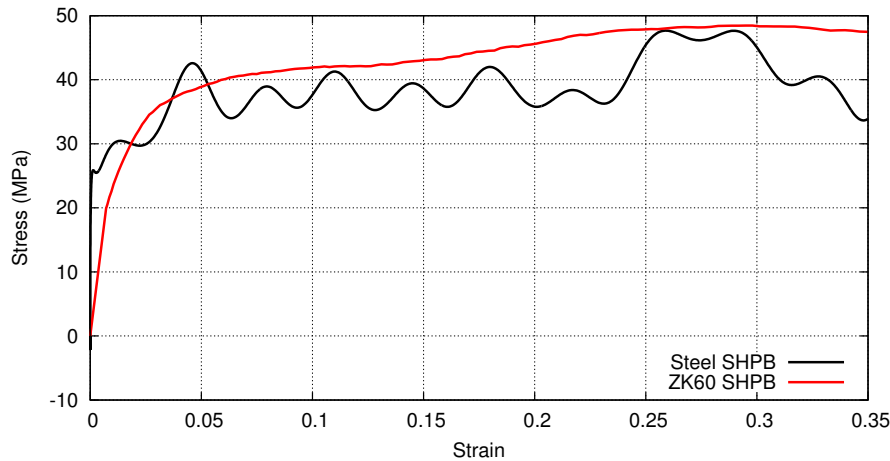


FIGURE 5.4: Comparison of stress-strain curves of LLDPE specimen in steel and ZK60 SHPBs.

5.1.1.1 Experimental validation

In order to validate that the ZK60 SHPB configuration provided accurate, reliable data, a high-speed digital video camera, on loan from the Engineering and Physical Sciences Research Council (EPSRC) Engineering Instrument Loan Pool, was employed to record the experiment. Details of the camera and the exact experimental methods used is discussed in Section 5.2 (page 129) below. The camera was set-up perpendicular to the pressure bars such that the camera would record the change in the length of the specimen along the axis of impact as well as the change in specimen diameter at a 90° angle to the impact. Video was recorded at a rate of 250,000 frames per second. Since the duration of the incident stress pulse is of the order of $150 \mu\text{s}$, this gives approximately 35 images showing specimen compression, each with a resolution of 312×260 pixels. Figure 5.5 shows six still images taken from one such recording at $32 \mu\text{s}$ intervals. The incident bar may be seen on the right of the images, with the transmitter bar on the left.

The images were used to ascertain the conservation of volume of the specimen and to assess the dependability of the standard method of measurement capture,

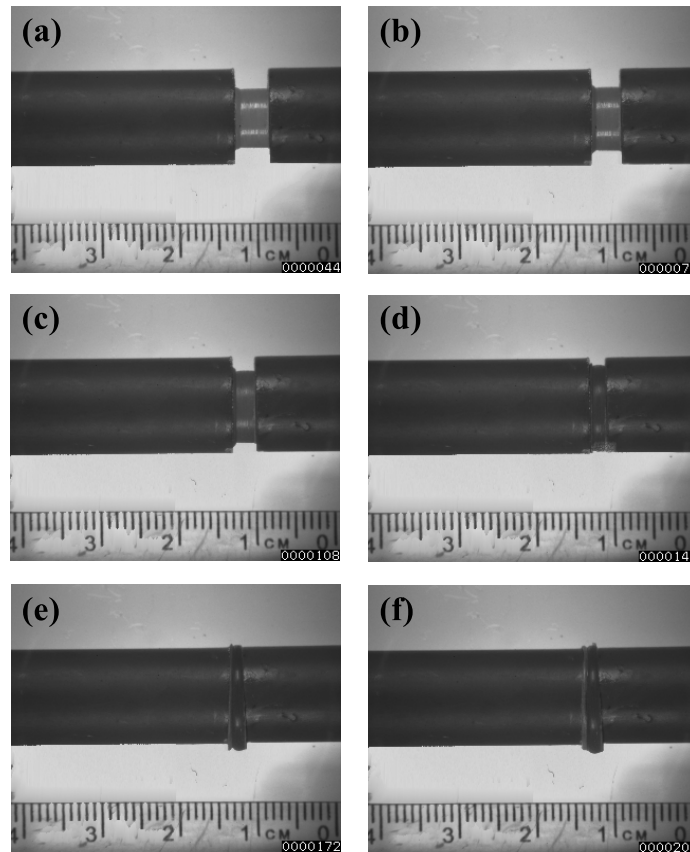


FIGURE 5.5: High-speed photography of LLDPE specimen in ZK60A SHPB. The images were taken at (a) $44 \mu\text{s}$, (b) $76 \mu\text{s}$, (c) $108 \mu\text{s}$, (d) $140 \mu\text{s}$, (e) $172 \mu\text{s}$ and (f) $204 \mu\text{s}$.

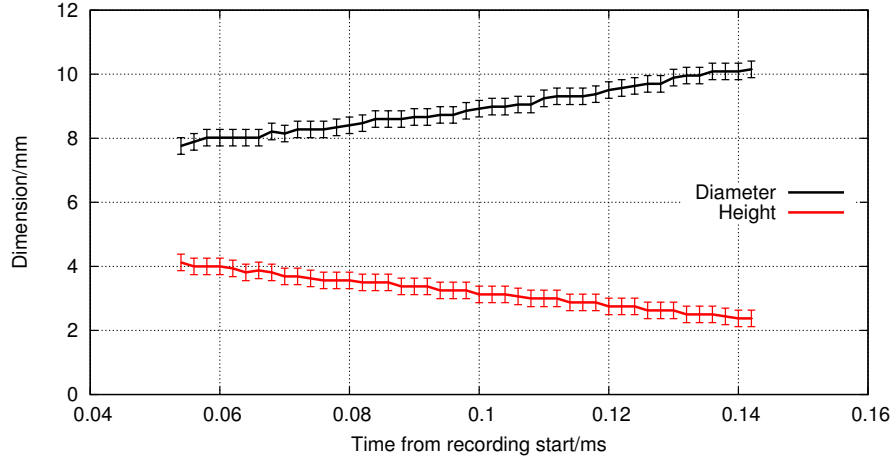
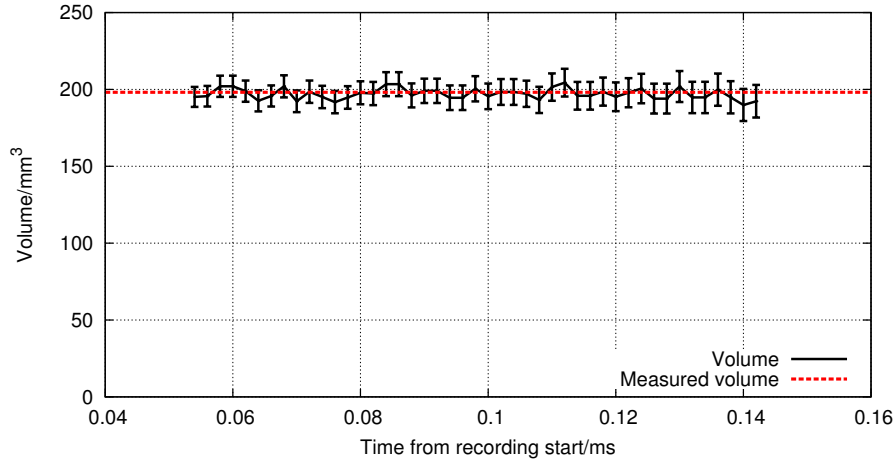
the pressure bar-mounted strain gauges, at least until the specimen diameter becomes greater than that of the bar, such as is the case in the images shown shown in Figure 5.5 (e) and (f).

5.1.1.1.1 Volume conservation. As mentioned briefly above, the images taken from the high speed camera were used to examine the conservation of volume within the experiment, and verify the incompressibility of the specimen materials that is assumed throughout the main analysis. Measurements of the length and diameter of a specimen (HDPE for the following example) were taken by eye using a graphics program by enlarging the image to the pixel-scale and counting the pixels over the course of the bar impact, and the results are shown in Figure 5.6.

As can be seen in Figure 5.6, the height of the specimen decreases in a linear fashion as the specimen is compressed by the movement of the bar. It must be noted that the slight *stepped* nature of the data is due to the measurement of the images to an accuracy of one pixel. Repeating the measurement for the specimen diameter shows that the diameter also increases linearly as expected.

Using these measurements and the usual formula relating the length and diameter dimensions of a cylinder to its volume, the dynamic volume of the specimen, compared to its measured initial volume during the test can be determined, as shown in Figure 5.7.

As is evident from the figure, given the uncertainty inherited from the measurement process, the volume is reasonably constant over the range of the figure

FIGURE 5.6: *Dynamic height and diameter of an SHPB specimen.*FIGURE 5.7: *Dynamic volume of an SHPB specimen.*

which confirms the incompressibility of the material and substantiates the volume assumptions made in the main SHPB analysis. Also, as the volume is seen to stay constant and the material is essentially incompressible it can be said that Poisson's Ratio is approximately 0.5, confirming the value found in the literature [Lechner et al., 2005].

5.1.1.1.2 Strain gauge signal dependability. The use of the high speed camera equipment also gave an opportunity to confirm that the signals received from the strain gauges correspond to the actual material properties and validate the standard SHPB analysis technique for the new magnesium alloy pressure bars. In the following figures, measurement of the initial length, ℓ_0 , and momentary lengths, ℓ , of the specimen, makes it possible to determine the instantaneous true strain, $\varepsilon_{\text{true}}$, using the relation

$$\varepsilon_{\text{true}} = \ln \left(\frac{\ell}{\ell_0} \right) \quad (5.2)$$

Figure 5.8 shows the result of the measurement of the photographic images for one of the LLDPE specimens (chosen at random). The uncertainty in the video

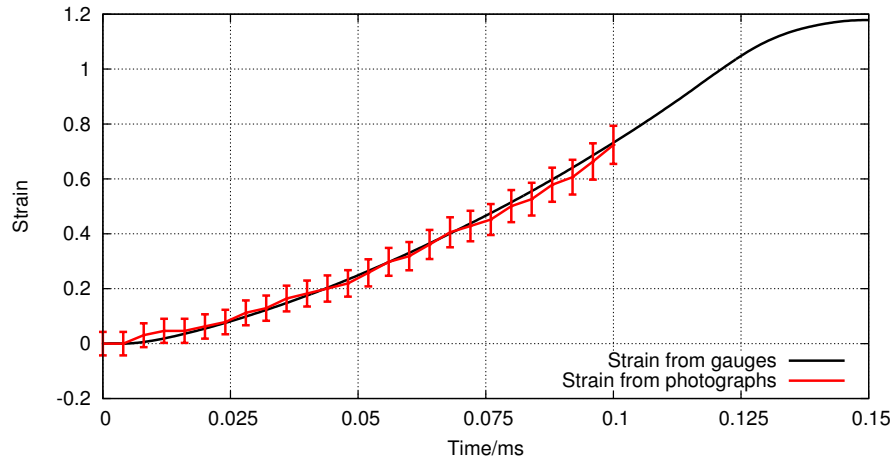


FIGURE 5.8: *Photographic strain of an LLDPE SHPB specimen.*

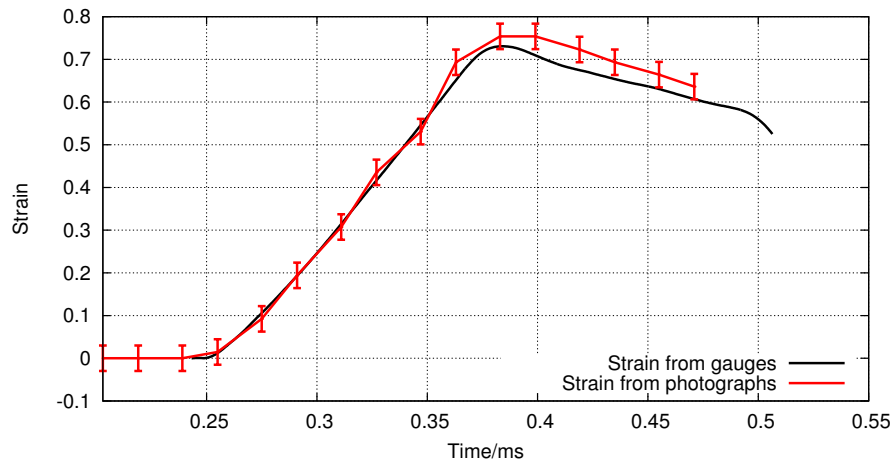


FIGURE 5.9: *Photographic strain of a UHMWPE SHPB specimen.*

data is due to the resolution of the images, with the specimen being measured to an accuracy of ± 1 pixel (corresponding to ± 0.14 mm, or 3% of the initial specimen length). As can be clearly seen, the strain measured from the images is very similar to the data recorded from the strain gauges, thereby validating the use of the strain gauges for accurate recording of the material strain without the time-consuming measurement of the photographic images. With LLDPE it was not possible to measure specimen deformation beyond around 70% from the high-speed video since, as may be seen in the last two images in Figure 5.5, the specimen expanded outside the pressure bar area, so measuring the diameter of the specimen was unreliable.

To ensure that the SHPB data was still accurate at strains over 70%, this was repeated using a specimen made of UHMWPE^a, the results of which are shown in Figure 5.9. The result shown should not be considered to be entirely representative for this technique, as it is actually the worst fitting data that was gathered. It is included here primarily to show how good the worst fitting result was. The photographically measured strain stays within the calculated error throughout

^aThis analysis was, in actual fact, performed on every material tested here.

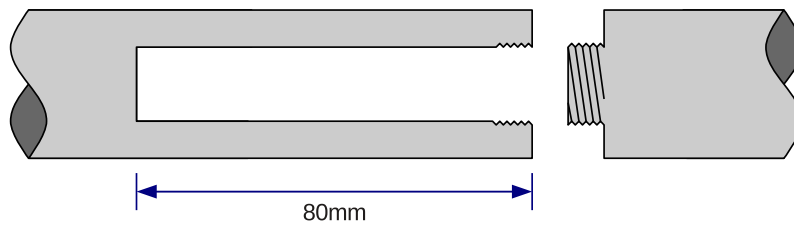


FIGURE 5.10: *Drilled section of SHPB transmitter bar.*

specimen loading, right up to the point at which the incident stress pulse ends. Since data after this point is of little interest, it is safe to assume that the strain measured by the strain gauges is accurate.

As both stress and strain are measured using the same technique in the traditional SHPB experiment, it stands to reason that the stress measurement taken from the transmitter bar gauges is also very likely to be an accurate representation of what is experienced by the specimen.

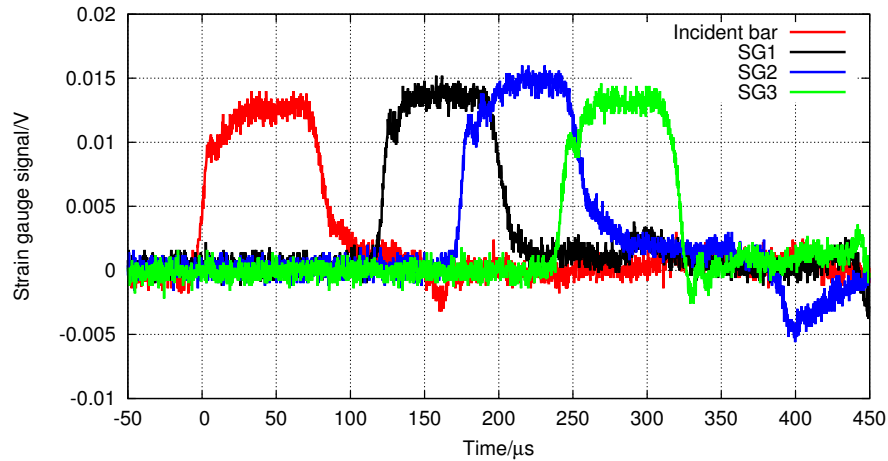
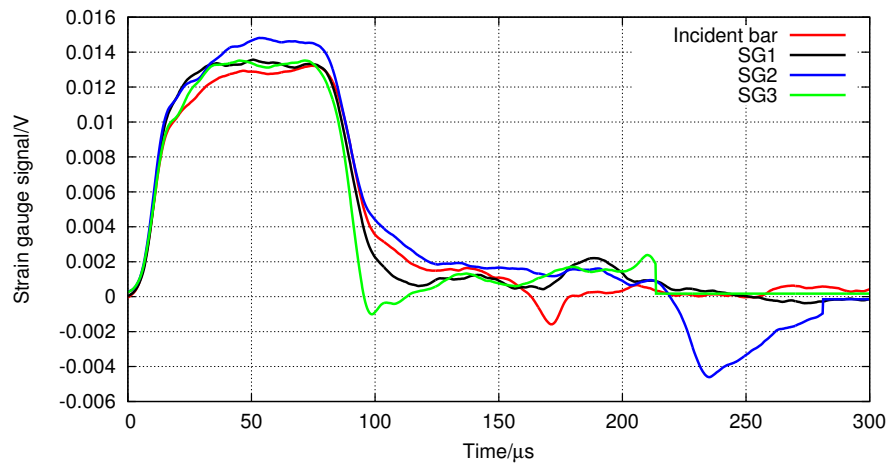
5.1.2 Tubular pressure bars.

As discussed above, concern has been expressed by the author, [Hughes et al., 2013], that employing a tubular pressure bar system could be detrimental to the quality of recorded data. In order to understand how the caps in a tubular system can affect data, a hybrid system was constructed. It was not possible to obtain tubular ZK60 pressure bars directly, so an ordinary solid transmitter bar was modified by cutting it in half and drilling a 4.5 mm diameter hole parallel to the bar sides. A tap and die was used to thread both halves so that they could be screwed together. A cross-section of this is shown in Figure 5.10.

This system proved convenient, since it permitted the attachment of multiple strain gauges along the length of the bar in order to see exactly how the stress pulse would behave on its journey through the pressure bar. Strain gauges were attached 20 cm from each end of the joined-together transmitter bar, along with a third directly on top of the tubular section. These were combined with the usual strain gauge on the incident bar. Experiments were performed without any specimen, a typical result of which is shown in Figure 5.11, where SG1 and SG3 are positioned at each end of the transmitter bar, while SG2 is directly over the tubular section.

From Figure 5.11, it appears that the signal at the tubular section (as read by SG2) has been amplified somewhat. Calculating just how much amplification this has resulted in is complicated by the amount of noise on the signal, so it was decided to filter each set of data using a 7th order Butterworth filter with a cutoff frequency of 50 kHz to remove as much noise as possible, and perform any measurements on that. Figure 5.12 shows the pulses extracted and superimposed on each other.

The predicted reflections caused by the tubular section may be seen in the SG1 curve between about 100 and 175 μs . The reflection, tensile in nature, causes a reduction in the apparent strain, however, it is not particularly significant. There is also a reflection visible in the incident bar at around 170 μs . This is caused by imperfect alignment of the incident and transmitter pressure bars, and is of no

FIGURE 5.11: *Data collected from tubular SHPB system.*FIGURE 5.12: *Superimposed pulses from tubular SHPB.*

concern. Taking that into account, the curves for the incident pressure bar and SG2 located at the tubular section are in remarkable agreement (which may be seen more easily in Figure 5.12). It appears, therefore, that the author's concerns over the use of tubular SHPB systems may have been misplaced.

In order to calculate the amplification given by this tubular system, the average value of a small reference range within the middle of the pulse were compared to that of the incident signal. This allowed the individual signals to be normalised as shown in Figure 5.12, and also provides a measure of the amplification from each section, shown in Table 5.2.

Although there appears to be a slight gain or 3 - 4% on the two ancillary gauges SG1 and SG3, this should be considered to be erroneous, and is likely to be caused by the technique used to calculate gain, or by the positioning of the strain gauges close to the ends of the pressure bar.

The apparent gain from the tubular section appears to be significantly greater, and should be compared to a theoretical gain from employing a tubular system. Since the amplitude of the transmitted pulse goes like $1/A$, where A is the surface

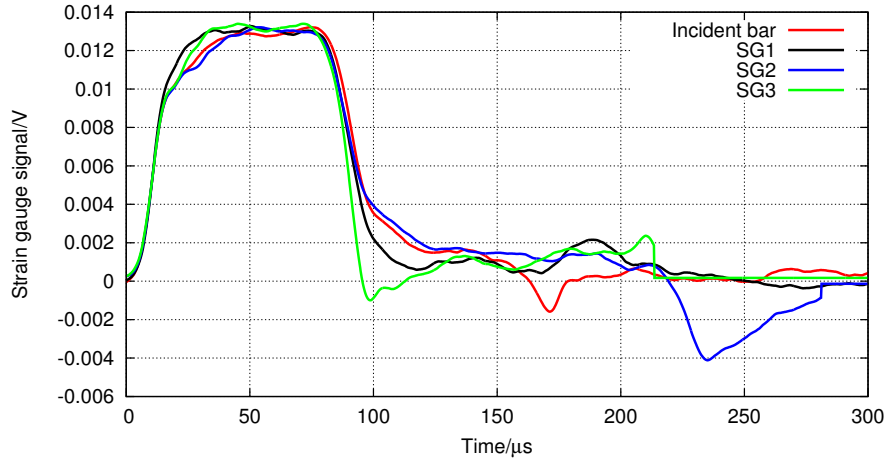


FIGURE 5.13: Pulses from tubular SHPB normalised and superimposed.

Strain gauge	Average amplitude in reference range	Gain
Incident	0.01286	1.000
SG1	0.01333	1.037
SG2	0.01467	1.141
SG3	0.01323	1.032

TABLE 5.2: Measured gain from tubular SHPB system.

area of the bar, the theoretical gain, G , in the tubular section may be calculated using

$$G = \frac{1/A}{1/A_{\text{tube}}} = \frac{A_{\text{tube}}}{A} \quad (5.3)$$

where A_{tube} is the surface area of the tubular section. Given that the bar has a diameter of 12.7 mm, and the hole drilled into it was 4.5 mm in diameter, giving the solid pressure bar a surface area of 126.7 mm², and the tubular section a surface area of 110.8 mm². This gives a theoretical gain of 1.144, or 14.4%. With the measured increase in amplitude being 1.141, or 14.1%, this shows quite remarkable correlation between these two values.

Care must be taken with this technique however, since from Equation 2.19 (page 59):

$$\sigma_S = \frac{EA}{A_S} \cdot \varepsilon_T$$

the stress on the bar, σ is inversely proportional to the area of the pressure bar. Reducing the cross-sectional area of the pressure bar by either using a tubular system or by using a drilled section as with the work here, will increase the stress which could lead to damage of the pressure bar if it gets too high.

5.1.3 Pressure bar 'necking'

The exact tubular SHPB technique discussed above, with a short tubular section in the middle of the pressure bar, is weaker than an entirely tubular system since the two bar sections are connected together using a threaded area. Since it may be

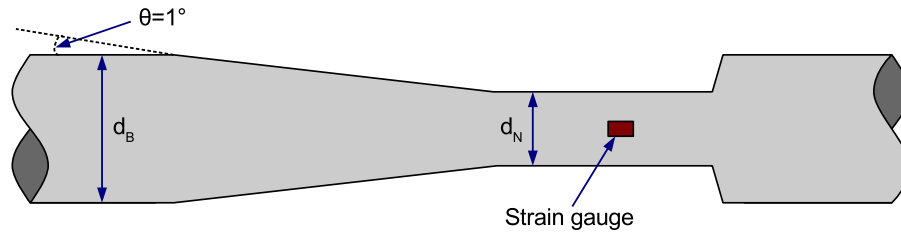


FIGURE 5.14: A necked pressure bar.

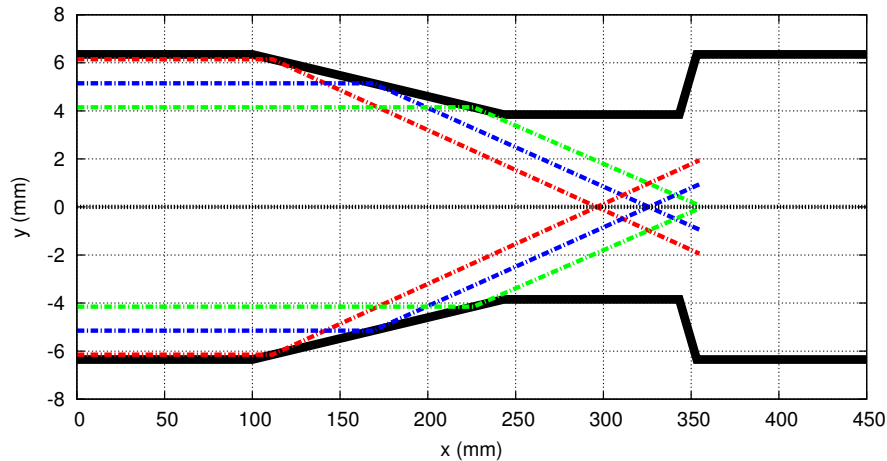


FIGURE 5.15: The movement of waves within a necked pressure bar.

more convenient to use a system of this design, for example when full length tubes of the desired material are not available, the author has devised an alternative method to achieve the same goal.

It should be noted, however, that due to time constraints the following design is untested at the time of writing. While there is no obvious reason why such a technique should not work perfectly well, this method should be treated purely as hypothesis.

It may be possible to reproduce the gain introduced from a tubular system without the need to source long tubular lengths, and without having to cut, drill and thread a solid bar. This can be done by *necking* a pressure bar, turning down a small section of the pressure bar using a lathe. The general design of this concept is shown in Figure 5.14, which has been exaggerated to make it easier to read.

It would, of course, be possible to simply reduce the diameter of a section of a pressure bar from its original diameter, d_B , to something smaller, d_N , by turning down the section on a lathe, but such a design would still induce reflections into the pressure bar. Changing the diameter of a pressure bar will always lead to reflections, however, by leading down to the necked section with a taper, assuming the angle of the taper, θ , is kept small enough, say 1° , the reflections may be deflected from the taper at such a shallow angle that they pass through the necked section on which the strain gauge is affixed, without having any affect on the measurement.

Figure 5.15, which is not drawn to scale, shows how an incident wave will travel through a necked pressure bar. The pressure bar surface is represented by

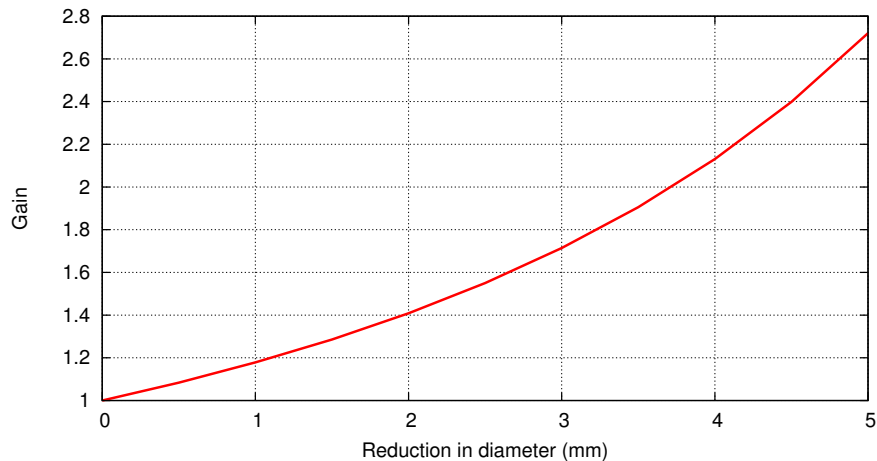


FIGURE 5.16: *Theoretical gain for a range of diameter reductions on a necked SHPB.*

the thick black lines, and the stress wave at various distances from the centre of the pressure bar, by the coloured lines. The bar has a diameter of 12.7 mm in which a 1° taper leads down to a 7.7 mm diameter neck for an overall reduction of 5 mm to the outside diameter. The incident wave is reflected at the taper with an angle $2\theta = 2^\circ$. The shallow angle allows the reflections to travel through the necked section without being incident with the pressure bar surface until well after the necked section, no matter at which point the wave is incident with the taper.

Reducing the pressure bar by a certain amount from the outside edge has a greater affect on the potential gain than drilling the same sized hole, due to physically more material being removed from the outside. For example, if a 1 mm diameter hole is drilled in the centre a 12.7 mm rod, the surface area reduces from 126.7 mm^2 to 125.9 mm^2 . Reducing the outside diameter of the same 12.7 mm rod by 1 mm reduces the surface area to 107.5 mm^2 .

By removing 2 mm from the external diameter, the same potential gain may be achieved as with the 4.5 mm hole drilled in the experiments discussed above. The gain can easily be fine-tuned to the required level. Figure 5.16 shows how the reduction in diameter ($= d_B - d_N$) affects the gain from a 12.7 mm pressure bar.

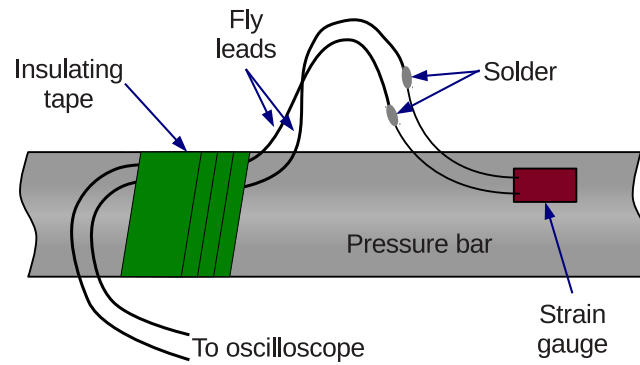
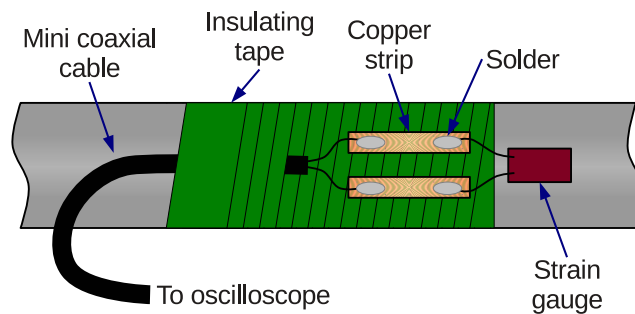
As with the drilled tubular section above, care must be taken when employing such a technique to ensure the increase in stress from the smaller bar area is not allowed to exceed the pressure bar's yield strength.

5.1.4 Strain gauge attachment

In the original configuration of the SHPB, the strain gauges were attached using a simple technique similar to that shown in Figure 5.17^b, where the strain gauge legs were soldered onto a pair of fly leads which were secured to the pressure bar using insulating tape.

During an experiment, the pressure bars undergo a violent, albeit relatively small movement. The small blob of solder attaching the fly leads to the strain

^bThe diagrams in this section show simplified versions of strain gauge attachment techniques, with only one strain gauge in place. In reality the SHPB uses pairs of strain gauges on opposite sides of the pressure bar, which are connected together electrically in series. The actual connection method used is therefore slightly more complicated than that shown.

FIGURE 5.17: *Original strain gauge attachment technique.*FIGURE 5.18: *New strain gauge attachment technique.*

gauge legs, being comparatively massive, tended to resist this movement. This put considerable strain on the delicate gauge legs, causing them to snap with frustrating regularity, which was typically around every dozen experiments or so.

It was thought that, by keeping the strain gauge legs flat to the bar, it would be possible to minimise their breakage. Several techniques were attempted with varying degrees of success, until the method shown in Figure 5.18 was developed. In this method, short lengths of adhesive-backed copper strips^c are attached to an insulated section of the pressure bar. The strain gauge legs are soldered onto one end of the copper strip without pulling them tight^d. The fly leads were replaced with lengths of mini-coaxial cable in order to provide some shielding from external electrical noise.

This technique has proved to be a great improvement over the original method, with strain gauges often lasting for several hundred experiments.

5.2 High-speed photography

Besides being interesting, the use of high-speed photography can also be invaluable in ensuring that the results taken from an experiment are valid, as it can provide an alternative means of measuring the specimen strain. Since the pressure bars had been changed to a magnesium alloy, and no detailed validation of the SHPB in this configuration could be found, this was particularly important

^cPeculiarly, the first adhesive-backed copper strips located were originally designed to provide electrical wiring in dolls houses.

^dTo allow a small amount of movement without pulling the legs tight, causing them to snap.

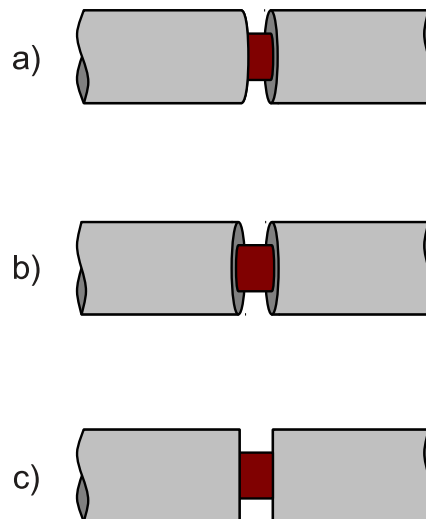


FIGURE 5.19: *Positioning and alignment of the camera.*

here. The results of this work are discussed in detail in Section 5.1.1.1 (page 120) above.

For the work presented here, a Shimadzu HPV-1 high speed camera was used, which turned out to be ideal for this purpose. The camera is discussed in Section 3.2.5.2 (page 99) and is capable of recording 100 images at a maximum frame rate of 1,000,000 frames per second.

5.2.1 Camera alignment and lens considerations

Care must be taken to ensure that the camera is positioned and aligned appropriately. The diagrams in Figure 5.19 show two situations where the camera is aligned incorrectly; in a) the camera is positioned too far to the left, resulting in one of the pressure bars obscuring the left-hand-side of the specimen, making accurate measurement impossible, while in b) the camera is positioned too close to the experiment so the faces of both bars are visible which may make the computational measurement of specimens difficult. c) shows the correct camera alignment.

A further consideration that should be made is that, during an experiment, the pressure bars and specimen will move. Positioning the camera so that the specimen is exactly central in the image could result in alignment issues similar to that in Figure 5.19 a). It is perhaps more appropriate to position the camera so that, at the beginning of the experiment, the specimen appears slightly over to the side of the incident pressure bar.

Clearly the camera should not be positioned too close to the experiment. In order to get decent resolution, the lens should be capable of a high level of zoom. It would most likely be best if the lens also had a macro (close-up) mode which will provide an extended focussing range. It should be noted, though, that a dedicated macro lens would not be appropriate as the focussing distance tends to be very short.

The lens used in this work was a Tamron[®] model A17^e, 70-300 mm $f/4-5.6$ lens which incorporated a 1:2 macro capability at zoom levels of 180-300 mm. The minimum focussing distance for this lens is 95 cm which proved to be ideal.

^e<http://www.tamron.com/>

5.2.2 Lighting

When taking video recordings at very high speeds, lighting becomes absolutely critical. Ordinary studio lights may be suitable for camera frame rates around 10^3 s^{-1} , but for speeds which are much greater than this, only a camera flash can provide sufficient illumination.

Before beginning to test lighting solutions, it is necessary to choose an appropriate aperture size to set on the lens. Opening the aperture (reducing the f -number) will allow more light through the lens, but reduces the depth of field so the camera will only be in focus for objects a very specific distance from the lens. Reducing the aperture (increasing the f -number) allows less light in, but increases the depth of field allowing for a more flexible focus. The lens used in this work had a fairly small maximum aperture ($f/5.6$ at the maximum zoom level) and so the aperture was fixed at its widest setting, which proved to be quite acceptable.

A wide array of commercial camera flashes are available, and any reasonable quality mains powered studio flash will certainly provide adequate light for frame rates in excess of 10^5 s^{-1} . They are, however, not usually constructed with scientific applications in mind. The electromagnetic shielding around studio flashes is often inadequate, which can lead to a significant amount of electrical noise being transferred to other devices, such as oscilloscopes.

In order to reduce this noise as much as possible, a number of battery powered SLR camera flashes were employed. These provided a huge improvement over the mains powered studio flash, and although some noise was still transferred to the oscilloscope, it was much less significant. The duration of the flash from the camera flashes was, however, much shorter than the studio flash ($\approx 1.0 \text{ ms}$ as compared to $\approx 1.5 \text{ ms}$) and so four battery flashes were used, and were triggered using a timer sequencer to allow a delay between flashes, extending the overall lighting duration.

Figure 5.20 shows the configuration of the lighting system that was used. Flashes were triggered in pairs, one providing foreground lighting and the other lighting the background. A diffuser screen was constructed to distribute the light of the rear flashes so that they helped to increase the contrast of captured images, without overloading the camera, causing it to *white out*.

5.2.3 Increasing contrast

Figure 5.21 shows a single frame from from a simple SHPB setup. As can be seen, there is a considerable amount of light reflected from the metal surface of the pressure bars. This can make analysis difficult, particularly if it is performed computationally (see Section 5.3) and ideally this should be reduced as much as possible.

The ends of the SHPB pressure bars in contact with the specimen were painted with a matt enamel paint. Several colours of paint were tried, and it became immediately apparent that matt white pressure bars resulted in poor contrast from the background, while matt black provided exceptional contrast, but lost any appearance of being a curved surface in the videos, which reduced the aesthetic quality of the images, and was not considered to be *publication quality*. After a number of additional experiments, it was found that N° 96 ‘RAF Blue’ matt enamel

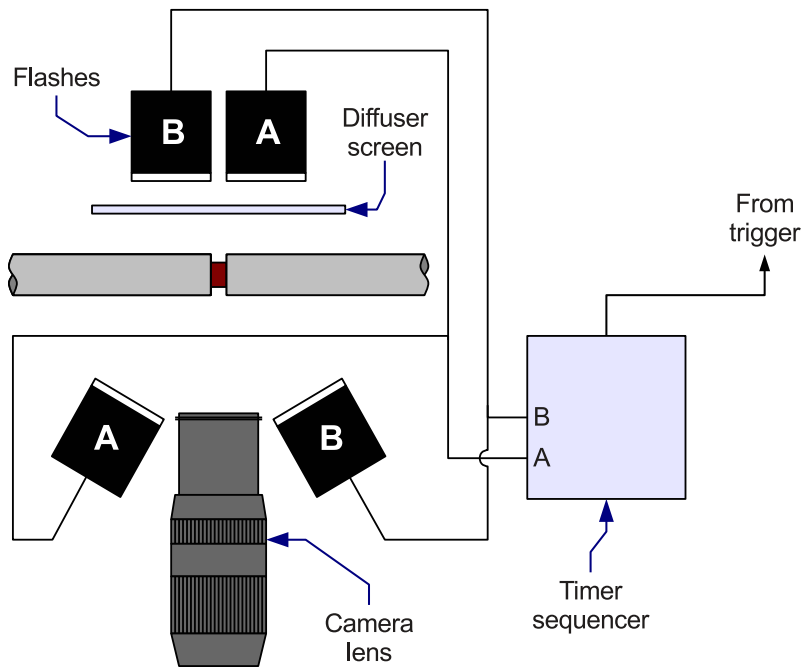


FIGURE 5.20: *The lighting configuration used in SHPB experiments.*

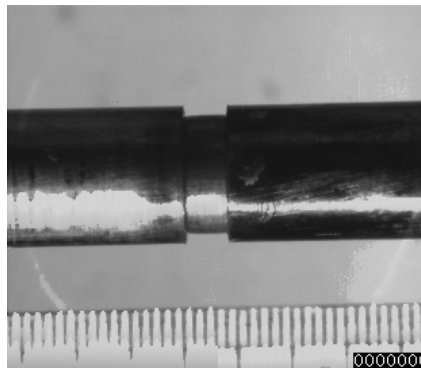


FIGURE 5.21: *A single video frame from an SHPB experiment.*

from Humbrol^f provided an ideal colour surface which was suitably dark to contrast easily with the background, whilst being light enough to be identifiable as a three-dimensional surface. This high-contrast configuration can be seen in a frame taken from the high-speed photography in Figure 5.22.

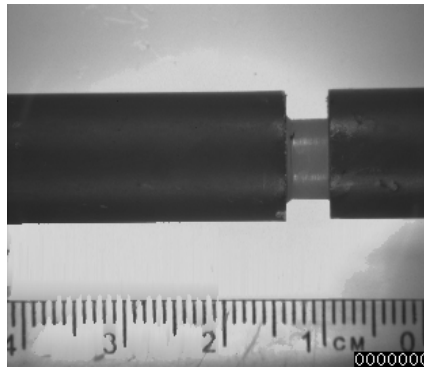
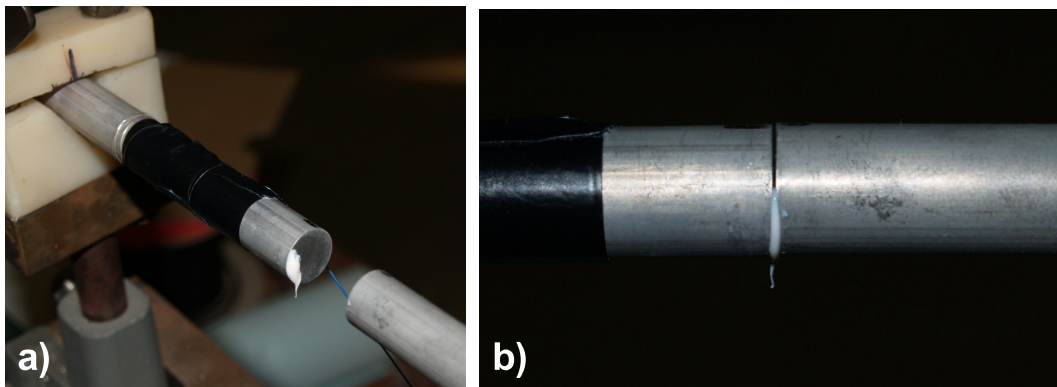
5.2.4 Triggering

A number of different triggering systems were experimented with, including the construction of an electronic module which measured the resistance of a strain gauge. When the resistance changed by a certain amount, the module produced a +5V DC TTL^g pulse to be used as a trigger. This system proved to be too unreliable, primarily due to the very low change in strain gauge resistance.

The configuration of the SHPB system at Loughborough University led to the design of an alternative triggering system which, in the author's opinion, is very

^f<http://www.humbrol.com/>

^gTransistor-transistor logic, the type of signal used in digital logic gate circuits.

FIGURE 5.22: *Improved contrast SHPB.*FIGURE 5.23: *SHPB photography triggering system.*

elegant in its simplicity. Loughborough's SHPB uses a four-bar system, employing a pre-loading bar installed between the projectile and the incident bar. If the pre-loading bar and the incident bar are separated by a tiny distance, as the incident strain pulse travels along the pre-loading bar it is accompanied by a horizontal displacement which closes the gap between the bars. With the addition of some very simple wires, the pre-loading and incident bars may then be used as a rudimentary electrical switch, with the connection closing as the incident strain pulse travels along them. The tiny separation between the two bars means that any effect on the pulse is negligible.

It was found that the bars could be kept separated by putting a tiny amount of an electrically insulating grease such as MolyKote®AS-828 silicone grease^h between them, not enough to cover the bar's surface, but a small smear on one edge. Photographs of this system are shown in Figure 5.23, with a) showing the small amount of grease smeared onto the end of the incident bar, and the small separation between the bars shown in b). This method of triggering has been affectionately nicknamed the *greased Swallowe* after the author's supervisor.

5.3 High-speed photography analysis

High-speed photography can be used to measure specimen strain during SHPB experiments by a simple comparison between the initial specimen length with the

^h<http://www.dowcorning.com/>

FIGURE 5.24: A *bitmap image*.

momentary lengths measured from the photographs. While this is a straightforward method, depending on the number of photographs in a data set, measuring specimen dimensions manually from, potentially, hundreds of frames of video can be extremely time consuming. It is therefore preferable to automate the task of measuring specimens with the use of a computer program.

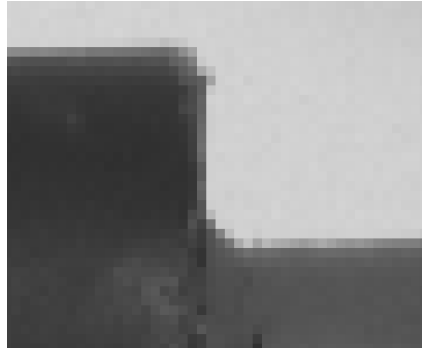
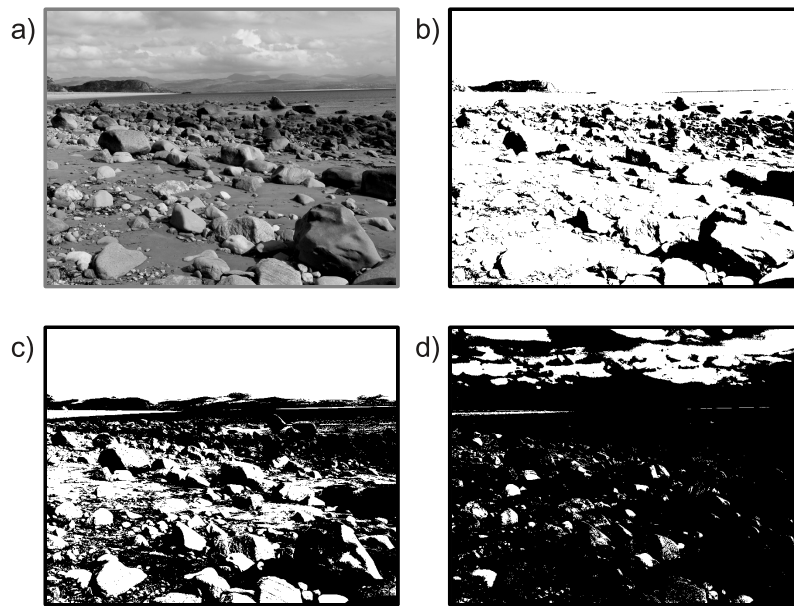
5.3.1 Understanding digital images.

The digital images which may be read and displayed on a computer come in a variety of forms. Many of the more commonly used image formats, including JPEG, GIF and PNG, utilise a range of different compression algorithms in order to reduce the size of the image data file. For the sake of brevity image compression will not be discussed further in this work, suffice to say that the analysis of compressed images is significantly more difficult than it is for their uncompressed counterparts.

Possibly the simplest image file format to work with is the bitmap (or BMP) file format. As its name implies, a bitmap contains a map of each pixel in the image. Figure 5.24 shows an example bitmap zoomed in to an extreme level to show the individual pixels within a small section of the image. Each pixel is given an intensity by the bitmap. In the case of a colour image, such as Figure 5.24, the intensity is broken into three distinct colour channels, red, green and blue. The intensity of each colour is represented by, typically, an 8-bit binary number, giving an intensity range of between 0 and 255. Since there are three colour channels, this type of image would be described as a 24-bit bitmap, which is capable of displaying a maximum of $256 \times 256 \times 256 = 16,777,216$ unique colours. In a colour bitmap, white would be represented by $R=255, G=255, B=255$, whereas black is $R=0, G=0, B=0$.

Greyscale bitmaps are simpler still. Instead of using three distinct colour channels, they only use a single 8-bit channel which is capable of representing 256 shades of grey from black (0) to white (255). With the use of a computer then, it is relatively simple to measure the intensity of each pixel and perform an operation accordingly. It may be important to note that, although various bit depths are available, the 24-bit bitmap is used almost exclusively. When working with greyscale images, the values for the RGB channels are set the same, for example $R=127, G=127, B=127$ creates a mid-level grey.

In Section 5.2.3 the optical contrast within the SHPB was maximised, however, even with extremely high contrast it can be difficult to define a precise boundary

FIGURE 5.25: *Zoomed in area of SHPB photograph..*FIGURE 5.26: *Three levels of thresholding.*

to measure. Figure 5.25 shows a zoomed in area, showing a pressure bar and the specimen from Figure 5.22, which highlights this difficulty. This complication may be averted by reducing the bit depth of the bitmap image from 8 to one. So called *binary* images contain only two colours, white and black, which makes locating boundaries within the image extremely simple. Converting an image from greyscale to binary is performed by a process known as thresholding. Simply put, a threshold intensity is chosen, a pixel having an intensity higher than this will become white, any pixel found to have a lower intensity will become black.

The difficulty comes in choosing the correct threshold value. Figure 5.26 a) shows a greyscale photograph and three alternative versions of the photograph having undergone thresholding with threshold values of b) 64, c) 128, and d) 192. Clearly, in choosing a threshold value it is important to ensure that it is neither too high nor too low.

5.3.2 Otsu's method

Otsu's method is a technique which automatically calculates the optimum threshold value for any given greyscale image. It assumes that the image contains two

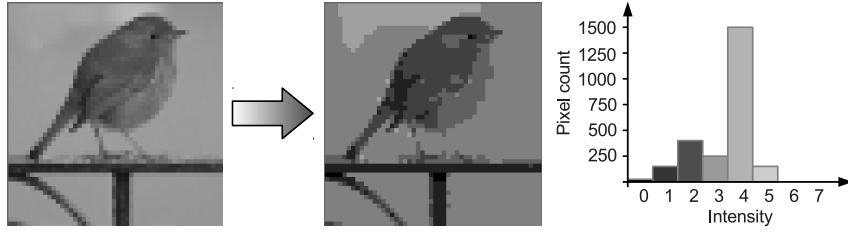


FIGURE 5.27: A 50×50 pixel 8-bit greyscale image converted to 3-bit greyscale.

classes of pixels, those in the foreground and those in the background. The optimal threshold is the value with which the combined spread of the two classes, the intra-class variance, is a minimum [Otsu, 1975].

The intra-class variance,

$$\sigma_w^2 = \omega_f \sigma_f^2 + \omega_b \sigma_b^2 \quad (5.4)$$

where ω_f and ω_b are the respective weights of the foreground and background pixels, and σ_f^2 and σ_b^2 are the variance within the foreground and background pixels respectively.

The weights ω_b and ω_f are simply the sum of the probabilities for each intensity, i.e.

$$\omega_b = \sum_{i=1}^{T-1} P(i) \quad (5.5)$$

and

$$\omega_f = \sum_{i=T}^{Max} P(i) \quad (5.6)$$

where T is the threshold level being tested, P is the probability for that intensity and Max is the maximum intensity value.

The variances σ_b^2 and σ_f^2 are calculated by

$$\sigma_b^2 = \sum_{i=1}^{T-1} P(i)(i - \mu_b)^2 \quad (5.7)$$

and

$$\sigma_f^2 = \sum_{i=T}^{Max} P(i)(i - \mu_f)^2 \quad (5.8)$$

where μ is the population mean for each set.

In order to reproduce Otsu's method computationally, it is necessary to build an algorithm which exhaustively calculates the intra-class variance for each possible threshold value. This will be explained with the use of the simplified image in Figure 5.27; converted from an 8-bit (256 greyscale) image to 3-bit (8 greyscale), this simplifies the calculations somewhat. The histogram for the 3-bit image is also shown, the values for which are shown in Table 5.3.

The algorithm to calculate the intra-class variance is:

Intensity	Pixel count
0	11
1	193
2	350
3	245
4	1524
5	177
6	0
7	0
Total	2500

TABLE 5.3: Pixel count by intensity for the 3-bit greyscale image in Figure 5.27.

1. **Select a threshold value, T :**

This is an integer between 1 and the maximum intensity value. For this example, $T = 1$ will be used.

2. **Calculate the foreground weight, ω_f :**

$$\omega_f = \frac{193 + 350 + 245 + 1524 + 177}{2500} = 0.996$$

3. **Calculate the background weight, ω_b :**

$$\omega_b = \frac{11}{2500} = 0.004$$

4. **Calculate the foreground population mean, μ_f :**

$$\mu_f = \frac{\left((1 \times 193) + (2 \times 350) + (3 \times 245) + \dots \right. \\ \left. \dots (4 \times 1524) + (5 \times 177) + (6 \times 0) + (7 \times 0) \right)}{2489} = 3.459$$

5. **Calculate the background population mean, μ_b :**

$$\mu_b = \frac{(0 \times 11)}{11} = 0.000$$

6. **Calculate the foreground variance, σ_f^2 :**

$$\sigma_f^2 = \frac{\left(\{ (1 - 3.459)^2 \times 193 \} + \{ (2 - 3.459)^2 \times 350 \} + \dots \right. \\ \left. \dots \{ (3 - 3.459)^2 \times 245 \} + \{ (4 - 3.459)^2 \times 1524 \} + \dots \right. \\ \left. \dots \{ (5 - 3.459)^2 \times 177 \} + \{ (6 - 3.459)^2 \times 0 \} + \dots \right. \\ \left. \dots \{ (6 - 3.459)^2 \times 0 \} \right)}{2489} = 1.137$$

7. **Calculate the background variance, σ_b^2 :**

$$\sigma_b^2 = \frac{(0 - 0.000)^2 \times 11}{11} = 0.000$$


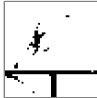





Threshold	$T = 1$	$T = 2$	$T = 3$	$T = 4$	$T = 5$	$T = 6$	$T = 7$
							
ω_f	0.996	0.918	0.778	0.680	0.071	0.000	0.000
ω_b	0.004	0.082	0.222	0.320	0.929	1.000	1.000
μ_f	3.459	3.666	3.965	4.104	5.000	0.000	0.000
μ_b	0.000	0.946	1.612	2.038	3.325	3.444	3.444
σ_f^2	1.137	0.682	0.216	0.093	0.000	0.000	0.000
σ_b^2	0.000	0.051	0.277	0.602	1.076	1.184	1.184
σ_w^2	1.132	0.630	0.229	0.256	1.000	1.184	1.184

TABLE 5.4: Calculating an optimal threshold value with Otsu's method.

8. Calculate the intra-class variance, σ_w^2 :

$$\begin{aligned}
 \sigma_w^2 &= \omega_f \sigma_f^2 + \omega_b \sigma_b^2 \\
 &= (0.996 \times 1.137) + (0.004 \times 0.000) \\
 &= 1.132
 \end{aligned}$$

9. Calculations complete.

Choose another threshold value and return to step 2. Continue until all possible threshold values have been exhausted. Otsu's optimal threshold value is that which produces the lowest σ_w^2 .

The results of this algorithm, when used with the 3-bit greyscale image in Figure 5.27 are shown in Table 5.4. The lowest intra-class variance calculated by the technique, and hence Otsu's optimal threshold, is at $T = 3$. The resulting images show that, indeed, using the calculated threshold is capable of producing an image which loses very little information from the original. It should be noted, however, that in this case the intra-class variances for $T = 3$ and $T = 4$ are quite similar, and both threshold values produce reasonable images although there is a marked difference between the two. This marked difference is an artefact of the extremely low bit-depth of the original image, with higher bit-depth images showing a much smaller difference between unitary threshold differences.

A program written in C++ which is capable of calculating a threshold value using Otsu's method, and then producing a binary image using the calculated threshold is shown in Appendix I. An example of a frame from the high-speed SHPB photography which has been analysed using Otsu's method and a suitable threshold applied is shown in Figure 5.28, which also shows a zoomed in section of the pressure bar-specimen interface.

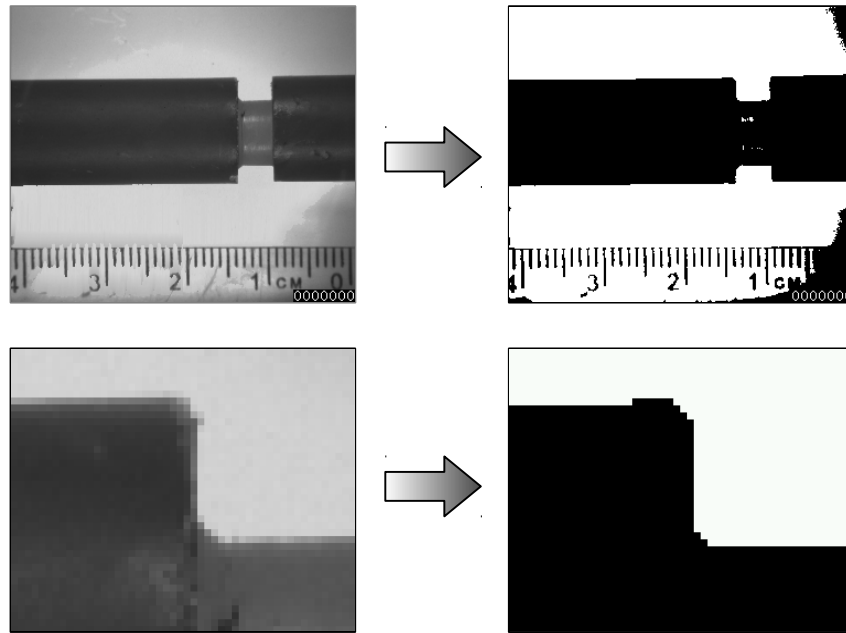


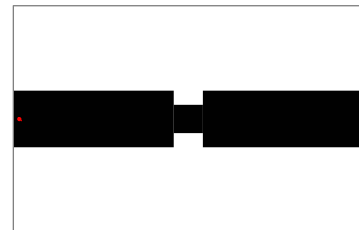
FIGURE 5.28: A frame from the high-speed photography after thresholding using Otsu's method.

5.3.3 Computational measurement of high-speed photographs

Now that each of the frames of the high-speed video have been converted to binary images, it is possible to begin to evaluate them computationally. While this is not a particularly difficult procedure, there are certain complications which must be taken into consideration. These are dealt with in the following procedure, which is based on an image of width w and height h .

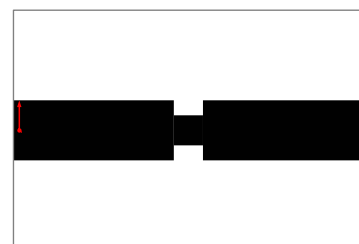
1. Locate and move to the start position.

The start position should be somewhere within the area of the pressure bar on the left of the image. Assuming that the camera has been aligned so that the pressure bars run through the middle of the image, a suitable start position is $x = 0$, $y = h/2$ as indicated by the red dot in the figure opposite.



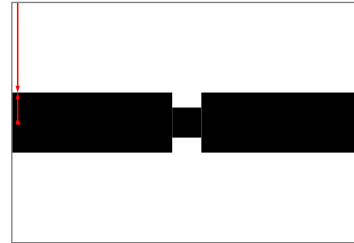
2. Find the upper edge of the pressure bar.

This is performed by moving up from the starting position, one pixel at a time, until the pixel colour changes from black to white.

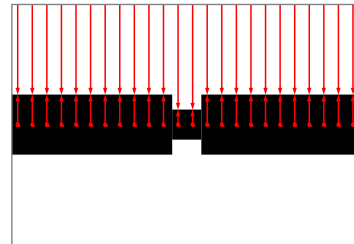


3. Find the upper edge again.

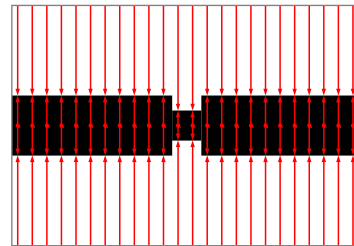
This operation is necessary to negate any problems with light areas on the pressure bars which could otherwise be interpreted as the bar edge. This can either be done from the very top of the image (at $y = 0$), or from an arbitrary point known to be above the upper bar edge. The latter option is usually preferable since, from Figure 5.28, slightly darker areas in the background, the corners especially, can be dark enough to become black in the thresholding process.

**4. Measure the complete upper profile.**

Repeat the preceding steps, incrementing the x -position by one and locating the upper edge repeatedly until the entire width of the image has been examined.

**5. Measure the complete lower profile.**

The whole process is repeated once more to locate the lower profile of the bar and specimen from the image.



After completing this process, the entire outline of the SHPB pressure bars and specimen is known. The next step is to locate the specimen. This is a trivial procedure, simply involving calculating the diameter of the system at each point along the x -axis. Points at which the diameter is >2 pixels smaller than the average diameter of, say, the first hundred-or-so diameters along x , must be the specimen. Allowing for a diameter change of >2 pixels is necessary to allow for imperfect camera alignment and to allow for any vertical displacement of the pressure bars during an experiment. To provide for the best error tolerance, points which appear to contain the specimen should be checked to ensure they are contiguous, with the largest contiguous group being the specimen.

Appendix J contains a C++ program which performs the above algorithm on a thresholded image.

5.4 Measurement of specimen temperature

During the course of this research, a thermal imaging camera was made available for a few days. The temperature increase in an SHPB specimen during an experiment seemed to be an interesting area of inquiry.

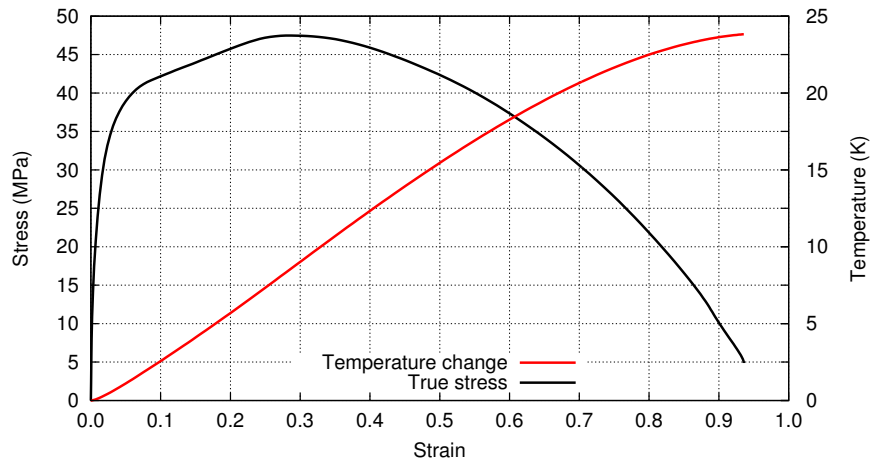


FIGURE 5.29: *Theoretical temperature increase of LLDPE in SHPB.*

5.4.1 Theoretical

Plastic deformation leads to the conversion of mechanical energy onto heat, increasing the specimen temperature. The change in temperature, ΔT , can be defined by

$$\Delta T = \frac{\eta}{\rho C} \cdot \int \sigma d\varepsilon \quad (5.9)$$

where C is the specimen heat capacity, ρ its density, σ and ε the stress and strain respectively, and η is the fraction of the total energy which goes into heating the specimen [Walley et al., 2009], [Kapoor and Nemat-Nasser, 1998], [Swallowe et al., 1986].

If it is assumed that all of the plastic work performed in the specimen is converted into heat, i.e. $\eta = 1$, and using values for C and ρ measured in [Prudom, 2012], it is possible to plot a curve showing the theoretical increase in temperature of an LLDPE specimen in the SHPB. The temperature increase with respect to strain for a typical LLDPE specimen is shown in Figure 5.29, and shows the maximum temperature increase to be 23.8 K.

Exactly how much of the energy goes into specimen heating is of some debate. Measuring specimen temperatures in high strain rate experiments is notoriously complicated. Experiments are completed in less than a millisecond and, assuming the specimen stays in contact with the pressure bars, the thermal conductivity of the bars can draw the heat out of the specimen rapidly. Being a destructive test, attaching measuring devices such as thermocouples can only provide an indication of the temperature increase up to the point at which the device is destroyed.

[Walley et al., 2009] compared the effectiveness of an infrared streak camera to thermocouples embedded in copper and iron test specimens. They found that the great majority, typically 90-100%, of the mechanical work performed on a specimen was converted into thermal energy, and concluded that the embedded thermocouples produced more reliable results.

[Kapoor and Nemat-Nasser, 1998] performed experiments on a range of metallic specimens with an imaging system in which infrared radiation from the specimen is reflected and focussed using a pair of paraboloid rhodium mirrors into an infrared detector. They found that “essentially all” of the plastic work in the deformation of a specimen is converted into heat.

5.4.2 Experimental

A FLIR Systemsⁱ ThermaCAM SC3000 thermal imaging camera, on loan to a project collaborator from the Engineering and Physical Sciences Research Council (EPSRC) Engineering Instrument Pool (EIP), was used. The camera uses a quantum well infrared photodetector to capture images with a maximum size of 320×240 pixels, with frame rates of up to 750 frames per second, with higher frame rates having a smaller image size.

With the maximum speed of the SC3000, which is clearly significantly slower than the high-speed video camera used in other experiments performed here, it was impossible to examine the dynamic temperature change with respect to specimen strain. It was hoped, however, that it would be possible to examine the specimen temperature a short time before and immediately after compression.

Before making any conclusions from recorded thermal imagery, the thermal camera needed an accurate coefficient of emissivity, e , for materials to be tested. A value of e for LLDPE was obtained by placing an SHPB specimen on a steel block with a known emissivity which was maintained at a constant 323 K (50° C). After a few minutes, at which point it was assumed that the specimen and the steel block had reached thermal equilibrium, a short video was taken with the thermal camera and the relative temperatures of the block and specimen recorded by the camera compared. This revealed the emissivity of LLDPE to be $e = 0.90$.

Subsequent experiments were performed at a frame rate of 250 frames per second, giving an inter-frame time of 4 ms, as this provided the best compromise of image resolution and frame rate that could be gleaned. With a typical SHPB incident pulse lasting around 0.1 ms, this configuration is only capable of capturing the specimen temperature a few milliseconds after the experiment is completed. It was hoped that a minimal amount of heat would have transferred from the specimen to the pressure bars by this time, giving a reasonable approximation of specimen heating.

Figure 5.30 shows a series of images taken from a video of an LLDPE specimen, starting with an image at time $t = 0$ ms, the frame prior to any specimen strain, up to $t = 76$ ms where the specimen falls from the pressure bars and out of view. Figure 5.31 shows a graph of the maximum temperature measured by the camera from the images.

The maximum temperature increase measured by the camera is 33.6 K at 28 ms, a clear 10 degrees higher than the maximum temperature predicted above. This is most likely due to the nature of SHPB experiments. After the incident pulse reaches the specimen, some of it is reflected back along the incident bar. When the reflection reaches the end of the incident bar, there is nothing to absorb its energy and so it reflects again, only to apply further stress to the specimen. In practice, the incident pulse will reflect up and down the incident bar, causing strain in the specimen a great number of times before all its energy dissipates away.

The temperature increase at 4 ms, a short time after the initial impact, is 19.0 K, which appears to be much closer to the predicted value.

ⁱ<http://www.flir.com/>

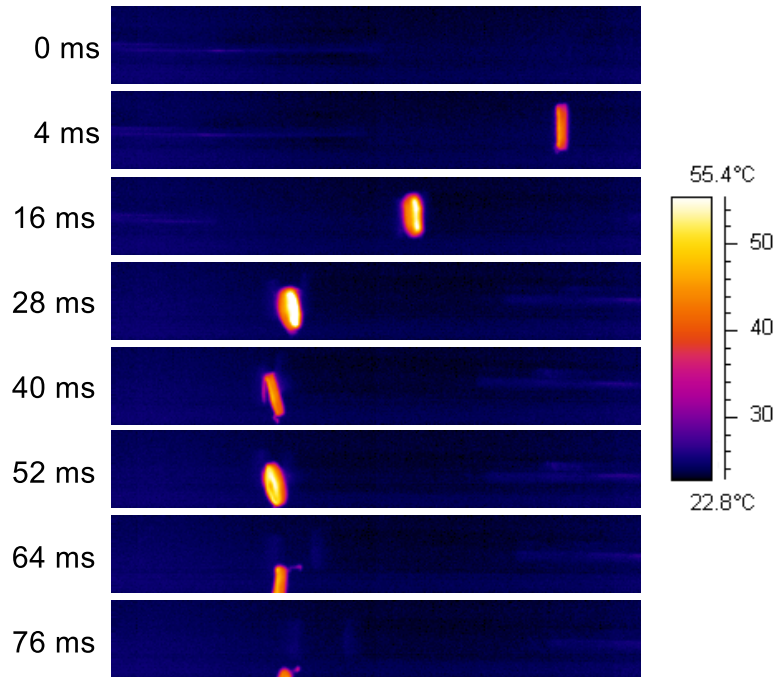


FIGURE 5.30: *Thermal imagery of LLDPE in SHPB.*

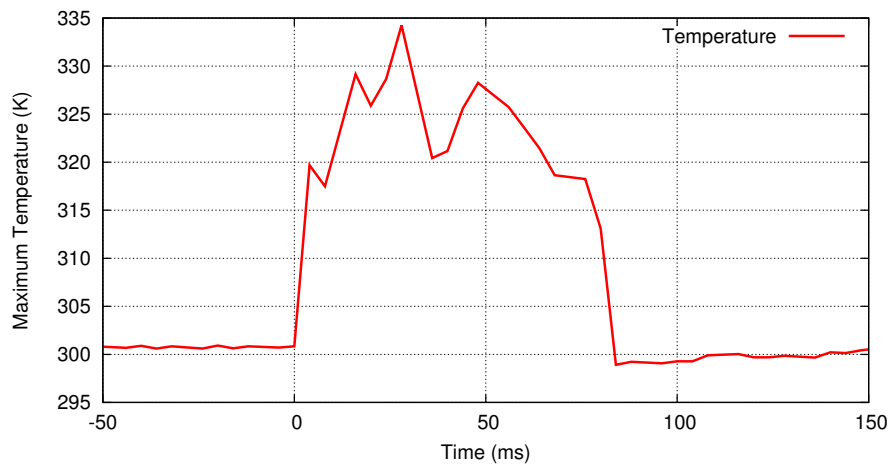


FIGURE 5.31: *Temperature in thermal imagery of LLDPE in SHPB.*

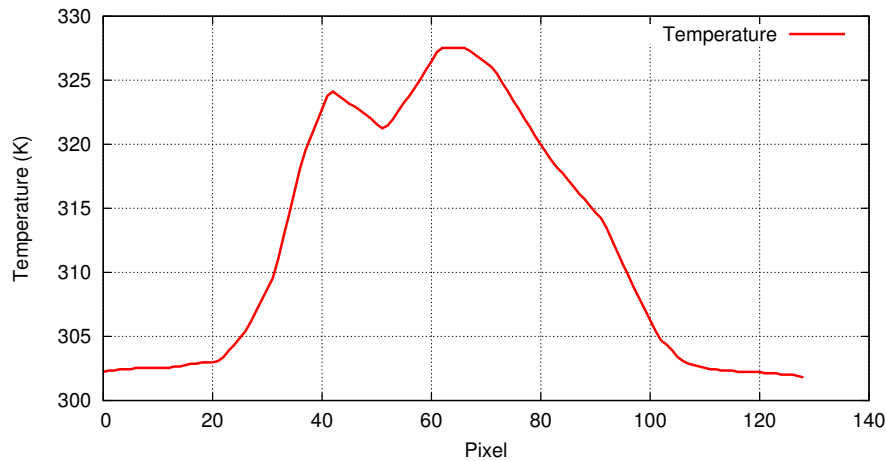


FIGURE 5.33: *Temperature across the specimen face.*

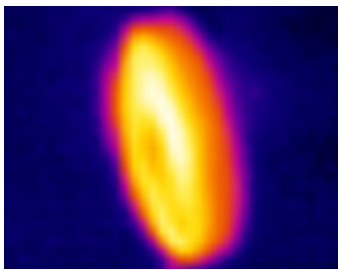


FIGURE 5.32: *Close up of specimen in thermal image at 52 ms.*

An interesting point to note from these images is the uniformity of specimen heating. Figure 5.32 shows a close up of the specimen in the above images at 52 ms, which is turned slightly toward the camera revealing how the specimen face has heated. The area in the centre of the specimen is slightly cooler than its surroundings, which is as a result of the relative strains. Under deformation, the material at the centre of the specimen is strained by a smaller amount than the outer edges, and so it attains less heat at this point. This is illustrated in greater detail by Figure 5.33, which shows the temperature measured of the central pixel across the length of the image, which shows a difference of around 7 K between the cooler center of the specimen to its hottest point.

With this being the case, it would seem logical that the outer edge of the specimen would be the area which underwent the greatest strain and therefore became the hottest, but the thermal imaging shows this to be an inaccurate assumption. The reason for this is, at the time of writing, unknown. Most of the available research appears to focus on the overall (i.e. average) increase in specimen temperature as a result of strain rather than the temperature distribution within the specimen. The author's conjecture is that the polymer chains within the body of the specimen are bordered on all sides by other chains, while around the circumference of the specimen are only in contact with other chains on one side. The increase in temperature comes as a result of interactions between neighbouring polymer chains. Since the chains on the outside edge have fewer neighbours, the temperature increase is less significant.

While this research proved interesting, the relatively low image capture rate of thermal cameras mean that they are not particularly useful for high strain rate experiments such as the SHPB.

Optical dropweight

“The true delight is in the finding out rather than in the knowing.”

—ISAAC ASIMOV

Since the ODW doesn't rely on the transmission of stresses from the specimen as with the SHPB, it is a remarkably simple technique to work with. In this work, the only real consideration necessary was how to measure the diameter of the specimen from the images taken by the high speed camera.

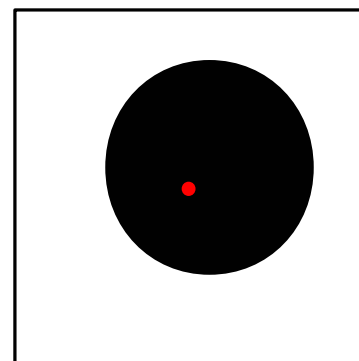
6.1 High-speed photography analysis

Measuring the dynamic specimen diameters by hand can be an extremely time consuming process, especially when working through a large number of images. This process can be automated using the following algorithm.

Prior to analysis, it may be sensible to convert the images from greyscale into binary (i.e. true monochrome) images. This is performed using a technique called *thresholding* which is discussed elsewhere in this report. See Sections 5.3.1 and 5.3.2 (pages 134 and 135 respectively) for more details of this technique as well as an explanation of how to understand digital images.

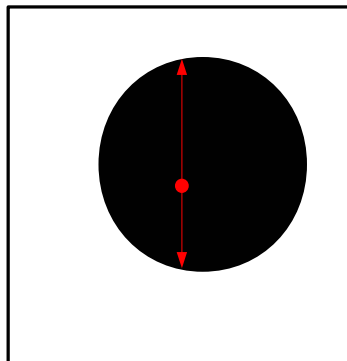
1. Locate the centre of the image.

Although, as with the diagram opposite, the specimen may not be exactly in the centre of the image, it is easy to position it so that some part of it is on top of the centre. This makes it simple to locate the specimen from the central point in the image.

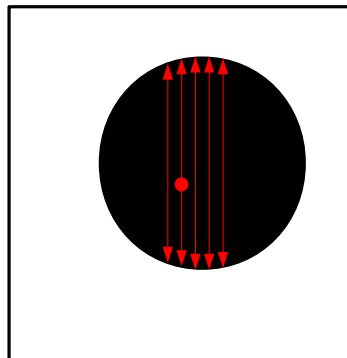


2. Find the edges of the specimen.

The edges of the specimen may be located by moving up or down one pixel at a time until the pixel intensity changes suddenly from dark to light. Finding the upper and lower edges gives the radius of the specimen at that point, but this is not necessarily the widest point.

**3. Find the widest part of the specimen.**

Move left or right one pixel and repeat step 2. This should be performed repeatedly until the widest section of the specimen is found. This should then be performed again moving left and right to find the widest point horizontally. The average of the vertical and horizontal widest measurements gives the diameter of the specimen.



A program written in C++ which can perform this algorithm on a single or multiple images is shown in Appendix K.

Results & Discussion

“Better to keep your mouth shut and appear stupid than to open it and remove all doubt.”

—MARK TWAIN

All of the graphs in this section are shown in a small format to facilitate easiness of reading. Should higher resolution images be required, they are also reproduced as full-page images in Appendix L, excluding the bar graphs comparing relative yield strengths and energy absorption.

7.1 Split-Hopkinson pressure bar

7.1.1 Polyethylene

7.1.1.1 Benchmark

Figures 7.1, 7.2 and 7.3 show the true stress-strain curves, Young’s modulus evolution and energy absorption respectively for the pure PE matrices used in this

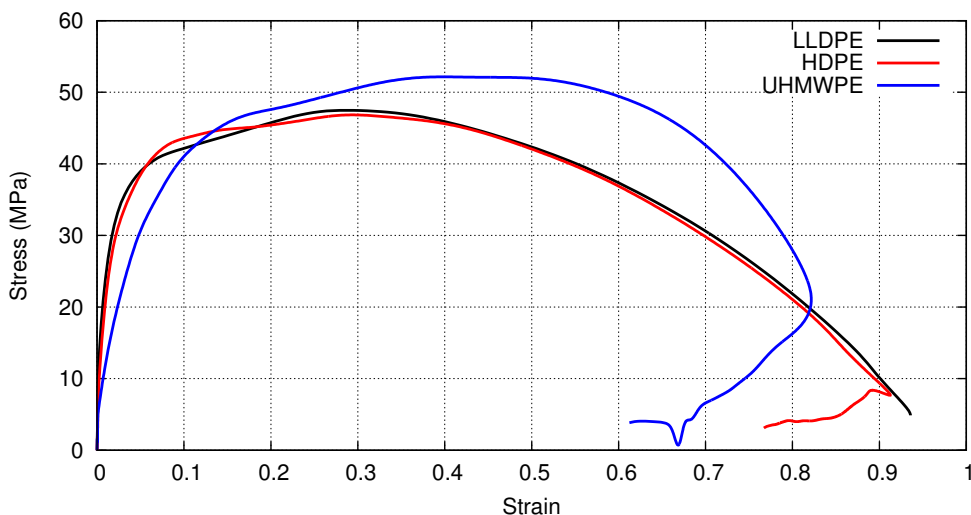


FIGURE 7.1: SHPB true stress/strain curves for LLDPE, HDPE and UHMWPE.

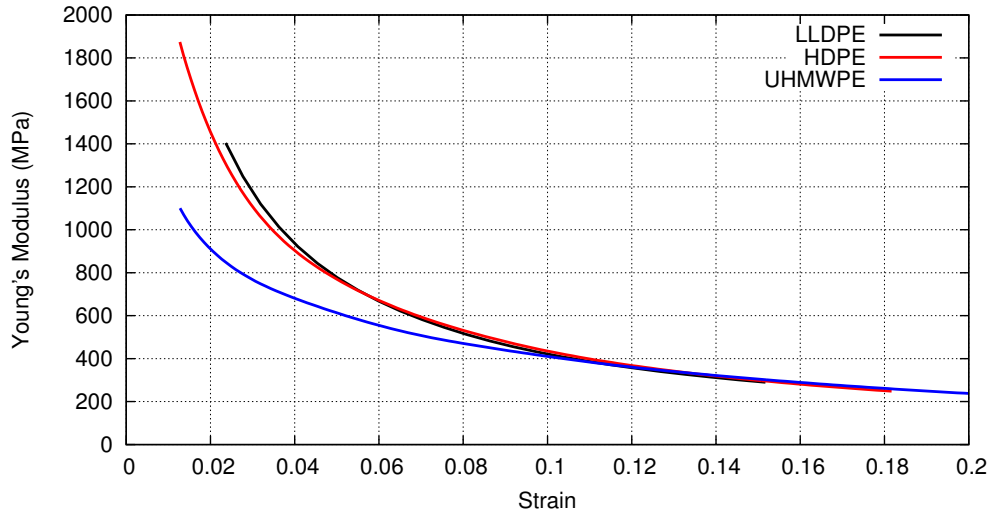


FIGURE 7.2: SHPB Young's modulus evolution for LLDPE, HDPE and UHMWPE.

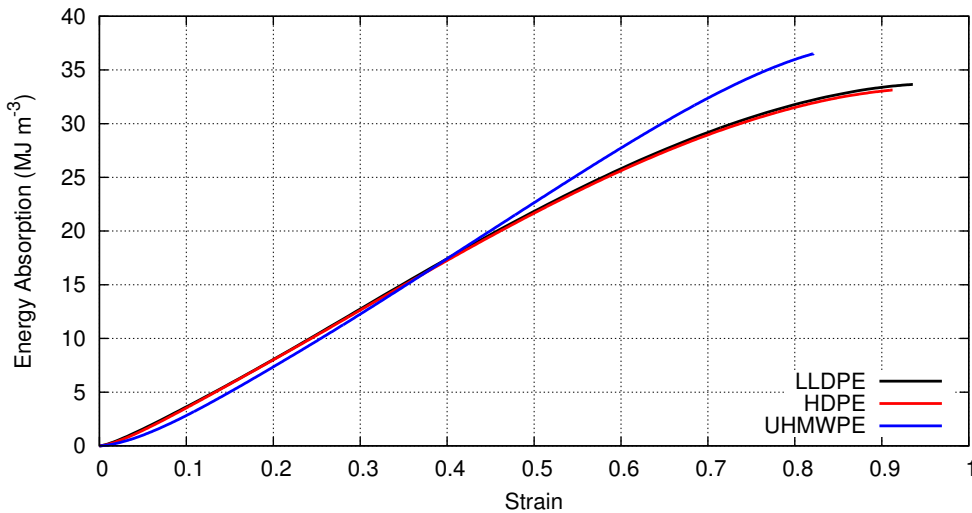


FIGURE 7.3: SHPB energy absorption for LLDPE, HDPE and UHMWPE.

section of the research. These act as a benchmark from which any improvements from nano-reinforcements may be measured. It is, perhaps, surprising that there is such a small difference between the three materials. Tensile testing at quasi-static strain rates have shown that PE tends to have a yield strength which is dependent on the molecular weight; in simple terms, longer chain lengths lead to a higher tensile strength. This is not entirely the case here, with LLDPE and HDPE being virtually identical and UHMWPE only marginally stronger. The primary mechanism behind this is thought to be the rapid temperature increase in the specimen which causes the specimen to soften extremely quickly. After yield, the UHMWPE curve exhibits significantly more strain hardening than the others.

The histories of Young's modulus for LLDPE and HDPE appear virtually identical. UHMWPE has a significantly lower initial value, appearing to deform more easily prior to yield.

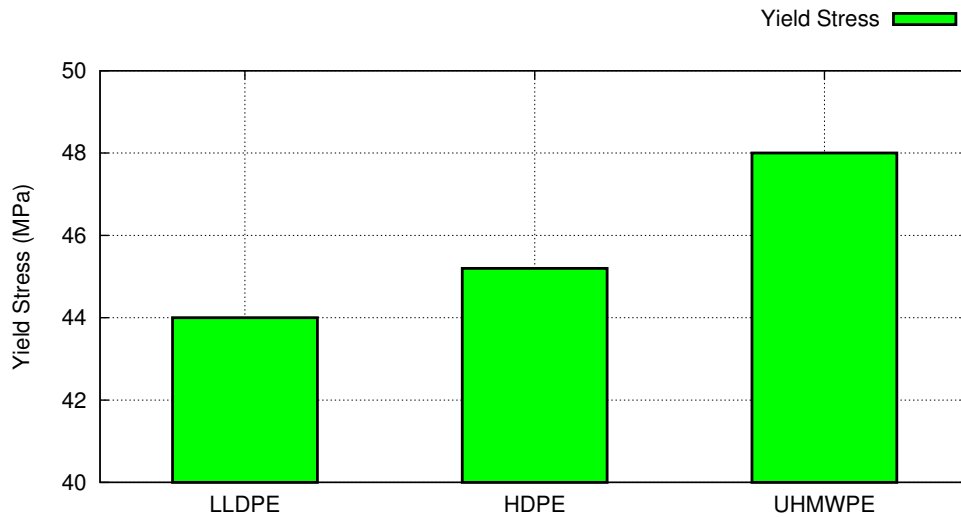


FIGURE 7.4: SHPB yield strengths of LLDPE, HDPE and UHMWPE.

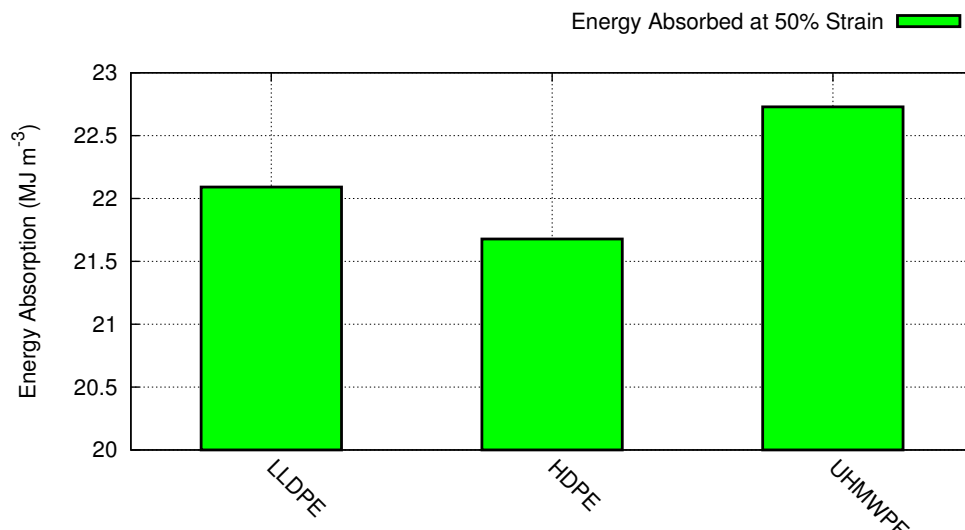


FIGURE 7.5: SHPB energy absorption at 50% strain of LLDPE, HDPE and UHMWPE.

The energy absorption graph illuminates the strain hardening of UHMWPE further. LLDPE and HDPE are all but indistinguishable, whereas, a little time after yield, the UHMWPE requires significantly more energy to keep it deforming.

Figure 7.4 shows a comparison of the yield strengths of the unreinforced PE matrices. With a total variation of less than 10% across the range, none of the materials could be considered to be significantly *stronger* than the others. The energy absorption of the three materials at a strain of 50%, shown in Figure 7.5, also shows very little difference between the three materials when they have rapidly strained by a significant amount.

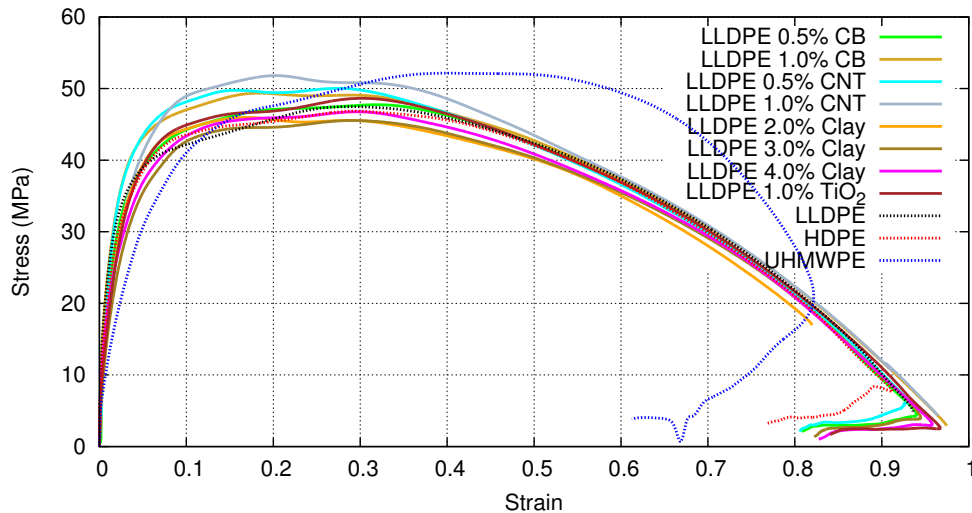


FIGURE 7.6: SHPB true stress/strain curves for LLDPE nanocomposites.

7.1.1.2 LLDPE nanocomposites

From Figure 7.6 it would appear that the addition of small quantities of carbon black or CNT reinforcements into an LLDPE matrix can give an increase in the yield strength as compared to that of the monolithic material. With carbon black, the addition of 0.5% by weight appears to increase the point of yield by around 8%, with a 1.0% addition provides a slightly higher increase. CNTs improve things further, with the 0.5% nanocomposite having a 12% higher yield strength, and the 1.0% increasing by 14%.

The addition of nanoclay as a reinforcement may provide a small increase in yield strength, however, each of the values shown here is within 5% of the monolithic material. These improvements are not significant enough to be clearly recognised as being outside ordinary experimental scatter

Energy absorption at 50% strain, as shown in Figure 7.10, also shows improvements for the CB and CNT nanocomposites. CNT shows a more significant increase in energy absorption, with the 0.5% and 1.0% composites showing improvements of 5% and 6% respectively. The nanoclay-based composites all show significant reductions in their ability to absorb energy.

Since the underlying chemistry of the different polyethylenes is effectively the same it would seem safe to assume that, if the trends seen here continue with the other materials, it would be clear that the improvements in mechanical behaviour are as a result of the nanofillers.

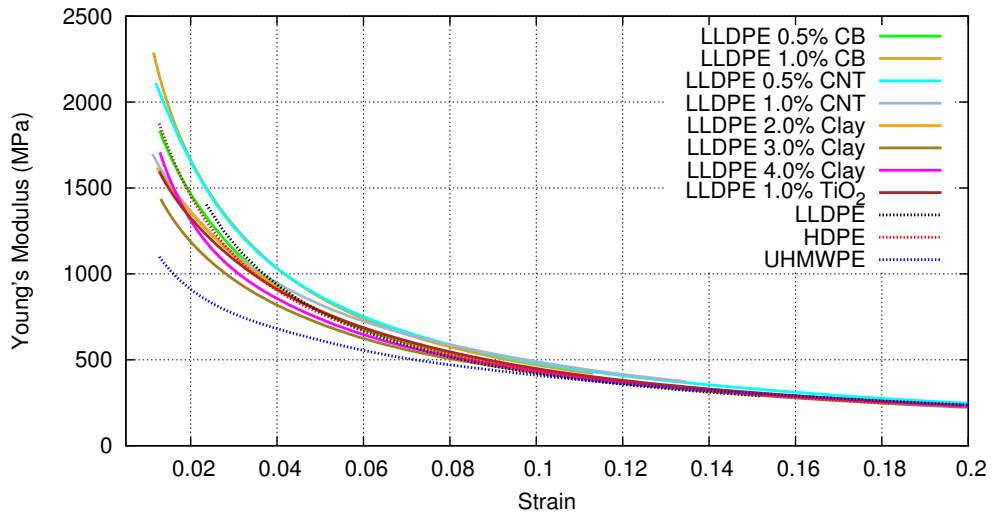


FIGURE 7.7: SHPB Young's modulus evolution for LLDPE nanocomposites.

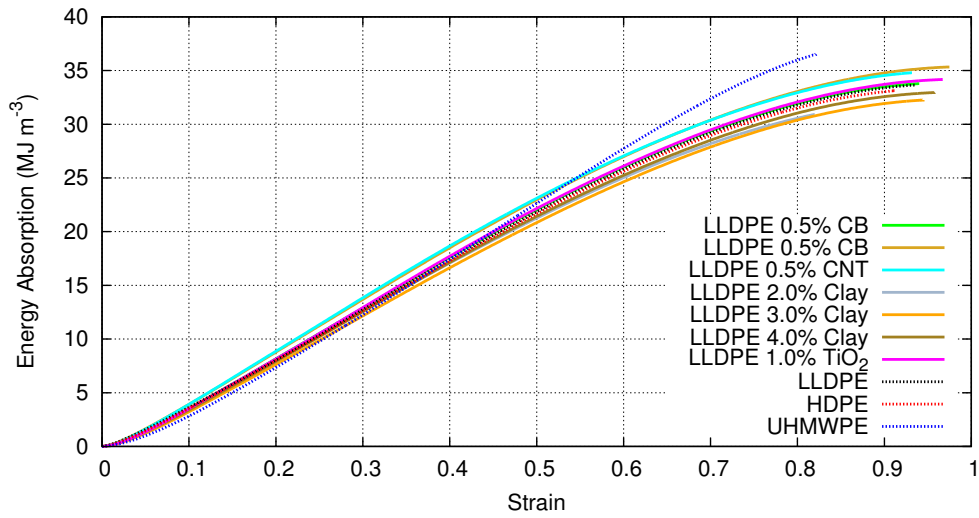


FIGURE 7.8: SHPB energy absorption for LLDPE nanocomposites.

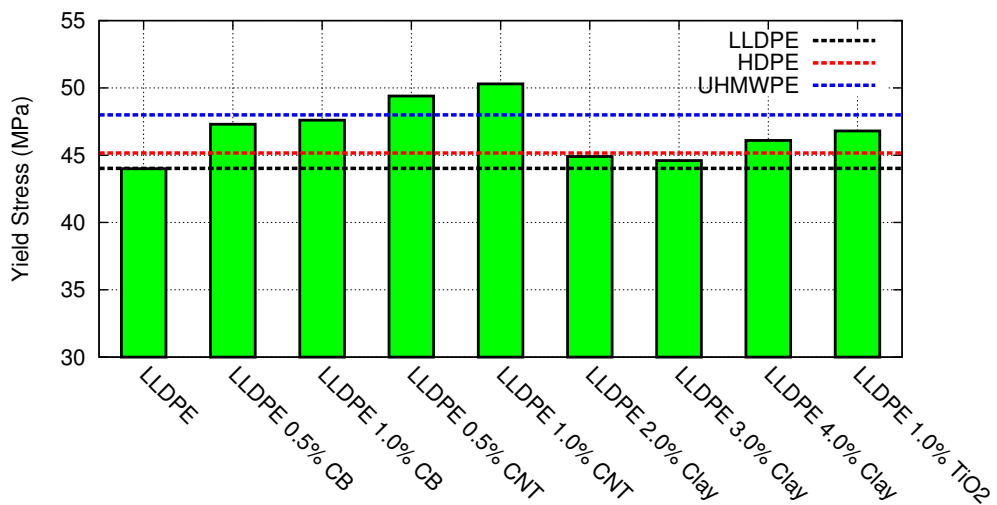


FIGURE 7.9: SHPB yield strengths of LLDPE nanocomposites.

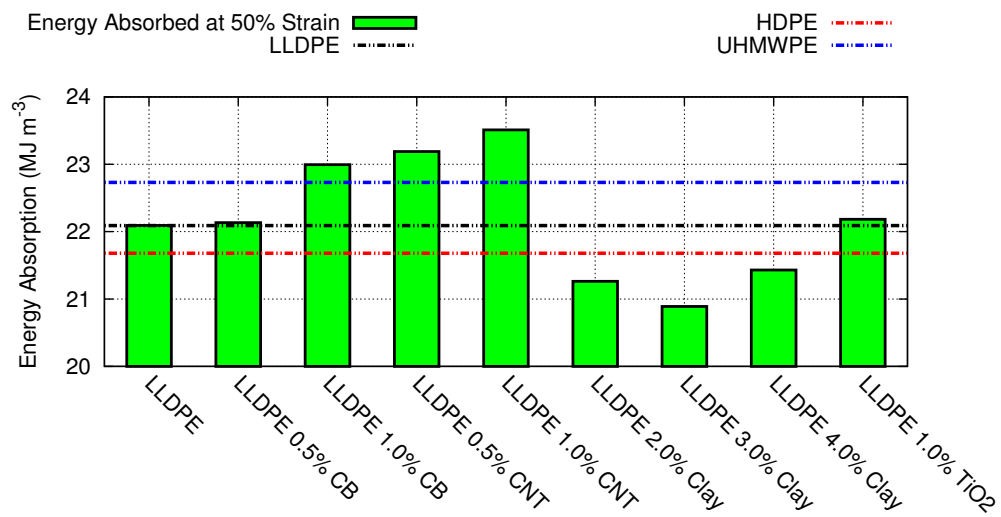


FIGURE 7.10: SHPB energy absorption at 50% strain of LLDPE nanocomposites.

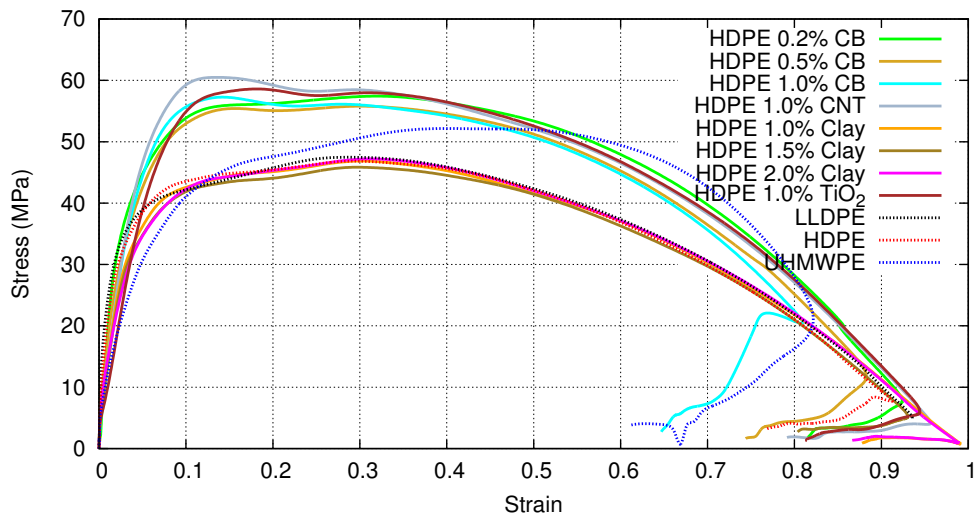


FIGURE 7.11: SHPB true stress/strain curves for HDPE nanocomposites.

7.1.1.3 HDPE nanocomposites

HDPE appears to show a marked increase in yield, Young's modulus and energy absorption when CB, CNTs or TiO_2 were added to it. Yield strength seems to have increased by around 25% with CB added to the mix (in any quantity), and the addition of CNTs or TiO_2 has given an increase of 30% or more. Similar trends may be seen in the energy absorption.

The astute reader may have observed some skepticism in the above paragraph. While some of the HDPE nanocomposites *appeared* to have some quite remarkable increases over the mechanical properties of the monolithic polymer, concern was expressed during the project that some of the HDPE specimens were not, in fact, HDPE. Materials were supplied at different times, and those having an improved response all came from a different batch to the materials for which the properties were barely affected.

A new set of HDPE specimens, all made from the same batch, were requested but could not be obtained in time.

For the sake of maintaining scientific rigour, the improvements in HDPE shown here were considered to be unreliable.

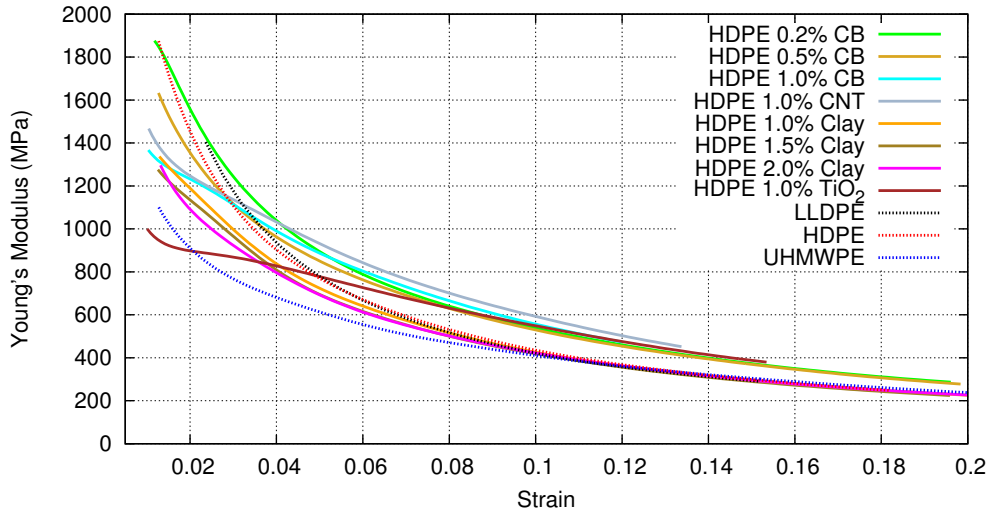


FIGURE 7.12: SHPB Young's modulus evolution for HDPE nanocomposites.

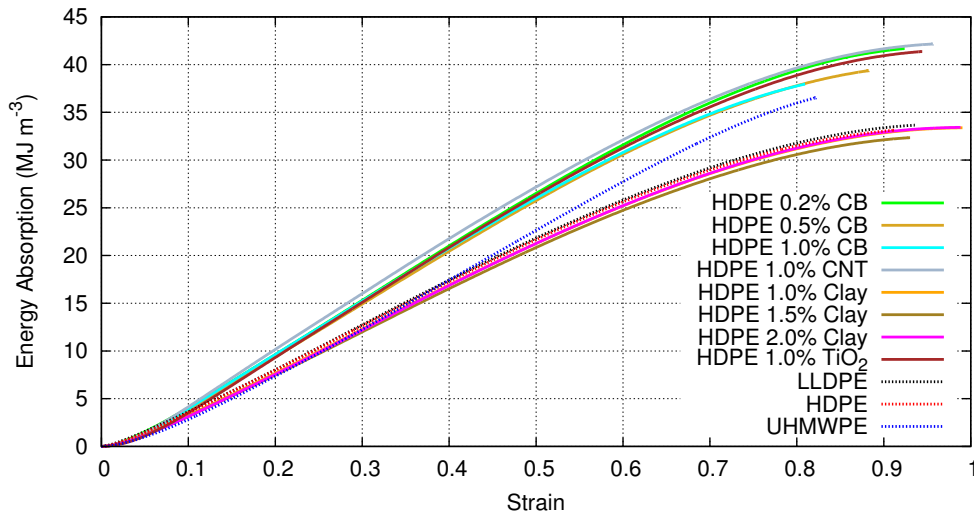


FIGURE 7.13: SHPB energy absorption for HDPE nanocomposites.

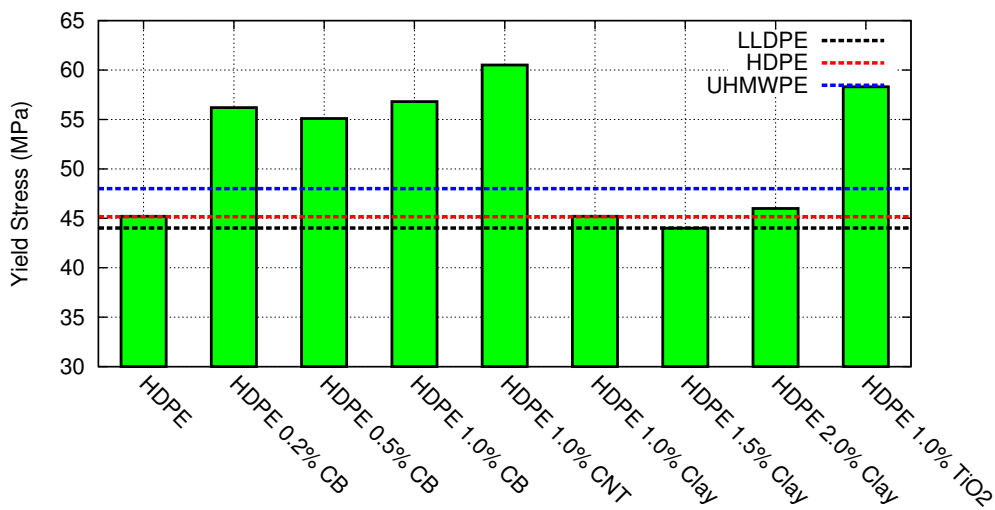


FIGURE 7.14: SHPB yield strengths of HDPE nanocomposites.

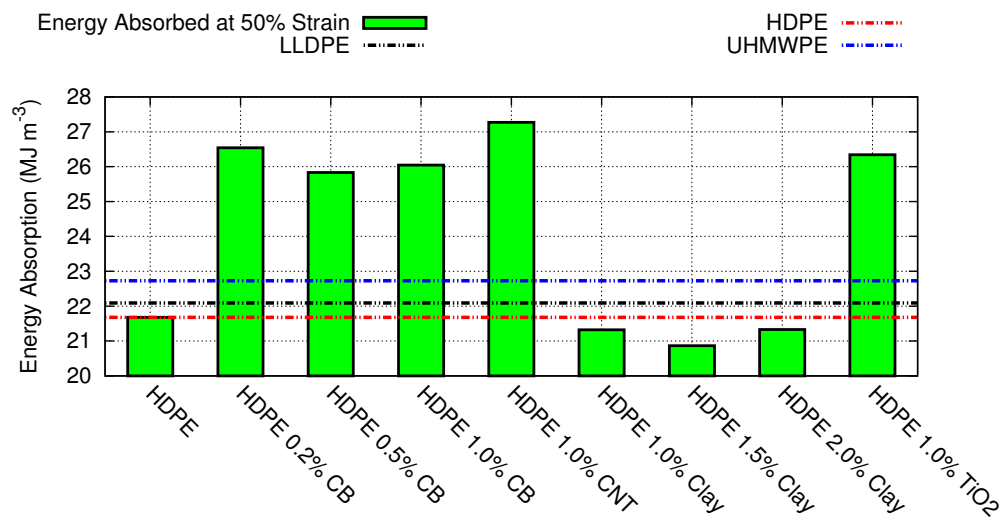


FIGURE 7.15: SHPB energy absorption at 50% strain of HDPE nanocomposites.

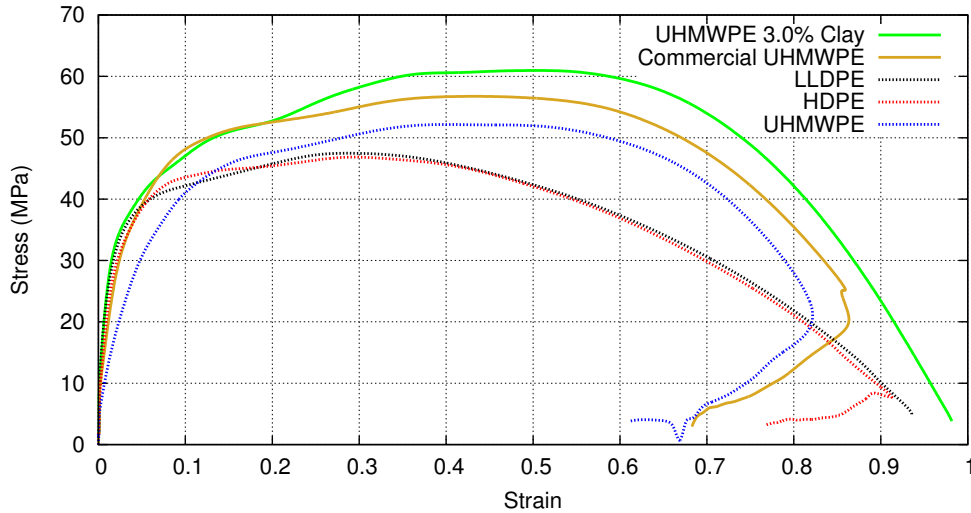


FIGURE 7.16: SHPB true stress/strain curves for UHMWPE nanocomposites.

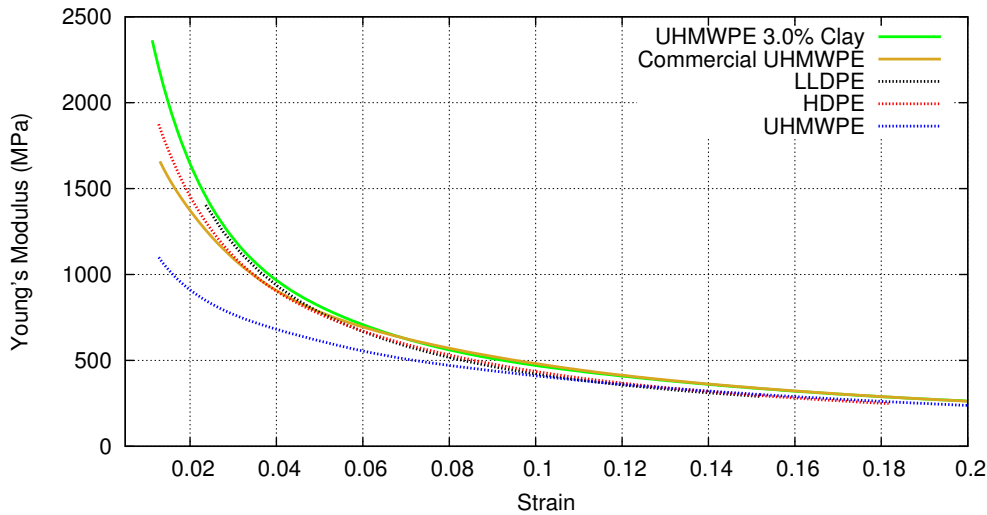


FIGURE 7.17: SHPB Young's modulus evolution for UHMWPE nanocomposites.

7.1.1.4 UHMWPE nanocomposites

The majority of the UHMWPE used in this work was sourced through a specialist chemical supply company. An alternative brand of UHMWPE was also tested to compare their properties. This commercial UHMWPE had a significantly higher yield strength, Young's modulus and energy absorption than the original UHMWPE.

3.0% by weight of nanoclay was added to the commercial product, which appeared to have very little effect prior to yield, after which it appears to induce an increase in strain hardening. From Figure 7.20 it appears that the addition of nanoclay is capable of increasing energy absorption.

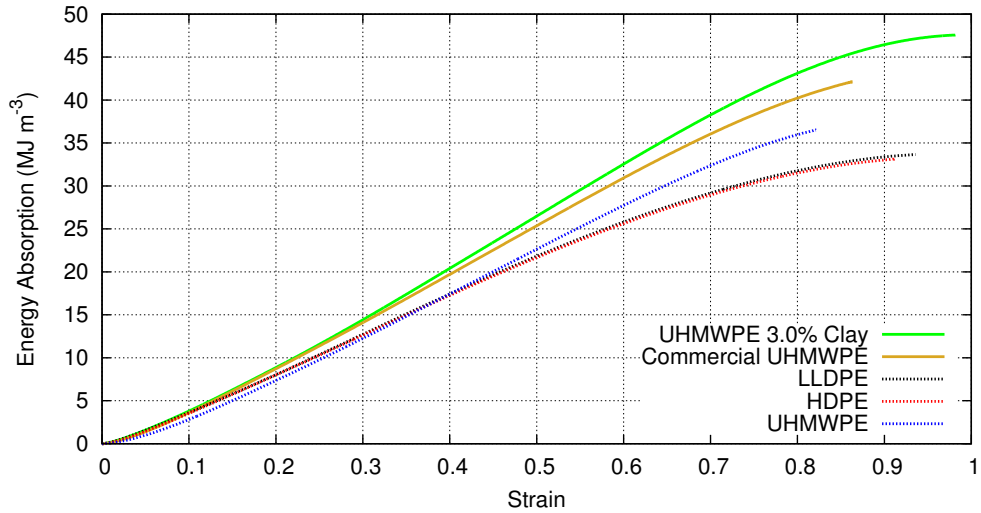


FIGURE 7.18: SHPB energy absorption for UHMWPE nanocomposites.

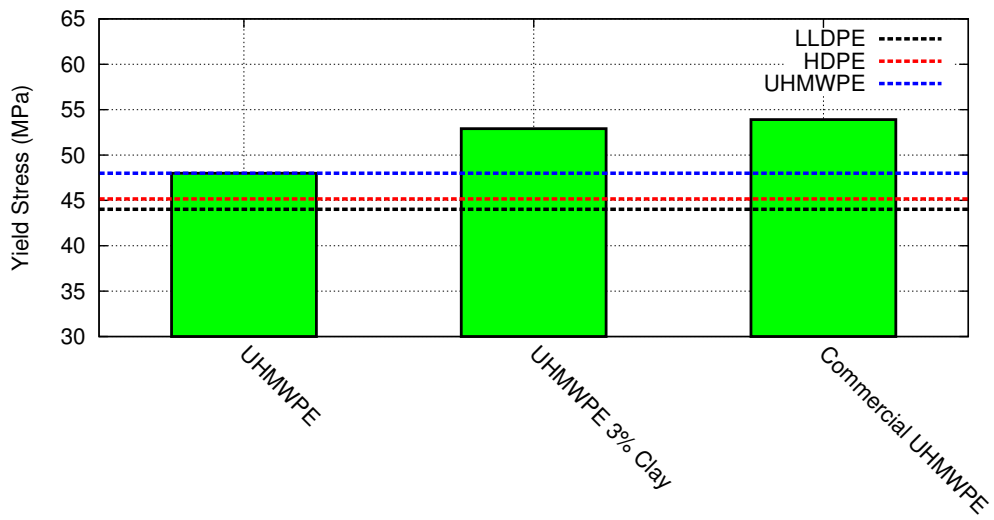


FIGURE 7.19: SHPB yield strengths of UHMWPE nanocomposites.

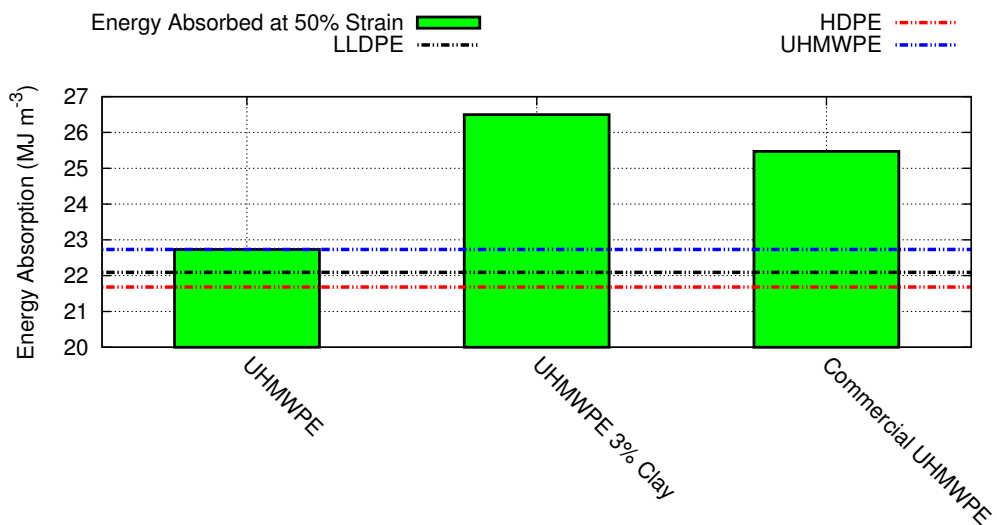


FIGURE 7.20: SHPB energy absorption at 50% strain of UHMWPE nanocomposites.

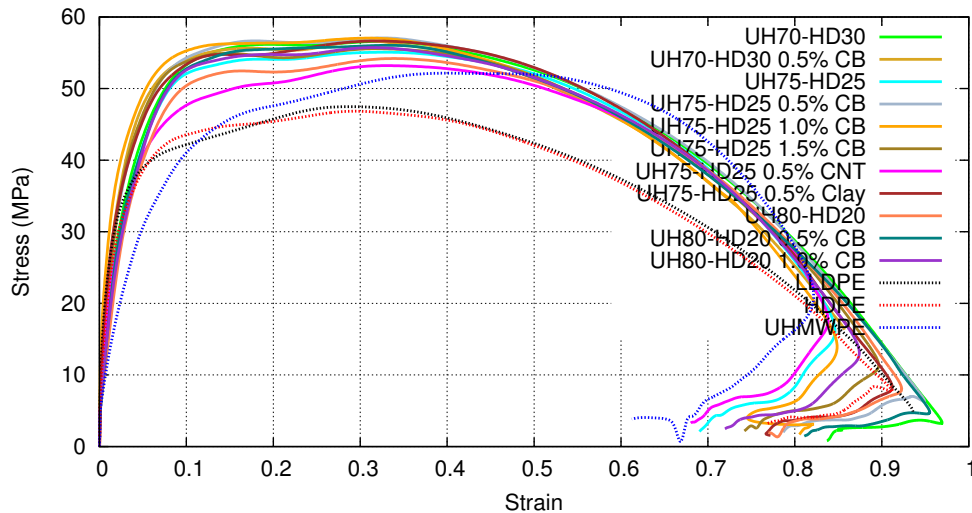


FIGURE 7.21: *SHPB true stress/strain curves for PE blends and nanocomposites.*

7.1.1.5 PE blends and nanocomposites

UHMWPE is notoriously difficult to process. It is extremely viscous when in a molten state, which makes it difficult to mould. Making a composite constructed from a matrix of UHMWPE and a reinforcement of HDPE^a can decrease the viscosity, making it easier to process.

From Figures 7.21, 7.24 and 7.25, these blended materials also appear to have a notable increase in both yield strength and energy absorption, with all of the tested materials exhibiting improvements over the monolithic polymers.

In Section 7.1.1.2 (page 150) where LLDPE nanocomposites were discussed, hope was expressed that the supposed trends in the improvements in mechanical properties would be apparent in other materials. The results from the PE blends show some similarities to the LLDPE trends. In the cases of the 75% UHMWPE/25% HDPE, and 80% UHMWPE/20% HDPE materials, the addition of carbon black seemed to give a slight increase in yield over the 'pure' blend, although this is not the case with the 70% UHMWPE/30% HDPE blend. The addition of nanoclay and carbon nanotubes, where tested, appears to have reduced the yield stress.

Energy absorption shows an increase over that of the 'pure' material wherever carbon black is used, but appears reduced by the addition of carbon nanotubes.

^aOr vice-versa if you prefer.

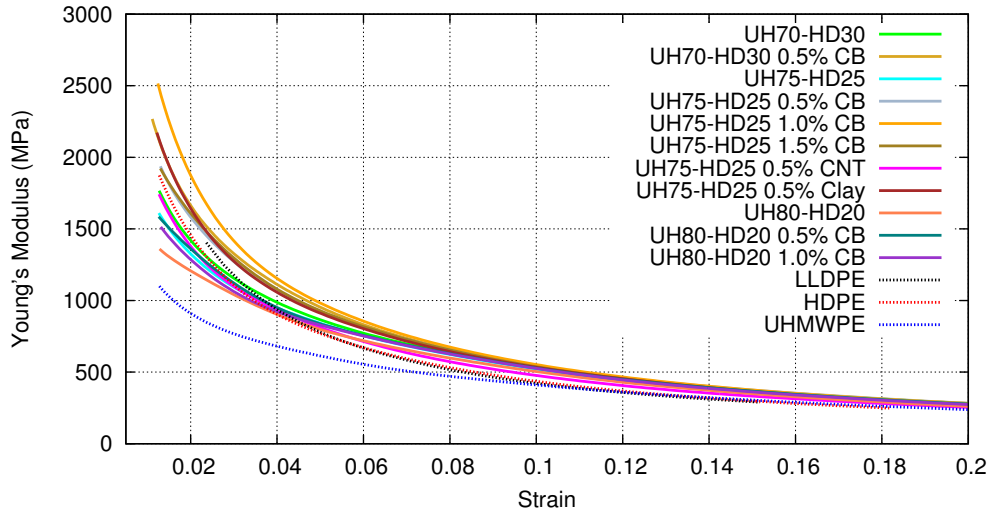


FIGURE 7.22: SHPB Young's modulus evolution for PE blends and nanocomposites.

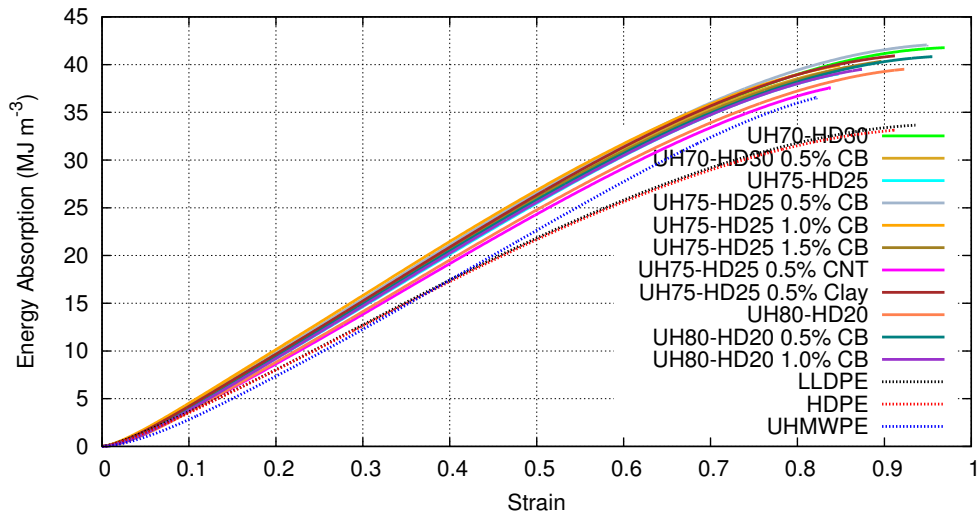


FIGURE 7.23: SHPB energy absorption for PE blends and nanocomposites.

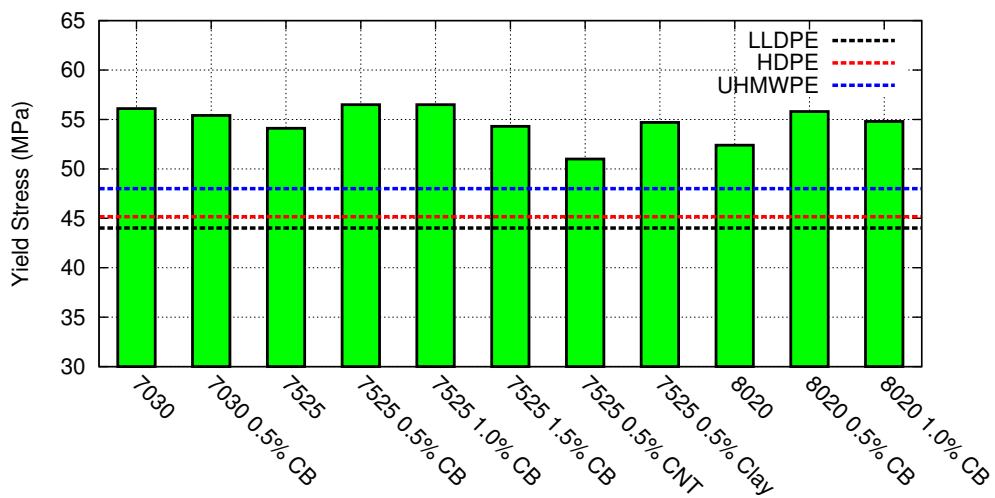


FIGURE 7.24: SHPB yield strengths of PE blends and nanocomposites.

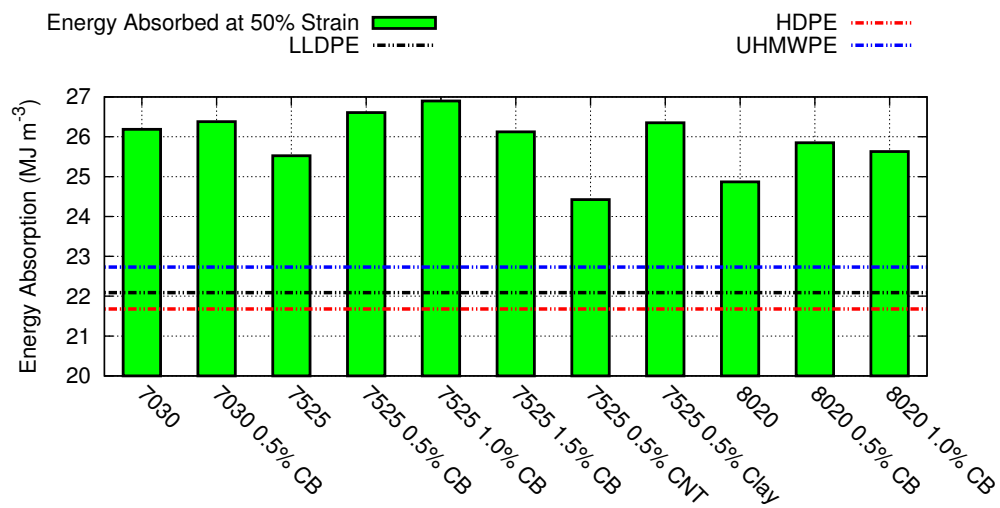


FIGURE 7.25: SHPB energy absorption at 50% strain of PE blends and nanocomposites.

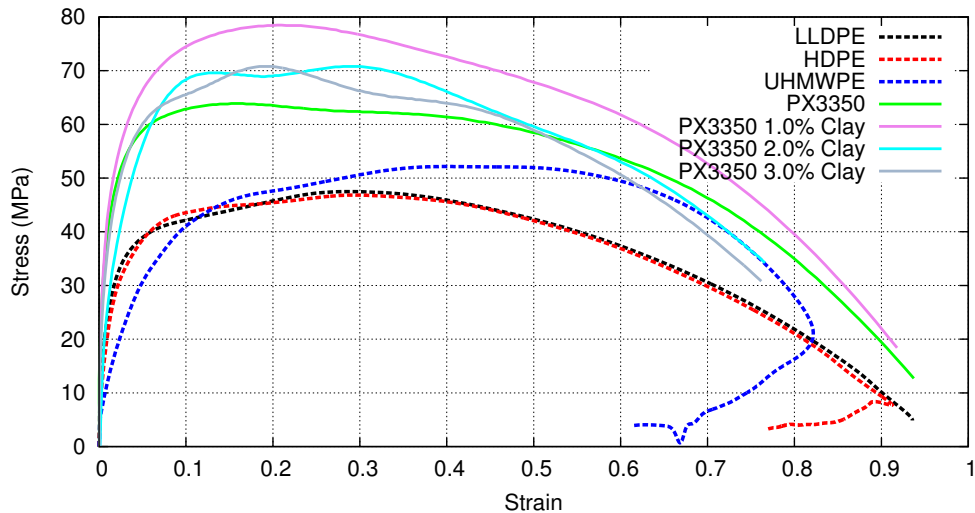


FIGURE 7.26: SHPB true stress/strain curves for polyurea and nanocomposites.

7.1.2 Polyurea

The polyurea tested in this work was produced and supplied by Line-X UK^b, who produce a variety of different types of PUr for use as protective coatings. The variety of PUr tested carries the name PX3350. The precise chemical composition of PX3350 is a trade secret.

The specimens used here were produced by spraying the PX3350 onto a steel substrate, building up additional layers until it was approximately 4 mm thick. Once cured, the PX3350 layer was peeled off the substrate. Specimens were constructed with the use of an ordinary 8 mm hole punch, which was capable of cutting through the PX3350 to produce specimens with dimensions of approximately 8×4 mm.

PX3350 proved to be fascinating, having a higher yield, Young's modulus and energy absorption than any of the PE-based materials. According to the results below, it would appear that adding 1%/wt nanoclay to the PX3350 has a marked effect, measurably increasing each of the mechanical properties. Being an elastomer, specimen recovery after compression was around 80% or more.

^b<http://www.line-x.co.uk/>

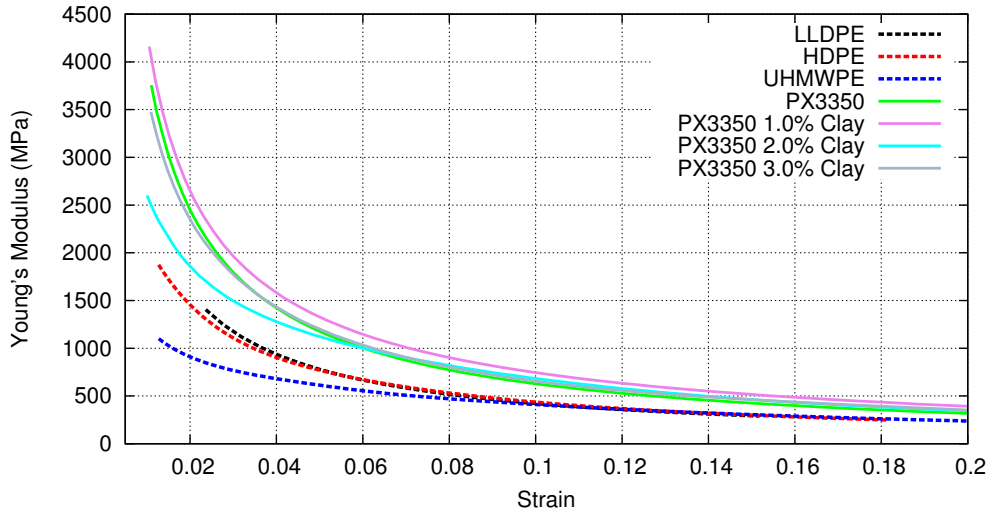


FIGURE 7.27: SHPB Young's modulus evolution for polyurea and nanocomposites.

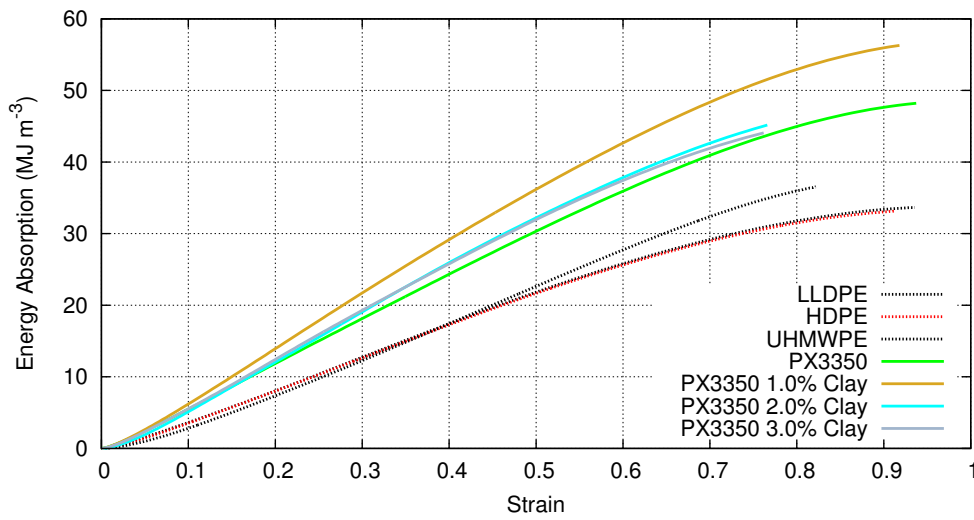


FIGURE 7.28: SHPB energy absorption for polyurea and nanocomposites.

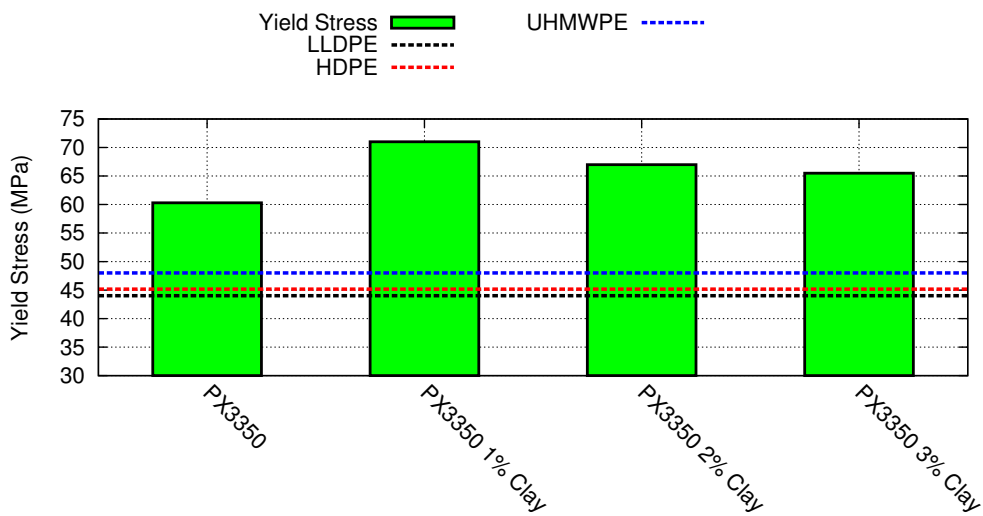


FIGURE 7.29: SHPB yield strengths of polyurea and nanocomposites.

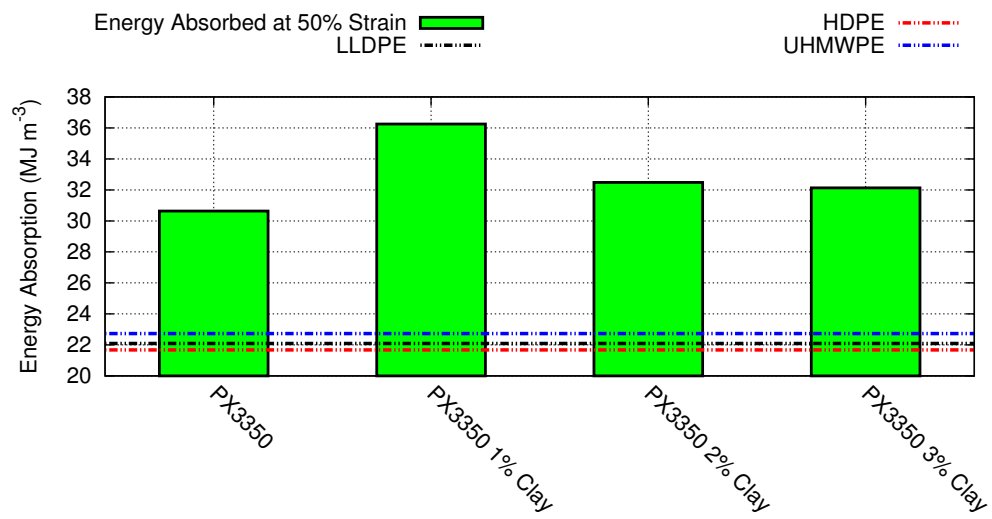


FIGURE 7.30: SHPB energy absorption at 50% strain of polyurea and nanocomposites.

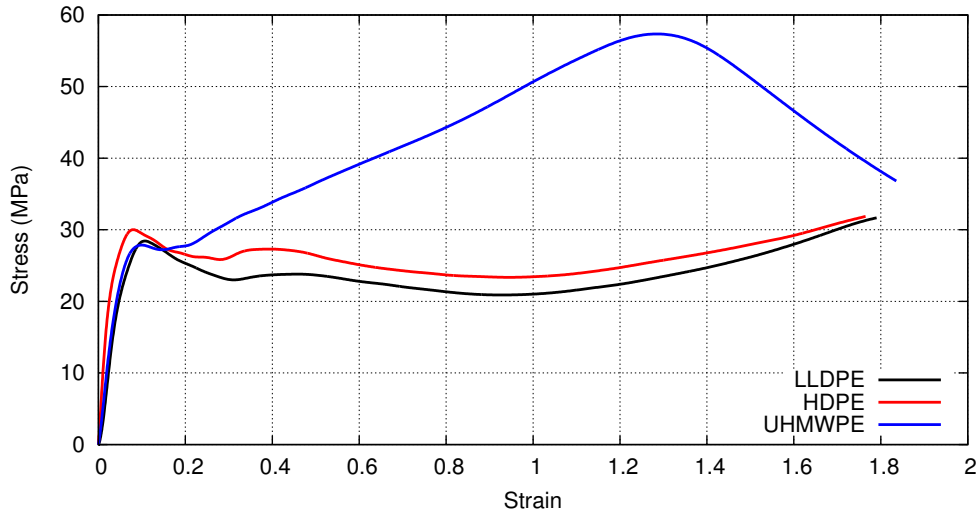


FIGURE 7.31: ODW true stress/strain curves for LLDPE, HDPE and UHMWPE.

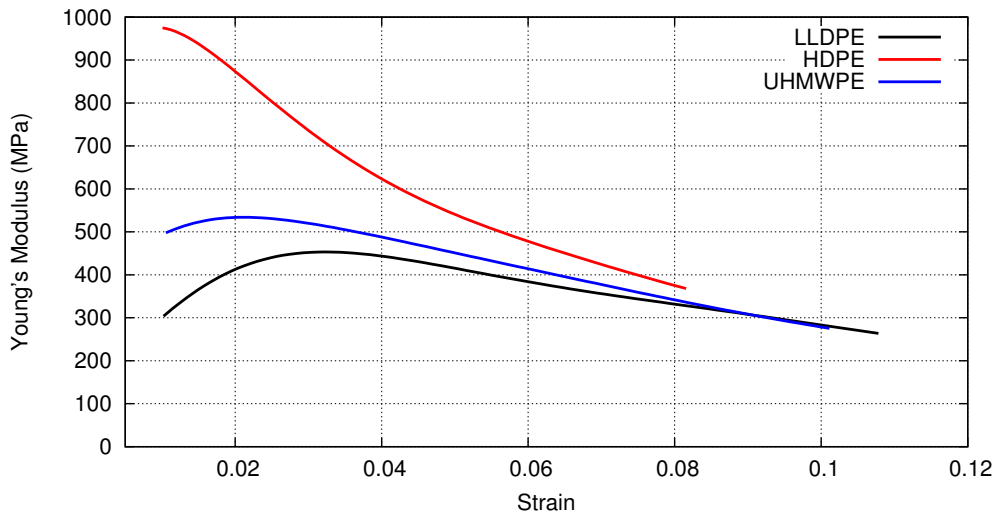


FIGURE 7.32: ODW Young's modulus evolution for LLDPE, HDPE and UHMWPE.

7.2 Optical Dropweight

7.2.1 Polyethylene

Figures 7.31, 7.32 and 7.33 show the true stress-strain curves, Young's modulus evolution and energy absorption respectively for the pure PE matrices used in this section of the research. As with the SHPB experimental results, these will act as a benchmark from which any improvements from nano-reinforcements may be measured.

Yield strengths of the three materials are extremely similar, as is the energy absorption of LLDPE and HDPE. The strain hardening of UHMWPE is extremely prominent in this experiment, leading to an energy absorption at 50% strain of almost double that of the other materials.

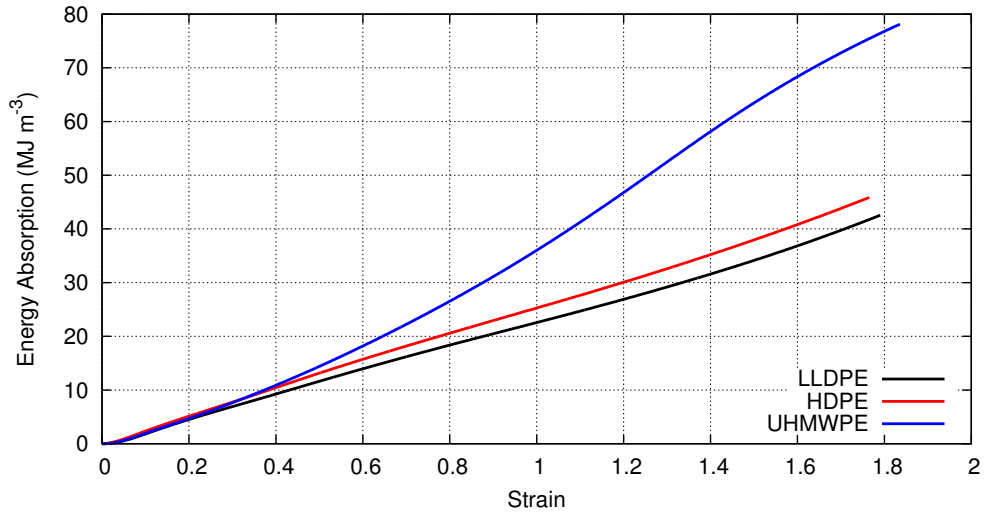


FIGURE 7.33: OWD energy absorption for LLDPE, HDPE and UHMWPE.

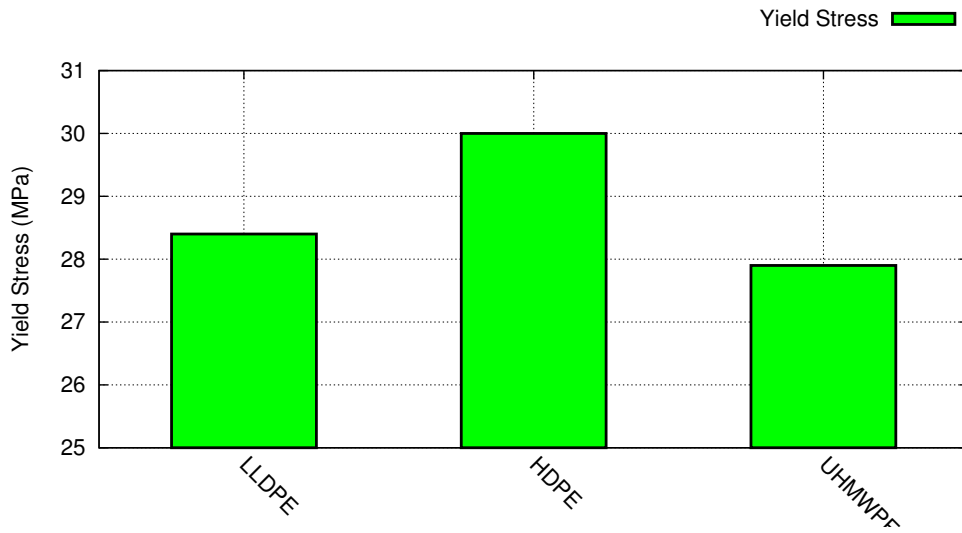


FIGURE 7.34: OWD yield strengths of LLDPE, HDPE and UHMWPE.

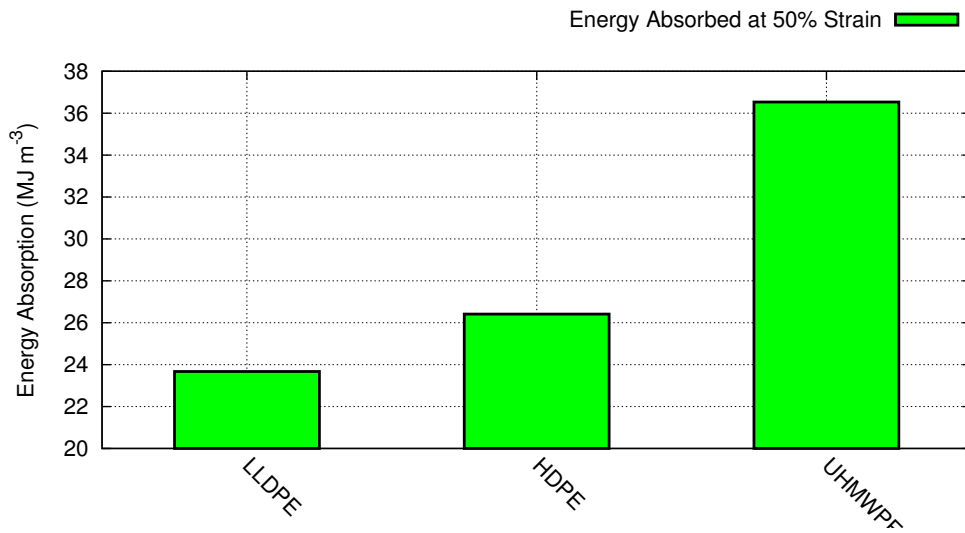


FIGURE 7.35: ODW energy absorption at 50% strain of LLDPE, HDPE and UHMWPE.

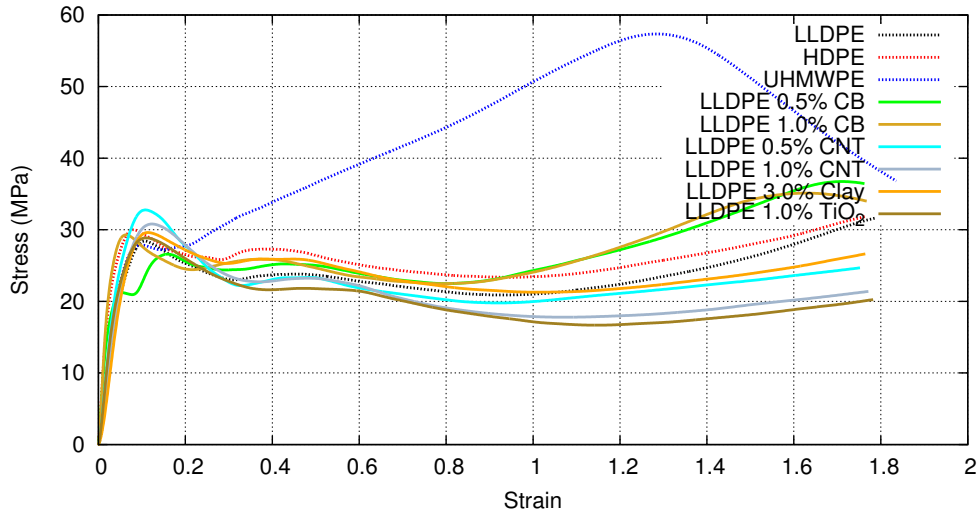


FIGURE 7.36: ODW true stress/strain curves for LLDPE nanocomposites.

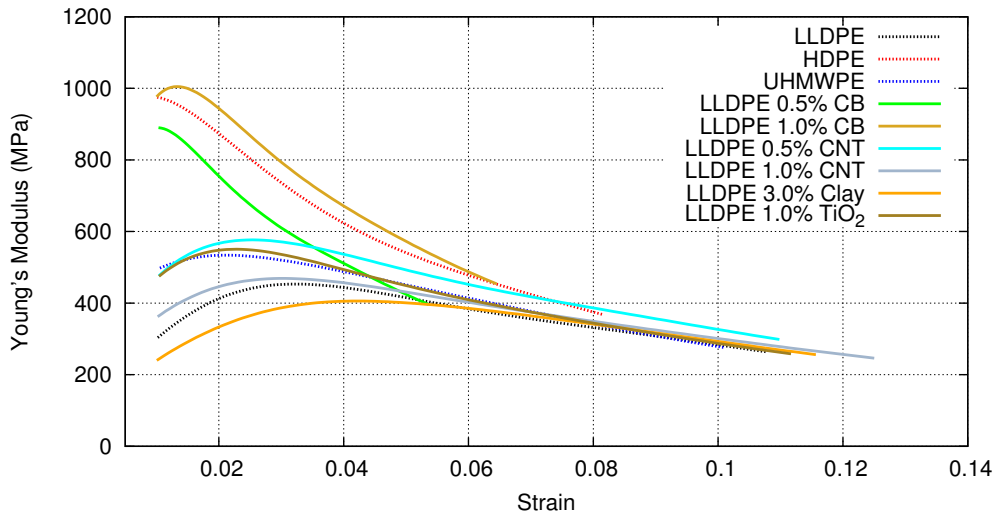


FIGURE 7.37: ODW Young's modulus evolution for LLDPE nanocomposites.

7.2.1.1 LLDPE nanocomposites

Figure 7.36 shows that, prior to yield, there is very little difference between the monolithic materials and their nanocomposites. The yield stress does appear to have increased by around 10% in the material reinforced with 0.5% by weight of carbon nanotubes, although any improvement, has vanished in the 1.0% CNT composite.

The two composites containing carbon black both show a small increase in strain hardening after the specimen has been strained beyond 100%.

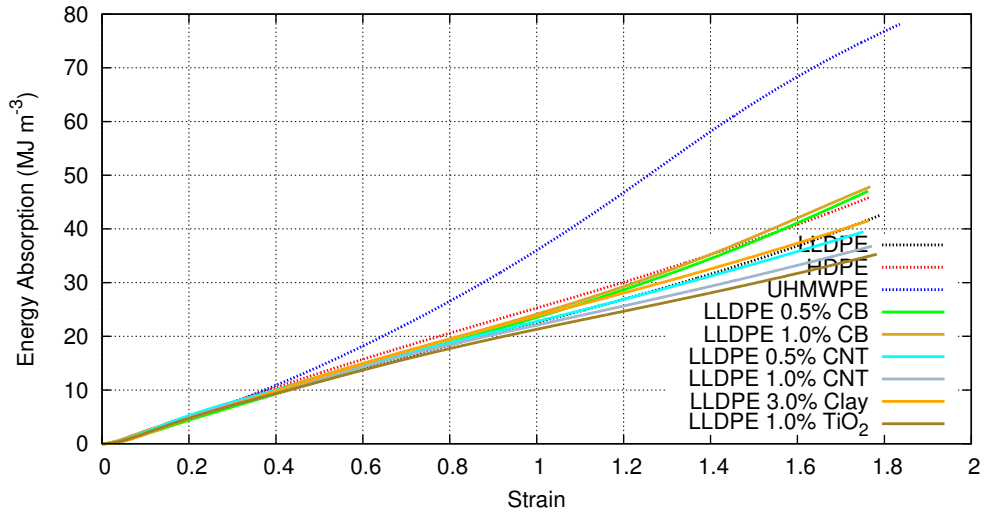


FIGURE 7.38: ODW energy absorption for LLDPE nanocomposites.

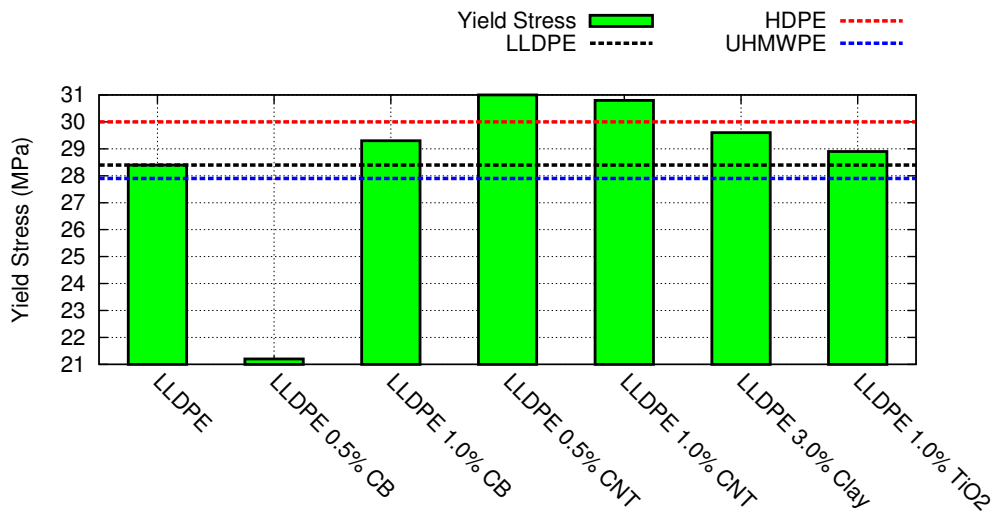


FIGURE 7.39: ODW yield strengths of LLDPE nanocomposites.

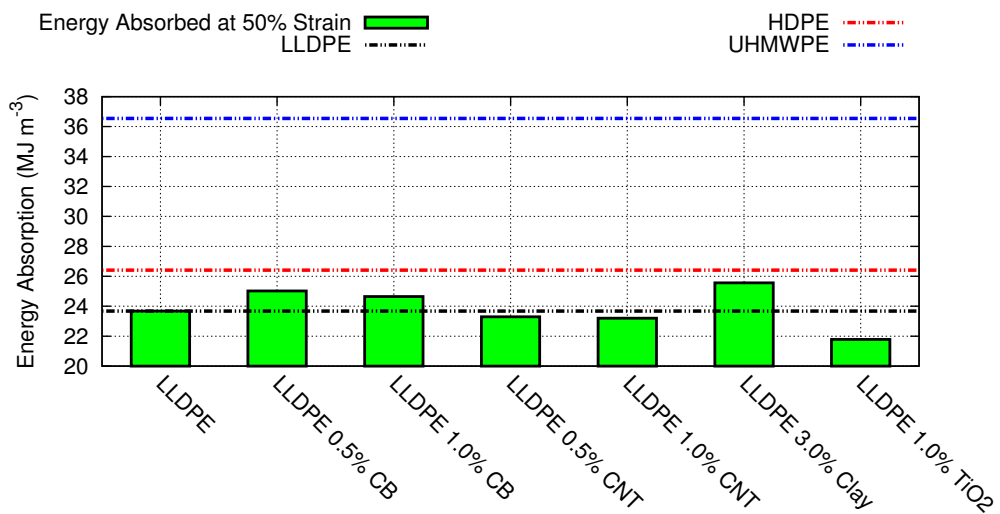


FIGURE 7.40: ODW energy absorption at 50% strain of LLDPE nanocomposites.

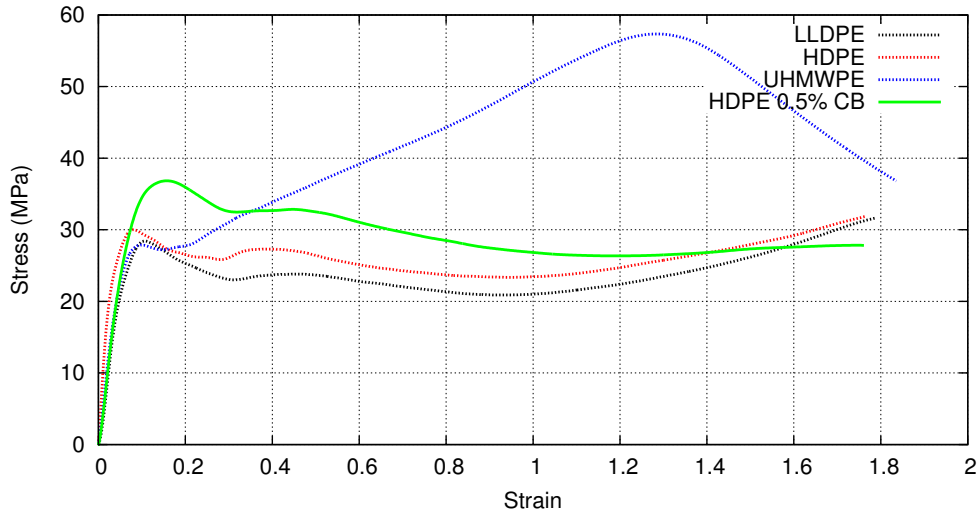


FIGURE 7.41: *ODW true stress/strain curves for HDPE nanocomposites.*

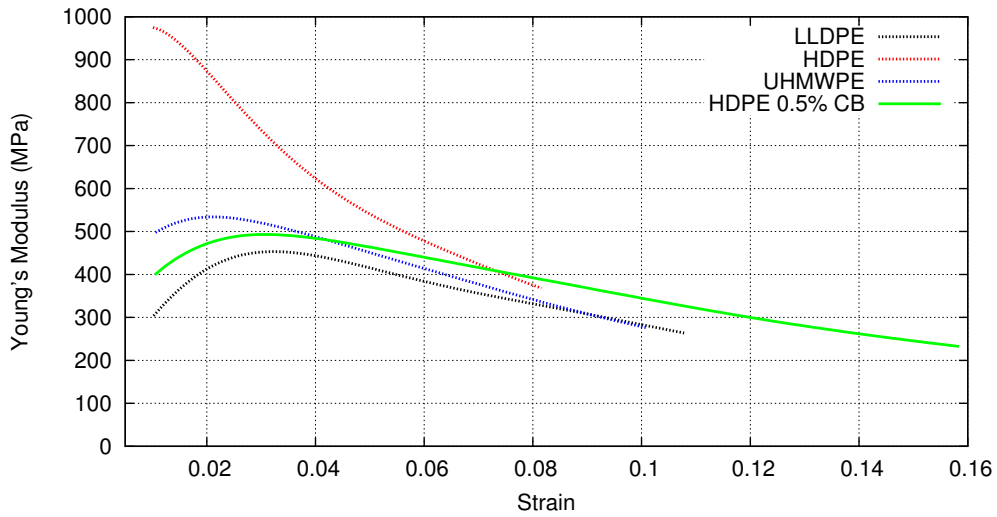


FIGURE 7.42: *ODW Young's modulus evolution for HDPE nanocomposites.*

7.2.1.2 HDPE nanocomposites

The addition of carbon black to HDPE *appears* to have a significant impact on the yield strength and energy absorption of HDPE, however, as with the specimens tested on the SHPB, concern has been expressed that the materials tested may not have actually been HDPE and so this result is considered spurious.

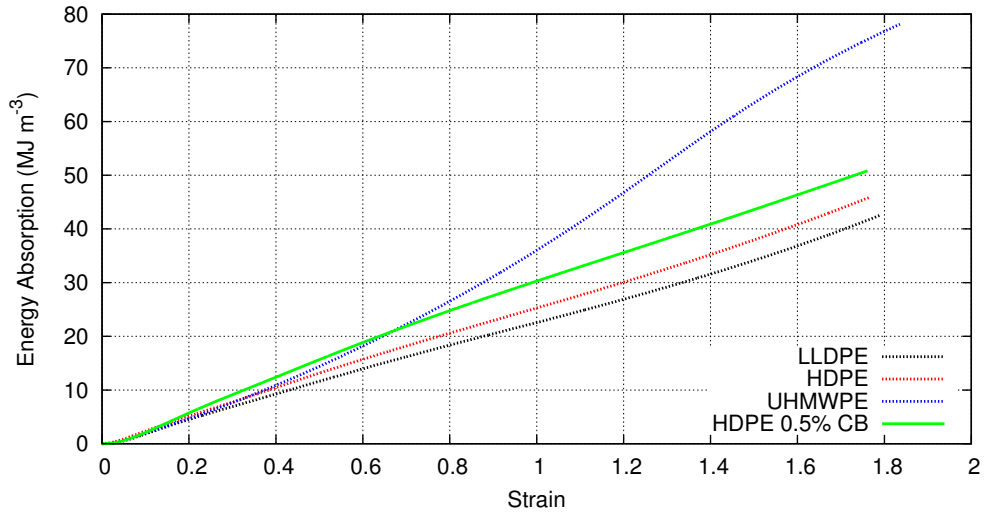


FIGURE 7.43: ODW energy absorption for HDPE nanocomposites.

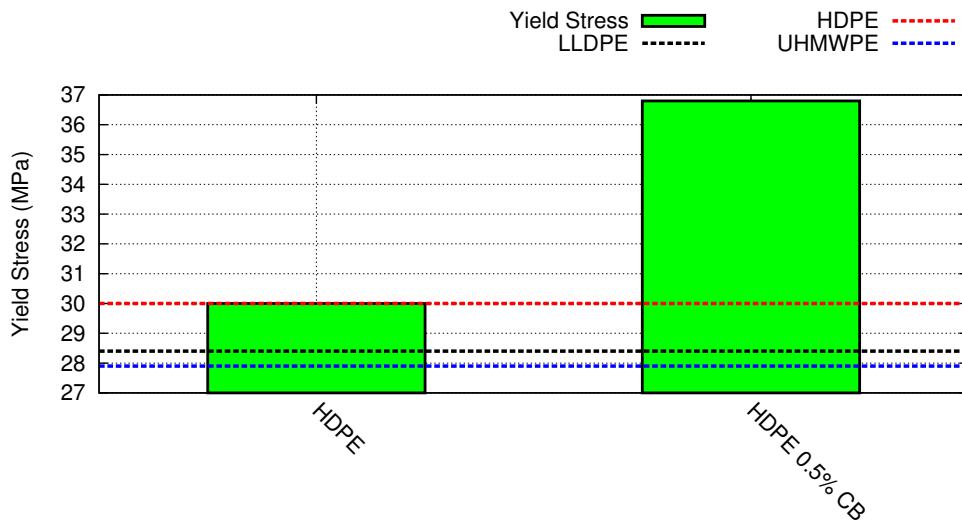


FIGURE 7.44: ODW yield strengths of HDPE nanocomposites.

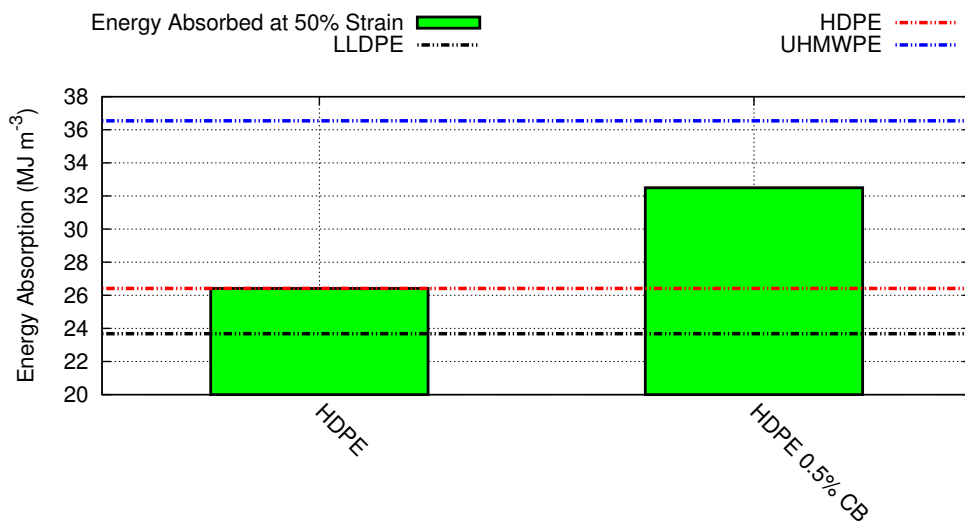


FIGURE 7.45: ODW energy absorption at 50% strain of HDPE nanocomposites.

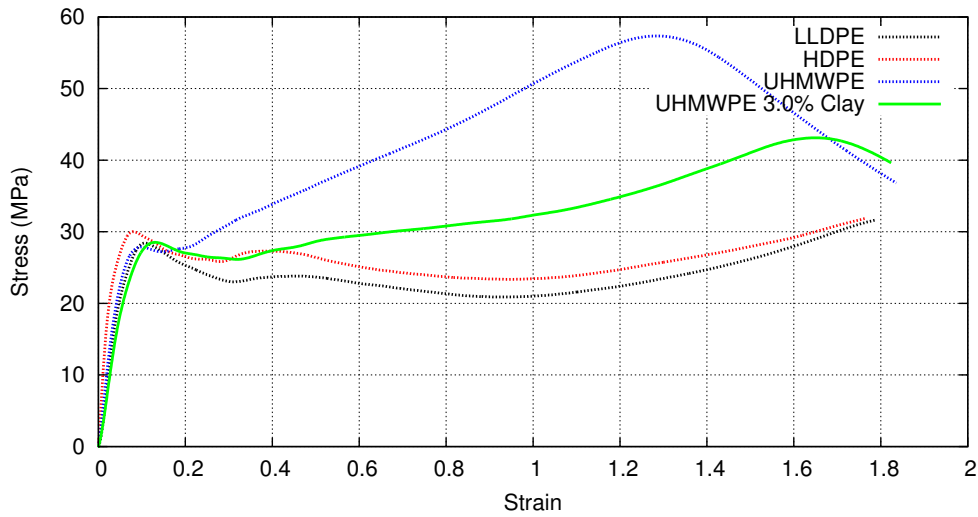


FIGURE 7.46: *ODW true stress/strain curves for UHMWPE nanocomposites.*

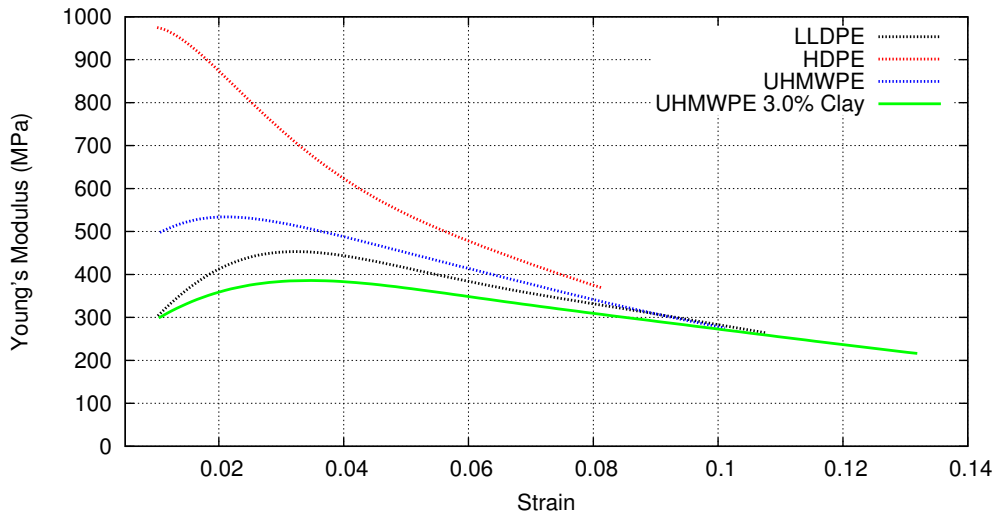


FIGURE 7.47: *ODW Young's modulus evolution for UHMWPE nanocomposites.*

7.2.1.3 UHMWPE nanocomposites

From Figure 7.46, the addition of nanoclay to UHMWPE appears to cause a significant reduction of the strain hardening effect, which results in a reduction in the energy absorption of the material.

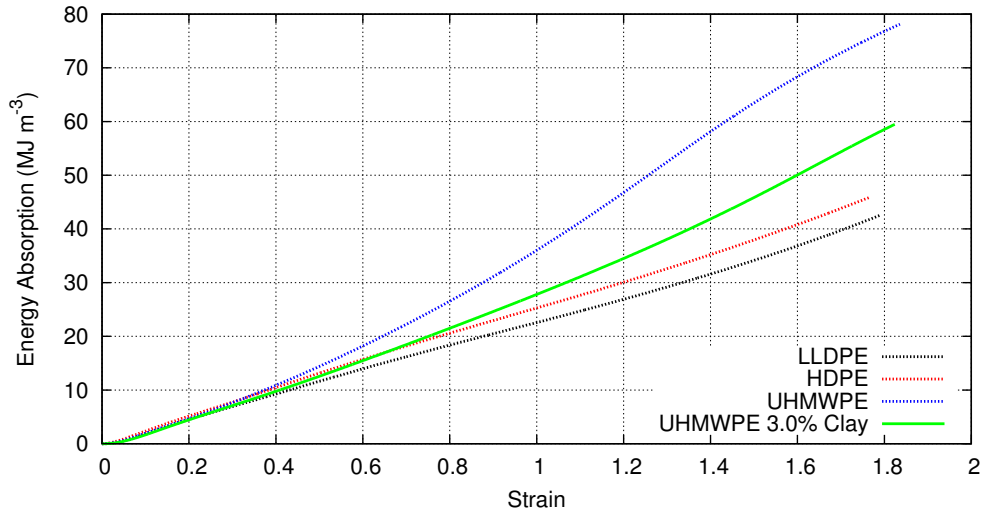


FIGURE 7.48: ODW energy absorption for UHMWPE nanocomposites.

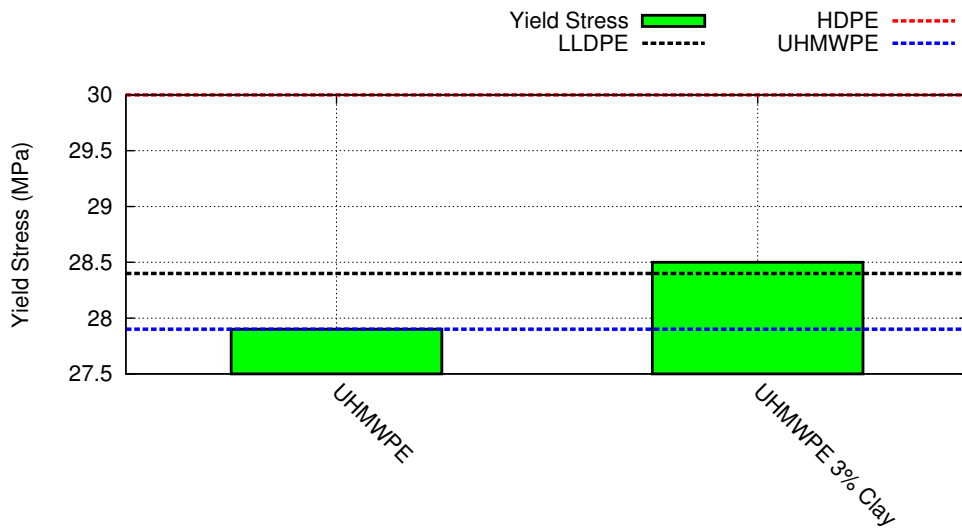


FIGURE 7.49: ODW yield strengths of UHMWPE nanocomposites.

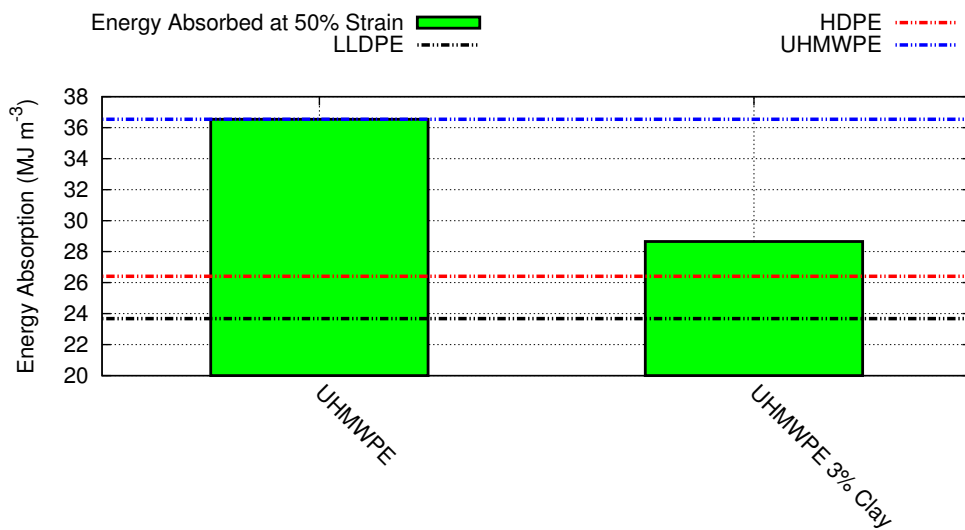


FIGURE 7.50: ODW energy absorption at 50% strain of UHMWPE nanocomposites.

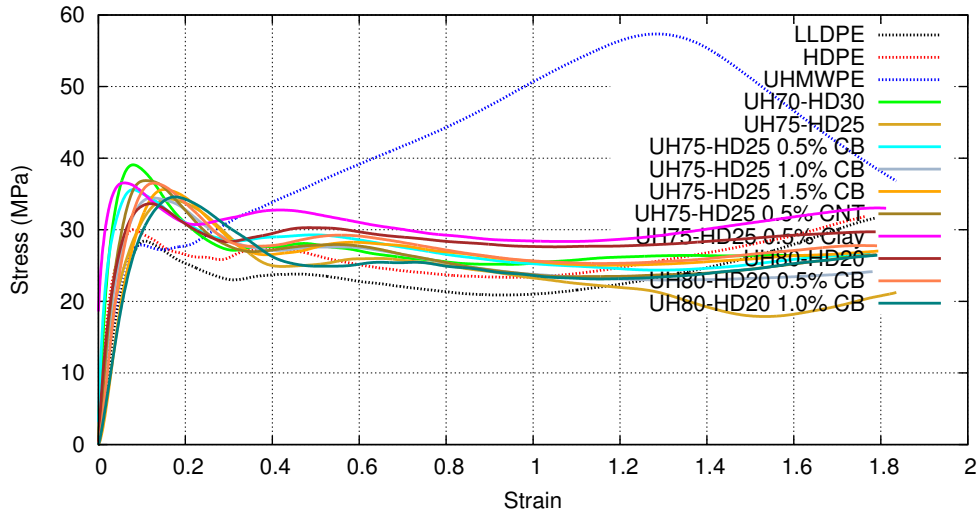


FIGURE 7.51: ODW true stress/strain curves for PE blends and nanocomposites.

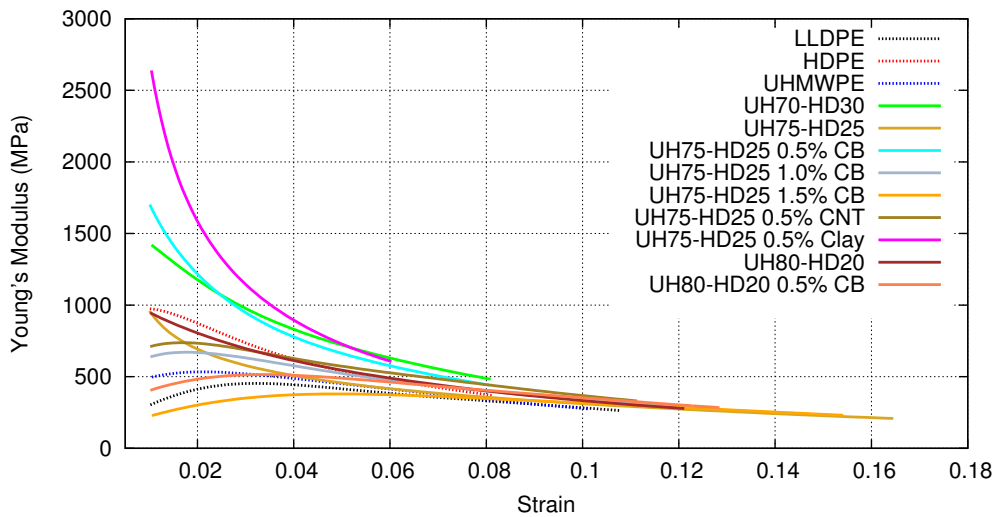


FIGURE 7.52: ODW Young's modulus evolution for PE blends and nanocomposites.

7.2.1.4 PE blends and nanocomposites

As with the SHPB experiments, each of the blended materials has an increase in yield strength over the monolithic polymers, regardless of the type of nano-reinforcement. Strain hardening is minimal, so the energy absorption of the blends still doesn't compete with monolithic UHMWPE.

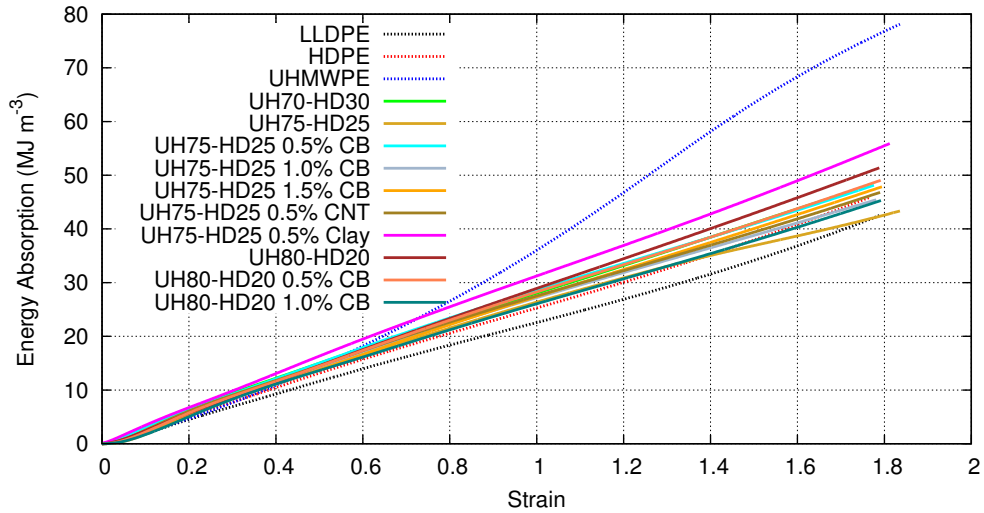


FIGURE 7.53: ODW energy absorption for PE blends and nanocomposites.

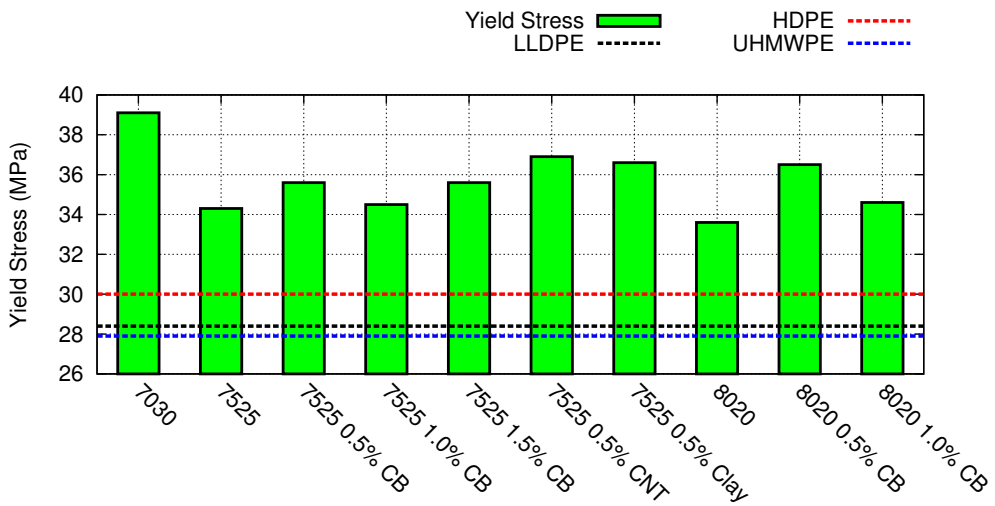


FIGURE 7.54: ODW yield strengths of PE blends and nanocomposites.

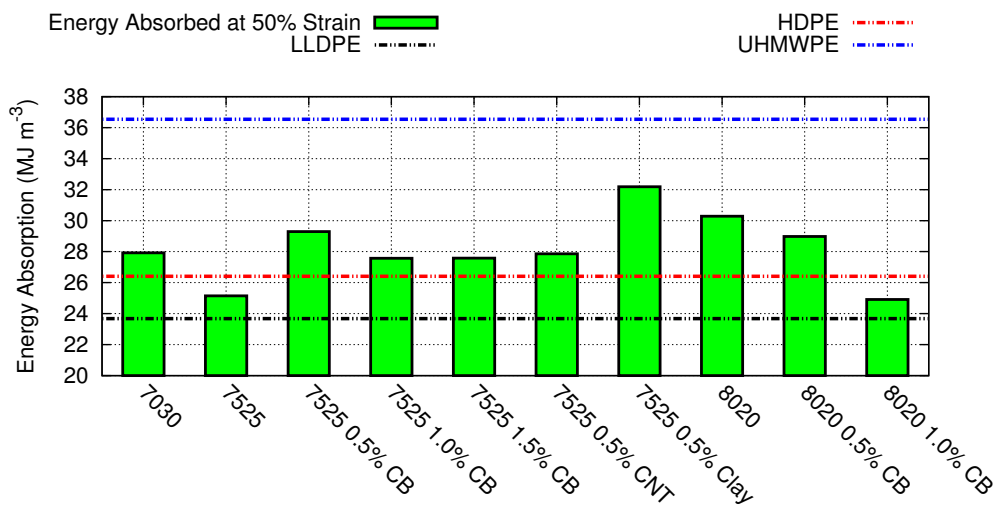


FIGURE 7.55: ODW energy absorption at 50% strain of PE blends and nanocomposites.

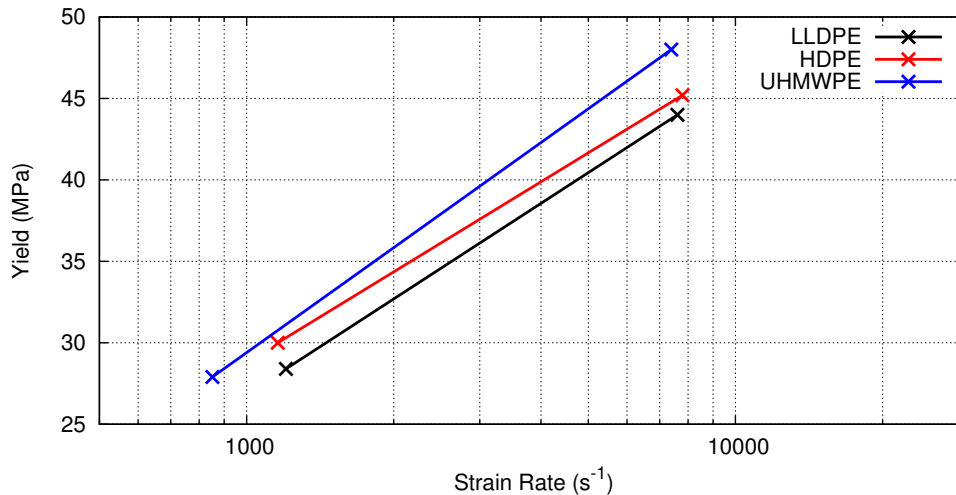


FIGURE 7.56: Yield strength by strain rate for pure PE matrices.

7.3 Strain rate dependence

7.3.1 Yield strength

It is well known that materials tend to behave differently at higher strain rates. The expected behaviour of the PE materials tested here was that their relative yield strengths would increase at higher rates. In theory then, with the SHPB operating at a higher rate to the ODW, yield for materials tested in the latter should be lower. Figures 7.56, 7.57, 7.58, 7.59 and 7.60 show the yield strength by strain rate for each PE-based material tested^c. The points with the lower strain rates, i.e. those on the left-hand-side of the graphs, are the results taken with the ODW. As expected the SHPB produced higher yields, on average 60% higher than the ODW results.

Two thirds of the materials exhibit a yield strength within 10% of the mean value, and all but two^d are within 15%.

The spread of strain rates is $852 - 1591 \text{ s}^{-1}$ for the ODW and $5564 - 10301 \text{ s}^{-1}$ for the SHPB, with averages of 1284 s^{-1} and 7726 s^{-1} respectively.

^cN.B. Where there is only one point for a particular material, it has only been examined in one experiment.

^dThe UH70-HD30 blend as tested on the ODW, being 120% of the mean, and the LLDPE with 0.5% CB - also from the ODW - which was 66% of mean.

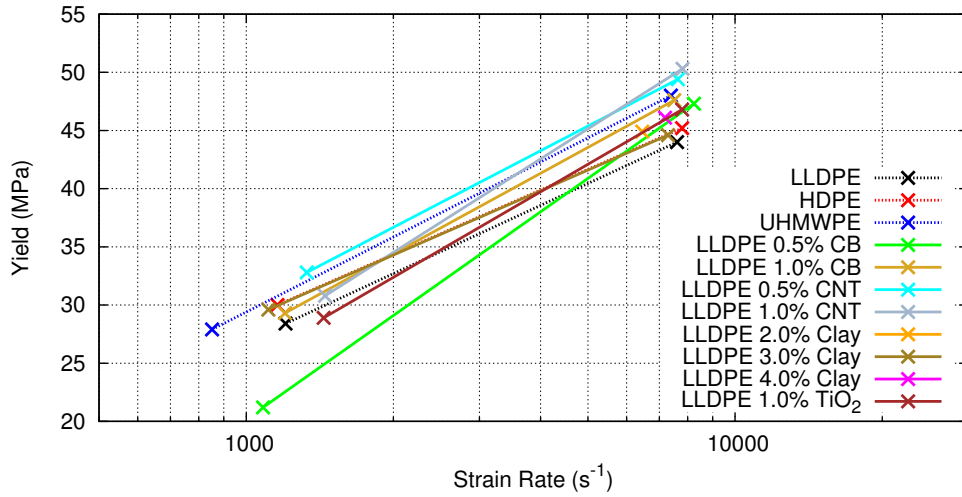


FIGURE 7.57: Yield strength by strain rate for LLDPE nanocomposites.

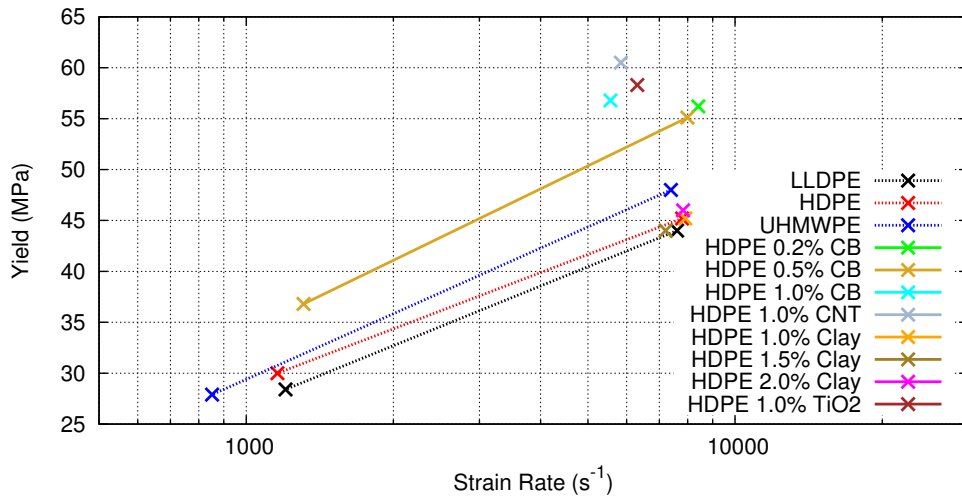


FIGURE 7.58: Yield strength by strain rate for HDPE nanocomposites.

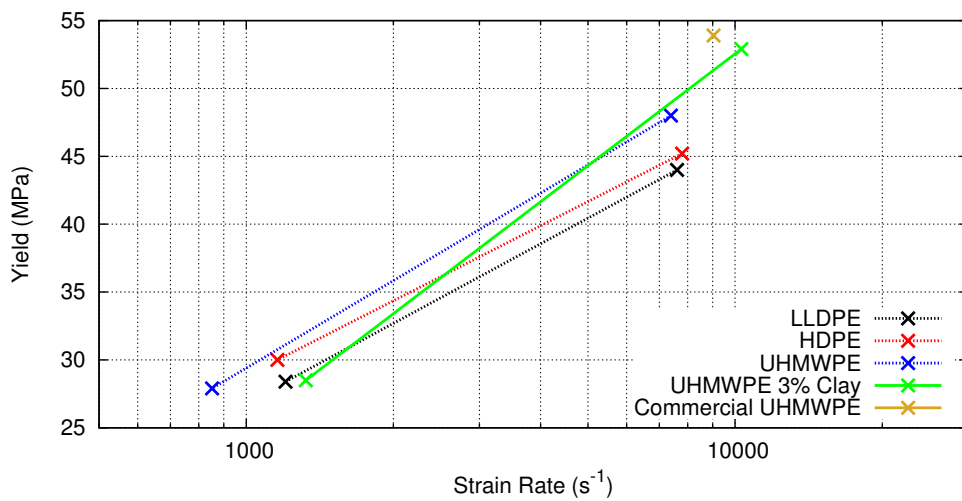


FIGURE 7.59: Yield strength by strain rate for UHMWPE nanocomposites.

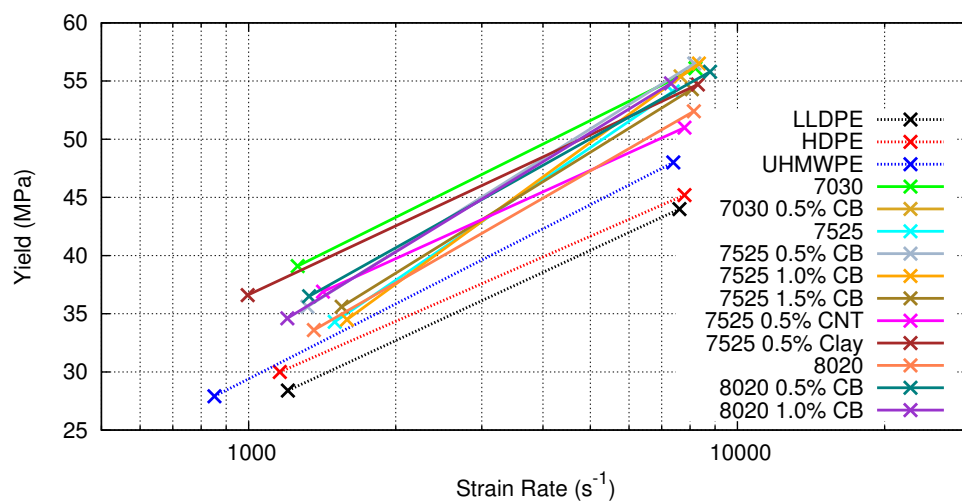


FIGURE 7.60: Yield strength by strain rate for PE blends and nanocomposites.

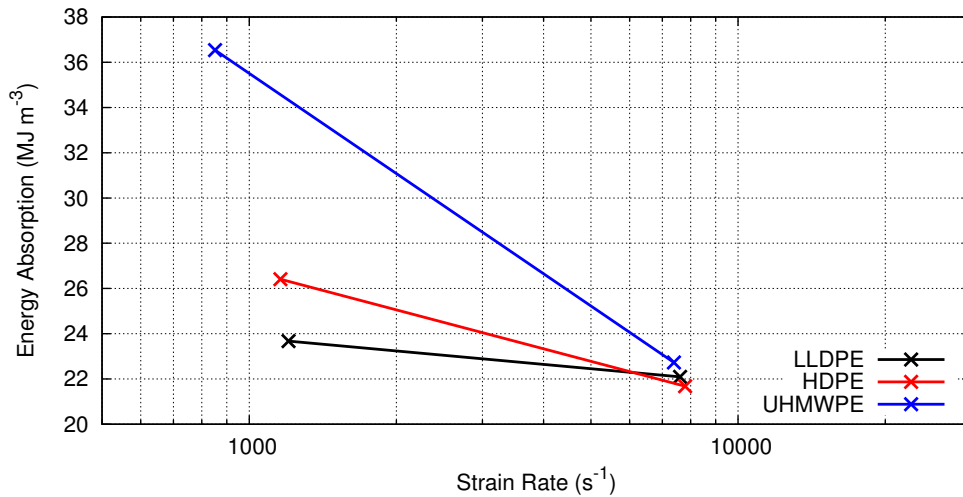


FIGURE 7.61: Energy absorption by strain rate for pure PE matrices.

7.3.2 Energy absorption

Figures 7.61, 7.62, 7.63, 7.64 and 7.65 show the energy absorption at 50% strain by strain rate.

For the most part, energy absorption for the materials presented here shows a slight downward trend at higher strain rates. At first glance this appears counter intuitive. Since the yield strength increases at high rates of strain, it would seem sensible to assume that the continuing deformation of the specimen also requires more energy. It is thought that the lower energy absorption may be attributed to the temperature increase in the specimens, softening them. Since almost all of the deformation energy is converted to specimen heat in SHPB experiments, they must get quite soft during an experiment. ODW experiments operate at a lower strain rate, allowing more time for the specimen to transfer its gained temperature into the surrounding system, so they may experience less softening allowing them to absorb more energy during deformation. Since there is no known research on the increase in specimen temperature in ODW experiments, this is a speculative answer.

Similar to the yield strengths above, with the SHPB experiments over two-thirds of the materials exhibit an energy absorption at 50% strain of within 10% of the mean value, with all being within 15%. The scatter from ODW experiments is greater, with slightly under two-thirds of the results being within 10% of mean, but only three-quarters are within 15%.

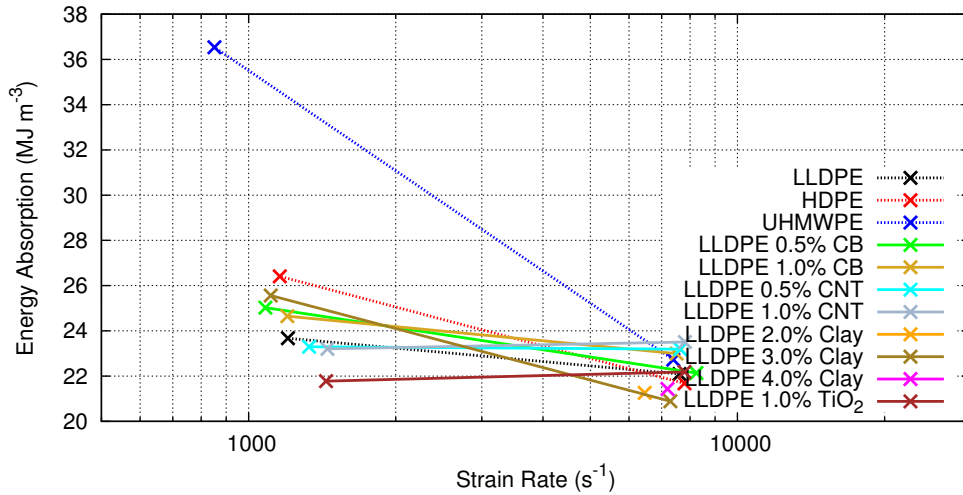


FIGURE 7.62: Energy absorption by strain rate for LLDPE nanocomposites.

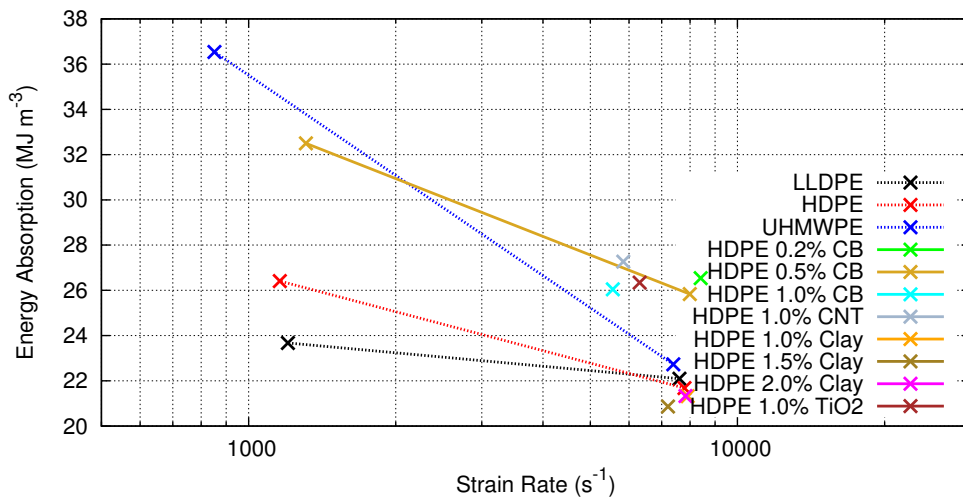


FIGURE 7.63: Energy absorption by strain rate for HDPE nanocomposites.

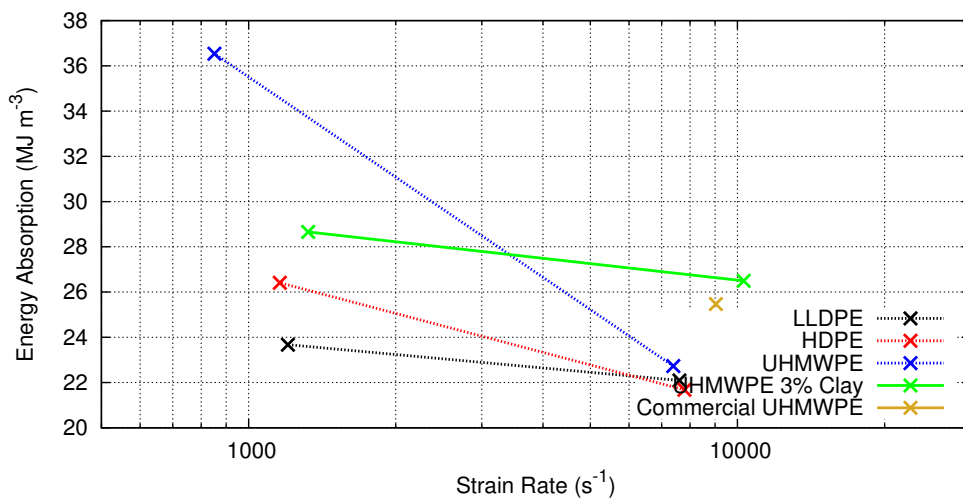


FIGURE 7.64: Energy absorption by strain rate for UHMWPE nanocomposites.

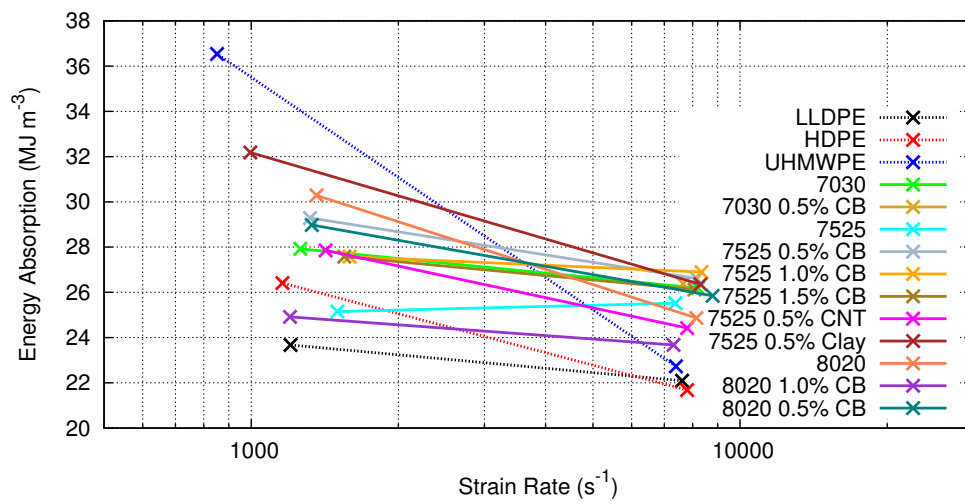


FIGURE 7.65: Energy absorption by strain rate for PE blends and nanocomposites.

Conclusions

“Traditional scientific method has always been, at the very best, 20-20 hindsight. It’s good for seeing where you’ve been. It’s good for testing the truth of what you think you know, but it can’t tell you where you ought to go.”

—ROBERT M. PIRSIG

ZEN AND THE ART OF MOTORCYCLE MAINTENANCE

In this work, a number of modifications were made to the standard split-Hopkinson pressure bar system, in order to improve its general use and to optimise it for use with low density polymer specimens. These modifications were very successful and have provided Loughborough University with an SHPB system which is, in the author’s opinion, a world leading tool for the investigation of polymeric materials at high rates of strain, with none of the down sides of some alternative techniques. The various computer programs written have proved to be invaluable in the rapid analysis of recorded data.

As to the grand question of whether the reinforcement of polyethylene matrices with small quantities of nanomaterials would improve their mechanical behaviour, the answer would appear to be “probably not”. The ostensible patterns of improvements to that were seen in LLDPE nanocomposites as tested in the SHPB, were not repeated in other materials or when tested in the ODW. Given the narrow spread of yield strengths observed in both SHPB and ODW experiments, a scatter which could be explained by ordinary experimental dispersal, it would appear that the yield strength is not greatly affected by the addition of small quantities of nanofillers into a polyethylene matrix. The same may be said for the energy absorption of the materials. None of the experiments carried out showed any sort of trend for any additive, in other words, the nanofillers had no noticeable effect. That given, it would seem that composites with small percentages of nano-reinforcements do not perform any differently from the monolithic matrix.

Commonplace composites such as glass or carbon fibre reinforced plastics typically use reinforcement to matrix ratios of 30-60% by weight in order to develop high compressive and tensile strengths. The specific mechanical properties of

nanomaterials are derived from their size. Graphene, for example, is strong because the carbon-carbon covalent bonding within the lattice is very strong. Being a single atomic layer, this gives graphene a high tensile strength in two dimensions. Graphite on the other hand, in which multiple layers of graphene are held together by much weaker electrostatic forces, loses the strength of graphene as the layers can easily slide over one another. In order to use graphene (or fully exfoliated nanoclays as was the intention in this work) as a composite reinforcement requires that the individual layers are kept a suitable distance from each other as the clumping together of layers would result in the formation of weak graphite.

The same can be said for CNTs. While they have a very high tensile strength in one dimension, ropes constructed from long CNTs would be of little use since they would simply slide over one another, becoming frayed and falling apart easily. Again, the individual tubes must remain separated.

As for carbon black, it is the opinion of the author that if they were used in large enough quantities, they could increase the elasticity of composites, but they have little or no effect on strength^a.

Nano-reinforcements, therefore, can only be employed in very small quantities, which ultimately has very little effect on the mechanical behaviour of their composite bulk. That said, no work was done to analyse the strength of nanocomposites with large reinforcement to matrix ratios, and this work should not be considered complete without such a comparison.

One area of interest which has been highlighted by this research is that of composites composed of different types of polyethylene chains. In both SHPB and ODW experiments, these PE blends showed an increase in yield strength and energy absorption at 50% strain, with or without nano-reinforcement. From the viewpoint of materials processing, blended PE composites may have a reduced molten viscosity which can make for easier processing. From a financial point of view, UHMWPE is significantly more expensive than either LLDPE or HDPE, and blended composites could provide for a considerably cheaper material.

Although it would appear that nanocomposites are not suitable for use in armour systems, the polyethylene blends could be an exciting new material in the production of, for example, spun fibres such as the ones used for Dyneema. Using them, it could be possible to produce a stronger material which is actually cheaper and simpler to produce.

For the protection of vehicles, polyurea in the form of Line-X spray coatings have already proven effective in capturing spall. The PUr nanocomposites that were made available for testing proved inconclusive. While the addition of 1%/wt of nanoclay appeared to increase the mechanical properties somewhat, the 2% and 3% materials had little effect. It is understandable that a certain amount of nanofiller could give positive benefits, but increasing the quantity could remove these benefits due to the clumping together of the fillers. If this was the case here, however, it would seem sensible for the nanocomposite to weaken further with increased quantities of fillers. With the PUr tests, the 2% and 3% materials had

^aConsider a relatively hard but ultimately ductile matrix filled with tiny rubber balls as a reinforcement. While they would do little to increase the strength of the composite, the overall mechanical behaviour of it would attain some of the rubber balls' elasticity.

mechanical properties which are barely discernible, and so it seems that this does not explain the situation here.

Since PUr is applied in the form of a spray coating, picking up air on its path from the spray gun to the substrate and forming bubbles in the deposited coating, its texture is similar to a dense foam. It is therefore inhomogeneous, and this is thought to be the primary reason behind the apparent increase in mechanical properties from the tests performed here.

The PX3550 PUr tested here proved to be a remarkable material. Having a higher yield strength and Young's modulus, and significantly greater energy absorption than any of the PE-based materials tested, this could make for a very interesting material in the development of new armours. Although the adhesion of PUr was not tested, qualitatively it appeared to be reasonable when applied to a steel or aluminium substrate, on a par with the elastomer backing put onto the plaster of Paris simulants discussed in Chapter 4, *Understanding armour*.

8.1 Recommendations for further investigation

For the sake of completeness, the author would like to see research performed on the mechanical behaviour of nanocomposites with high reinforcement to matrix ratios. Although it is not thought that they will work particularly well, they may prove to have some novel properties.

An obvious piece of further research, would be a test to see how well polyethylene blends could be turned into spun fibres in a spinneret. This should be tested alongside a competing product, Dyneema or Spectra, in realistic ballistic tests, to understand how they behave in a real world scenario.

Although in SHPB experiments it seems that the majority of deformation energy is converted to heat in the specimen, there is no known research on specimen temperature increases in ODW experiments.

From Section 4, *Understanding armour*, it would be extremely interesting to attempt to scale up the constructed simulants using actual armour materials and subject them to realistic projectile impacts. If the realistic materials proved to behave as predicted by the simulant test method, it could prove to be an invaluable technique, allowing for truly affordable *blue-sky* experimentation in a traditionally expensive field.

Part IV

Bibliography

Bibliography

- [A to Z of Materials, 2001a] A to Z of Materials (2001a). High density polyethylene - hdpe. <http://www.azom.com/article.aspx?ArticleID=421>. Accessed: January 2013.
- [A to Z of Materials, 2001b] A to Z of Materials (2001b). Linear low density polyethylene - lldpe. <http://www.azom.com/article.aspx?ArticleID=430>. Accessed: January 2013.
- [A to Z of Materials, 2001c] A to Z of Materials (2001c). Low density polyethylene - ldpe. <http://www.azom.com/article.aspx?ArticleID=428>. Accessed: January 2013.
- [A to Z of Materials, 2001d] A to Z of Materials (2001d). Ultra-high molecular weight polyethylene - uhmwpe. <http://www.azom.com/article.aspx?ArticleID=854>. Accessed: January 2013.
- [Al-Maliky, 1997] Al-Maliky, N. S. J. (1997). *Strain Rate Behaviour of Thermoplastic Polymers*. PhD thesis, Department of Physics, Loughborough University.
- [Andreev, 1991] Andreev, G. E. (1991). A review of the brazilian test for rock tensile strength determination. part i: calculation formula. *Min. Sci. Technol.*, 13:445–456.
- [AR500 Armor, 2013] AR500 Armor (2013). Welcome to ar500armor.com. <http://www.ar500armor.com/>. Accessed: April 2013.
- [Armored Mobility Inc., 2013] Armored Mobility Inc. (2013). Tac3s tactical plate. http://www.armoredmobility.com/products_tac3s.php. Accessed: April 2013.
- [Bacon, 1998] Bacon, C. (1998). An experimental method for considering dispersion and attenuation in a viscoelastic hopkinson bar. *Exp. Mech.*, 38(4):242–249.
- [Bashford, 2008] Bashford, D. (2008). *Helmets And Body Armor In Modern Warfare*. Read Books.
- [Blackmore, 1990] Blackmore, D. (1990). *Arms & Armour of the English Civil Wars*. The Trustees of the Royal Armouries.
- [Briscoe and Nosker, 1984] Briscoe, B. and Nosker, R. (1984). The influence of interfacial friction on the deformation of high density polyethylene in a split hopkinson pressure bar. *Wear*, 95(3):241 – 262.

- [Butterworth, 1930] Butterworth, S. (1930). On the theory of filter amplifiers. *Experimental Wireless and the Wireless Engineer*, 7:536–541.
- [Cannon, 2001] Cannon, L. (2001). Behind armour blunt trauma - an emerging problem. *J R Army Med Corps*, 147:87–96.
- [Casem et al., 2003] Casem, D., Fourney, W., and Chang, P. (2003). A polymeric split hopkinson pressure bar instrumented with velocity gages. *Experimental Mechanics*, 43(4):420–427.
- [Cashdollar and Zlochower, 2007] Cashdollar, K. L. and Zlochower, I. A. (2007). Explosion temperatures and pressures of metals and other elemental dust clouds. *J. Loss. Prevent. Proc.*, 20:337–348.
- [Chen and Song, 2011] Chen, W. and Song, B. (2011). *Split Hopkinson (Kolsky) Bar: Design, Testing and Applications*. Springer.
- [Chen et al., 1999] Chen, W., Zhang, B., and Forrestal, M. J. (1999). A split hopkinson bar technique for low-impedance materials. *Experimental Mechanics*, 39(2):81–85.
- [Corriveau et al., 2013] Corriveau, D., Tanguay, V., Harris, P., Laou, P., and Wong, F. (2013). Development of an automatic target engagement system for small-arms. In *27th International Symposium on Ballistics, Freiburg, Germany*.
- [Croft and Longhurst, 2007] Croft, J. and Longhurst, D. (2007). *HOSDB Body Armour Standards for UK Police (2007) Part 2: Ballistic Resistance*. Home Office Scientific Development Branch.
- [Davies, 1948] Davies, R. M. (1948). A critical study of the hopkinson pressure bar. *Phil. Trans. R. Soc. A*, 240, 821:375–457.
- [Dawson, 1993] Dawson, P. C. (1993). *The Mechanical and Thermal Behaviour of Polymers Under High Strain Rate Compression*. PhD thesis, Loughborough University, Department of Physics.
- [DE & S Joint Supply Chain, 2013] DE & S Joint Supply Chain (2013). Osprey mk 4 body armour: User care and assembly instructions. http://www.army.mod.uk/documents/general/20120215-0sprey_Mk4_Instruction_Booklet-R.pdf. Accessed: January 2013.
- [Dioh et al., 1995] Dioh, N. N., Ivankovic, A., Leever, P. S., , and Williams, J. G. (1995). Stress wave propagation effects in split hopkinson pressure bar tests. *Proc. R. Soc., A* 449:187–204.
- [Dunstan and Volstad, 1984] Dunstan, S. and Volstad, R. (1984). *Flak Jackets: 20th-century military body armour*. Osprey Publishing.
- [DuPont, 2013] DuPont (2013). Technical guide: Kevlar aramid fiber. http://www2.dupont.com/Kevlar/en_US/assets/downloads/KEVLAR_Technical_Guide.pdf. Accessed: April 2013.

- [Durmuş et al., 2007] Durmuş, A., Woo, M., Kaşgöz, A., Macosko, C. W., and Tsapatsis, M. (2007). Intercalated linear low density polyethylene (lldpe)/clay nanocomposites prepared with oxidized polyethylene as a new type compatibilizer: Structural, mechanical and barrier properties. *European Polymer Journal*, 43(9):3737 – 3749.
- [Ellwood et al., 1982] Ellwood, S., Griffiths, L. J., and Parry, D. J. (1982). A tensile technique for materials testing at high strain rates. *J. Phys. E:Sci. Instrum.*, 15:1169–1172.
- [Eskandari and Nemes, 2000] Eskandari, H. and Nemes, J. A. (2000). Dynamic testing of composite laminates with a tensile split hopkinson bar. *J. Compos. Mater.*, 34:260–273.
- [Gabriel, 2007] Gabriel, R. A. (2007). *The Ancient World: Soldiers' Lives Through History*. Greenwood Publishing Group.
- [Ghosh, 2009] Ghosh, A. K. (2009). *Introduction to Measurements and Instrumentation*. PHI Learning.
- [GlobalSecurity.org, 2011] GlobalSecurity.org (2011). Body armor history. <http://www.globalsecurity.org/military/systems/ground/body-armor2.htm>. Accessed: April 2013.
- [Grantham et al., 2004] Grantham, S. G., Siviour, C. R., Proud, W. G., and Field, J. E. (2004). High-strain rate brazilian testing of an explosive simulant using speckle metrology. *Meas. Sci. Technol.*, 15:1867–1870.
- [Gray et al., 1997] Gray, G., Blumenthal, W., Trujillo, W., and Carpenter, R. (1997). Influence of temperature and strain rate on the mechanical behaviour of adiprene I-100. *J. Phys. (France) IV Colloq. C3 (EURODYMAT 97)*, 7:523–528.
- [Hamdan, 1994] Hamdan, S. (1994). *The Thermomechanical Properties of Aromatic Polymers*. PhD thesis, Loughborough University, Department of Physics.
- [Holcomb et al., 2007] Holcomb, J. B., McMullin, N. R., Pearse, L., Caruso, J., Wade, C. E., Oetjen-Gerdes, L., Champion, H. R., Lawnick, M., Farr, W., Rodriguez, S., and Butler, F. K. (2007). Causes of death in u.s. special operations forces in the global war on terrorism. *Ann. Surg.*, 245(6):986–991.
- [Hopkinson, 1914] Hopkinson, B. (1914). A method of measuring the pressure produced in the detonation of high explosives or by the impact of bullets. *Philos. Trans. R. Soc. (London) A*, 213:437–456.
- [Hughes et al., 2013] Hughes, F., Prudom, A., and Swallowe, G. (2013). The high strain-rate behaviour of three molecular weights of polyethylene examined with a magnesium alloy split-hopkinson pressure bar. *Polym. Test.*, 32(5):827 – 834.
- [James, 2003] James, L. (2003). *Warrior Race: A History of the British at War*. St. Martin's Press.
- [Kapoor and Nemat-Nasser, 1998] Kapoor, R. and Nemat-Nasser, S. (1998). Determination of temperature rise during high strain rate deformation. *Mech. Mater.*, 27:1–12.

- [Kolsky, 1949] Kolsky, H. (1949). An investigation of the mechanical properties of materials at very high rates of loading. *Proc. Phys. Soc. London*, B 62:676.
- [Lechner et al., 2005] Lechner, M. D., Martienssen, W., and Warlimont, H., editors (2005). *Springer Handbook of Condensed Matter and Materials Data*. Springer.
- [LINE-X.com, 2010] LINE-X.com (2010). Military applications - paxcon. <http://www.linex.com/pages/2010/military/>. Accessed: April 2013.
- [Midwest Armor & Strategic Solutions, 2013] Midwest Armor & Strategic Solutions (2013). Mass iii. <http://midwestarmor.com/Midwest%20Armor%20MASS%20III%20Body%20Armor%20Torso%20Plate.aspx>. Accessed: April 2013.
- [Miller, 2003] Miller, D. (2003). *Illustrated Directory of 20th Century Guns*. Zenith Imprint.
- [Mitsubishi Chemical Corporation, 2006] Mitsubishi Chemical Corporation (2006). What is carbon black? <http://www.carbonblack.jp/en/cb/index.html>. Accessed: April 2013.
- [Nemat-Nasser, 2000] Nemat-Nasser, S. (2000). *ASM Handbook Volume 8: Mechanical Testing and Evaluation*, chapter Introduction to High Strain Rate Testing. ASM International.
- [Nicholson, 2003] Nicholson, H. J. (2003). *Medieval Warfare: Theory and Practice of War in Europe, 300-1500*. Palgrave Macmillan.
- [Novoselov, 2011] Novoselov, K. S. (2011). Nobel lecture: Graphene: Materials in the flatland. *Rev. Mod. Phys.*, 83:837–849.
- [Otsu, 1975] Otsu, N. (1975). A threshold selection method from gray-level histograms. *Automatica*, 11(285-296):23–27.
- [Parry et al., 1994] Parry, D. J., Dixon, P. R., Hodson, S., and Al-Maliky, N. (1994). Stress equilibrium effects with hopkinson bar specimens. *J. Phys. IV*, 4 (C8):107–112.
- [Parry and Griffiths, 1979] Parry, D. J. and Griffiths, L. J. (1979). A compact gas gun for materials testing. *J. Phys. E: Sci. Instrum.*, 12:56–58.
- [Parry et al., 1995] Parry, D. J., Walker, A. G., and Dixon, P. R. (1995). Hopkinson bar pulse smoothing. *Meas. Sci. Technol*, 6:443–446.
- [Patrick, 1989] Patrick, U. W. (1989). *Handgun Wounding Factors and Effectiveness*. Firearms Training Unit, FBI Academy.
- [Prudom, 2012] Prudom, A. J. (2012). *Performance of Multi-Component Polymers at High Strain Rates*. PhD thesis, Loughborough University.
- [Raza, 2012] Raza, H., editor (2012). *Graphene Nanoelectronics: Metrology, Synthesis, Properties and Applications*. Springer Berlin Heidelberg.
- [Robins, 1805] Robins, B. (1805). *New Principles of Gunnery*. F. Wingrave.

- [Rodriguez et al., 1994] Rodriguez, J., Navarro, C., and Sanchez-Galvez, V. (1994). Splitting tests: an alternative to determine the dynamic tensile strength of ceramic materials. *J. Phys. IV, Colloque C8*:101–106.
- [Samanta, 1971] Samanta, S. (1971). Dynamic deformation of aluminium and copper at elevated temperatures. *Journal of the Mechanics and Physics of Solids*, 19(3):117 – 135.
- [Sawas et al., 1998] Sawas, O., Brar, N. S., and Brockman, R. A. (1998). Dynamic characterization of compliant materials using an all-polymeric split hopkinson bar. *Exp. Mech.*, 38(3):204–210.
- [Selvin et al., 2003] Selvin, T. P., Kuruvilla, J., and Sabu, T. (2003). Mechanical properties of titanium dioxide-filled polystyrene microcomposites. *Mat. Lett.*, 58:281–289.
- [Serridge and Licht, 1987] Serridge, M. and Licht, T. R. (1987). *Piezoelectric Accelerometer and Vibration Preamplifier Handbook*. K Larson & Son A/S.
- [Shelke et al., 2010] Shelke, A., Khatavkar, K., Rane, N., and Patil, P., editors (2010). *The Bullet*. PediaPress.
- [Shergold et al., 2006] Shergold, O. A., Fleck, N. A., and Radford, D. (2006). The uniaxial stress versus strain response of pig skin and silicone rubber at low and high strain rates. *International Journal of Impact Engineering*, 32:1384–1402.
- [Sigma-Aldrich Co., 2013] Sigma-Aldrich Co. (2013). Products. <http://www.sigmaaldrich.com/catalog>. Accessed: April 2013.
- [Skinner, 1962] Skinner, A. (1962). Versatile high speed rotating mirror cameras. *J. Sci. Instrum.*, 39:336–343.
- [Song and Cai, 2012] Song, M. and Cai, D. (2012). *RSC Nanoscience & Nanotechnology No. 26: Polymer-Graphene Nanocomposites - Chapter 1: Graphene Functionalization: A Review*. Royal Society of Chemistry.
- [Sperling, 2005] Sperling, L. H. (2005). *Introduction to Physical Polymer Science*. Wiley-Interscience, 4 edition.
- [Stirling, 2012] Stirling, R. (2012). *SAS Ultimate Guide to Combat: How to Fight and Survive in Modern Warfare*. Osprey Publishing.
- [Swallowe et al., 1986] Swallowe, G. M., Field, J. E., and Horn, L. A. (1986). Measurements of transient high temperatures during the deformation of polymers. *J. Mater. Sci.*, 21:4089–4096.
- [Taylor, 1998] Taylor, P. (1998). *Behind The Mask: The IRA and Sinn Fein*. TV Books.
- [Tennent, 1971] Tennent, R. M., editor (1971). *Science Data Book*. Oliver & Boyd.
- [Tennent, 1864] Tennent, S. J. E. (1864). *The Story of the Guns*. Longman, Green, Longman, Roberts, & Green.
- [The Royal Swedish Academy of Sciences, 2010] The Royal Swedish Academy of Sciences (2010). Scientific background on the nobel prize in physics 2010: Graphene. Technical report.

- [Tokyo Measuring Instruments Laboratory Co., 2013] Tokyo Measuring Instruments Laboratory Co. (2013). F series leadwire integrated foil strain gauge. http://www.tml.jp/e/product/strain_gauge/gauge_list/flead_list.html. Accessed: March 2013.
- [U.S. Department of the Army, 2012] U.S. Department of the Army, editor (2012). *U.S. Army Improvised Munitions Handbook*. Skyhorse Publishing.
- [USNIJ, 2000] USNIJ (2000). Ballistic resistance of personal body armor. U.S. National Institute of Justice. Accessed September 2010 <http://www.ncjrs.gov/pdffiles1/nij/189633.pdf>.
- [Walley et al., 2009] Walley, S. M., Proud, W. G., Rae, P. J., and Field, J. E. (2009). The dynamic temperature measurement of split hopkinson bar specimens using small thermocouples and infrared streak photography. *DYMAT 2009*, pages 511–516.
- [Wang et al., 2009] Wang, X., Li, Q., Xie, J., Jin, Z., Wang, J., Li, Y., Jiang, K., and Fan, S. (2009). Fabrication of ultralong and electrically uniform single-walled carbon nanotubes on clean substrates. *Nano Lett.*, 9 (9):3137–3141.
- [Williams, 2003] Williams, A. (2003). *The Knight and the Blast Furnace: A History of the Metallurgy of Armour in the Middle Ages & the Early Modern Period*. Brill Academic Publishers.
- [Zaloga and Sarson, 1993] Zaloga, S. J. and Sarson, P. (1993). *M1 Abrams Main Battle Tank, 1982-92*. Osprey Publishing.
- [Zhao et al., 1997] Zhao, H., Gary, G., and Klepaczko, J. (1997). On the use of viscoelastic split hopkinson pressure bar. *Int. J. Impact Eng.*, 19:319–330.
- [Zukas, 1980] Zukas, J. A. (1980). Impact dynamics: Theory and experiment. Technical report, US Army Armament Research and Development Command, Ballistic Research Laboratory.

Part V

Publications

The high strain-rate behaviour of three molecular weights of polyethylene examined with a magnesium alloy split-Hopkinson pressure bar

Abstract

A traditional split-Hopkinson pressure bar system has been modified by the addition of ZK60A magnesium alloy pressure bars in order to increase the resolution of data when examining specimens of low-density, high-density and ultra-high molecular weight polyethylene. It was found that the low density of the ZK60A allowed a decent increase in transmitted pulse amplitude, whilst its relatively high yield strength afforded long-term reliability of the system. The accuracy of data obtained from the fitted strain gauges was verified with the use of a high-speed video camera, and was found to be an excellent match.

Authors

F. Hughes, A. Prudom, G. Swallowe

Analysis of the high strain-rate behaviour of polyethylene based nanocomposites

Abstract

Advanced polymeric materials and polymer based nanocomposites are finding an increasing range of industrial and defence applications. These materials have the potential to improve combat survivability, whilst reducing cost and weight. This study deals with nanocomposites manufactured from blends of low density polyethylene (LDPE) with various nanofillers. The high strain rate behaviour of these materials was investigated using the split Hopkinson pressure bar (SHPB) test. The experimental results for non-reinforced materials were used as a reference to analyse the effect of the nanofillers on the properties and performance of the nanocomposites. These results, together with those obtained from other mechanical tests, will be used as input into finite-element analyses to simulate the performance of these materials in lightweight armour applications. In the first step, the finite element model was validated by simulating the SHPB test and comparing the predicted results with those from the experiments. Explicit finite element analysis was used for the simulation. The fully developed model was able to demonstrate the behaviour of the test bar and specimen interaction correctly and reasonably good agreement between predicted and experimental results was observed.

Authors

Chandragupt Gorwade, Foz Hughes, Dongyu Cai, Ian Ashcroft, Vadim Silberschmidt, Gerry Swallowe, Mo Song, Steve Shaw.

Experimental and numerical analysis of stress wave propagation in polymers and the role of interfaces in armour systems

Abstract

Advanced polymeric materials are finding an increasing range of industrial and defence applications. These materials have the potential to improve combat survivability, whilst reducing the cost and weight of armour systems. In this paper the results from a split Hopkinson pressure bar (SHPB) test of a high density polyethylene (HDPE) sample involving multiple stress waves is discussed with aid of a finite element model of the test. It is seen that the phenomenon of impedance mismatch at interfaces plays an important role in the levels of stress and deformation seen in the sample. A multi-layer armour system is then investigated using the finite element model. This case study illustrates the role of impedance mismatch and interface engineering in the design and optimisation of armour solutions.

Authors

Chandragupt V. Gorwade, Ian A. Ashcroft , Vadim V. Silberschmidt, Foz T.R. Hughes, Gerry M. Swallowe

Part VI

Appendices

Low-pass filter GNU Octave code

The following code was written to clean SHPB data with a low-pass filter. It was written to be run in GNU Octave, if necessary however, converting it to run in MathWorks MatLab should be trivial.

For this script to work correctly in this form, data must exist in two comma-separated value (CSV) files, `incident.csv` and `transmitter.csv`. Each file should consist of two columns, the first being the sample time and the second being the recorded value.

The result of the script are two output CSV files, in this case called `incidentfiltered.csv` and `transmitterfiltered.csv`, each containing two columns; time, filtered signal.

```
1 % Sampling frequency in Hz
2 Fsam = 5000000;
3
4 % Nyquist frequency in Hz (=Fsam/2)
5 Fnyq = Fsam/2;
6
7 % Cut-off frequency of low-pass filter in Hz
8 Fc = 100000;
9
10 % Create a seventh-order Butterworth low-pass
11 [b,a]=butter(7, Fc/Fnyq);
12
13 % Load incident data file and filter
14 data = csvread("incident.csv");
15 time = data(:,1);
16 incident = filter(b,a,data(:,2));
17
18 % Load transmitter data file and filter
19 data = csvread("transmitter.csv");
20 transmitter = filter(b,a,data(:,2));
21
22 % Plot results
23 plot(time, [incident, transmitter]);
24
25 % Collate filtered data
26 outputi = [time, incident];
27 outputt = [time, transmitter];
28
29 % Write output to CSV files
```

A. LOW-PASS FILTER GNU OCTAVE CODE

```
30 csvwrite("incidentfiltered.csv", outputi);  
31 csvwrite("transmitterfiltered.csv", outputt);
```

Bézier smoothing C++ code

The following program was written to produce a Bézier representation of a two-column comma-separated-value file named `input.csv`, where the first column contains x and the second column the y values.

The number of Bézier steps, N , can be adjusted by changing the stepsize variable to the value $\frac{1}{N}$.

This program is written to be compiled with GCC, the GNU compiler collection.

```
1 #include <iostream>
2 #include <fstream>
3 #include <vector>
4 #include <stdlib.h>
5
6 using namespace std;
7
8 int throwerror(char* errorname)
9 {
10     cout << endl << "ERROR:" << endl << errorname << endl << endl;
11     exit(1);
12 }
13
14 int main()
15 {
16     vector<double> vectorX;
17     vector<double> vectorY;
18     vector<double> resultX;
19     vector<double> resultY;
20     vector<double> rawX;
21     vector<double> rawY;
22
23     vector<double> newX;
24     vector<double> newY;
25     vector<double> tempX;
26     vector<double> tempY;
27
28     double stepsize = 0.01;
29     double size, numpoints;
30     int counter = 0;
31     int iPos = 0;
```

```
32     string cLineInput;
33
34     ofstream outfile;
35     ifstream infile;
36
37     infile.open("input.csv");
38     if (!infile)
39     {
40         throwerror("Unable to open file.");
41     }
42
43     while(! infile.eof())
44     {
45         counter++;
46         vectorX.resize(counter);
47         vectorY.resize(counter);
48         getline(infile, cLineInput);
49         iPos=cLineInput.find(",");
50         vectorX[counter -1] = atof(cLineInput.substr(0, iPos).c_str())
51         ;
52         vectorY[counter -1] = atof(cLineInput.substr(iPos +1).c_str())
53         ;
54     }
55     counter=0;
56
57     //initial population of main vector
58     size = vectorX.size();
59     newX.resize (size);
60     newY.resize (size);
61     for (int i = 0; i < size; i++)
62     {
63         newX[i] = vectorX[i];
64         newY[i] = vectorY[i];
65     }
66
67     //main loop
68     for (double i = 0.00; i <= 1.00; i+= stepsize)
69     {
70         //find bezier values
71         while (newX.size() > 0)
72         {
73             //resize tempX
74             tempX.resize (newX.size()-1);
75             tempY.resize (newY.size()-1);
76
77             //reduce bezier points
78             for (int j = 0; j < tempX.size(); j++)
79             {
80                 tempX[j] = newX[j] + ((newX[j+1] - newX[j]) * i);
81                 tempY[j] = newY[j] + ((newY[j+1] - newY[j]) * i);
82             }
83
84             //resize and repopulate newX
85             newX.resize (tempX.size());
86             newY.resize (tempY.size());
87             for (int k = 0; k <= tempX.size(); k++)
88             {
89                 newX[k] = tempX[k];
90                 newY[k] = tempY[k];
91             }
92         }
93     }
94 }
```

```

90     }
91
92     resultX.resize (counter +1);
93     resultY.resize (counter +1);
94
95     for (int k = 0; k <= newX.size(); k++)
96     {
97
98         resultX[counter] = newX[k];
99         resultY[counter] = newY[k];
100        counter++;
101    }
102
103    //repopulate temporary vector
104    newX.resize (size);
105    newY.resize (size);
106    for (int i = 0; i < size; i++)
107    {
108        newX[i] = vectorX[i];
109        newY[i] = vectorY[i];
110    }
111 }
112
113 outfile.open("results.csv");
114 for (int q = 0; q < (resultX.size() -20); q++)
115 {
116     outfile << resultX[q] << "," << resultY[q] << endl;
117 }
118
119 outfile.close();
120
121 cout << endl << "Finished." << endl;
122 return 0;
123 }

```


Polynomial fitting GNU Octave code

The following script was written to fit an n^{th} order polynomial to a dataset. It was designed to be run in GNU Octave, if necessary however, converting it to run in MathWorks MatLab should be trivial.

For this script to work correctly in this form, data must exist in a two-column comma-separated value (CSV) file named `incident.csv`. The first column should contain the x data, and the second column, the y .

The order of the polynomial calculated by adjusting the order variable.

The result of the script is an output CSV file, in this case called `poly.csv`, containing two columns; time and calculated value of polynomial curve.

```
1 order = 20;
2
3 %open input CSV file
4 data = csvread('input.csv');
5
6 %calculate best fit polynomials
7 p = polyfit (data(:,1), data(:,2), order);
8
9 %calculate individual y values
10 data(:,3) = zeros;
11 for i = 1:order
12     data(:,3) = data(:,3) + (data(:,1).^((order+1)-i) * p(i));
13 endfor
14 data(:,3) = data(:,3) + p(order+1);
15
16 %write data
17 csvwrite('poly.csv', [data(:,1), data(:,3)]);
```


Normalisation C++ code

The following program was written to calculate the average zero, and normalise a two-column comma-separated-value file named `input.csv`, where the first column contains x and the second column the y values, with the latter being the values to normalise.

The result of the program is a comma-separated value file containing the normalised values called `results.csv`.

This program is written to be compiled with GCC, the GNU compiler collection.

```
1 #include <iostream>
2 #include <fstream>
3 #include <sstream>
4 #include <stdio.h>
5 #include <stdlib.h>
6 #include <math.h>
7
8 using namespace std;
9
10 int throwerror(char* errorname)
11 {
12     cout << endl << "ERROR:" << endl << errorname << endl << endl;
13     exit(1);
14 }
15
16 int main ()
17 {
18     string cInFile = "input.csv";
19     string cOutFile = "results.csv";
20     string cLineInput, cTime;
21     int iPos, iCounter;
22     double dMax=0.00000, dMin=0.00000, dValue, dAverage, dTime
23         =0.00000;
24     ifstream InFile;
25
26     InFile.open (cInFile.c_str());
27
28     //Check the file can be opened, if not, return an error
29     if (!InFile)
```

```
30     {
31         throwerror("Unable to open file.");
32     }
33     //cout << "Input file " << cInFile << " opened" << endl << endl;
34
35     //Find maximum and minimum values in the data
36     while (! InFile.eof() )
37     {
38         getline (InFile,cLineInput);
39         iPos=cLineInput.find(",");
40         dValue = atof(cLineInput.substr(iPos +1).c_str());
41         if (dValue > dMax)
42         {
43             dMax = dValue;
44         }
45
46         if (dValue < dMin)
47         {
48             dMin = dValue;
49         }
50     }
51     InFile.close();
52
53     //Find average of first 500 records, ignoring peaks > 5% of
54     //maximum/minimum signal
55     iCounter = 0;
56     InFile.open (cInFile.c_str());
57     for (int i = 1; i < 501; i++)
58     {
59         getline (InFile,cLineInput);
60         iPos=cLineInput.find(",");
61         dValue = atof(cLineInput.substr(iPos +1).c_str());
62
63         //If data > max/20 or < min/20, skip (ignores peaks in first
64         //500 records)
65         if (dValue > dMax/20)
66         {
67             //Do nothing
68         }
69         else if (dValue < dMin/20)
70         {
71             //Do nothing
72         }
73         else
74         {
75             dAverage+=dValue;
76             iCounter++;
77         }
78     }
79
80     dAverage = dAverage / iCounter;
81
82     //Subtract average zero and write normalised file
83     InFile.open (cInFile.c_str());
84     ofstream OutFile;
85     OutFile.open (cOutFile.c_str());
86
87     while (! InFile.eof() )
```

```
88     {
89         getline (InFile,cLineInput);
90         iPos=cLineInput.find(",");
91         dTime = atof(cLineInput.substr(0, iPos).c_str());
92         dValue = atof(cLineInput.substr(iPos +1).c_str());
93         dValue -= dAverage;
94         OutFile << dTime << "," << dValue << "\n";
95     }
96
97     OutFile.close();
98     InFile.close();
99
100     cout << "Offset=" << dAverage << endl;
101
102 }
```


Pulse extraction C++ code

The following program was written to extract the incident, reflected and transmitted pulses from a pair of a two-column comma-separated-value files named `incident.csv` and `transmitter.csv`, where the first column contains x and the second column the y values.

It searches for pulses which are (as default) greater in length than 0.000075 s ($75\ \mu\text{s}$), but this value may be altered by changing the initial value of the variable `dPulseLength`.

The result of the program are three comma-separated value files containing the extracted pulses called `incidentpulse.csv`, `reflectedpulse.csv` and `transmittedpulse.csv`.

This program is written to be compiled with GCC, the GNU compiler collection.

```
1 #include <iostream>
2 #include <fstream>
3 #include <stdlib.h>
4 #include <cmath>
5
6 using namespace std;
7
8 int throwerror(char* errorname)
9 {
10     cout << endl << "ERROR:" << endl << errorname << endl << endl;
11     exit(1);
12 }
13
14 int main()
15 {
16     string cInFile, cPosOutFile, cNegOutFile, cLineInput;
17     int iCounter, iPos;
18     double dValue, dTime=0.00000;
19     double dPosStartTime=0.00000, dPosEndTime=0.00000, dNegStartTime
20         =0.00000, dNegEndTime=0.00000;
21     int iPosStart=0, iNegStart=0, iPosEnd=0, iNegEnd=0, iIncidentEnd
22         =0;
23
24     double dPulseLength = 0.000075;
```



```
23
24     dPosStartTime=0.00000;
25     dPosEndTime=0.00000;
26     dNegStartTime=0.00000;
27     dNegEndTime=0.00000;
28     iPosStart=0;
29     iNegStart=0;
30     iPosEnd=0;
31     iNegEnd=0;
32     iCounter=0;
33
34
35
36     ifstream InFile;
37
38     cInFile = "incident.csv";
39
40     //Open the normalised incident file
41     InFile.open (cInFile.c_str());
42
43     cout << "Finding pulses in " << cInFile << "... ";
44
45     //Find +ve peak (+ve value for at least 0.075ms)
46     while (! InFile.eof() )
47     {
48         iCounter++;
49         getline (InFile,cLineInput);
50         iPos=cLineInput.find(",");
51         //dTime = atof(cLineInput.substr(0, cLineInput.length() -
52             cLineInput.find(",")).c_str());
53
54         dTime = atof(cLineInput.substr(0, cLineInput.length() - (
55             cLineInput.length() - cLineInput.find(","))).c_str());
56
57         dValue = atof(cLineInput.substr(iPos +1).c_str());
58         dValue = pow(dValue,3);
59
60         if (dValue > 0)
61         {
62             if (dNegStartTime != 0 && dNegEndTime == 0)
63             {
64                 if (dTime - dNegStartTime > dPulseLength)
65                 {
66                     dNegEndTime = dTime;
67                     iNegEnd = iCounter;
68                 }
69                 else
70                 {
71                     dNegStartTime = 0;
72                     iNegStart = 0;
73                 }
74             }
75
76             if (dPosStartTime == 0)
77             {
78                 dPosStartTime = dTime;
79                 iPosStart = iCounter;
80             }
81         }
82     }
```

```

81     else if (dValue < 0)
82     {
83         if (dPosStartTime != 0 && dPosEndTime == 0)
84         {
85             if (dTime - dPosStartTime > dPulseLength)
86             {
87                 dPosEndTime = dTime;
88                 iPosEnd = iCounter;
89             }
90             else
91             {
92                 dPosStartTime = 0;
93                 iPosStart = 0;
94             }
95         }
96     }
97
98     if (dNegStartTime == 0)
99     {
100         dNegStartTime = dTime;
101         iNegStart = iCounter;
102     }
103
104 }
105 else
106 {
107     //Do nothing
108 }
109
110 }
111
112
113 InFile.close();
114
115 if (iPosEnd == 0)
116 {
117     throwerror("Unable to find positive pulse");
118 }
119
120 if (iNegEnd == 0)
121 {
122     throwerror("Unable to find negative pulse");
123 }
124
125 //Work out which is the incident and which the reflected pulse
126 if (iPosEnd < iNegEnd)
127 {
128     cPosOutFile = "incidentpulse.csv";
129     cNegOutFile = "reflectedpulse.csv";
130     iIncidentEnd = iPosEnd;
131 }
132 else
133 {
134     cPosOutFile = "reflectedpulse.csv";
135     cNegOutFile = "incidentpulse.csv";
136     iIncidentEnd = iNegEnd;
137 }
138 cout << "Done" << endl;
139
140 cout << "Extracting pulses from " << cInFile << "... ";

```

```
141     InFile.open (cInFile.c_str());
142     ofstream OutFile;
143     OutFile.open (cPosOutFile.c_str());
144     iCounter = 0;
145
146     while (! InFile.eof() )
147     {
148         iCounter++;
149         getline (InFile,cLineInput);
150         if (iCounter >= iPosStart && iCounter <= iPosEnd)
151         {
152             iPos=cLineInput.find(",");
153             dTime = atof(cLineInput.substr(0, cLineInput.length() - (
                cLineInput.length() - cLineInput.find(","))).c_str());
154
155             dValue = atof(cLineInput.substr(iPos +1).c_str());
156             dValue = pow(pow(dValue, 2), 0.5);
157             OutFile << dTime << "," << dValue << "\n";
158         }
159     }
160
161     InFile.close();
162     OutFile.close();
163
164     InFile.open (cInFile.c_str());
165     OutFile.open (cNegOutFile.c_str());
166     iCounter = 0;
167
168     while (! InFile.eof() )
169     {
170         iCounter++;
171         getline (InFile,cLineInput);
172         if (iCounter >= iNegStart && iCounter <= iNegEnd)
173         {
174             iPos=cLineInput.find(",");
175             dTime = atof(cLineInput.substr(0, cLineInput.length() -
                cLineInput.find(",")).c_str());
176             dValue = atof(cLineInput.substr(iPos +1).c_str());
177             dValue = pow(pow(dValue, 2), 0.5);
178             OutFile << dTime << "," << dValue << "\n";
179         }
180
181     }
182     InFile.close();
183     OutFile.close();
184
185     cout << "Done" << endl;
186
187
188
189
190
191
192
193
194
195
196
197
198
```

```

199     dPosStartTime=0.00000;
200     dPosEndTime=0.00000;
201     dNegStartTime=0.00000;
202     dNegEndTime=0.00000;
203     iPosStart=0;
204     iNegStart=0;
205     iPosEnd=0;
206     iNegEnd=0;
207     iCounter=0;
208
209     double dMax=0.00000, dMin=0.00000;
210     int iStart=0, iStop=0;
211
212
213
214     cInFile = "transmitter.csv";
215
216     //Open the normalised transmitter file
217     InFile.open (cInFile.c_str());
218
219     cout << "Finding pulses in " << cInFile << "... ";
220
221     //Find +ve peak (+ve value for at least 0.075ms which starts after
222         the end of the incident pulse)
223     while (! InFile.eof() )
224     {
225         iCounter++;
226         getline (InFile,cLineInput);
227         iPos=cLineInput.find(",");
228         dTime = atof(cLineInput.substr(0, cLineInput.length() -
229             cLineInput.find(",")).c_str());
230         dValue = atof(cLineInput.substr(iPos +1).c_str());
231         dValue = pow(dValue,3);
232
233         if (dValue > 0)
234         {
235             if (dNegStartTime != 0 && dNegEndTime == 0)
236             {
237                 if (dTime - dNegStartTime > dPulseLength)
238                 {
239                     dNegEndTime = dTime;
240                     iNegEnd = iCounter;
241                 }
242                 else
243                 {
244                     dNegStartTime = 0;
245                     iNegStart = 0;
246                 }
247             }
248             if (dPosStartTime == 0)
249             {
250                 dPosStartTime = dTime;
251                 iPosStart = iCounter;
252             }
253         }
254         else if (dValue < 0)
255         {
256

```

```
257         if (dPosStartTime != 0 && dPosEndTime == 0)
258         {
259             if (dTime - dPosStartTime > dPulseLength)
260             {
261                 dPosEndTime = dTime;
262                 iPosEnd = iCounter;
263             }
264             else
265             {
266                 dPosStartTime = 0;
267                 iPosStart = 0;
268             }
269         }
270     }
271
272     if (dNegStartTime == 0)
273     {
274         dNegStartTime = dTime;
275         iNegStart = iCounter;
276     }
277
278 }
279 else
280 {
281     //Do nothing
282 }
283
284 }
285
286
287 InFile.close();
288
289 if (iPosEnd == 0 && iNegEnd == 0)
290 {
291     throwerror("Unable to find transmitted pulse");
292 }
293
294
295
296 //Work out which is the transmitted pulse by finding the pulse
with the largest amplitude
297 InFile.open (cInFile.c_str());
298 iCounter=0;
299 while (! InFile.eof() )
300 {
301     iCounter++;
302     getline (InFile,cLineInput);
303     if (iCounter >= iPosStart && iCounter <= iPosEnd)
304     {
305         iPos=cLineInput.find(",");
306         dTime = atof(cLineInput.substr(0, cLineInput.length() -
307             cLineInput.find(",")).c_str());
308         dValue = atof(cLineInput.substr(iPos +1).c_str());
309
310         if (dValue > dMax)
311         {
312             dMax = dValue;
313             //cout << dMax;
314         }
315     }
316 }
```

```

315         if (iCounter >= iNegStart && iCounter <= iNegEnd)
316         {
317             iPos=cLineInput.find(",");
318             dTime = atof(cLineInput.substr(0, cLineInput.length() -
319                 cLineInput.find(",")).c_str());
320             dValue = atof(cLineInput.substr(iPos +1).c_str());
321
322             if (dValue < dMin)
323             {
324                 dMin = dValue;
325                 //cout << dMin;
326             }
327         }
328     }
329     InFile.close();
330
331     if (dMax > pow(pow(dMin, 2), 0.5))
332     {
333         iStart = iPosStart;
334         iStop = iPosEnd;
335     }
336     else
337     {
338         iStart = iNegStart;
339         iStop = iNegEnd;
340     }
341     cout << "Done" << endl;
342
343     //Extract transmitted pulse
344     cout << "Extracting pulses from " << cInFile << "... ";
345     InFile.open (cInFile.c_str());
346     OutFile.open ("transmittedpulse.csv");
347     iCounter = 0;
348
349     while (! InFile.eof() )
350     {
351
352         iCounter++;
353         getline (InFile,cLineInput);
354         if (iCounter >= iStart && iCounter <= iStop)
355         {
356             //if (cLineInput == "") {break;}
357             iPos=cLineInput.find(",");
358             dTime = atof(cLineInput.substr(0, iPos).c_str());
359             dValue = atof(cLineInput.substr(iPos +1).c_str());
360             dValue = abs (dValue);
361             OutFile << dTime << "," << dValue << endl;
362
363         }
364         if (iCounter > iStop)
365         {
366             break;
367         }
368     }
369
370     InFile.close();
371
372     OutFile.close();
373     cout << "Done" << endl; 0;

```

374 }

SHPB analysis C++ code

The following program was written to calculate stress-strain data from a pair of two-column comma-separated-value files named `reflectedpulse.csv` and `transmittedpulse.csv`, where the first column contains the time and the second column the measured voltage picked up from the strain gauges. After producing the stress/strain data, it calculates the representative Bézier curve.

The result of the program are two comma-separated value files containing the extracted pulses called `stress_strain.csv` and `bezier_stress_strain.csv`.

When run, it presents a menu which allows the user to choose from a list of the most common SHPB configurations presently used at Loughborough University, along with an additional option to customise the configuration.

This program is written to be compiled with GCC, the GNU compiler collection.

```
1 #include <iostream>
2 #include <fstream>
3 #include <stdlib.h>
4 #include <cmath>
5 #include <vector>
6
7 using namespace std;
8
9 int throwerror(char* errorname)
10 {
11     cout << endl << "ERROR:" << endl << errorname << endl << endl;
12     exit(1);
13 }
14
15 bool fexists(string filename)
16 {
17     ifstream infile(filename.c_str());
18     return infile;
19 }
20
21 int main()
22 {
23     //Show welcome screen
```



```

24     cout << "
           *****
           " << endl;
25     cout << "***                               SHPB data analyser
           ****" << endl;
26     cout << "
           *****
           " << endl;
27     cout << "*** Copyright 2012 Foz Hughes, Department of Physics,
           Loughborough University ***" << endl;
28     cout << "
           *****
           " << endl;
29     cout << endl;
30
31     //Find files matching FnnnnCH1.CSV and FnnnnCH2.csv
32     string cChannel1, cChannel2;
33
34     //Get settings for current experiment from user
35     int iUserInput;
36     double C0, E;
37     double IAmp, TAmp;
38     cout << "Please choose SHPB configuration for current experiment:"
           << endl << endl;
39     cout << "1. ZK60, no amplification" << endl;
40     cout << "2. ZK60, Incident bar amplified" << endl;
41     cout << "3. ZK60, Transmitter bar amplified" << endl;
42     cout << "4. ZK60, both bars amplified" << endl << endl;
43     cout << "5. Maraging steel, no amplification" << endl;
44     cout << "6. Maraging steel, Incident bar amplified" << endl;
45     cout << "7. Maraging steel, Transmitter bar amplified" << endl;
46     cout << "8. Maraging steel, both bars amplified" << endl << endl;
47     cout << "9. Other" << endl << endl;
48
49     cout << "Enter choice: ";
50     cin >> iUserInput;
51     cout << endl;
52
53     switch (iUserInput)
54     {
55         case 1:
56             cout << "ZK60, no amplification selected." << endl << endl
57                 ;
58             C0 = 4956; //Pressure bar sound speed (m/s)
59             E = 44600000000; //Young's modulus of pressure bar
60             IAmp = 1; //Incident bar amplification
61             TAmp = 1; //Transmitter bar amplification
62             break;
63         case 2:
64             cout << "ZK60, Incident bar amplified selected." << endl
65                 << endl;
66             C0 = 4956; //Pressure bar sound speed (m/s)
67             E = 44600000000; //Young's modulus of pressure bar
68             IAmp = 100; //Incident bar amplification
69             TAmp = 1; //Transmitter bar amplification
70             break;
71         case 3:
72             cout << "ZK60, Transmitter bar amplified selected." <<
73                 endl << endl;
74             C0 = 4956; //Pressure bar sound speed (m/s)

```

```

72         E = 44600000000; //Young's modulus of pressure bar
73         IAmp = 1; //Incident bar amplification
74         TAmp = 100; //Transmitter bar amplification
75         break;
76     case 4:
77         cout << "ZK60, both bars amplified selected." << endl <<
            endl;
78         C0 = 4956; //Pressure bar sound speed (m/s)
79         E = 44600000000; //Young's modulus of pressure bar
80         IAmp = 100; //Incident bar amplification
81         TAmp = 100; //Transmitter bar amplification
82         break;
83     case 5:
84         cout << "Maraging steel, no amplification selected." <<
            endl << endl;
85         C0 = 4936; //Pressure bar sound speed (m/s)
86         E = 187000000000; //Young's modulus of pressure
87         IAmp = 1; //Incident bar amplification
88         TAmp = 1; //Transmitter bar amplification
89         break;
90     case 6:
91         cout << "Maraging steel, Incident bar amplified selected."
            << endl << endl;
92         C0 = 4936; //Pressure bar sound speed (m/s)
93         E = 187000000000; //Young's modulus of pressure
94         IAmp = 100; //Incident bar amplification
95         TAmp = 1; //Transmitter bar amplification
96         break;
97     case 7:
98         cout << "Maraging steel, Transmitter bar amplified
            selected." << endl << endl;
99         C0 = 4936; //Pressure bar sound speed (m/s)
100        E = 187000000000; //Young's modulus of pressure
101        IAmp = 1; //Incident bar amplification
102        TAmp = 100; //Transmitter bar amplification
103        break;
104    case 8:
105        cout << "Maraging steel, both bars amplified selected." <<
            endl << endl;
106        C0 = 4936; //Pressure bar sound speed (m/s)
107        E = 187000000000; //Young's modulus of pressure
108        IAmp = 100; //Incident bar amplification
109        TAmp = 100; //Transmitter bar amplification
110        break;
111    case 9:
112        cout << "Enter speed of sound in pressure bar in m/s: ";
113        cin >> C0;
114        cout << "Enter Young's modulus of pressure bar in Pa: ";
115        cin >> E;
116        cout << "Incident amplification = ";
117        cin >> IAmp;
118        cout << "Transmitter amplification = ";
119        cin >> TAmp;
120        cout << endl;
121        break;
122    default:
123        throwerror("Invalid entry.");
124        break;
125 }
126

```

```
127     cout << "Speed of sound in pressure bar, C0=" << C0 << "m/s" <<
        endl;
128     cout << "Young's modulus of pressure bar, E=" << E << "Pa" << endl
        ;
129     cout << "Incident bar amplification, Ai=" << IAmp << endl;
130     cout << "Transmitter bar amplification, At=" << TAmp << endl <<
        endl;
131
132     double len1, len2, len3, L0;
133     double dia1, dia2, dia3, Ds;
134
135     cout << "Please enter three measurements of initial specimen
        length in mm:" << endl;
136     cout << "1st measurement: ";
137     cin >> len1;
138     cout << "2nd measurement: ";
139     cin >> len2;
140     cout << "3rd measurement: ";
141     cin >> len3;
142     L0 = (len1 + len2 + len3)/3;
143     cout << endl << "Average specimen length: " << L0 << "mm" << endl
        << endl;
144     L0 = L0/1000;
145
146     cout << "Please enter three measurements of initial specimen
        diameter in mm:" << endl;
147     cout << "1st measurement: ";
148     cin >> dia1;
149     cout << "2nd measurement: ";
150     cin >> dia2;
151     cout << "3rd measurement: ";
152     cin >> dia3;
153     Ds = (dia1 + dia2 + dia3)/3;
154     cout << endl << "Average specimen diameter: " << Ds << "mm" <<
        endl << endl;
155     Ds = Ds/1000;
156
157     int iSmooth;
158
159     //Extract data into incident.csv and transmitter.csv
160     string cLineInput;
161     int iPos;
162
163     cout << "Producing stress/strain curve... ";
164
165     //Declare and populate constants
166     double Pi = 3.1415926535;           //Pi
167
168     double Rb = 2200;                   //Ballast resistance (Ohms)
169     double Rs = 240;                   //Resistance of strain-gauge
        pair (Ohms)
170     double K = 2.15;                   //Gauge factor
171     double Vin = 50;                   //Power supply input voltage (
        V)
172     double D = 12.7;                   //Pressure bar diameter (mm)
173     double A = Pi * pow((D/2000),2); //Pressure bar surface area (m
        ^2)
174
175     //Experiment specific constants
176     double As = Pi * pow((Ds/2),2); //Initial specimen surface area
```

```

177     double dTime;
178
179     //File names
180     string cReflect      = "reflectedpulse.csv";
181     string cTransmit    = "transmittedpulse.csv";
182     string cOutFile     = "stress_strain.csv";
183
184     //Some variables
185     cLineInput = "";
186     double VoutT=0.00000, VoutI=0.00000, dVoutI=0.00000, dVoutT
           =0.00000, N=0.00000, epsilonR=0.00000, intepsilonR=0.00000,
           epsilonT=0.00000, dT=0.00000;
187     double engstress=0.00000, truestress=0.00000, engstrain=0.00000,
           truestrain=0.00000;
188     double trapesium=0.00000, oldstrain=0.00000, Q=0.00000;
189     iPos = 0;
190     dTime = 0.00000;
191
192     N = Rb/Rs;
193     Q = (pow((N+1), 2)) / (N * K);
194
195     //Open reflected and transmitted CSV files
196     ifstream reflect;
197     ifstream transmit;
198     ofstream OutFile;
199
200     reflect.open (cReflect.c_str());
201     transmit.open (cTransmit.c_str());
202
203     //Check the files can be opened, if not, return an error
204     if (!reflect)
205     {
206         throwerror("Unable to open Reflected data file.");
207     }
208
209     if (!transmit)
210     {
211         throwerror("Unable to open Transmitted data file.");
212     }
213
214     //Calculate time step
215     getline (reflect,cLineInput);
216     iPos=cLineInput.find(",");
217     dTime = atof(cLineInput.substr(0, cLineInput.length() - (
           cLineInput.length() - cLineInput.find(","))).c_str());
218     getline (reflect,cLineInput);
219     iPos=cLineInput.find(",");
220     dT = atof(cLineInput.substr(0, cLineInput.length() - (cLineInput.
           length() - cLineInput.find(","))).c_str()) - dTime;
221
222     //Close & re-open reflected signal file
223     reflect.close();
224     reflect.open (cReflect.c_str());
225
226     dTime = 0.00000;
227     int recordcount = 0;
228     while (! reflect.eof() | ! transmit.eof())
229     {
230         getline (reflect,cLineInput);
231         getline (transmit,cLineInput);

```

```
232     recordcount++;
233 }
234 reflect.close();
235 transmit.close();
236 reflect.open (cReflect.c_str());
237 transmit.open (cTransmit.c_str());
238
239 double AdTime[recordcount], Aengstrain[recordcount], Atruestrain[
    recordcount], Aengstress[recordcount], Atruestress[recordcount
    ];
240 recordcount = 0;
241
242 while (! reflect.eof() | ! transmit.eof())
243 {
244     //Get reflected signal
245     getline (reflect,cLineInput);
246     iPos=cLineInput.find(",");
247     dVoutI = VoutI;
248     VoutI = atof(cLineInput.substr(iPos +1).c_str());
249     VoutI = VoutI / IAmp;
250     dVoutI = VoutI - dVoutI;
251
252     //Convert to strain in pressure bar
253     oldstrain = epsilonR;
254     epsilonR = (Q/Vin) * VoutI;
255     trapesium = ((oldstrain + epsilonR) * dT) / 2;
256
257     //Convert to strain in specimen
258     intepsilonR += trapesium;
259
260     //engstrain = pow(pow((((-2 * C0) / L0) * intepsilonR), 2),
        0.5);
261     engstrain = ((2 * C0) / L0) * intepsilonR;
262
263     //Calculate true strain
264     truestrain = abs (log (1 - abs (engstrain)));
265
266     //Get transmitted signal
267     getline (transmit,cLineInput);
268     iPos=cLineInput.find(",");
269     dVoutT = VoutT;
270     VoutT = atof(cLineInput.substr(iPos +1).c_str());
271     VoutT = VoutT / TAMP;
272     dVoutT = VoutT - dVoutT;
273
274     //Convert to strain in pressure bar
275     epsilonT = (Q/Vin) * VoutT;
276
277     //Convert to stress on specimen
278     engstress = ((A/As)*E) * epsilonT;
279
280
281     //Calculate true stress
282     truestress = engstress * (1 - abs (truestrain));
283
284     //Write out results
285     dTime += dT;
286
287     AdTime[recordcount] = dTime;
288     Aengstrain[recordcount] = abs(engstrain);
```

```

289     Atruestrain[recordcount] = truestrain;
290     Aengstress[recordcount] = engstress;
291     Atruestress[recordcount] = truestress;
292     recordcount++;
293
294 }
295 cout << "Done" << endl;
296
297 cout << "Writing data... ";
298
299 int iArraysize;
300 iArraysize = sizeof AdTime/sizeof(double);
301
302 OutFile.open (cOutFile.c_str());
303 OutFile << "Time,Engineering Strain,True Strain,Engineering Stress
      ,True Stress" << endl;
304 OutFile << "0,0,0,0,0 \n";
305
306 //Write out the rest of the data
307 for (int i = 0; i < iArraysize; i++)
308 {
309     if (Atruestress[i] < 0)
310     {
311         break;
312     }
313 OutFile << AdTime[i] << "," << Aengstrain[i] << "," << Atruestrain
      [i] << "," << Aengstress[i] << "," << Atruestress[i] << endl;
314 }
315
316 OutFile.close();
317 reflect.close();
318 transmit.close();
319 cout << "Done" << endl;
320
321 cout << "Calculating Engineering stress/strain Bezier curve... ";
322
323 vector<double> vectorX;
324 vector<double> vectorY;
325
326 vector<double> newX;
327 vector<double> newY;
328 vector<double> tempX;
329 vector<double> tempY;
330
331 vector<double> vengstress;
332 vector<double> vengstrain;
333 vector<double> vtruestress;
334 vector<double> vtruestrain;
335
336 vector<double> vtimestress;
337 vector<double> vstress;
338 vector<double> vtimestrain;
339 vector<double> vstrain;
340
341 vector<double> vstrainrate;
342
343 double stepsize = 0.001;
344 double size, numpoints;
345 int anothercounter = 0;
346

```

```
347     //resize and populate vectorX and vectorY
348     vectorX.resize (iArraysize);
349     vectorY.resize (iArraysize);
350
351     for (int i = 0; i < iArraysize; i++)
352     {
353         vectorX[i] = Aengstrain[i];
354         vectorY[i] = Aengstress[i];
355     }
356
357     size = vectorX.size();
358
359     //initial population of temporary vector
360     newX.resize (size);
361     newY.resize (size);
362     for (int i = 0; i < size; i++)
363     {
364         newX[i] = vectorX[i];
365         newY[i] = vectorY[i];
366     }
367
368     //main loop
369     for (double i = 0.00; i <= 1.00; i+= stepsize)
370     {
371         //find bezier values
372         while (newX.size() >= 1)
373         {
374             //resize tempX
375             tempX.resize (newX.size()-1);
376             tempY.resize (newY.size()-1);
377
378             //reduce bezier points
379             for (int j = 0; j < tempX.size(); j++)
380             {
381                 tempX[j] = newX[j] + ((newX[j+1] - newX[j]) * i);
382                 tempY[j] = newY[j] + ((newY[j+1] - newY[j]) * i);
383             }
384             //resize and repopulate newX
385             newX.resize (tempX.size());
386             newY.resize (tempY.size());
387
388             for (int k = 0; k <= tempX.size(); k++)
389             {
390                 newX[k] = tempX[k];
391                 newY[k] = tempY[k];
392             }
393         }
394     }
395
396     //save in final vector
397     vengstress.resize (anothercounter + 1);
398     vengstrain.resize (anothercounter + 1);
399     vengstrain[anothercounter] = newX[0];
400     vengstress[anothercounter] = newY[0];
401     anothercounter++;
402
403     //repopulate temporary vector
404     newX.resize (size);
405     newY.resize (size);
406     for (int i = 0; i < size; i++)
```

```

407     {
408         newX[i] = vectorX[i];
409         newY[i] = vectorY[i];
410     }
411 }
412
413
414
415 cout << "Done" << endl;
416
417 cout << "Calculating True stress/strain Bezier curve... ";
418
419 stepsize = 0.001;
420 anothercounter = 0;
421
422 //resize and populate vectorX and vectorY
423 vectorX.resize (iArraysSize);
424 vectorY.resize (iArraysSize);
425
426 for (int i = 0; i < iArraysSize; i++)
427 {
428     vectorX[i] = Atruestrain[i];
429     vectorY[i] = Atruestress[i];
430 }
431
432 size = vectorX.size();
433
434 //initial population of temporary vector
435 newX.resize (size);
436 newY.resize (size);
437 for (int i = 0; i < size; i++)
438 {
439     newX[i] = vectorX[i];
440     newY[i] = vectorY[i];
441 }
442
443 //main loop
444 for (double i = 0.00; i <= 1.00; i+= stepsize)
445 {
446
447     //find bezier values
448     while (newX.size() >= 1)
449     {
450         //resize tempX
451         tempX.resize (newX.size()-1);
452         tempY.resize (newY.size()-1);
453
454         //reduce bezier points
455         for (int j = 0; j < tempX.size(); j++)
456         {
457             tempX[j] = newX[j] + ((newX[j+1] - newX[j]) * i);
458             tempY[j] = newY[j] + ((newY[j+1] - newY[j]) * i);
459
460         }
461
462         //resize and repopulate newX
463         newX.resize (tempX.size());
464         newY.resize (tempY.size());
465
466         for (int k = 0; k <= tempX.size(); k++)

```



```
467         {
468             newX[k] = tempX[k];
469             newY[k] = tempY[k];
470         }
471     }
472
473     //save in final vector
474     vtruestress.resize (anothercounter + 1);
475     vtrustrain.resize (anothercounter + 1);
476     vtrustrain[anothercounter] = newX[0];
477     vtruestress[anothercounter] = newY[0];
478     anothercounter++;
479
480     //repopulate temporary vector
481     newX.resize (size);
482     newY.resize (size);
483     for (int i = 0; i < size; i++)
484     {
485         newX[i] = vectorX[i];
486         newY[i] = vectorY[i];
487     }
488 }
489
490
491 cout << "Done" << endl;
492
493 cout << "Calculating Time Bezier curve... ";
494
495 stepsize = 0.001;
496 anothercounter = 0;
497
498 //resize and populate vectorX and vectorY
499 vectorX.resize (iArraysSize);
500 vectorY.resize (iArraysSize);
501
502 for (int i = 0; i < iArraysSize; i++)
503 {
504     vectorX[i] = AdTime[i];
505     vectorY[i] = Atruestress[i];
506 }
507
508 //return 0;
509
510 size = vectorX.size();
511
512 //initial population of temporary vector
513 newX.resize (size);
514 newY.resize (size);
515 for (int i = 0; i < size; i++)
516 {
517     newX[i] = vectorX[i];
518     newY[i] = vectorY[i];
519 }
520
521 //main loop
522 for (double i = 0.00; i <= 1.00; i+= stepsize)
523 {
524
525     //find bezier values
526     while (newX.size() >= 1)
```

```

527     {
528         //resize tempX
529         tempX.resize (newX.size()-1);
530         tempY.resize (newY.size()-1);
531
532         //reduce bezier points
533         for (int j = 0; j < tempX.size(); j++)
534         {
535             tempX[j] = newX[j] + ((newX[j+1] - newX[j]) * i);
536             tempY[j] = newY[j] + ((newY[j+1] - newY[j]) * i);
537
538         }
539         //resize and repopulate newX
540         newX.resize (tempX.size());
541         newY.resize (tempY.size());
542
543         for (int k = 0; k <= tempX.size(); k++)
544         {
545             newX[k] = tempX[k];
546             newY[k] = tempY[k];
547         }
548     }
549
550     //save in final vector
551     vtimestress.resize (anothercounter + 1);
552     vstress.resize (anothercounter + 1);
553     vtimestress[anothercounter] = newX[0];
554     vstress[anothercounter] = newY[0];
555     anothercounter++;
556
557     //repopulate temporary vector
558     newX.resize (size);
559     newY.resize (size);
560     for (int i = 0; i < size; i++)
561     {
562         newX[i] = vectorX[i];
563         newY[i] = vectorY[i];
564     }
565 }
566 cout << "Done" << endl;
567
568 cout << "Calculating true strain rates... ";
569 vstrainrate.resize (vtruestrain.size());
570 vstrainrate[0] = 0;
571 for (int i = 1; i < vtruestrain.size(); i++)
572 {
573     vstrainrate[i] = ((vtruestrain[i] - vtruestrain[i-1]) / (
574         vtimestress[i] - vtimestress[i-1]));
575 }
576 cout << "Done" << endl;
577
578 cout << "Finding maximum stress... ";
579 double maxtruestress = 0.00000;
580 double maxtruestresstrain = 0.00000;
581 double maxtruestresstime = 0.00000;
582 double strainrate = 0.00000;
583 for (int i = 1; i < vtruestress.size(); i++)
584 {
585     if (vtruestress[i] > maxtruestress)

```

```
586         maxtruestress = vtruestress[i];
587         maxtruestressstrain = vtruestrain[i];
588         maxtruestresstime = vtimestress[i];
589         strainrate = vstrainrate[i];
590     }
591 }
592 ofstream outfile;
593 outfile.open("maxstress.csv");
594 outfile << "Time,Maximum True Stress,Strain at Maximum Stress,
        Strain Rate" << endl;
595 outfile << maxtruestresstime << "," << maxtruestress << "," <<
        maxtruestressstrain << "," << strainrate << endl;
596 outfile.close();
597 cout << "Done" << endl;
598
599 cout << "Saving Bezier stress/strain data... ";
600 outfile.open("bezier_stress_strain.csv");
601 outfile << "Time,Engineering Strain,True Strain,Engineering Stress
        ,True Stress,Strain Rate" << endl;
602 outfile << "0,0,0,0,0,0" << endl;
603
604 for (int i = 0; i < vtruestrain.size(); i++)
605 {
606     if (vtruestress[i] < 0)
607     {
608         break;
609     }
610     outfile << vtimestress[i] << "," << vengstrain[i] << "," <<
        vtruestrain[i] << "," << vengstress[i] << "," <<
        vtruestress[i] << "," << vstrainrate[i] << endl;
611 }
612
613 outfile.close();
614 cout << "Done" << endl;
615
616 cout << endl << "Program terminated." << endl;
617
618 return 0;
619 }
```

Yield Strength GNU Octave code

The following code was written to calculate the yield stress of a stress-strain curve produced with a SHPB. It was written to be run in GNU Octave, if necessary however, converting it to run in MathWorks MatLab should be trivial.

For this script to work correctly in this form, data must exist in a comma-separated value (CSV) file, `input.csv`. Each file should consist of two columns, the first being the strain and the second being the stress.

The result of the script are two output CSV files, called `poly.csv` containing the data, its polynomial and its first and second derivatives, and `yield.csv`, which contains values for the strain and stress at yield.

```
1 octave
2 order = 20;
3
4 %open input CSV file
5 data = csvread('input.csv');
6 strain = data(:,1);
7 stress = data(:,2);
8
9 %find maximum stress
10 [null, maxstress] = max(stress);
11
12 %delete elements after max stress
13 strain(maxstress+3:end) = [];
14 stress(maxstress+3:end) = [];
15
16 %calculate best fit polynomials
17 p = polyfit (strain, stress, order);
18
19 %calculate individual y values
20 poly = 0;
21 for i = 1:order
22     poly = poly + (strain.^((order+1)-i) * p(i));
23 endfor
24 poly = poly + p(order+1);
25
26 %calculate first & second differential of the polynomial w.r.t. strain
27 first = diff(poly) ./ diff(strain);
28 second = diff(first) ./ diff(strain(1:end-1));
29
```

```
30 %tidy up
31 strain(maxstress+1:end) = [];
32 stress(maxstress+1:end) = [];
33 poly(maxstress+1:end) = [];
34 first(maxstress+1:end) = [];
35 second(maxstress+1:end) = [];
36
37 %find first point where second derivative >= 0
38 for i = 1:maxstress
39     if (second(i) >= 0)
40         yieldstrain = strain(i);
41         yieldstress = stress(i);
42         break;
43     endif
44 endfor
45
46 %write data
47 csvwrite('poly.csv', [strain, stress, poly, first, second]);
48
49 filename = 'yield.csv';
50
51 fid = fopen(filename, 'w');
52 fprintf(fid, 'Yield Strain, Yield Stress\n');
53 fclose(fid)
54
55 dlmwrite(filename, [yieldstrain, yieldstress], '-append');
```

Young's Modulus C++ code

The following program was written to calculate the yield strength and the Young's modulus history of a two-column comma-separated-value file named `stress_strain.csv`, where the first column contains the true strain and the second column the true stress.

The results of running this program are saved in `stress_strain.csv.yield.csv`, containing the stress and strain at the turning point (i.e. at yield) of the curve, and `stress_strain.csv.youngsmodulushistory.csv` which contains the history of Young's modulus up to yield.

This program is written to be compiled with GCC, the GNU compiler collection.

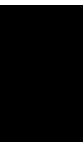
```
1
2 #include <iostream>
3 #include <fstream>
4 #include <stdio.h>
5 #include <stdlib.h>
6 #include <math.h>
7
8 using namespace std;
9
10 int throwerror(char* errorname)
11 {
12     cout << endl << "ERROR:" << endl << errorname << endl << endl;
13     return 1;
14 }
15
16 int main(int argc, char* argv[])
17 {
18
19     string cLineInput;
20     int iPos;
21     double strain = 0.00000, stress = 0.00000, strainrate = 0.00000,
22         thetime = 0.00000;
23     double laststrain = 0.00000, laststress = 0.00000;
24     double maxstress = 0.00000, maxstrain = 0.00000, maxstrainrate =
25         0.00000, maxtime = 0.00000;
26     double yieldstrain = 0.00000, yieldstress = 0.00000;
27     double E = 0.00000, E1 = 0.00000, E2 = 0.00000, E3 = 0.00000;
```

```
26     double Ex[10];
27     double Strainhist[10];
28     double Stresshist[10];
29     string cChannel1 = "stress_strain.csv";
30
31     for (int i = 0; i < 10; i++)
32     {
33         Ex[i] = 0.00000;
34         Strainhist[i] = 0.00000;
35         Stresshist[i] = 0.00000;
36     }
37
38     //setup input and output files
39     char* inputfile = argv[1];
40
41     if (inputfile == NULL)
42     {
43         cout << "Usage:" << endl;
44         cout << "getyield <filename.csv>" << endl;
45         throwerror("No arguments specified.");
46     }
47     string infile = inputfile;
48
49     string youngsout = inputfile;
50     youngsout += ".youngsmodulushistory.csv";
51     string yieldout = inputfile;
52     yieldout += ".yield.csv";
53     string stressout = inputfile;
54     stressout += ".maxstress.csv";
55
56     ifstream channel1;
57     ofstream outfile;
58
59     channel1.open (infile.c_str());
60
61     if (!channel1)
62     {
63         throwerror("Unable to open data file.");
64     }
65
66     //Work through file, look for point where rate of change of stress
67     w.r.t. strain <= 0
68     //also calculate strain rate at point of maximum stress
69     while (! channel1.eof() )
70     {
71         getline (channel1, cLineInput);
72         //True strain is column 1
73         iPos=cLineInput.find(",");
74         strain = atof(cLineInput.substr(0,iPos).c_str());
75         cLineInput = cLineInput.substr(iPos +1);
76         //True stress is column 2
77         iPos=cLineInput.find(",");
78         stress = atof(cLineInput.substr(0,iPos).c_str());
79
80         if (yieldstress == 0)
81         {
82             if ((stress - laststress) / (strain - laststrain) <= 0)
83             {
84                 yieldstress = stress;
85                 yieldstrain = strain;
```

```

85         }
86     }
87
88     channel1.open (infile.c_str());
89
90     outfile.open (youngsout.c_str());
91     outfile << "Strain,Young's Modulus" << endl;
92
93     while (! channel1.eof() )
94     {
95         getline (channel1, cLineInput);
96
97         //True strain is column 1
98         iPos=cLineInput.find(",");
99         strain = atof(cLineInput.substr(0,iPos).c_str());
100        cLineInput = cLineInput.substr(iPos +1);
101
102        //True stress is column 2
103        iPos=cLineInput.find(",");
104        stress = atof(cLineInput.substr(0,iPos).c_str());
105
106        if (strain <= yieldstrain)
107        {
108            outfile << strain << "," << stress / strain << endl;
109        }
110    }
111
112
113    outfile.close();
114    outfile.open (yieldout.c_str());
115    outfile << "Yield strain,Yield stress" << endl;
116    outfile << yieldstrain << "," << yieldstress << endl;
117    outfile.close();
118
119    channel1.close();
120
121    return 0;
122 }

```

Otsu thresholding C++ code

The following program was written to calculate appropriate threshold values, using Otsu's method, and hence convert the greyscale bitmap images taken during high-speed photography into binary images.

Should it be necessary to convert a 24-bit colour bitmap to greyscale, the intensity, I of a given colour pixel is given by:

$$I = 0.299R + 0.587G + 0.114B \quad (\text{I.1})$$

where R , G and B are the individual intensity values of, respectively, the red, green and blue channels for the pixel in question.

For ease of programming, the EasyBMP C++ bitmap library was used for the reading, creation and manipulation of bitmaps.

This program is written to be compiled with GCC, the GNU compiler collection.

```
1 #include <iostream>
2 #include <fstream>
3 #include <string>
4 #include <stdio.h>
5 #include <stdlib.h>
6 #include <math.h>
7 #include "EasyBMP.h"
8 #include "EasyBMP_BMP.h"
9 #include "EasyBMP_DataStructures.h"
10 #include "EasyBMP_VariousBMPutilities.h"
11
12 using namespace std;
13
14 int throwerror(char* errorname)
15 {
16     cout << endl << "ERROR:" << endl << errorname << endl << endl;
17     exit(1);
18 }
19
20 int main( int argc, char* argv[] )
21 {
22     /** thresh by Foz Hughes, Department of Physics, Loughborough
23         university, UK, LE11 3TU
```

```
23      /** computes Otsu threshold of a greyscale BMP file
24      /** results saved as <filename>.otsu.bmp
25      /**
26      /** uses the EasyBMP C++ bitmap library under the GNU general
        public license
27      /** see http://easybmp.sourceforge.net/
28
29      //Declare Variables
30      long histo[256]; //array to hold histogram values
31
32      //initialise variables
33      for (int i = 0; i < 256; i++)
34      {
35          histo[i] = 0;
36      }
37
38      //setup input and output files
39      char* inputfile = argv[1]; //gets input file name from command
        line arguments
40      //inputfile = "1.bmp";
41      if (inputfile == NULL)
42      {
43          cout << "Usage:" << endl;
44          cout << "histo <bmpfilename>" << endl;
45          throwerror("No arguments specified.");
46      }
47      string outputfile = inputfile;
48      outputfile += ".otsu.bmp";
49      const char * outfile = outputfile.c_str();
50
51      //open BMP file
52      cout << "Opening bitmap... ";
53      BMP input;
54      input.ReadFromFile(inputfile);
55      cout << "Done (" << input.TellHeight() << "x" << input.TellWidth()
        << " pixels)" << endl;
56
57      //build histogram
58      cout << "Calculating histogram... ";
59      for (int j = 0; j < input.TellHeight(); j++)
60      {
61          for (int i=0; i < input.TellWidth(); i++)
62          {
63              histo[input(i,j)->Red]++;
64          }
65      }
66      cout << "Done" << endl;
67
68      //calculate total pixels in BMP file
69      cout << "Calculating Otsu threshold...";
70      int totalpixels = input.TellHeight() * input.TellWidth();
71
72      //variables for Otsu threshold
73      double Wb[256], Mb[256], Vb[256];
74      double Wf[256], Mf[256], Vf[256];
75      double Vw[256];
76      int backpixels[256], forepixels[256];
77
78      //zero Otsu variables
79      for (int i = 0; i < 256; i++)
```

```

80     {
81         Wb[i] = 0.00000;
82         Mb[i] = 0.00000;
83         Vb[i] = 0.00000;
84         Wf[i] = 0.00000;
85         Mf[i] = 0.00000;
86         Vf[i] = 0.00000;
87         Vw[i] = 0.00000;
88         backpixels[i] = 0;
89         forepixels[i] = 0;
90     }
91
92     //calculate the weight and mean for each threshold
93     for (int i = 0; i < 256; i++)
94     {
95         for (int j = 0; j < 256; j++)
96         {
97             if (j < i)
98             {
99                 Wb[i] += histo[j];
100                Mb[i] += j * histo[j];
101                backpixels[i] += histo[j];
102            }
103            else
104            {
105                Wf[i] += histo[j];
106                Mf[i] += j * histo[j];
107                forepixels[i] += histo[j];
108            }
109        }
110        Wb[i] = Wb[i] / totalpixels;
111        Mb[i] = Mb[i] / backpixels[i];
112        Wf[i] = Wf[i] / totalpixels;
113        Mf[i] = Mf[i] / forepixels[i];
114    }
115
116     //calculate the variance for each threshold
117     for (int i = 0; i < 256; i++)
118     {
119         for (int j = 0; j < 256; j++)
120         {
121             if (j < i)
122             {
123                 Vb[i] += pow(j - Mb[i], 2) * histo[j] / backpixels[i];
124             }
125             else
126             {
127                 Vf[i] += pow(j - Mf[i], 2) * histo[j] / forepixels[i];
128             }
129         }
130
131         //calculate within class variance
132         Vw[i] = (Wb[i] * Vb[i]) + (Wf[i] * Vf[i]);
133     }
134
135     //lowest Vw[i] is Otsu threshold
136     double smallest = Vw[1];
137     int otsu = 0;
138     for (int i = 0; i < 256; i++)
139     {

```

```
140     if (smallest > Vw[i])
141     {
142         smallest = Vw[i];
143         otsu = i;
144     }
145 }
146 cout << "Done (" << otsu << ")" << endl;
147
148 //threshold the image and save
149 cout << "Thresholding image... ";
150 for (int j = 0; j < input.TellHeight(); j++)
151 {
152     for (int i=0; i < input.TellWidth(); i++)
153     {
154         if (input(i,j)->Red < otsu)
155         {
156             input(i,j)->Red = 0;
157             input(i,j)->Green = 0;
158             input(i,j)->Blue = 0;
159         }
160         else
161         {
162             input(i,j)->Red = 255;
163             input(i,j)->Green = 255;
164             input(i,j)->Blue = 255;
165         }
166     }
167 }
168 input.WriteToFile(outfile);
169 cout << "Done" << endl;
170
171 return 0;
172 }
```

Barfinder C++ code

The following program was written to locate the position of the SHPB pressure bars in a pre-thresholded image, hence locating and measuring the length and diameter of the specimen in the image.

For ease of programming, the EasyBMP C++ bitmap library was used for the reading, creation and manipulation of bitmaps.

This program is written to be compiled with GCC, the GNU compiler collection.

```
1 #include <iostream>
2 #include <fstream>
3 #include <string>
4 #include <stdio.h>
5 #include <stdlib.h>
6 #include <math.h>
7 #include "EasyBMP.h"
8 #include "EasyBMP_BMP.h"
9 #include "EasyBMP_DataStructures.h"
10 #include "EasyBMP_VariousBMPutilities.h"
11
12 using namespace std;
13
14 int throwerror(char* errorname)
15 {
16     cout << endl << "ERROR:" << endl << errorname << endl << endl;
17     exit(1);
18 }
19
20 int main( int argc, char* argv[] )
21 {
22     /** barfinder by Foz Hughes, Department of Physics, Loughborough
23         university, UK, LE11 3TU
24     /**
25     /**
26     /** uses the EasyBMP C++ bitmap library under the GNU general
27         public license
28     /** see http://easybmp.sourceforge.net/
29     /** setup input and output files
```

```
30     char* inputfile = argv[1]; //gets input file name from command
      line arguments
31     //inputfile = "Bmp005.bmp.otsu.bmp";
32     if (inputfile == NULL)
33     {
34         cout << "Usage:" << endl;
35         cout << "barfinder <bmpfilename>" << endl;
36         throwerror("No arguments specified.");
37     }
38     string outputfile = inputfile;
39     outputfile += ".barfinder.bmp";
40     const char * outfile = outputfile.c_str();
41
42     //open BMP file
43     BMP input;
44     input.ReadFromFile(inputfile);
45     int width = input.TellWidth();
46     int height = input.TellHeight();
47
48     //calculate starting point (ignore first and last columns)
49     int barcentre = 0;
50     barcentre = int (height / 2);
51     //cout << barcentre;
52
53     //is barcentre inside a bar? (i.e. is pixel black) if not, shift
      up
54     while (input(1,barcentre)->Red != 0)
55     {
56         barcentre--;
57         //cout << barcentre << endl;
58     }
59     int bartop[width], barbottom[width];
60     int up = 0, down = 0;
61     for (int i = 0; i < width; i++)
62     {
63         bartop[i] = 0;
64         barbottom[i] = 0;
65     }
66     for (int i = 0; i < (height / 2); i++)
67     {
68         if (input(20,barcentre - i)->Red == 255)
69         {
70             up = barcentre - (i-1);
71         }
72         if (input(20,barcentre + i)->Red == 255)
73         {
74             down = barcentre + (i-1);
75         }
76     }
77     //throwerror if nothing found
78     if (up == 0)
79     {
80         throwerror("    Unable to locate top of bar.");
81     }
82     else if (down == 0)
83     {
84         throwerror("    Unable to locate bottom of bar.");
85     }
86     barcentre = up + ((down - up) / 2);
87     for (int i = 0; i < width; i++)
```

```

88     {
89         bartop[i] = 0;
90         barbottom[i] = 0;
91     }
92
93     //find top and bottom of whole silhouette
94     for (int column = 0; column < width - 2; column++)
95     {
96         for (int row = 0; row < (height / 2); row++)
97         {
98             if (barcentre - row == 0)
99             {
100                 bartop[column] = 1;
101             }
102             if ((input(column,barcentre - row)->Red == 255) && (bartop
103                 [column] == 0))
104             {
105                 bartop[column] = barcentre - (row-1);
106             }
107             if (barcentre + row == height - 1)
108             {
109                 barbottom[column] = 1;
110             }
111             if ((input(column,barcentre + row)->Red == 255) && (
112                 barbottom[column] == 0))
113             {
114                 barbottom[column] = barcentre + (row-1);
115                 //cout << ", " << barbottom[column];
116             }
117             if ((barbottom[column] != 0) && (bartop[column] != 0))
118             {
119                 break;
120             }
121         }
122     }
123
124     //find average bar centre
125     double totalleft = 0.00000, totalright = 0.00000;
126     double averagedia = 0.00000;
127     double averagebottom = 0.00000, averagetop = 0.00000;
128     double averagebottom2 = 0.00000, averagetop2 = 0.00000;
129
130     for (int column = 1; column < 50; column++)
131     {
132         averagebottom += (double) barbottom[column];
133         averagetop += (double) bartop[column];
134         totalleft += (double) barbottom[column] - bartop[column];
135         averagebottom2 += (double) barbottom[width-column-2];
136         averagetop2 += (double) bartop[width-column-2];
137         totalright += (double) barbottom[width-column-2] - bartop[
138             width-column-2];
139     }
140     totalleft = totalleft / 50;
141     averagebottom = averagebottom / 50;
142     averagetop = averagetop / 50;
143     totalright = totalright / 50;
144     averagebottom2 = averagebottom2 / 50;
145     averagetop2 = averagetop2 / 50;
146     if (totalright < totalleft)

```



```
145     {
146         averagedia = (totalright);
147     }
148     else
149     {
150         averagedia = (totalleft);
151     }
152
153     //find silhouette from outside, resolves problems with bright
154     spots on bars/sample
155     int bars[width][2];
156     for (int i = 0; i < width; i++)
157     {
158         bars[i][0] = 0;
159         bars[i][1] = 0;
160     }
161     for (int column = 0; column < width; column++)
162     {
163         for (int row = averagetop - 10; row < barcentre; row++)
164         {
165             if ((input(column, row)->Red == 0) && (bars[column][0] ==
166                 0))
167             {
168                 bars[column][0] = row;
169                 break;
170             }
171         }
172         for (int row = averagebottom + 10; row > barcentre; row--)
173         {
174             if ((input(column, row)->Red == 0) && (bars[column][1] ==
175                 0))
176             {
177                 bars[column][1] = row;
178                 break;
179             }
180         }
181     }
182
183     //search for areas where diameter < (averagedia - 2)
184     int counter = 0;
185     //count potential sample columns
186     for (int column = 0; column < width; column++)
187     {
188         if ((barbottom[column] - bartop[column]) < (averagedia - 3))
189         {
190             counter++;
191         }
192     }
193
194     //create array to hold sample candidates and populate with their
195     columns
196     int candidates[counter];
197     int rightbarend = 0;
198     counter = 0;
199     for (int column = 0; column < width; column++)
200     {
201         if ((barbottom[column] - bartop[column]) < (averagedia - 3))
202         {
203             candidates[counter] = column;
204             counter++;
205         }
206     }
207 }
```

```

201         rightbarend = column;
202     }
203 }
204
205 //create & initialise array to find largest contiguity
206 int cont[(sizeof(candidates) / sizeof(int))[2];
207 for (int i = 0; i < (sizeof(candidates) / sizeof(int)); i++)
208 {
209     cont[i][0] = 0;
210     cont[i][1] = 0;
211 }
212
213 //scan through candidates, store start and end of each contiguity
214 int start=-1;
215 counter = 0;
216 for (int i = 0; i < (sizeof(candidates) / sizeof(int) - 1); i++)
217 {
218     if (start == -1)
219     {
220         start = i;
221     }
222     if ((candidates[i+1] - candidates[i]) > 1)
223     {
224         cont[counter][0] = candidates[start + 1];
225         cont[counter][1] = candidates[i];
226         start = -1;
227         counter++;
228     }
229     else if (i == (sizeof(candidates) / sizeof(int)) - 2) //last
        column in set
230     {
231         cont[counter][0] = candidates[start];
232         cont[counter][1] = candidates[i];
233         start = -1;
234         counter++;
235     }
236 }
237
238 for (int i = 0; i < (sizeof(candidates) / sizeof(int)); i++)
239 {
240     if (cont[i][0] != 0)
241     {
242
243     }
244 }
245
246 //find largest contiguity (assumed to be the sample)
247 int longest = 0;
248 int longestindex = -1;
249 for (int i = 0; i < (sizeof(candidates) / sizeof(int)); i++)
250 {
251     if (cont[i][1] - cont[i][0] > longest)
252     {
253         longest = cont[i][1] - cont[i][0];
254         longestindex = i;
255     }
256 }
257
258 //for each column in largest contiguity, check if they're >>
        average sample diameter

```

```
259     //first find average sample diameter
260     double averagesample = 0.00000;
261     double averagesamletop = 0.00000;
262     double averagesamplebottom = 0.00000;
263     for (int i = cont[longestindex][0]; i <= cont[longestindex][1]; i
        ++)
264     {
265         averagesample += (double) (bars[i][1] - bars[i][0]);
266         averagesamletop += (double) bars[i][0];
267         averagesamplebottom += (double) bars[i][1];
268     }
269     averagesample = averagesample / (cont[longestindex][1] - cont[
        longestindex][0]);
270     averagesamletop = averagesamletop / (cont[longestindex][1] -
        cont[longestindex][0]);
271     averagesamplebottom = averagesamplebottom / (cont[longestindex][1]
        - cont[longestindex][0]);
272
273
274     int sampleleft = cont[longestindex][0];
275     int sampleright = cont[longestindex][1];
276
277     if (averagesamletop - bars[sampleleft][0] > 2)
278     {
279         if (averagesamletop - bartop[sampleleft] > 2)
280         {
281             sampleleft++;
282         }
283         else
284         {
285             bars[sampleleft][0] = bartop[sampleleft];
286         }
287     }
288
289     if (averagesamletop - bars[sampleright][0] > 2)
290     {
291         if (averagesamletop - bartop[sampleright] > 2)
292         {
293             sampleright--;
294         }
295         else
296         {
297             bars[sampleright][0] = bartop[sampleright];
298         }
299     }
300
301     if (bars[sampleleft][1] - averagesamplebottom > 2)
302     {
303         if (averagesamplebottom - barbottom[sampleleft] > 2)
304         {
305             sampleleft++;
306         }
307         else
308         {
309             bars[sampleleft][0] = barbottom[sampleleft];
310         }
311     }
312
313     if (bars[sampleright][1] - averagesamplebottom > 2)
314     {
```

```

315         if (averagesamplebottom - barbottom[sampleright] > 2)
316         {
317             sampleleft--;
318         }
319         else
320         {
321             bars[sampleright][0] = barbottom[sampleright];
322         }
323     }
324
325     averagesample = 0.00000;
326     for (int i = sampleleft; i <= sampleright; i++)
327     {
328         averagesample += (double) (bars[i][1] - bars[i][0]);
329     }
330     averagesample = averagesample / (sampleright - sampleleft);
331
332     cout << inputfile << "," << averagedia << "," << sampleleft - 1 <<
333         "," << sampleright + 1 << "," << sampleright - sampleleft <<
334         "," << averagesample << endl;
335
336     input.CreateStandardColorTable();
337     for (int i = 1; i < width; i++)
338     {
339         input(i, bars[i][0])->Red = 255;
340         input(i, bars[i][0])->Green = 0;
341         input(i, bars[i][0])->Blue = 0;
342         input(i, bars[i][1])->Red = 255;
343         input(i, bars[i][1])->Green = 0;
344         input(i, bars[i][1])->Blue = 0;
345     }
346     for (int i = sampleleft; i <= sampleright; i++)
347     {
348         input(i, bars[i][0])->Red = 0;
349         input(i, bars[i][0])->Green = 255;
350         input(i, bars[i][0])->Blue = 0;
351         input(i, bars[i][1])->Red = 0;
352         input(i, bars[i][1])->Green = 255;
353         input(i, bars[i][1])->Blue = 0;
354     }
355     input.WriteToFile(outfile);
356 }

```


Optical drop weight C++ code

The following program was written to measure the maximum diameter of a specimen in a single bitmap image taken from an optical drop weight experiment. While this program only measures the specimen in one image, it can be made to run multiple times using a for loop by running it in the command prompt of whichever operating system it is run on. For example, in a Microsoft Windows environment:

```
for %a in (*.bmp) do D:\DIR\DW.exe %a >> specimen.txt
```

or in a GNU/Linux environment:

```
for item in *.bmp
do
/dir/dw $item >> specimen.txt
done
```

will run the program for each file named *.bmp in the current folder, and save the results in a file called specimen.txt. The latter may also work in Apple MacOS X with little modification.

For ease of programming, the EasyBMP C++ bitmap library was used for the reading of bitmaps.

This program is written to be compiled with GCC, the GNU compiler collection.

```
1 #include <iostream>
2 #include "EasyBMP.h"
3 #include "EasyBMP_BMP.h"
4 #include "EasyBMP_DataStructures.h"
5 #include "EasyBMP_VariousBMPutilities.h"
6
7 using namespace std;
8
9 int getrightpixel( const char* filename, int row, int thresh)
10 {
11     int intensity, oldintensity=0, rightpixel;
```

```
12     BMP AnImage;
13     AnImage.ReadFromFile( filename );
14
15     for( int j=AnImage.TellWidth()/2 ; j < AnImage.TellWidth() ; j++)
16     {
17         intensity = AnImage(j, row)->Red + AnImage(j, row)->Green +
18             AnImage(j, row)->Blue;
19
20         if(oldintensity == 0)
21         {
22             oldintensity=intensity;
23         }
24
25         if(oldintensity - intensity < -thresh)
26         {
27             rightpixel = j;
28             oldintensity=0;
29             break;
30         }
31         oldintensity=intensity;
32         intensity=0;
33         rightpixel=0;
34     }
35     return (rightpixel);
36 }
37
38 int getleftpixel( const char* filename, int row, int thresh)
39 {
40     int intensity, oldintensity=0, leftpixel;
41     BMP AnImage;
42     AnImage.ReadFromFile( filename );
43
44     for( int j=AnImage.TellWidth()/2 ; j > 0 ; j--)
45     {
46         intensity = AnImage(j, row)->Red + AnImage(j, row)->Green +
47             AnImage(j, row)->Blue;
48
49         if(oldintensity == 0)
50         {
51             oldintensity=intensity;
52         }
53
54         if(oldintensity - intensity < -thresh)
55         {
56             leftpixel = j;
57             oldintensity=0;
58             break;
59         }
60         oldintensity=intensity;
61         intensity=0;
62         leftpixel=0;
63     }
64     return (leftpixel);
65 }
66
67 int getbottompixel( const char* filename, int column, int thresh)
68 {
69     int intensity, oldintensity=0, bottompixel;
```

```

70     BMP AnImage;
71     AnImage.ReadFromFile( filename );
72
73     for( int j=AnImage.TellHeight()/2 ; j < AnImage.TellHeight() ; j
74         ++)
75     {
76         intensity = AnImage(column, j)->Red + AnImage(column, j)->
77             Green + AnImage(column, j)->Blue;
78
79         if(oldintensity == 0)
80         {
81             oldintensity=intensity;
82         }
83
84         if(oldintensity - intensity < -thresh)
85         {
86             bottompixel = j;
87             oldintensity=0;
88             break;
89         }
90         oldintensity=intensity;
91         intensity=0;
92         bottompixel=0;
93     }
94     return (bottompixel);
95 }
96 int gettoppixel( const char* filename, int column, int thresh)
97 {
98     int intensity, oldintensity=0, toppixel;
99     BMP AnImage;
100    AnImage.ReadFromFile( filename );
101
102    for( int j=AnImage.TellHeight()/2 ; j > 0 ; j--)
103    {
104        intensity = AnImage(column, j)->Red + AnImage(column, j)->
105            Green + AnImage(column, j)->Blue;
106
107        if(oldintensity == 0)
108        {
109            oldintensity=intensity;
110        }
111
112        if(oldintensity - intensity < -thresh)
113        {
114            toppixel = j;
115            oldintensity=0;
116            break;
117        }
118        oldintensity=intensity;
119        intensity=0;
120        toppixel=0;
121    }
122    return (toppixel);
123 }
124
125 int main(int argc, char* argv[])
126 {

```



```
127     int leftpixel, rightpixel, toppixel, bottompixel, samplewidth=0,
128         sampleheight=0, threshold=30;
129
130     if( argc != 2 )
131     {
132         cout << "Usage: DW <input_filename>"
133         << endl << endl;
134         return 1;
135     }
136
137     //Open file
138     BMP AnImage;
139     AnImage.ReadFromFile( argv[1] );
140
141     //middle working down
142     for (int j = AnImage.TellHeight()/2 ; j < AnImage.TellHeight() ; j
143         ++ )
144     {
145         rightpixel = getrightpixel(argv[1], j, threshold);
146         leftpixel = getleftpixel(argv[1], j, threshold);
147         if (samplewidth > rightpixel - leftpixel)
148         {
149             break;
150         }
151         samplewidth = rightpixel - leftpixel;
152     }
153
154     //middle working up
155     for (int j = AnImage.TellHeight()/2 ; j > 0 ; j-- )
156     {
157         rightpixel = getrightpixel(argv[1], j, threshold);
158         leftpixel = getleftpixel(argv[1], j, threshold);
159         if (samplewidth > rightpixel - leftpixel)
160         {
161             break;
162         }
163         samplewidth = rightpixel - leftpixel;
164     }
165
166     //middle working right
167     for (int j = AnImage.TellWidth()/2 ; j < AnImage.TellWidth() ; j
168         ++ )
169     {
170         bottompixel = getbottompixel(argv[1], j, threshold);
171         toppixel = gettoppixel(argv[1], j, threshold);
172         if (sampleheight > bottompixel - toppixel)
173         {
174             break;
175         }
176         sampleheight = bottompixel - toppixel;
177     }
178
179     //middle working left
180     for (int j = AnImage.TellWidth()/2 ; j > 0 ; j-- )
181     {
182         bottompixel = getbottompixel(argv[1], j, threshold);
183         toppixel = gettoppixel(argv[1], j, threshold);
184         if (sampleheight > bottompixel - toppixel)
185         {
186             break;
187         }
188     }
```

```
184     }
185     sampleheight = bottompixel - toppixel;
186 }
187
188 cout << samplewidth << "," << sampleheight << endl;
189
190 return 0;
191 }
```


Full page graphs

This appendix contains full page graphs from the *Results & Discussion* section.

L.1 Split-Hopkinson Pressure Bar

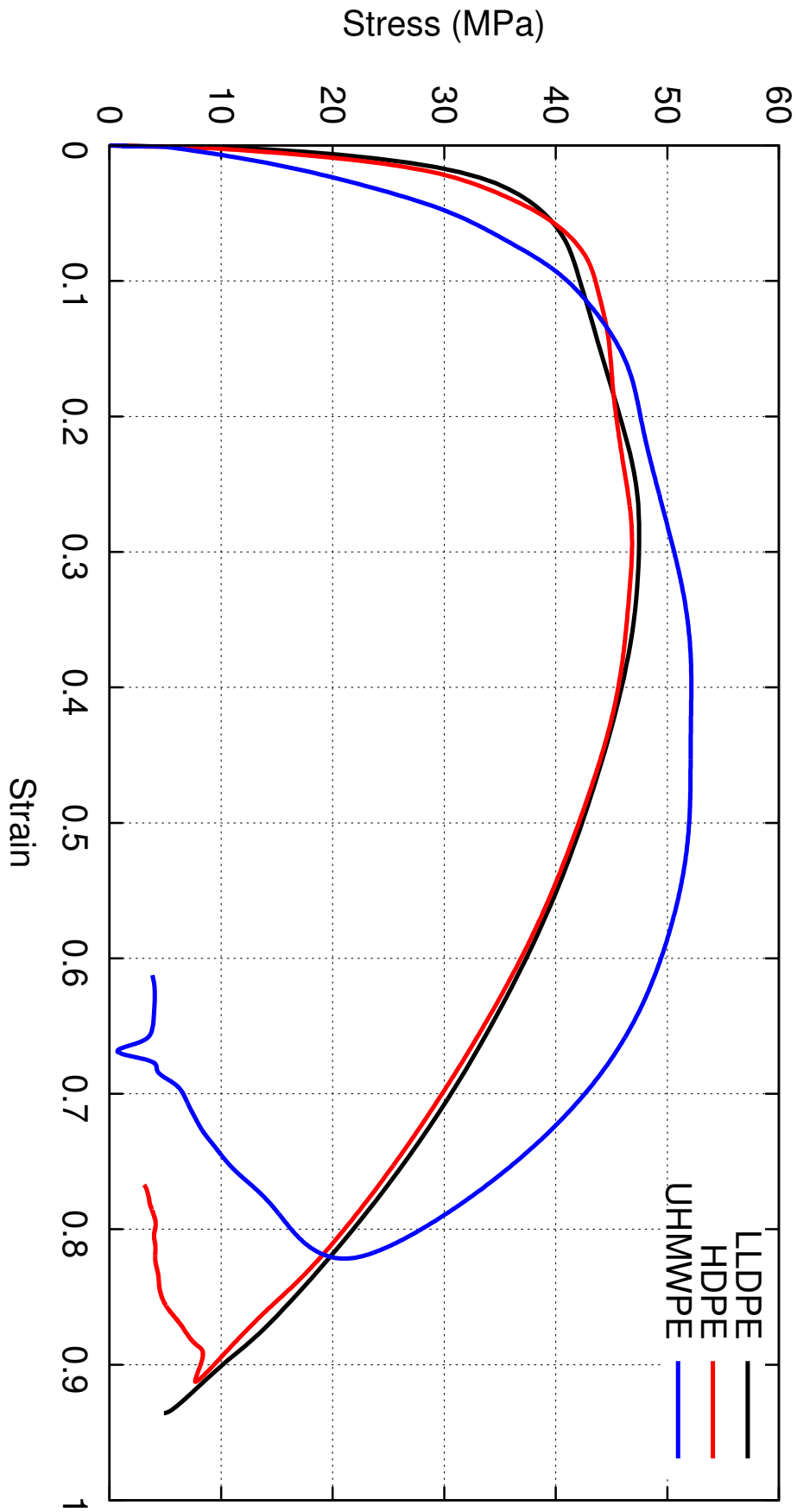


FIGURE L.1: SHPB true stress/strain curves for LLDPE, HDPE and UHMWPE.

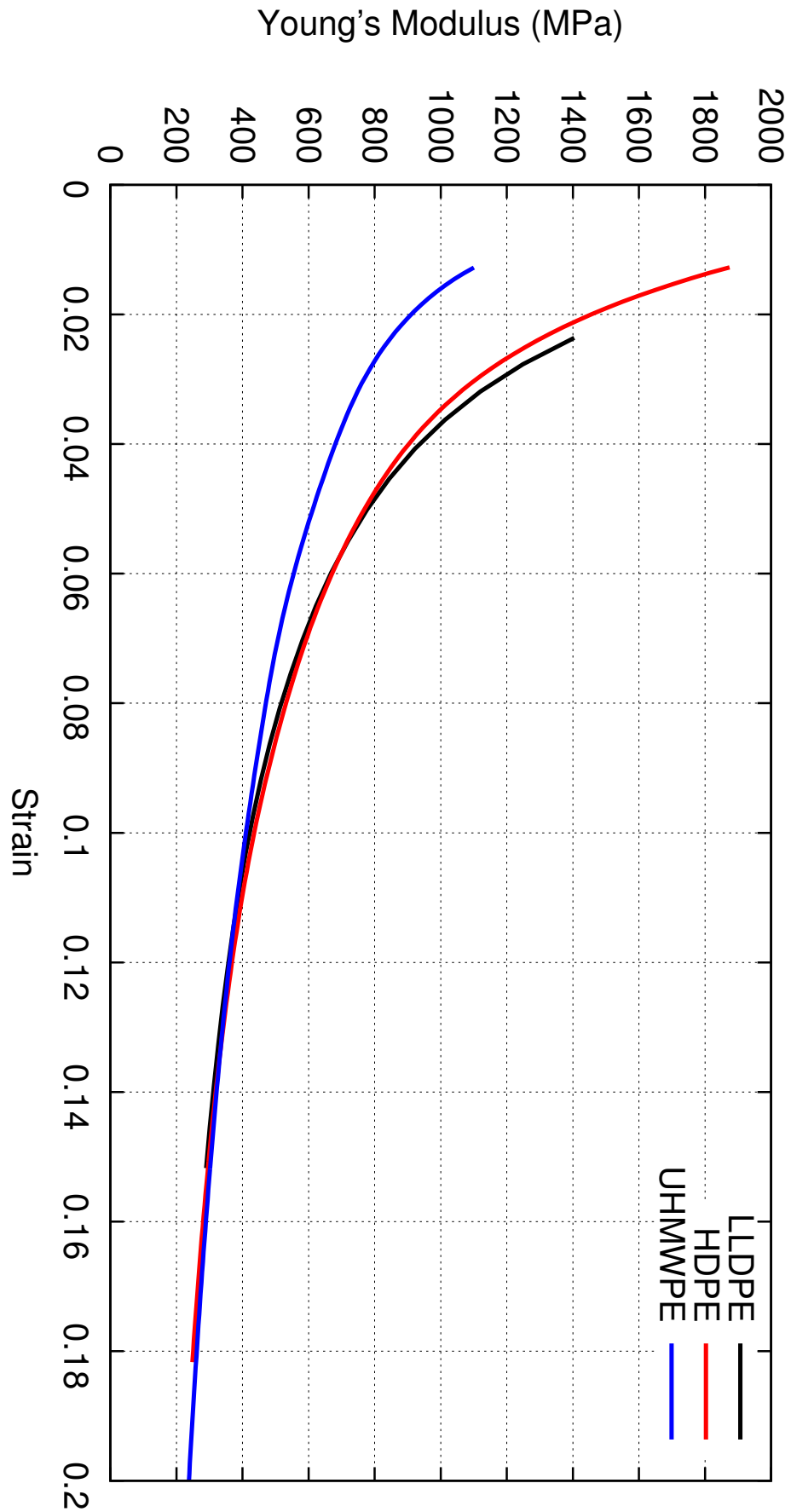


FIGURE L.2: SHPB Young's modulus evolution for LLDPE, HDPE and UHMWPE.

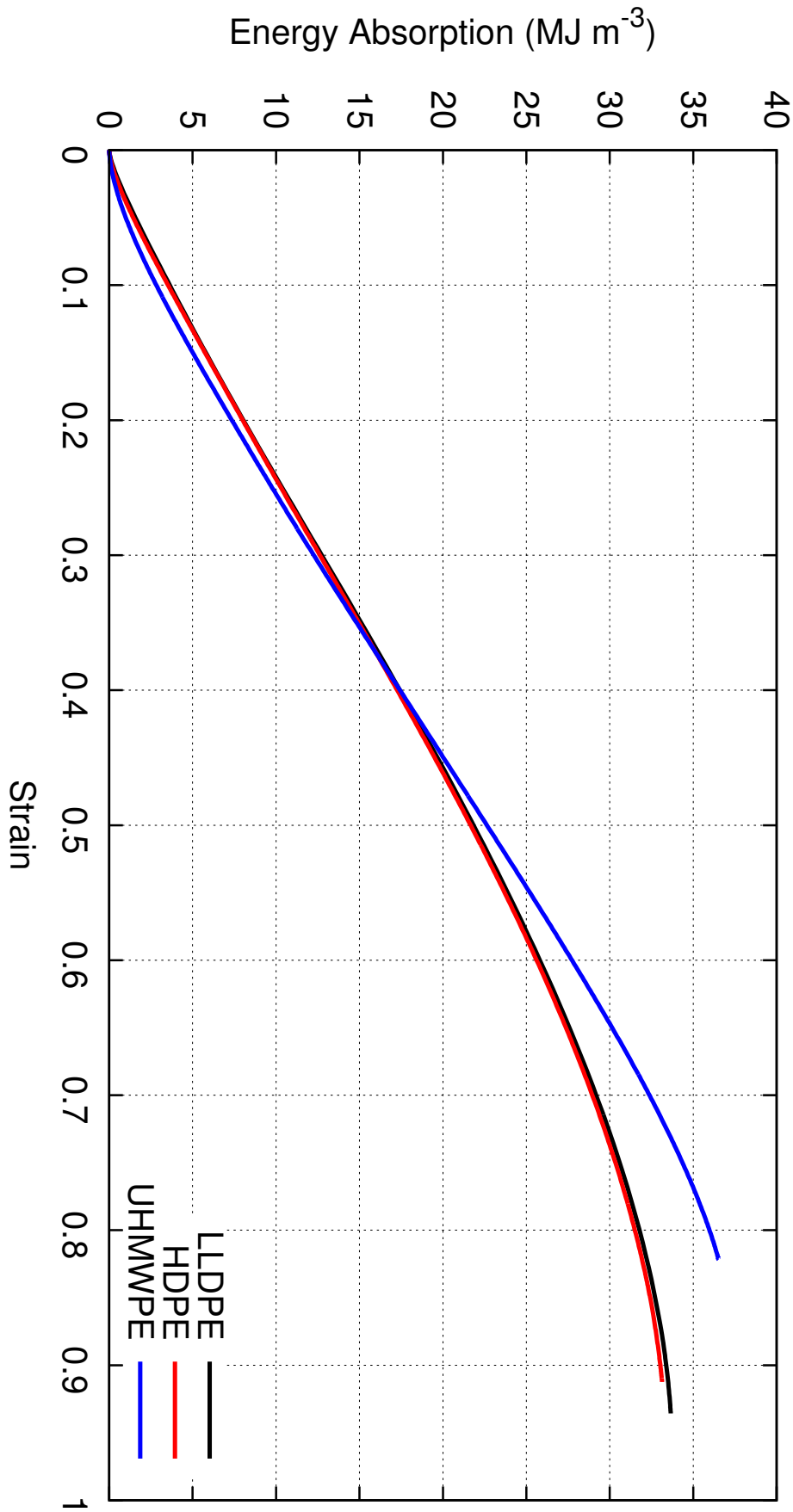


FIGURE L.3: SHPB energy absorption for LLDPE, HDPE and UHMWPE.

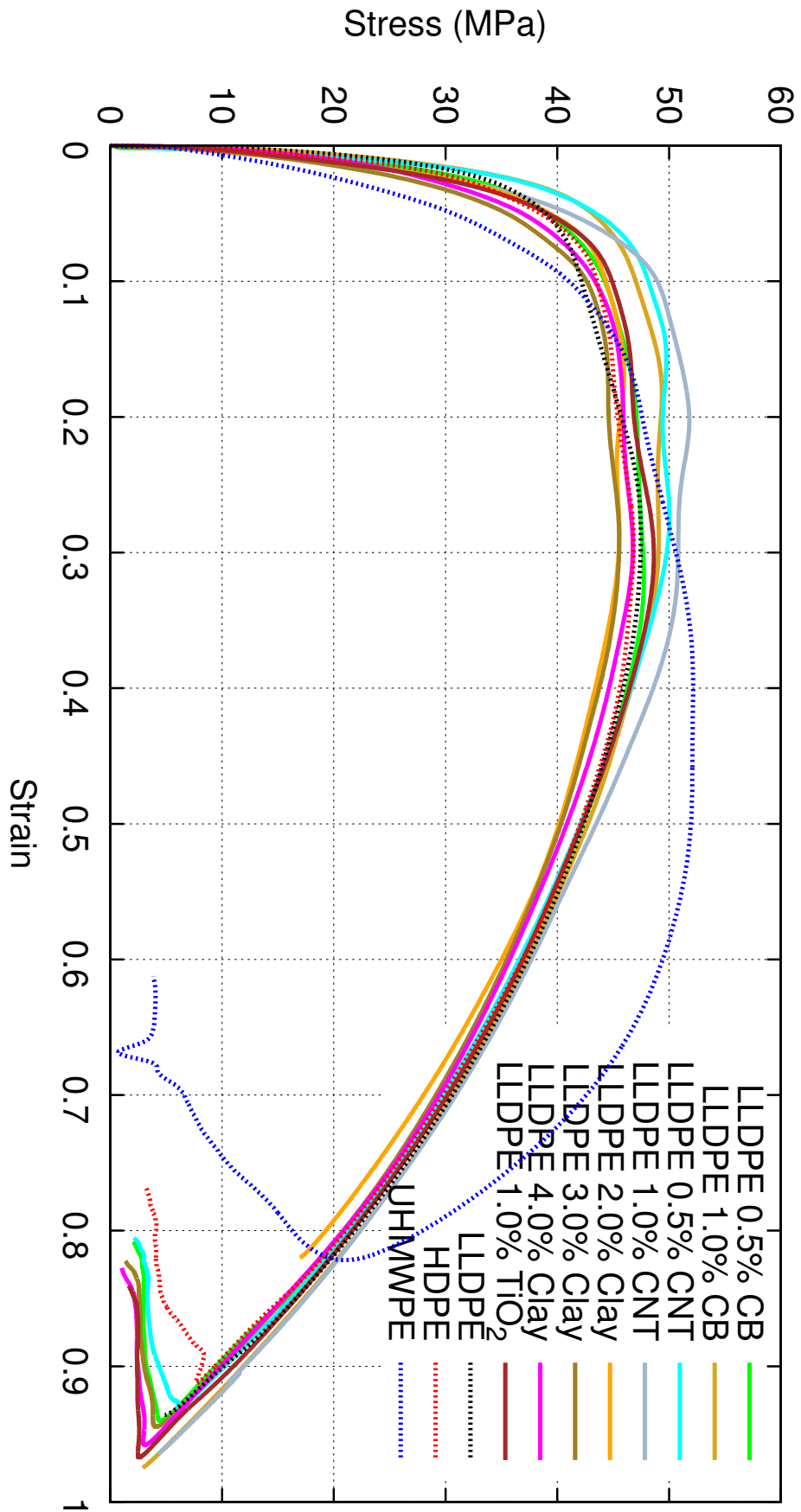


FIGURE L.4: SHPB true stress/strain curves for LLDPE nanocomposites.

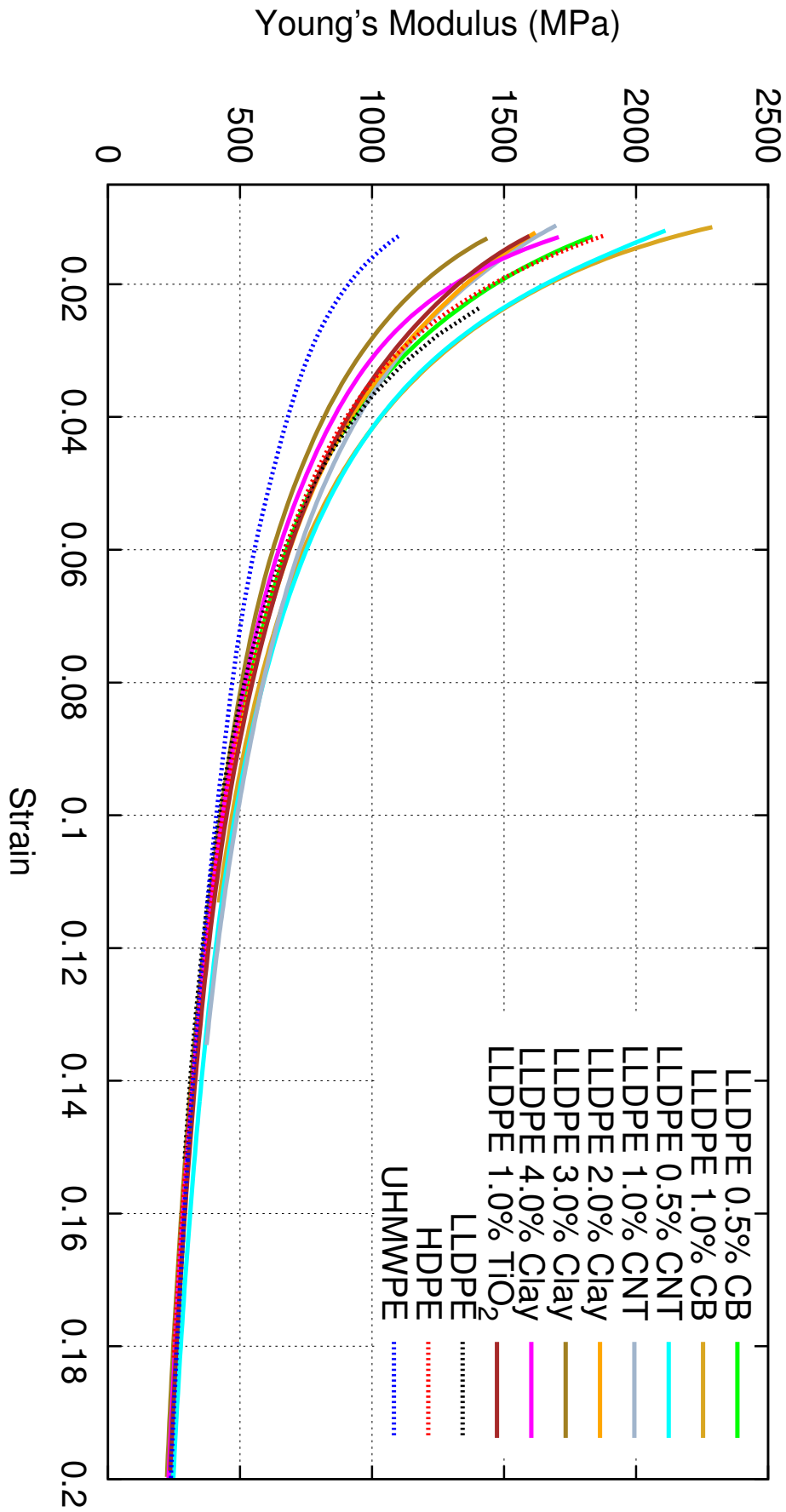


FIGURE L.5: SHPB Young's modulus evolution for LLDPE nanocomposites.

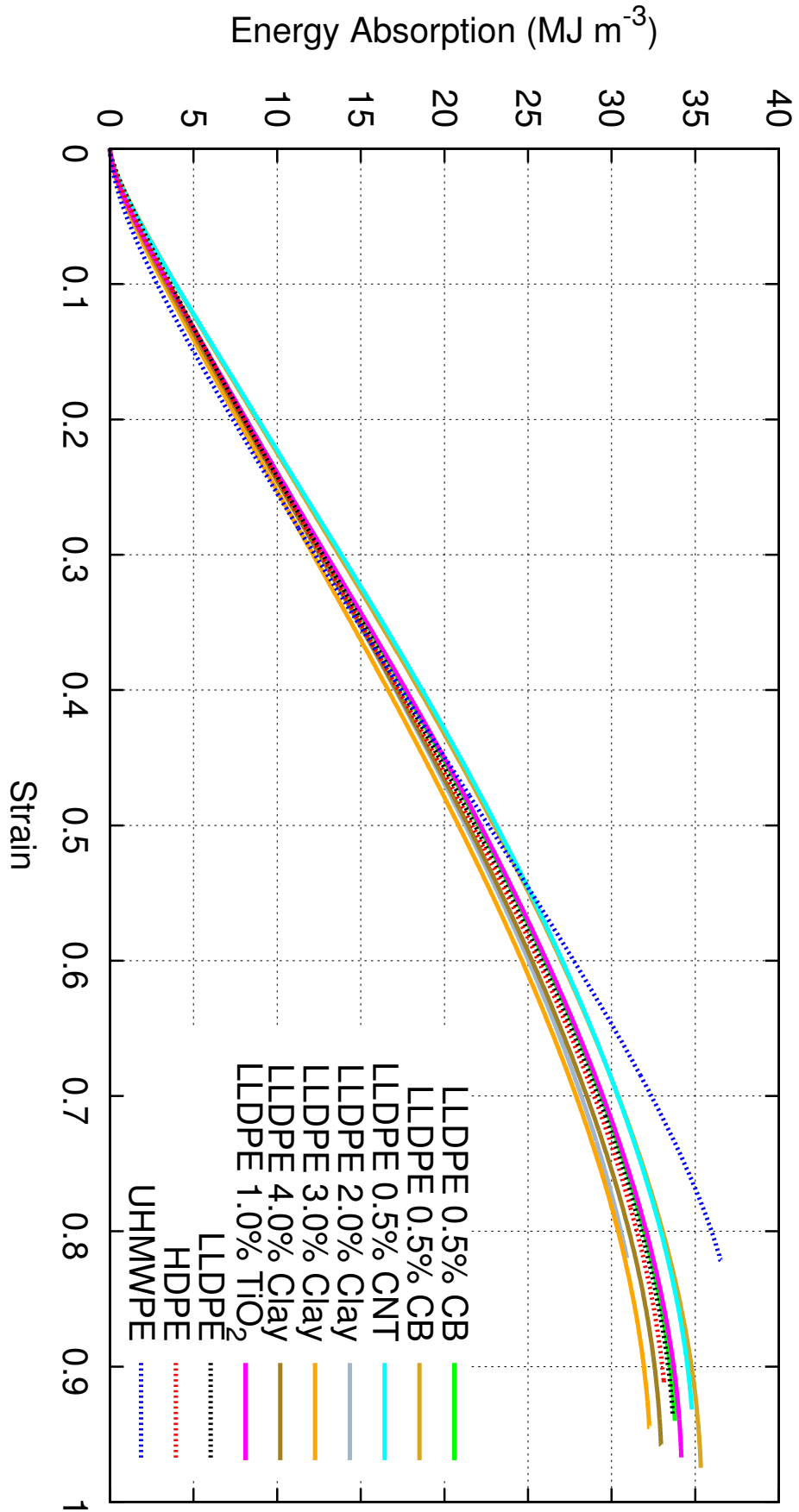


FIGURE L.6: SHPB energy absorption for LLDPE nanocomposites.

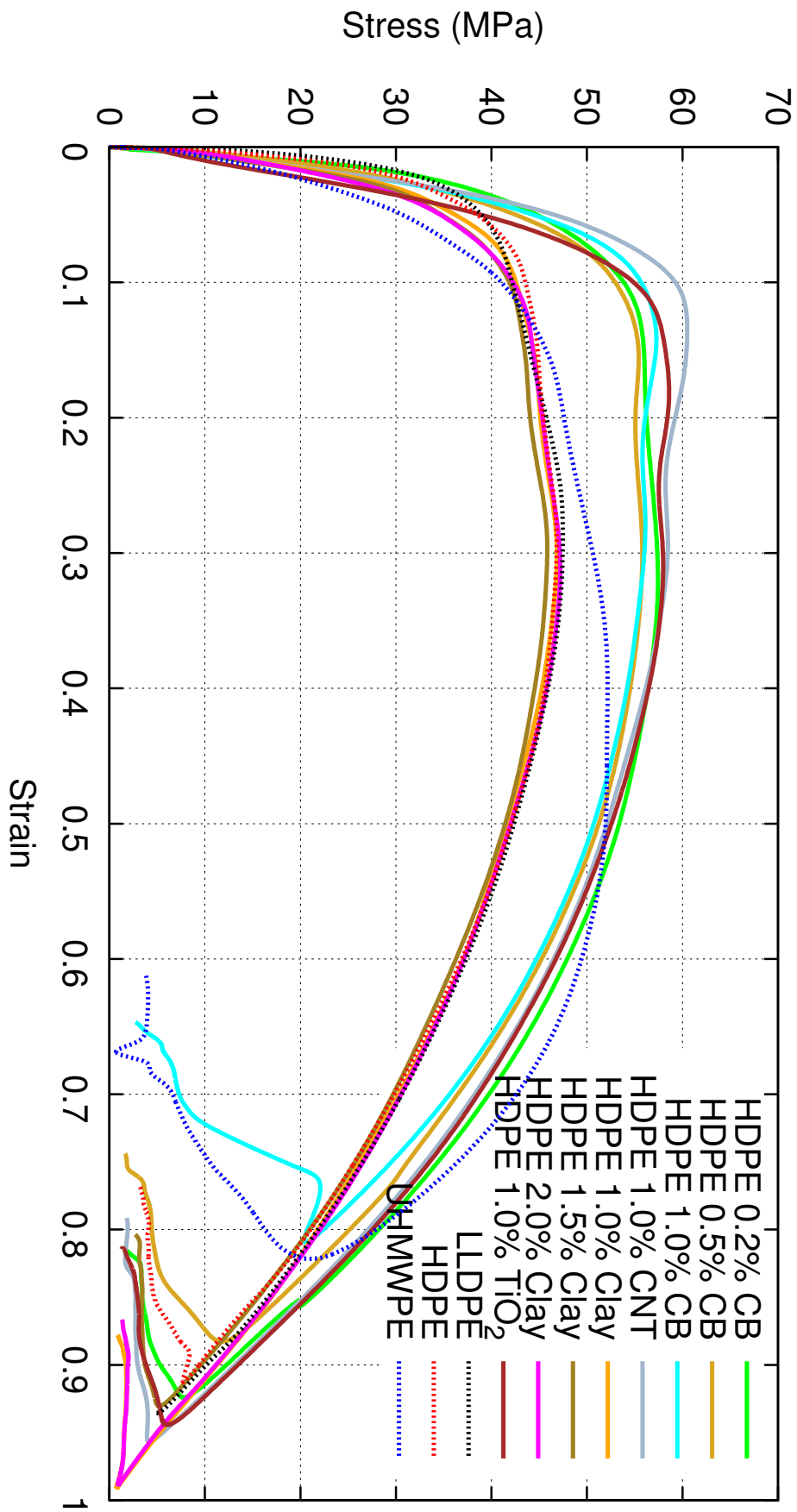


FIGURE L.7: SHPB true stress/strain curves for HDPE nanocomposites.

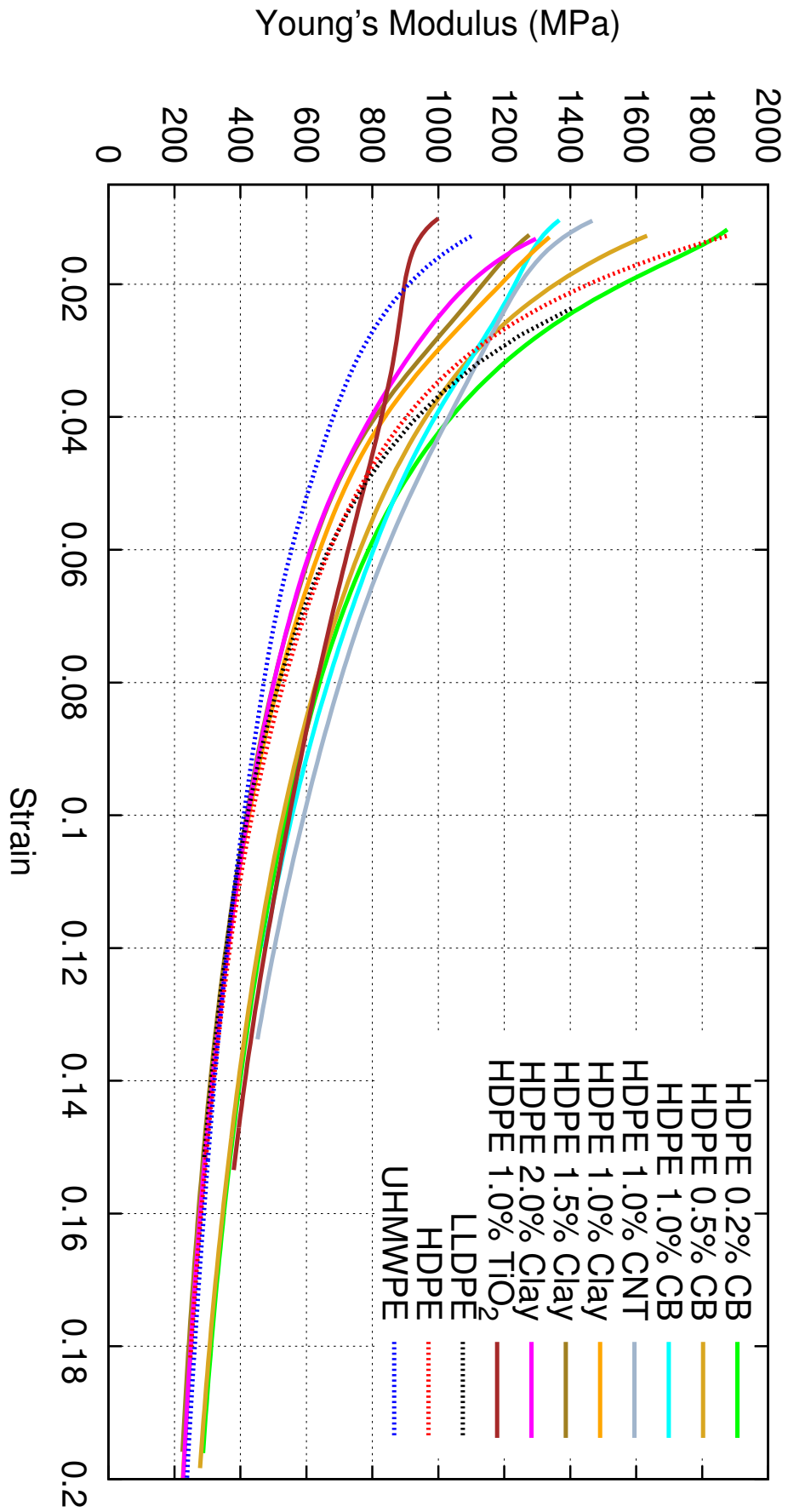


FIGURE L.8: SHPB Young's modulus evolution for HDPE nanocomposites.

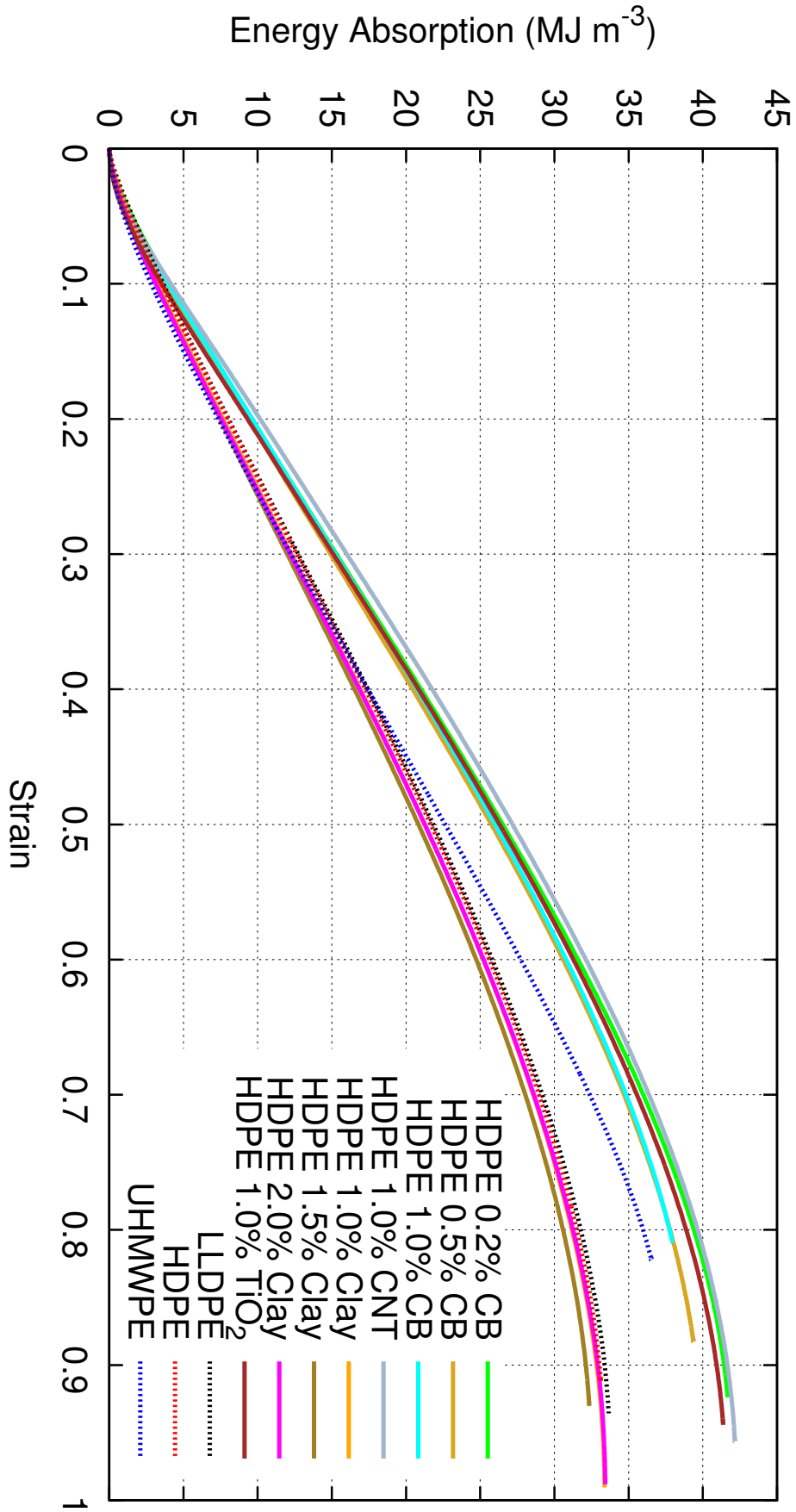


FIGURE L.9: SHPB energy absorption for HDPE nanocomposites.

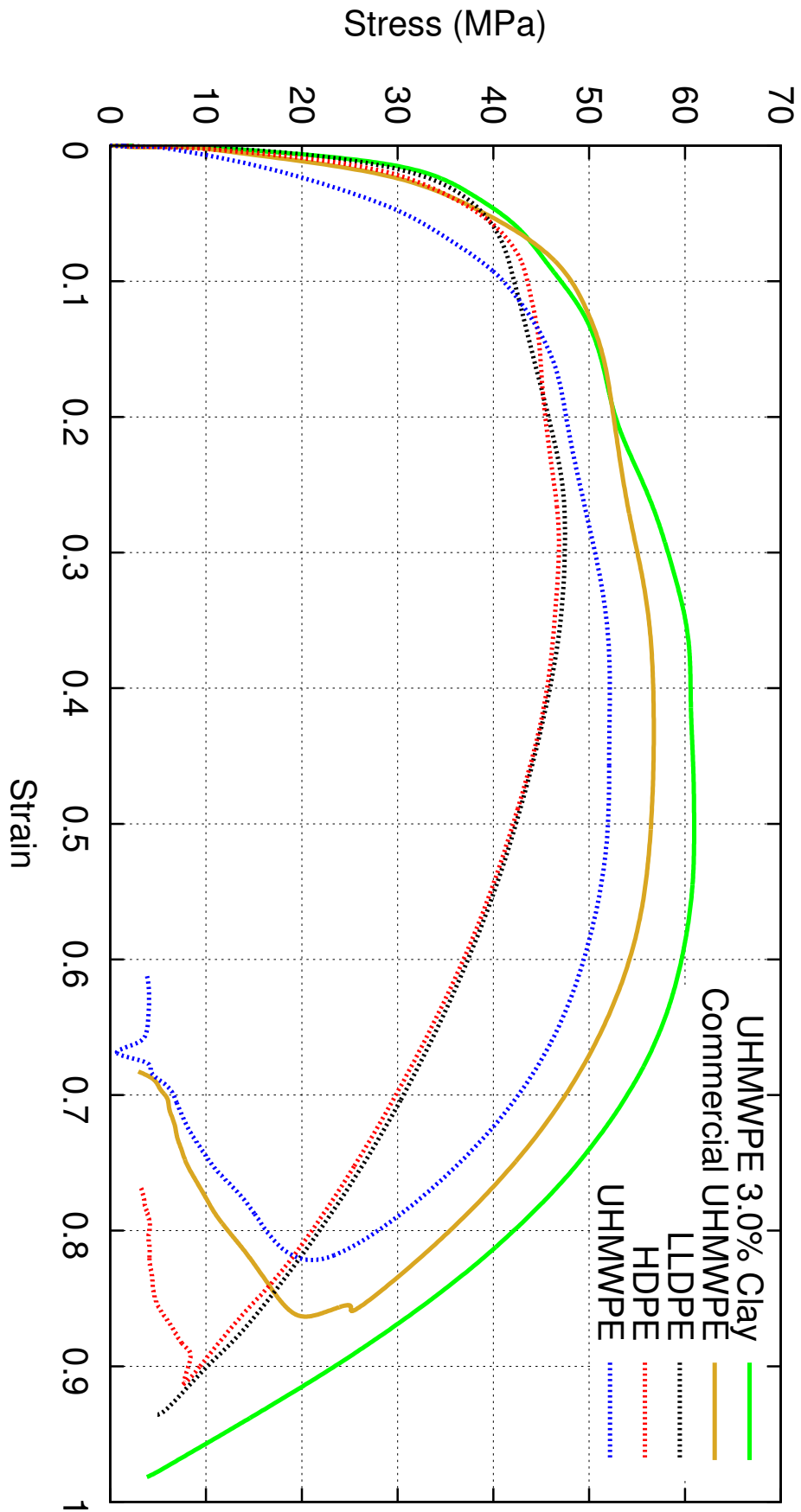


FIGURE L.10: SHPB true stress/strain curves for UHMWPE nanocomposites.

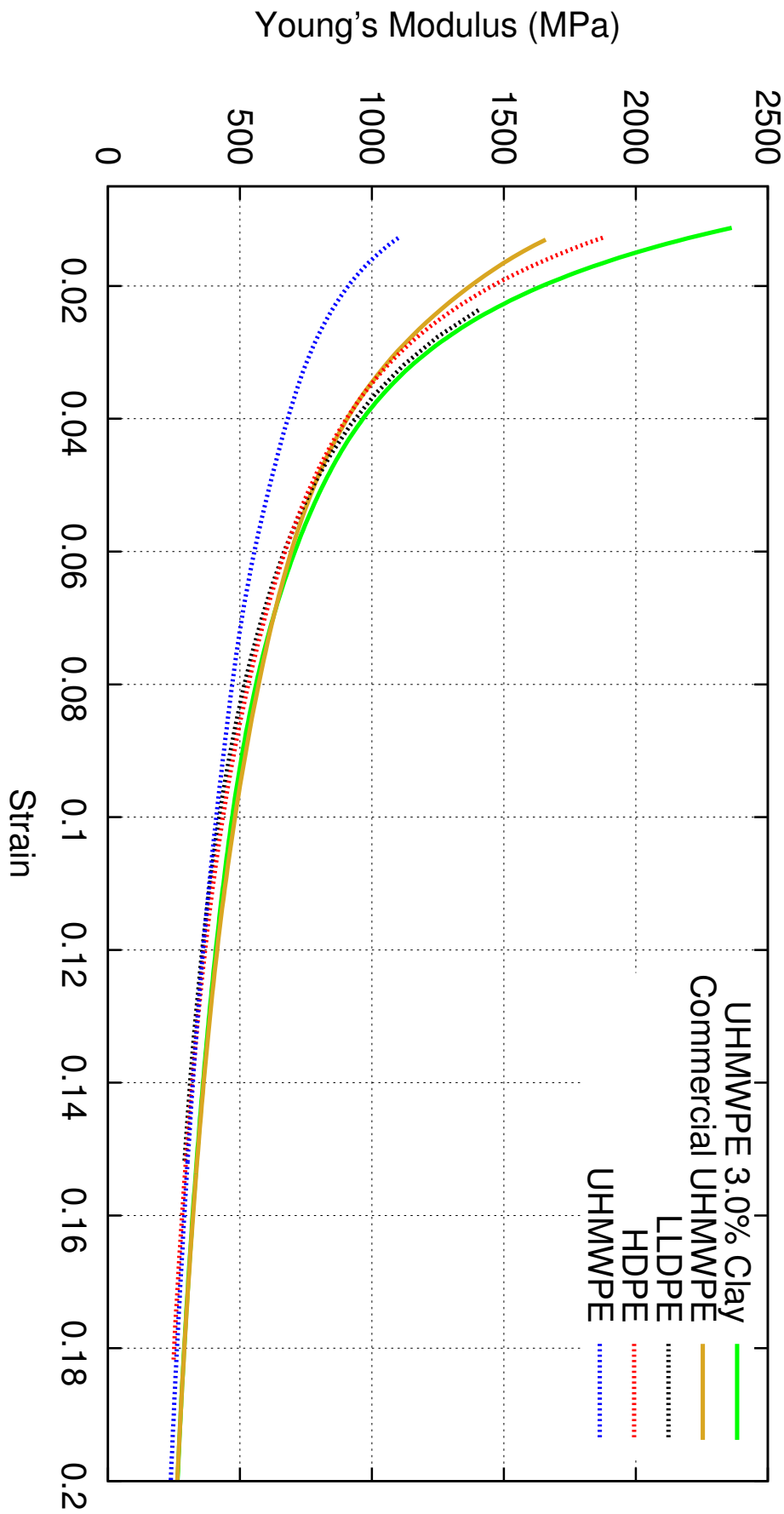


FIGURE L.11: SHPB Young's modulus evolution for UHMWPE nanocomposites.

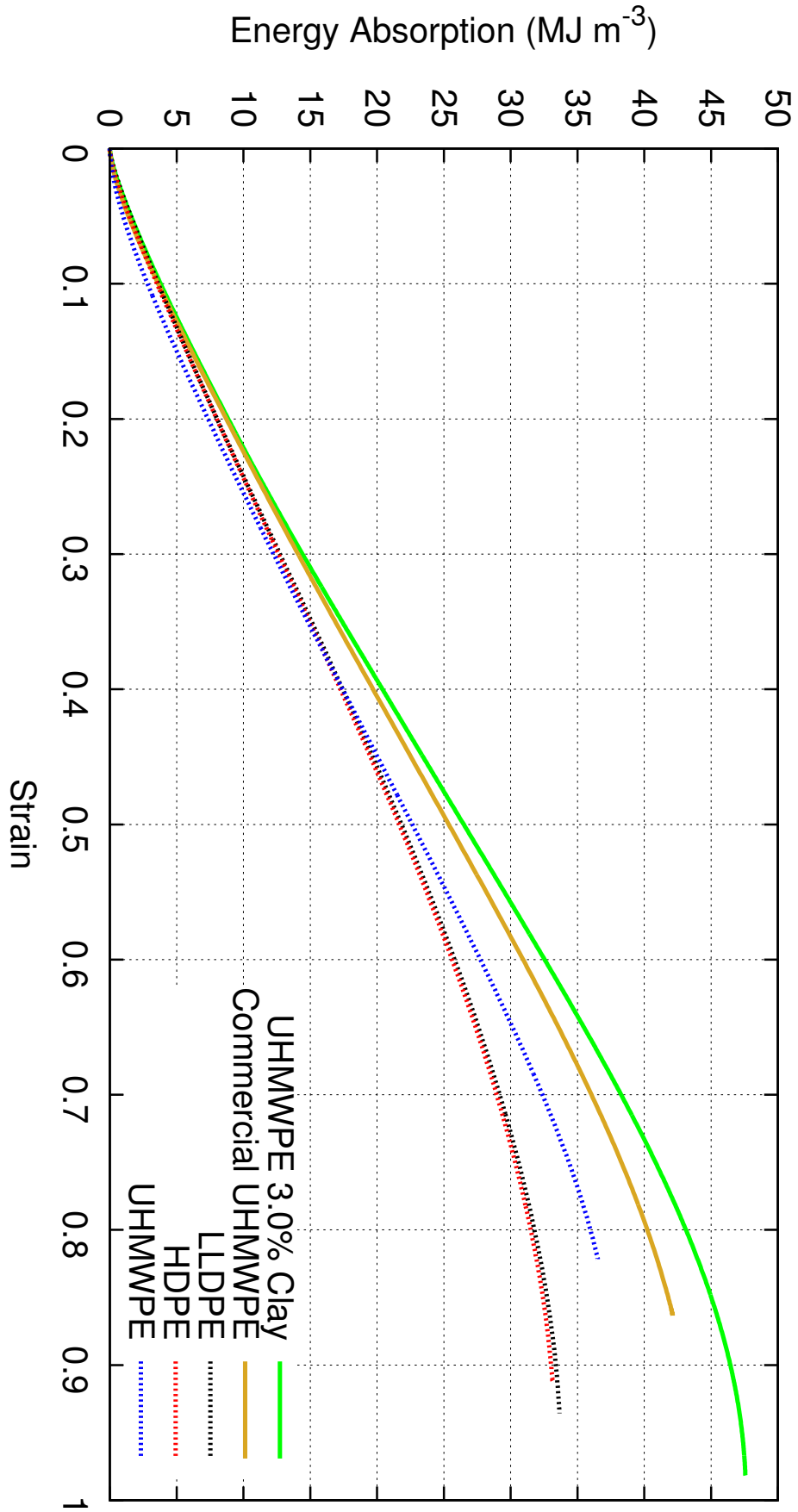


FIGURE L.12: SHPB energy absorption for UHMWPE nanocomposites.

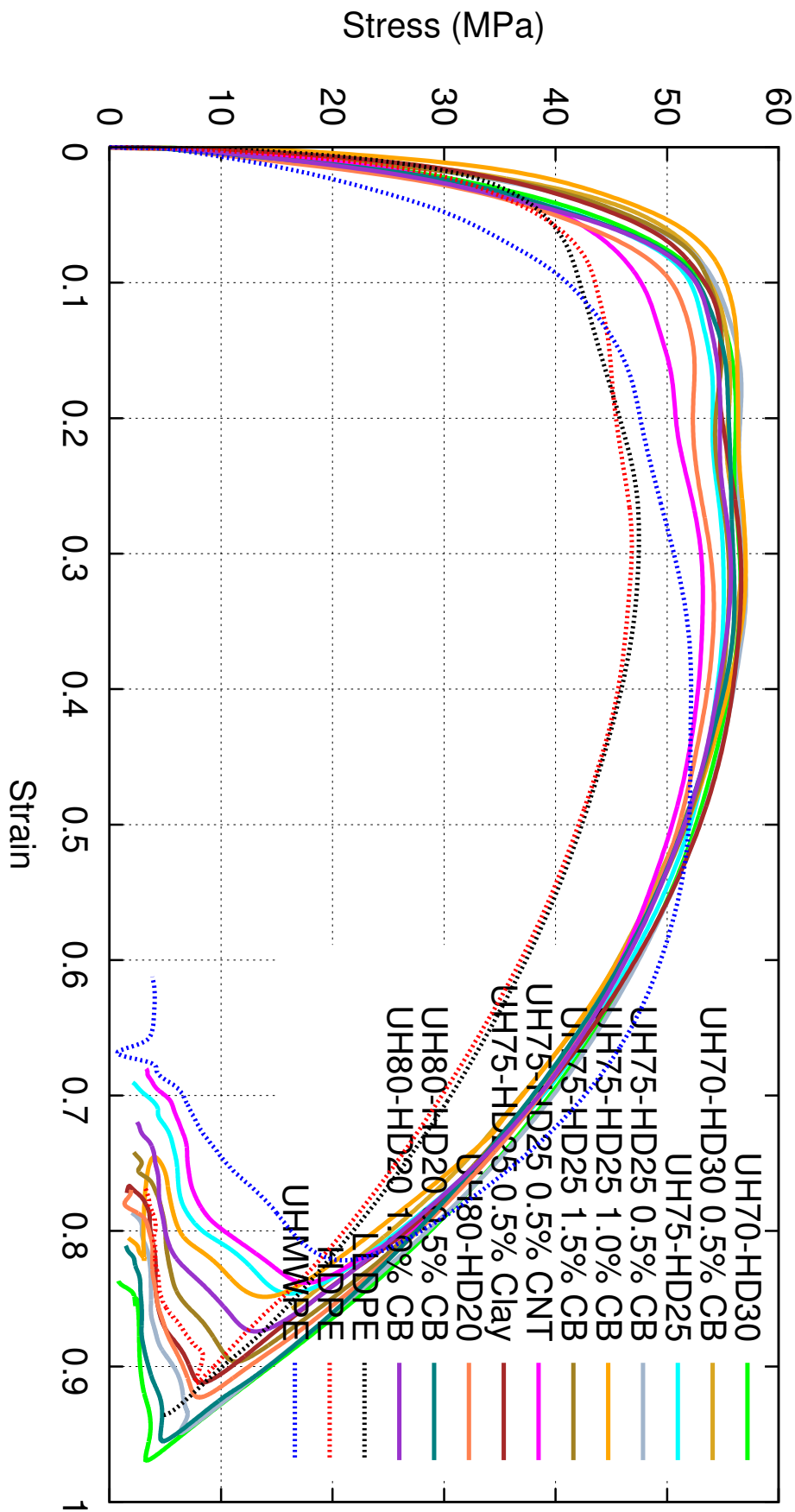


FIGURE L.13: SHPB true stress/strain curves for PE blends and nanocomposites.

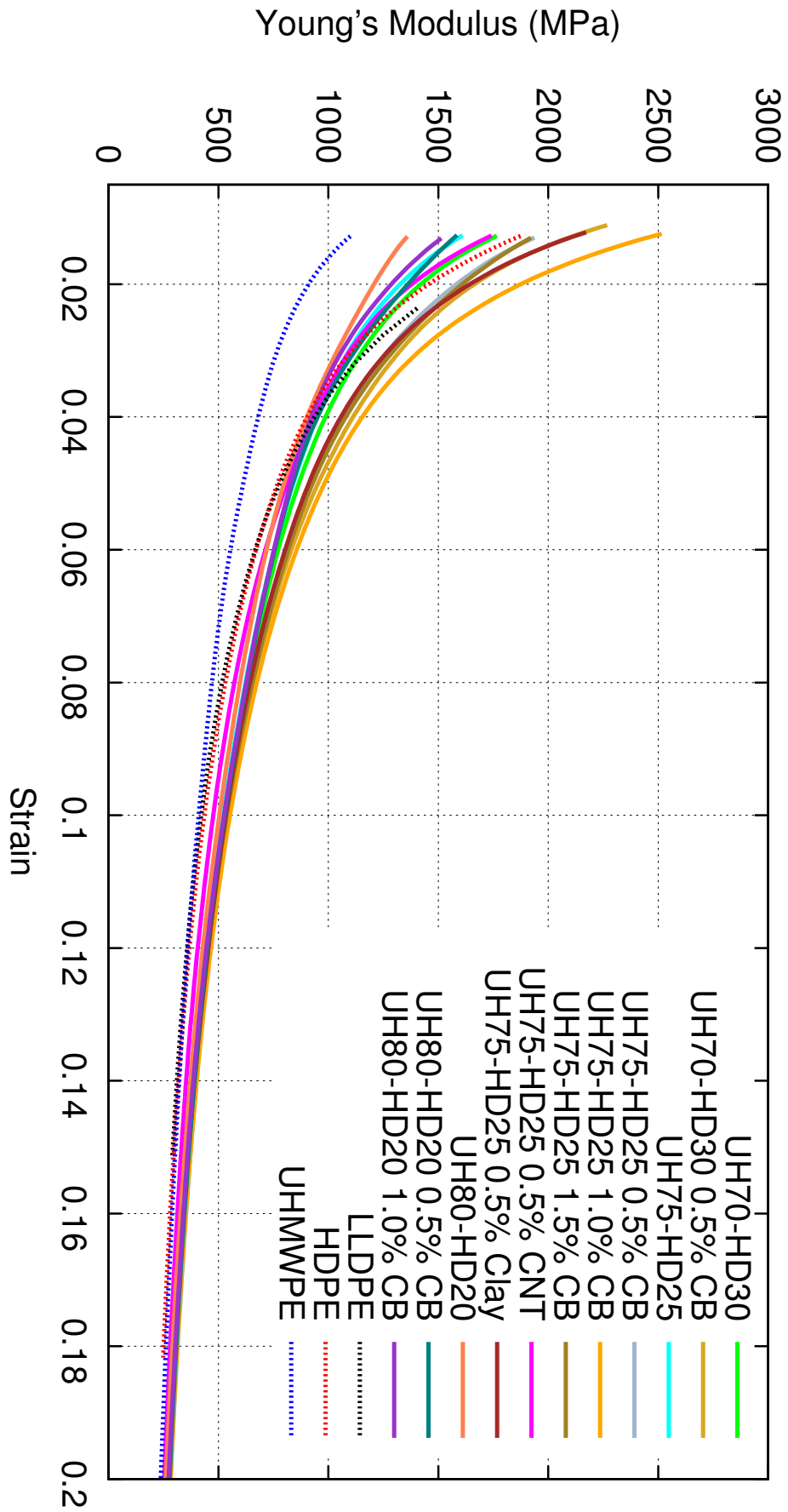


FIGURE L.14: SHPB Young's modulus evolution for PE blends and nanocomposites.

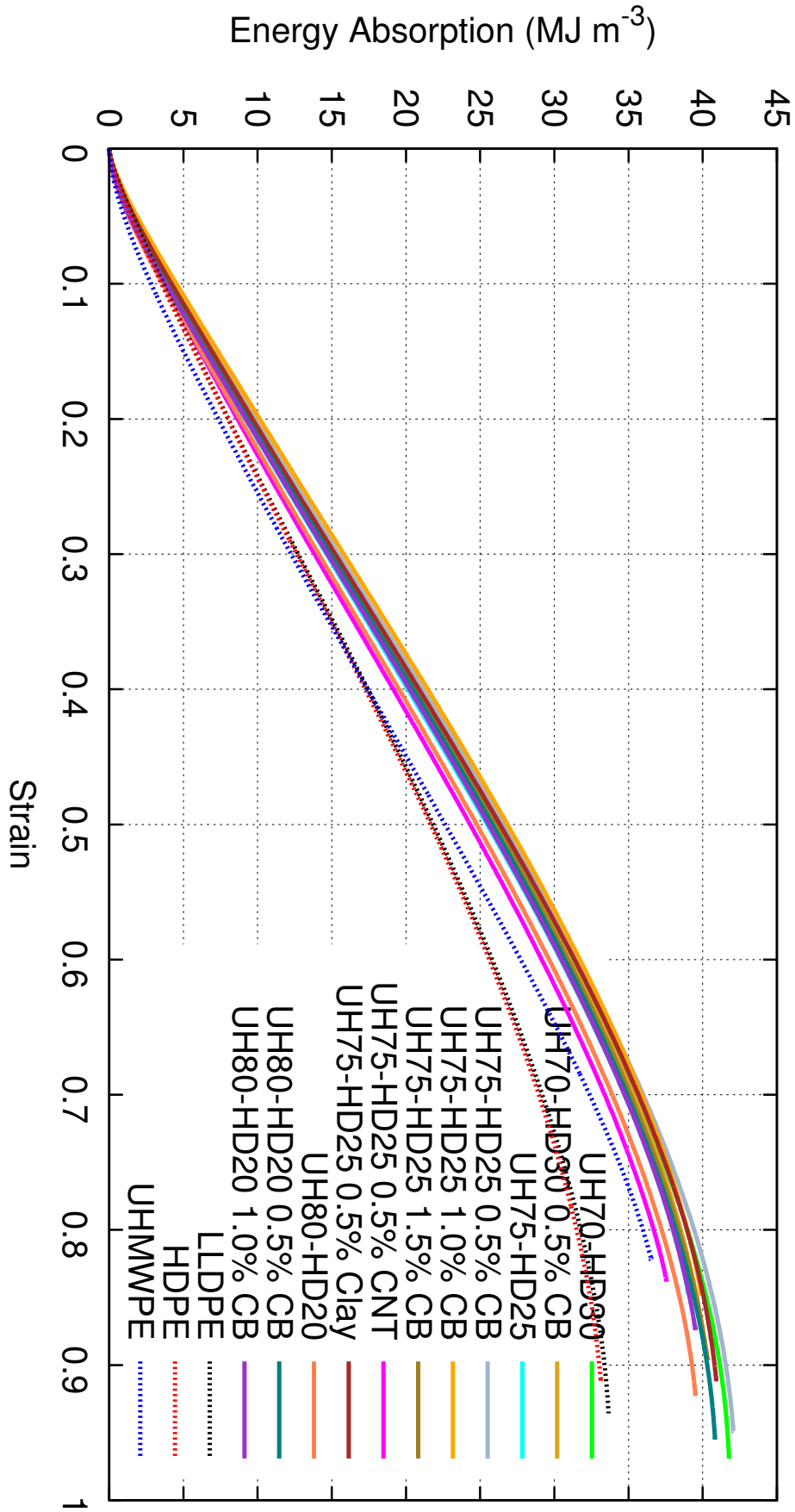


FIGURE L.15: SHPB energy absorption for PE blends and nanocomposites.

L.2 Optical Dropweight

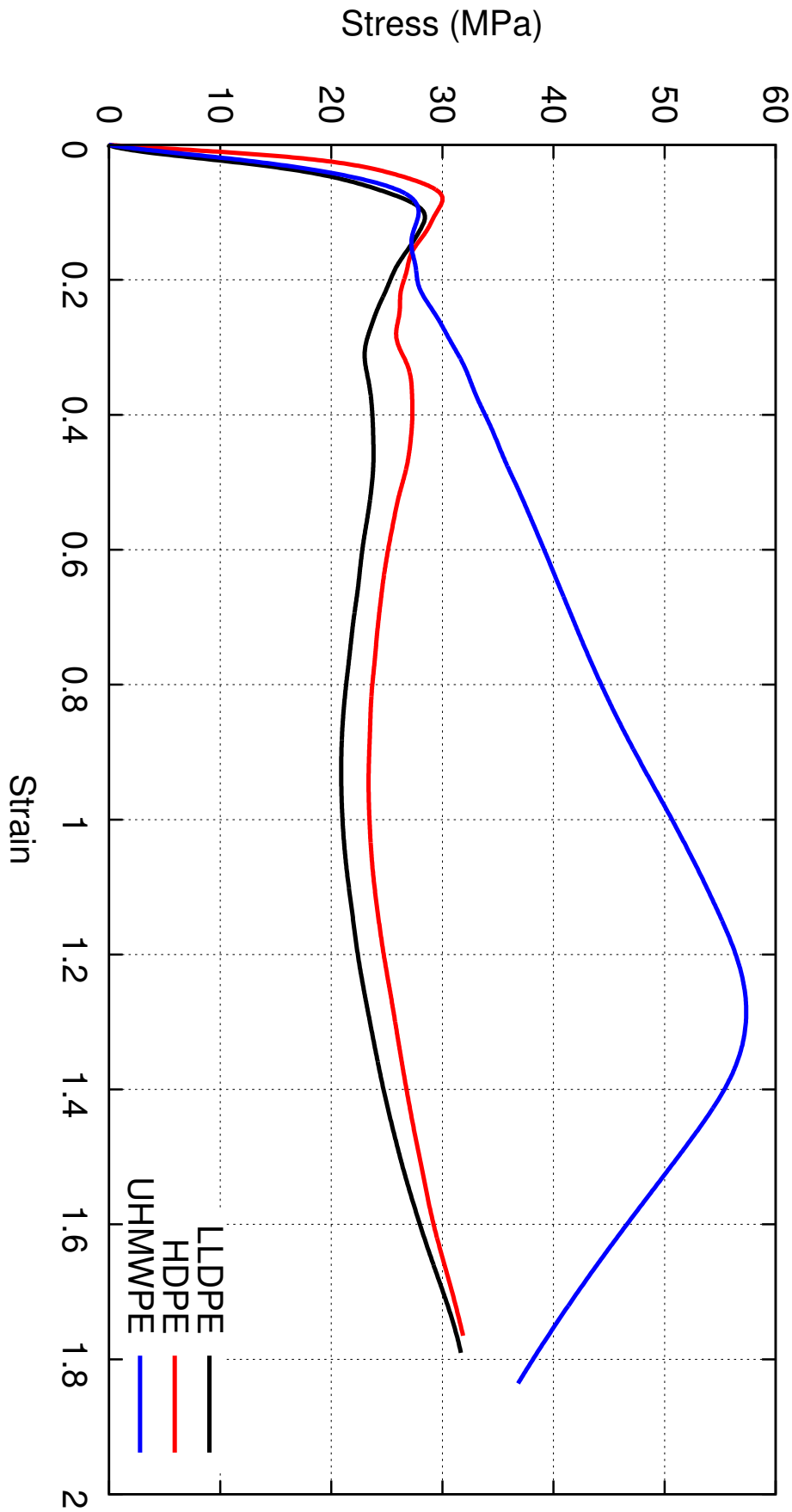


FIGURE L.16: ODW true stress/strain curves for LLDPE, HDPE and UHMWPE.

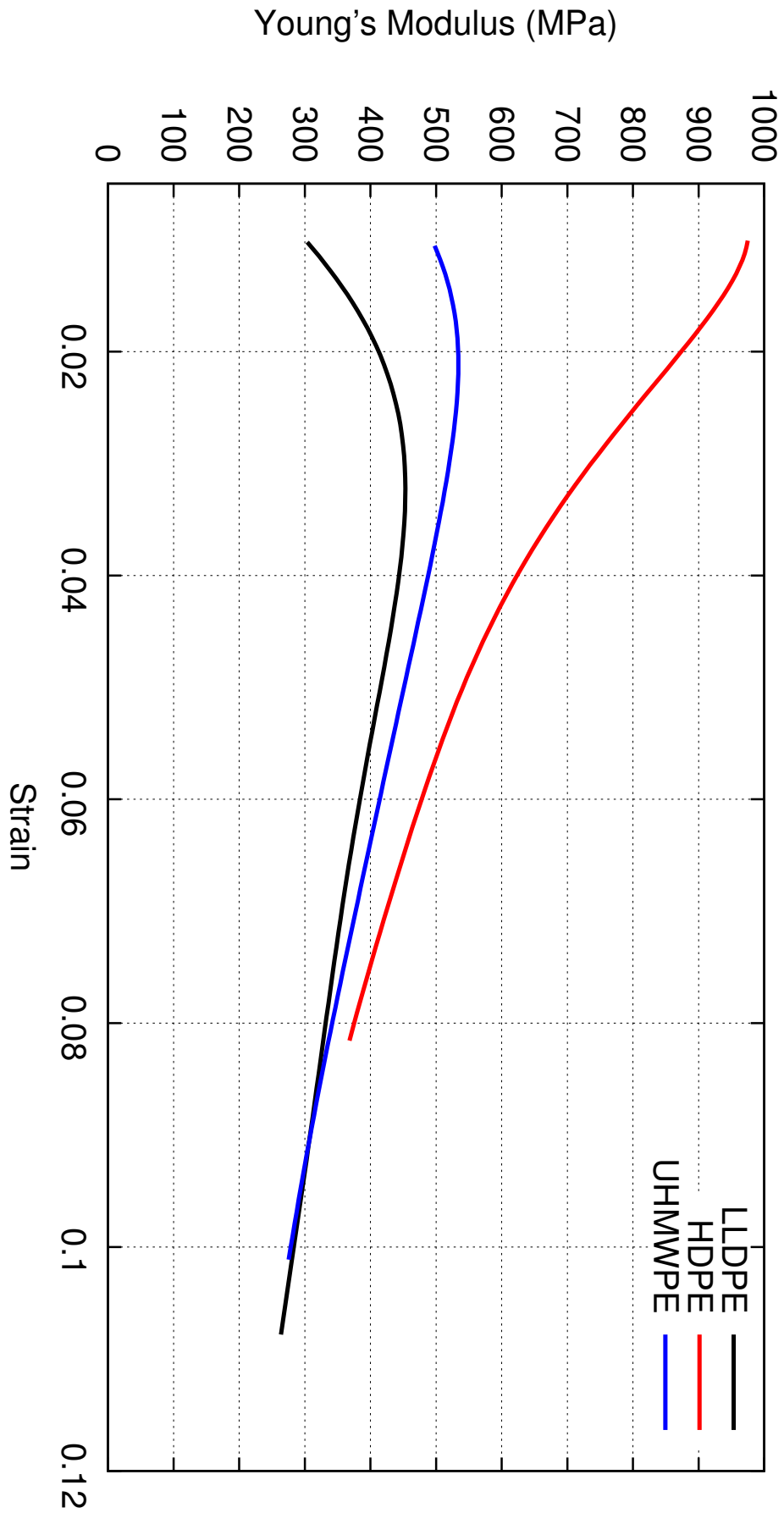


FIGURE L.17: ODW Young's modulus evolution for LLDPE, HDPE and UHMWPE.

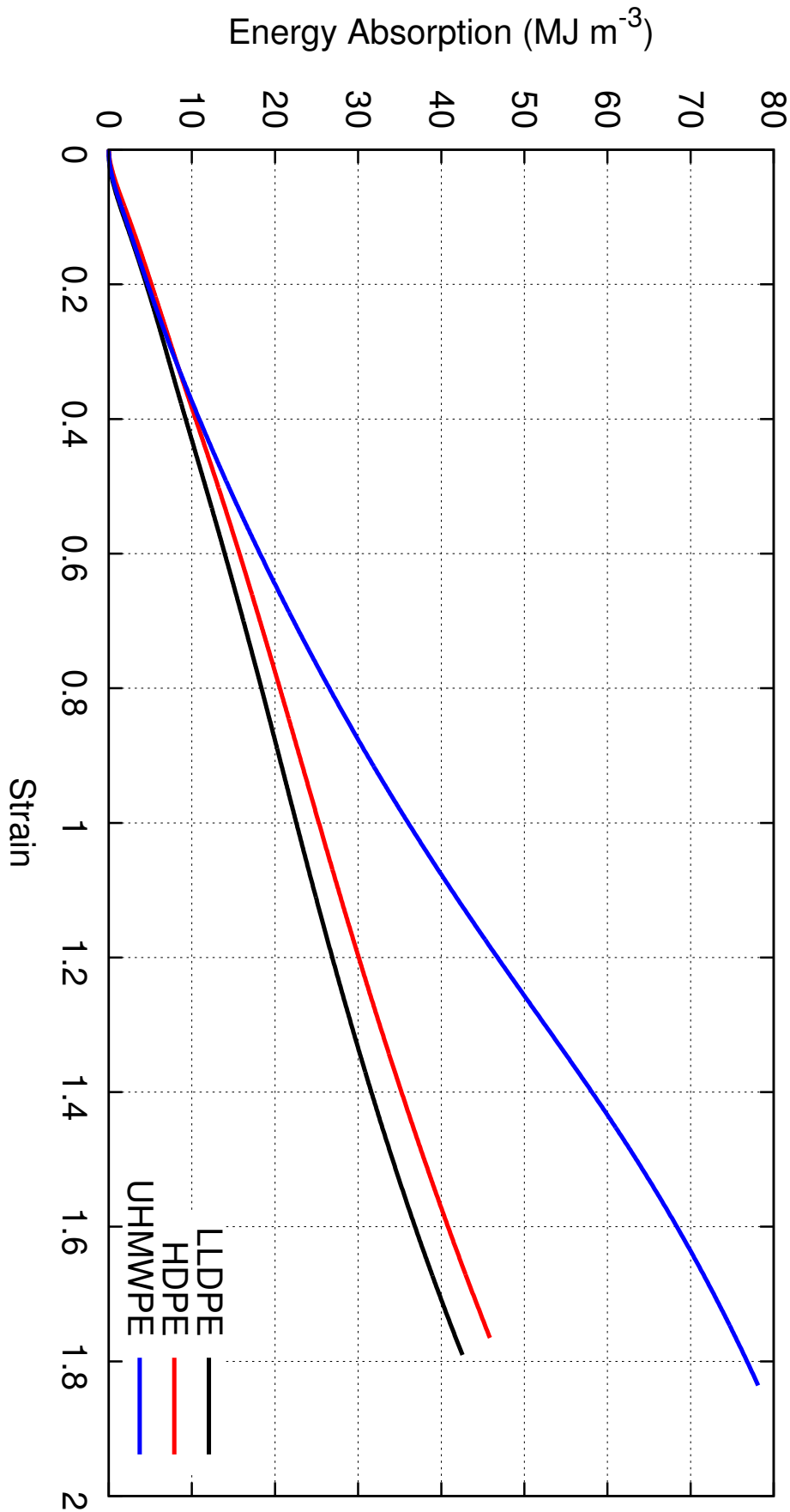


FIGURE L.18: ODW energy absorption for LLDPE, HDPE and UHMWPE.

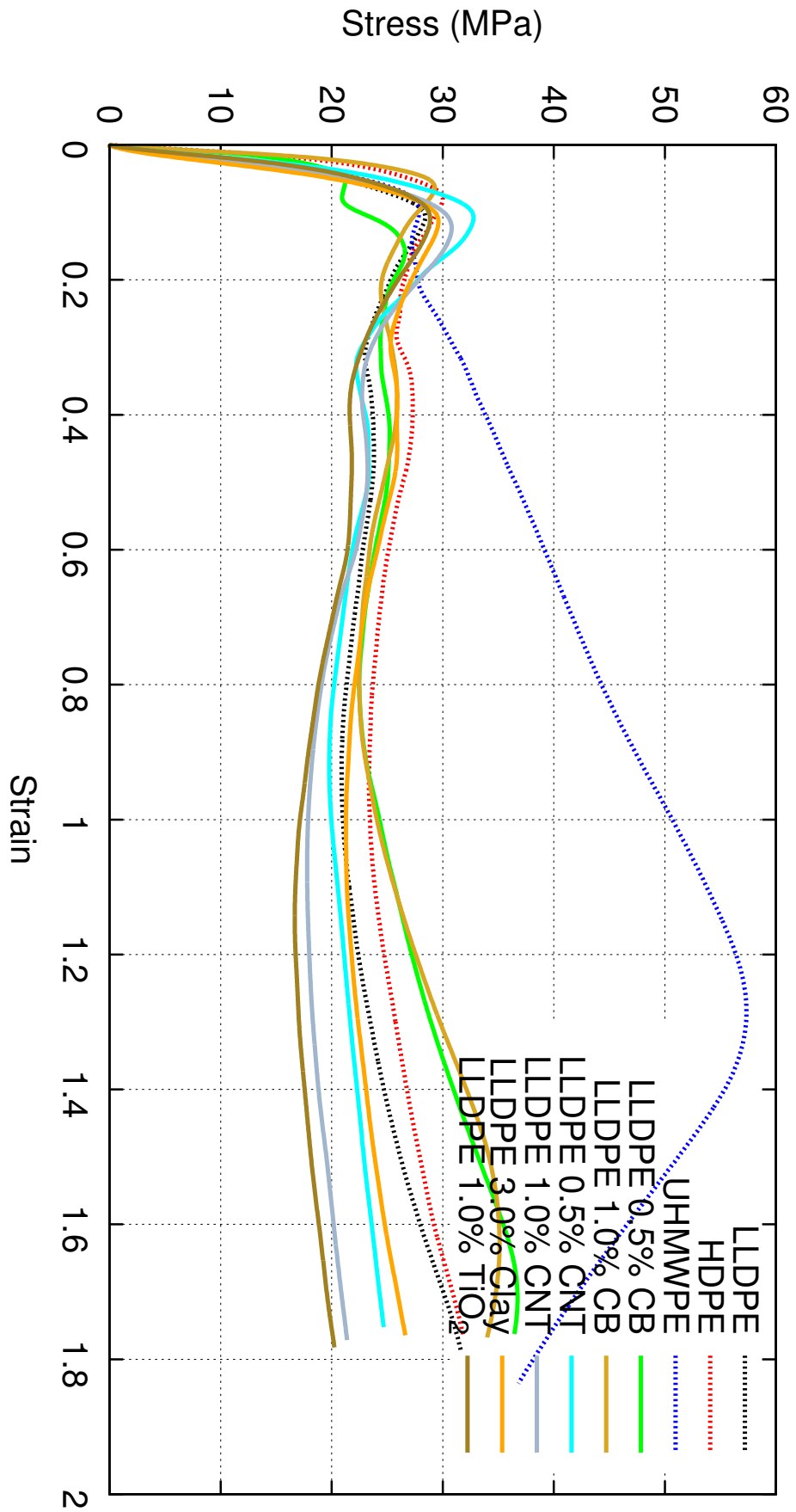


FIGURE L.19: ODW true stress/strain curves for LLDPE nanocomposites.

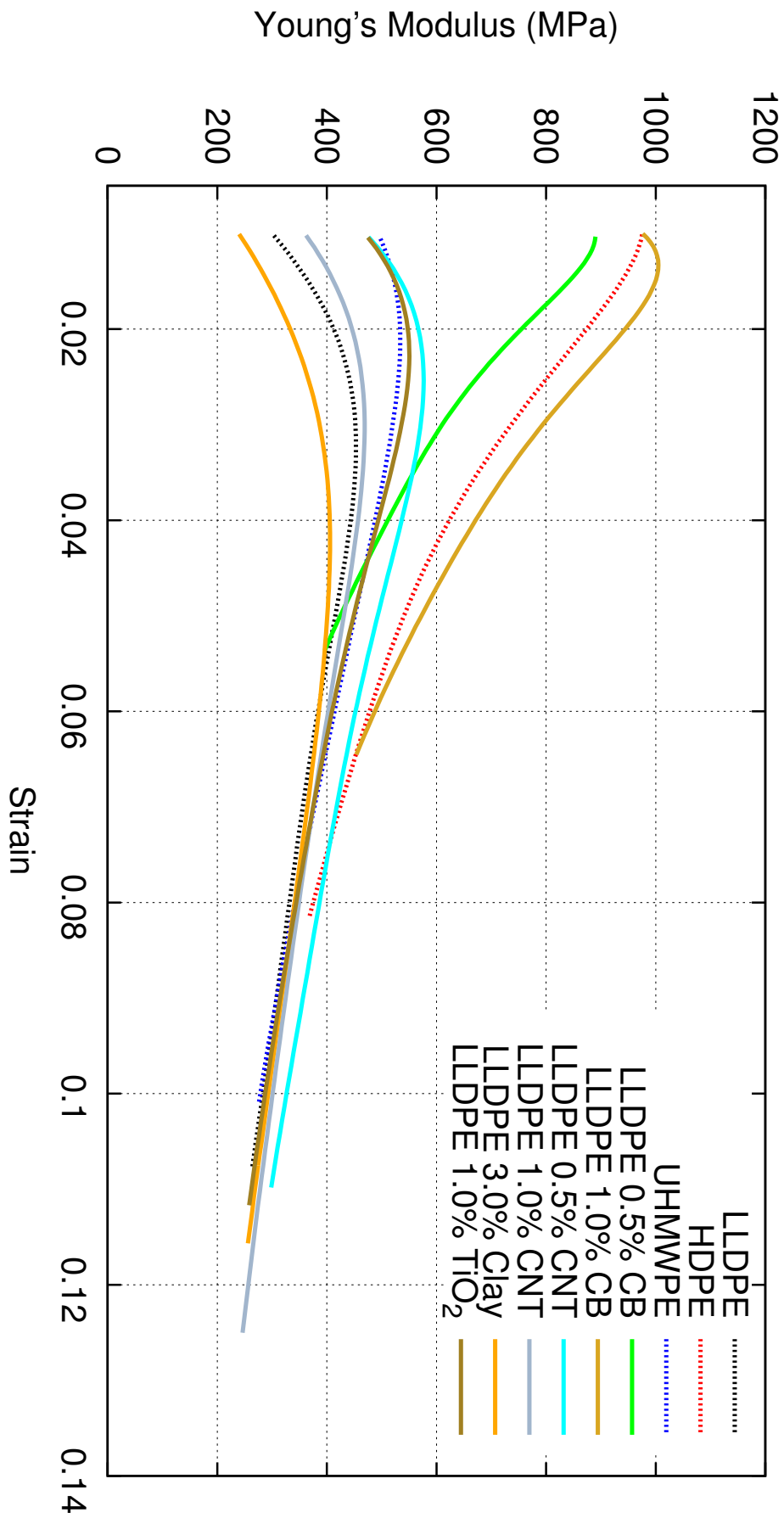


FIGURE L.20: ODW Young's modulus evolution for LLDPE nanocomposites.

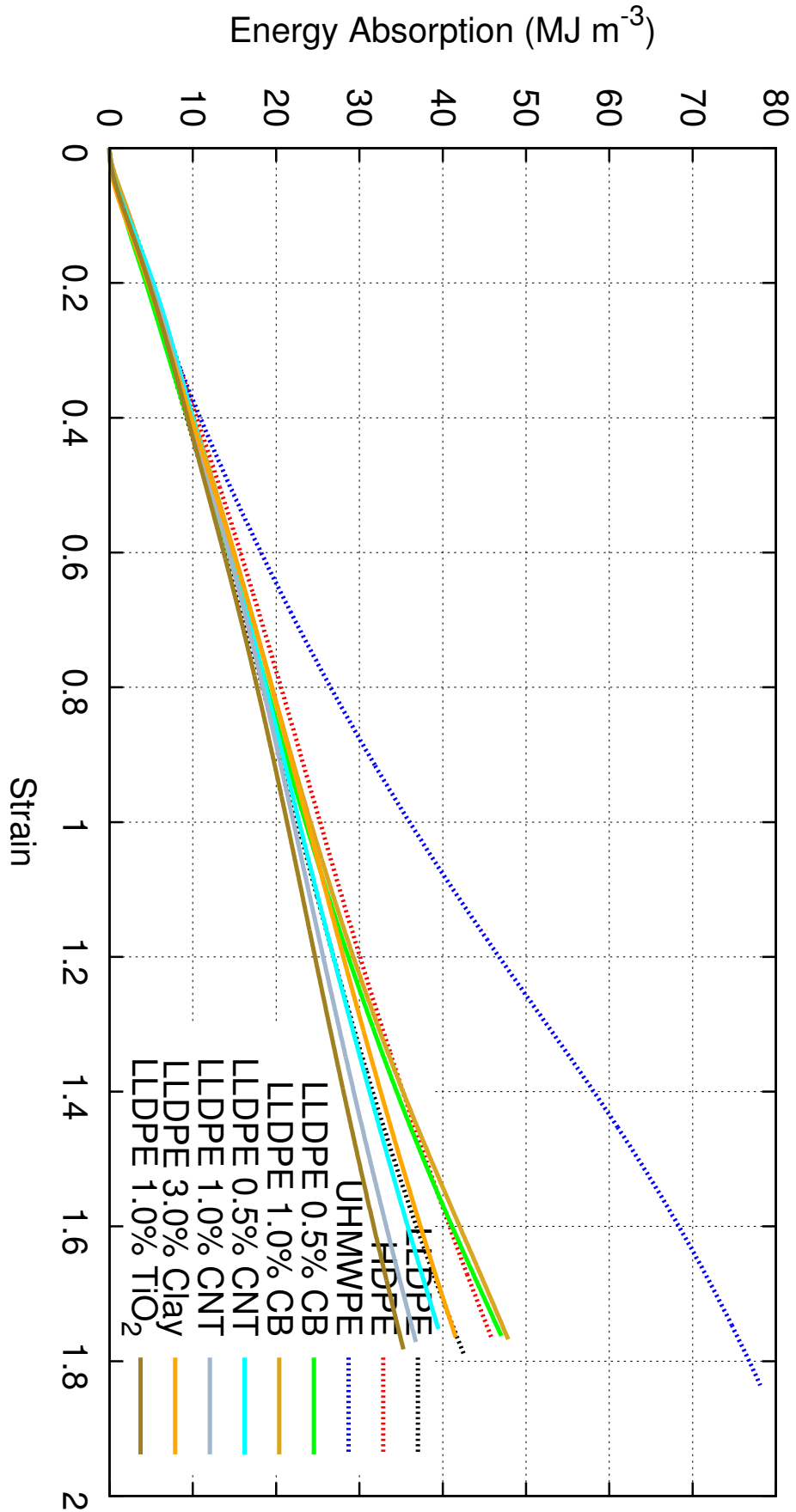


FIGURE L.21: ODW energy absorption for LLDPE nanocomposites.

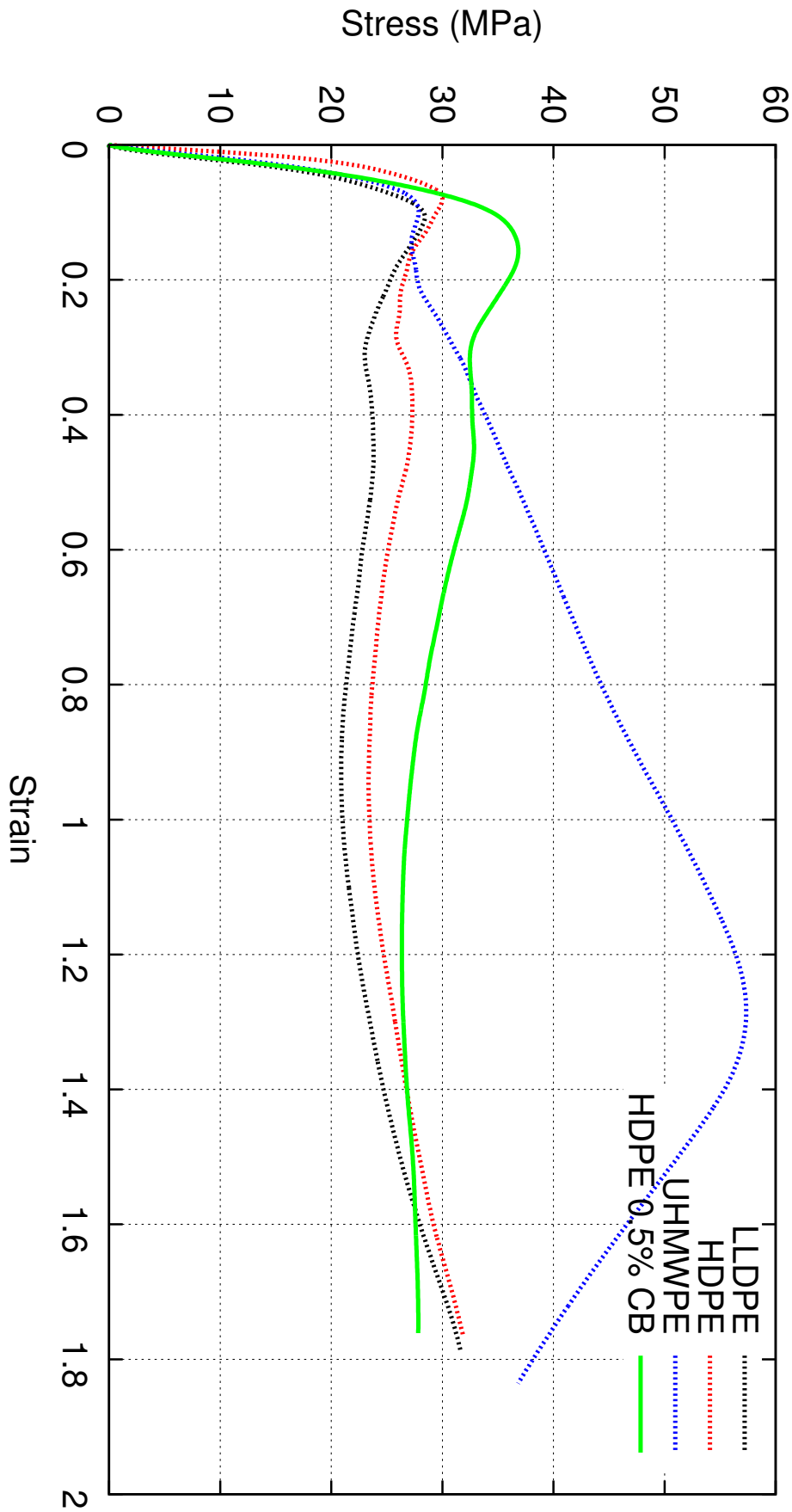


FIGURE L.22: ODW true stress/strain curves for HDPE nanocomposites.

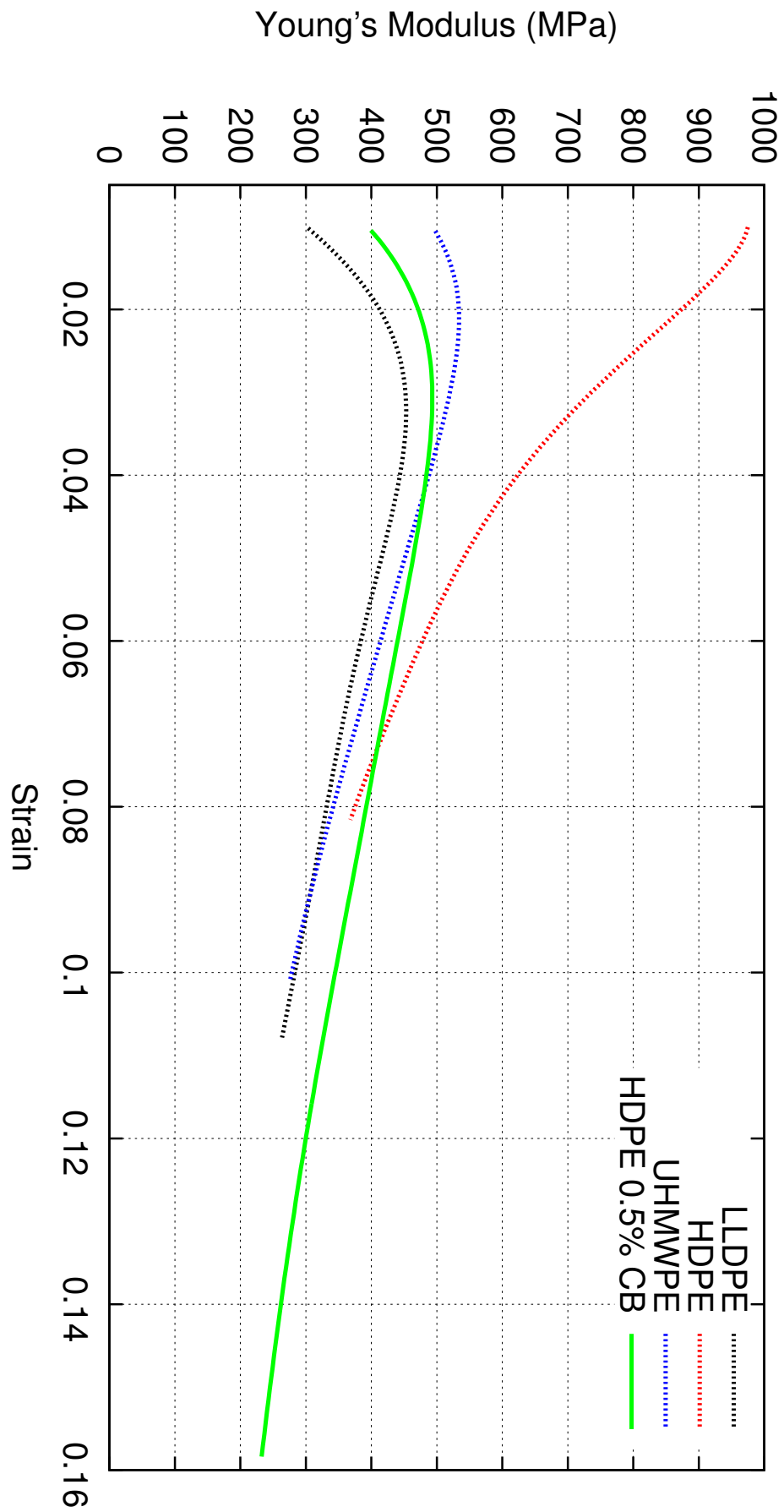


FIGURE L.23: ODW Young's modulus evolution for HDPE nanocomposites.

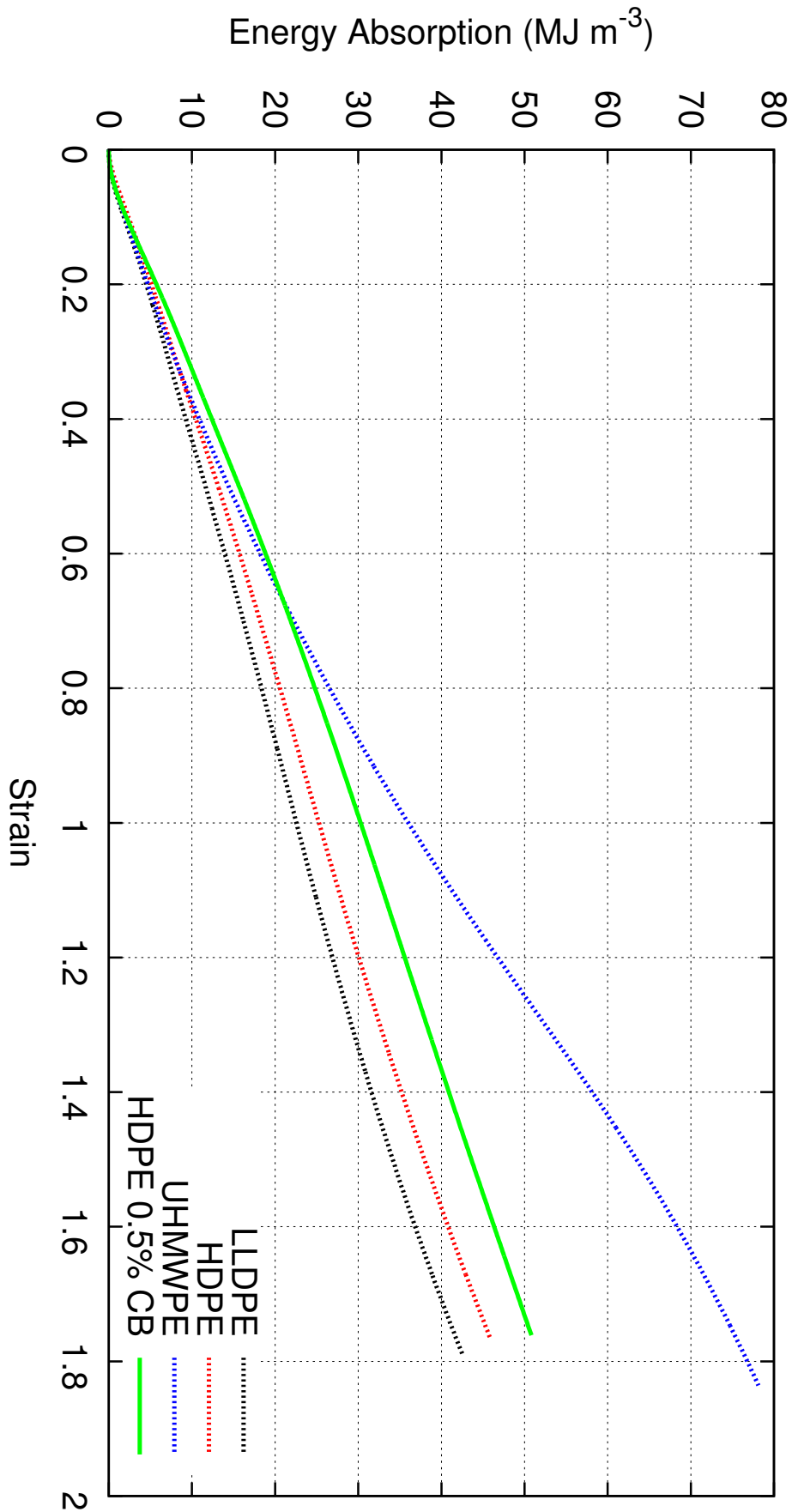


FIGURE L.24: ODW energy absorption for HDPE nanocomposites.

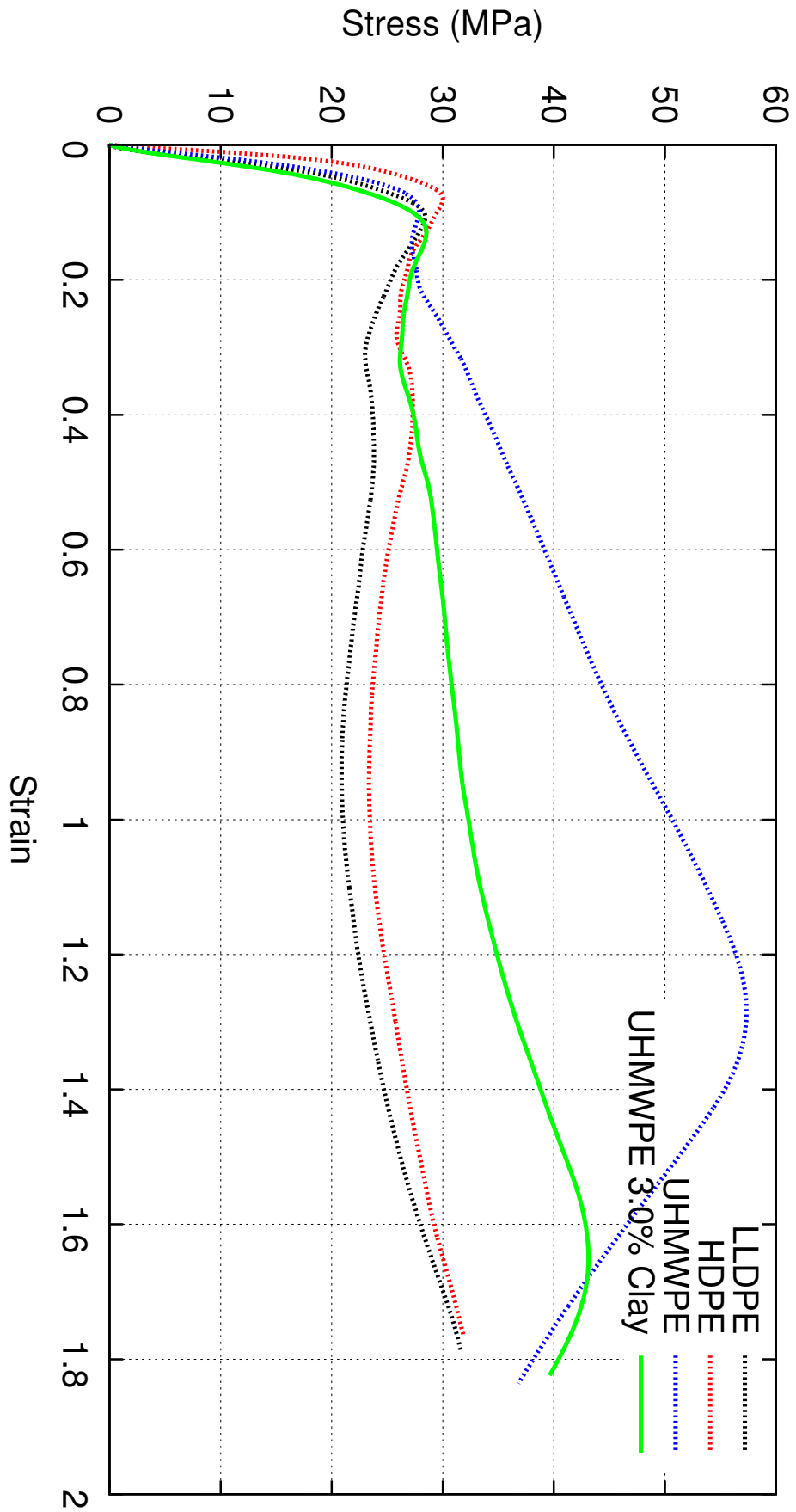


FIGURE L.25: ODW true stress/strain curves for UHMWPE nanocomposites.

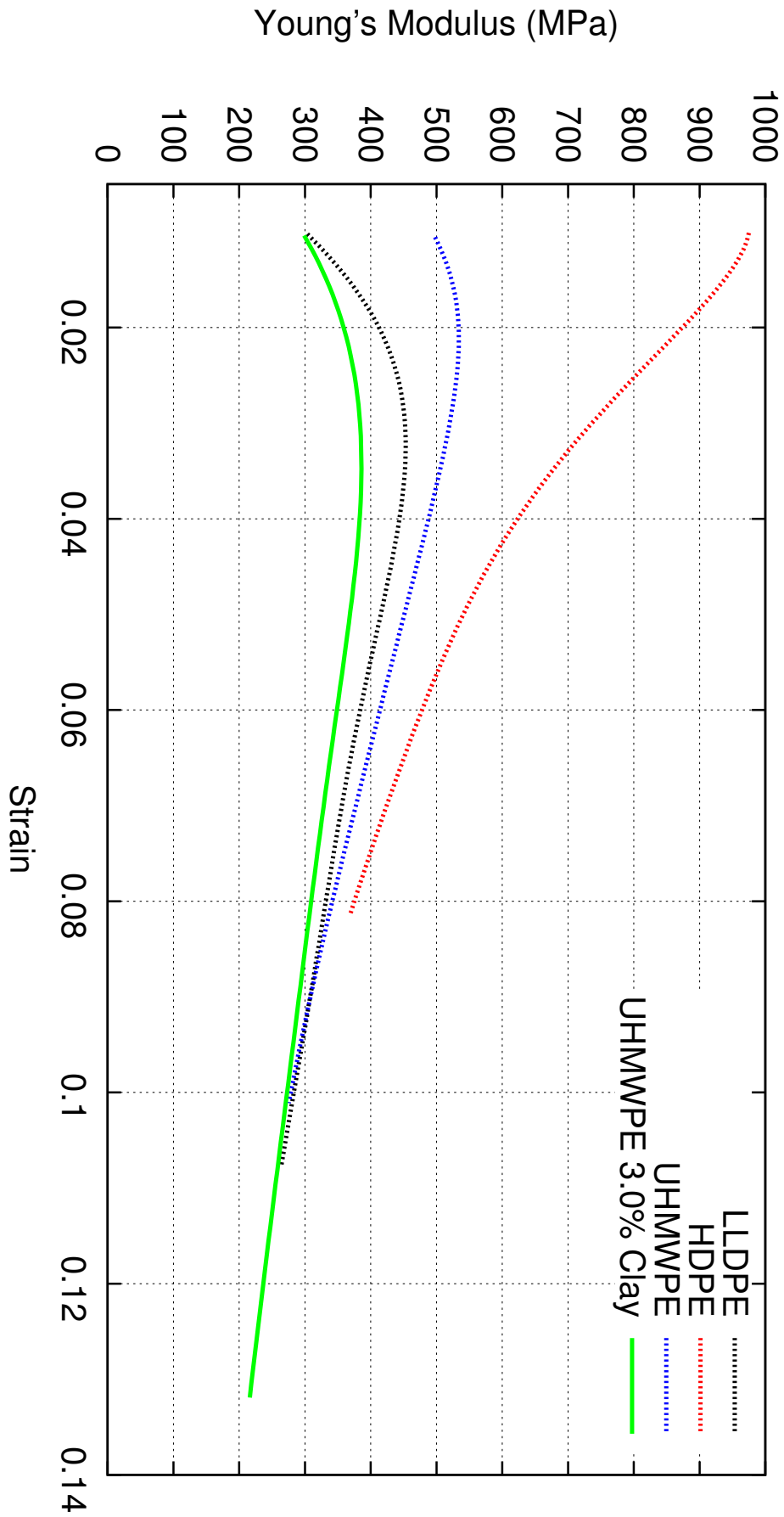


FIGURE L.26: ODW Young's modulus evolution for UHMWPE nanocomposites.

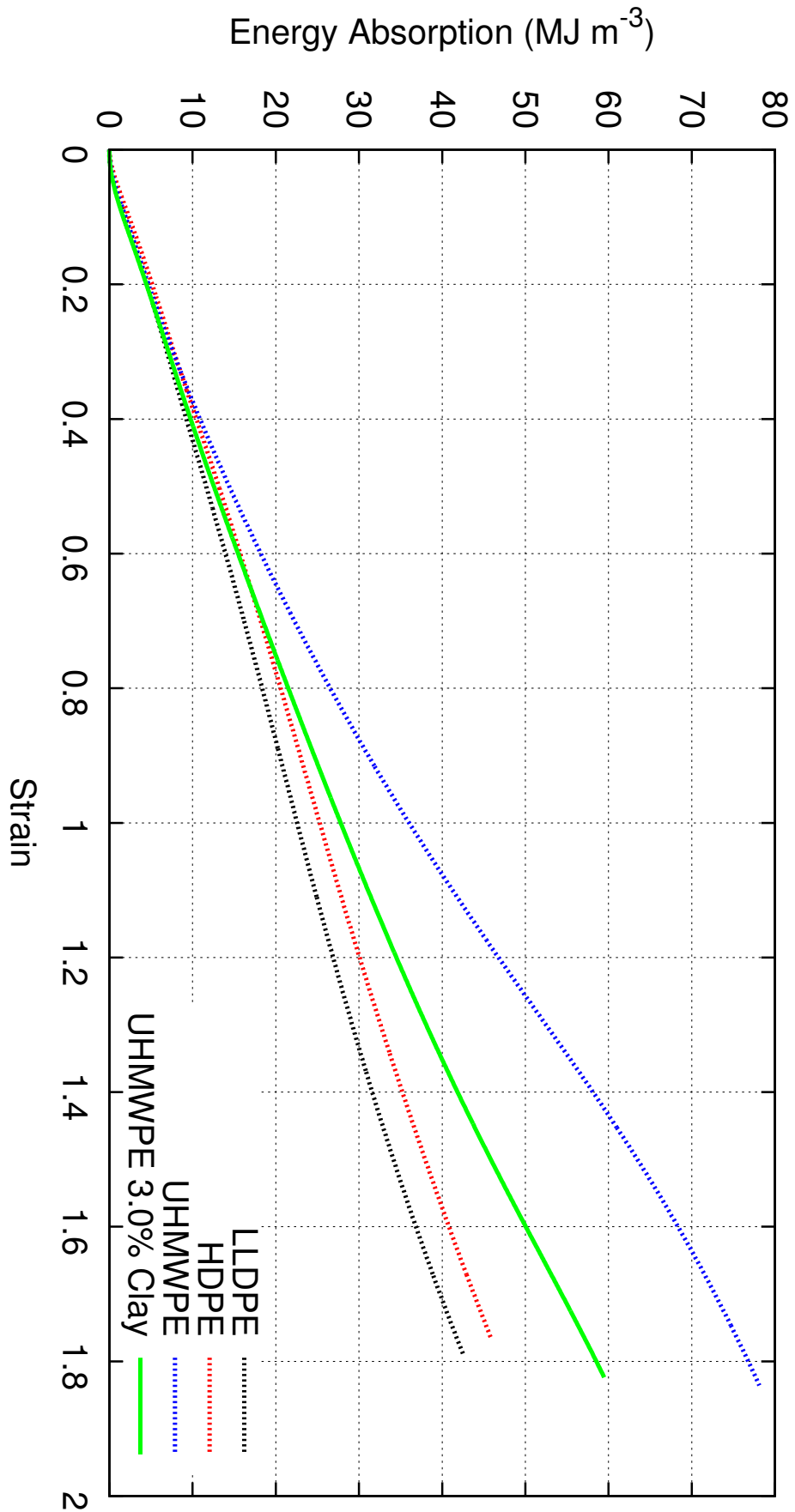


FIGURE L.27: ODW energy absorption for UHMWPE nanocomposites.

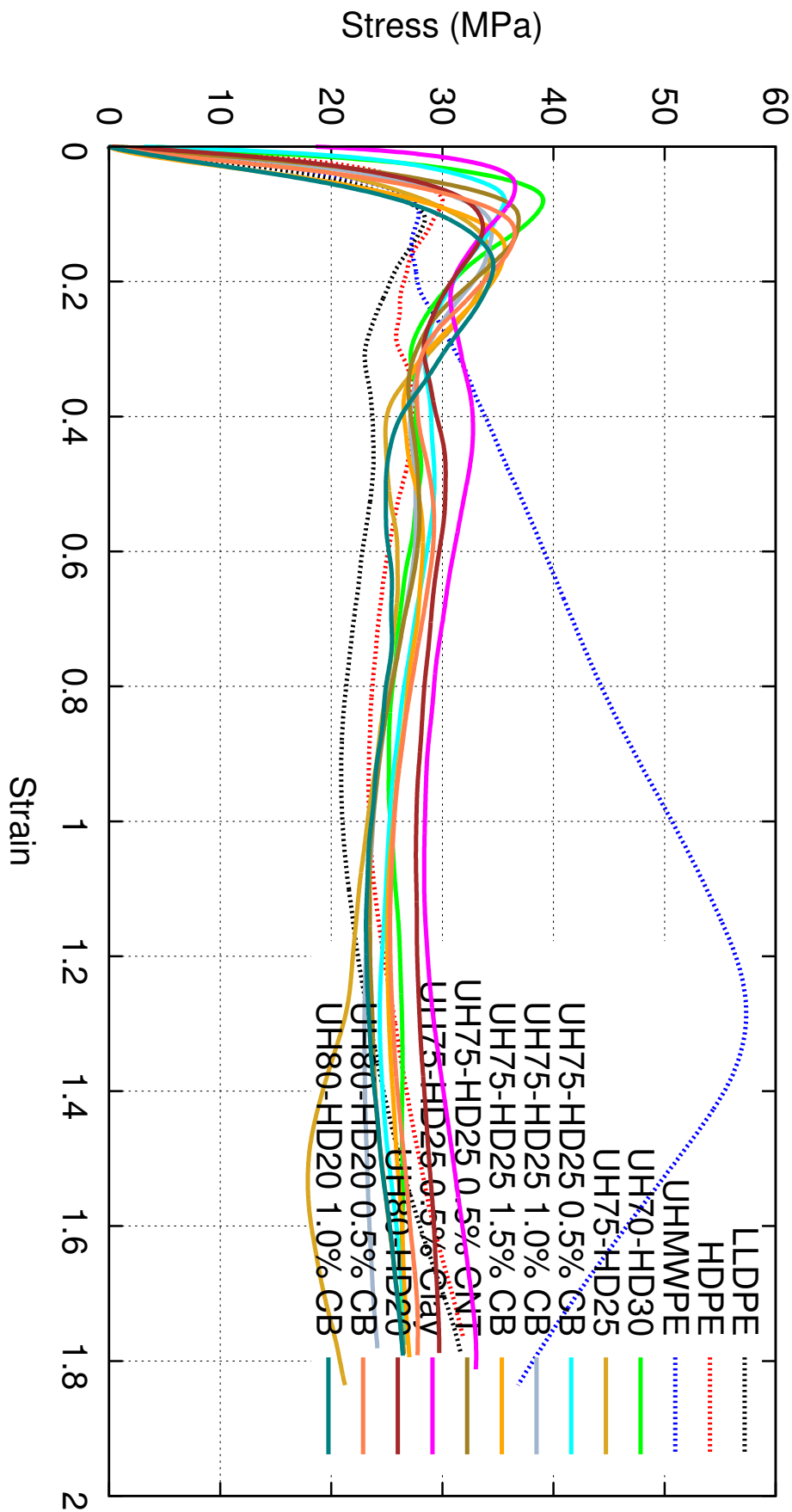


FIGURE L.28: ODW true stress/strain curves for PE blends and nanocomposites.

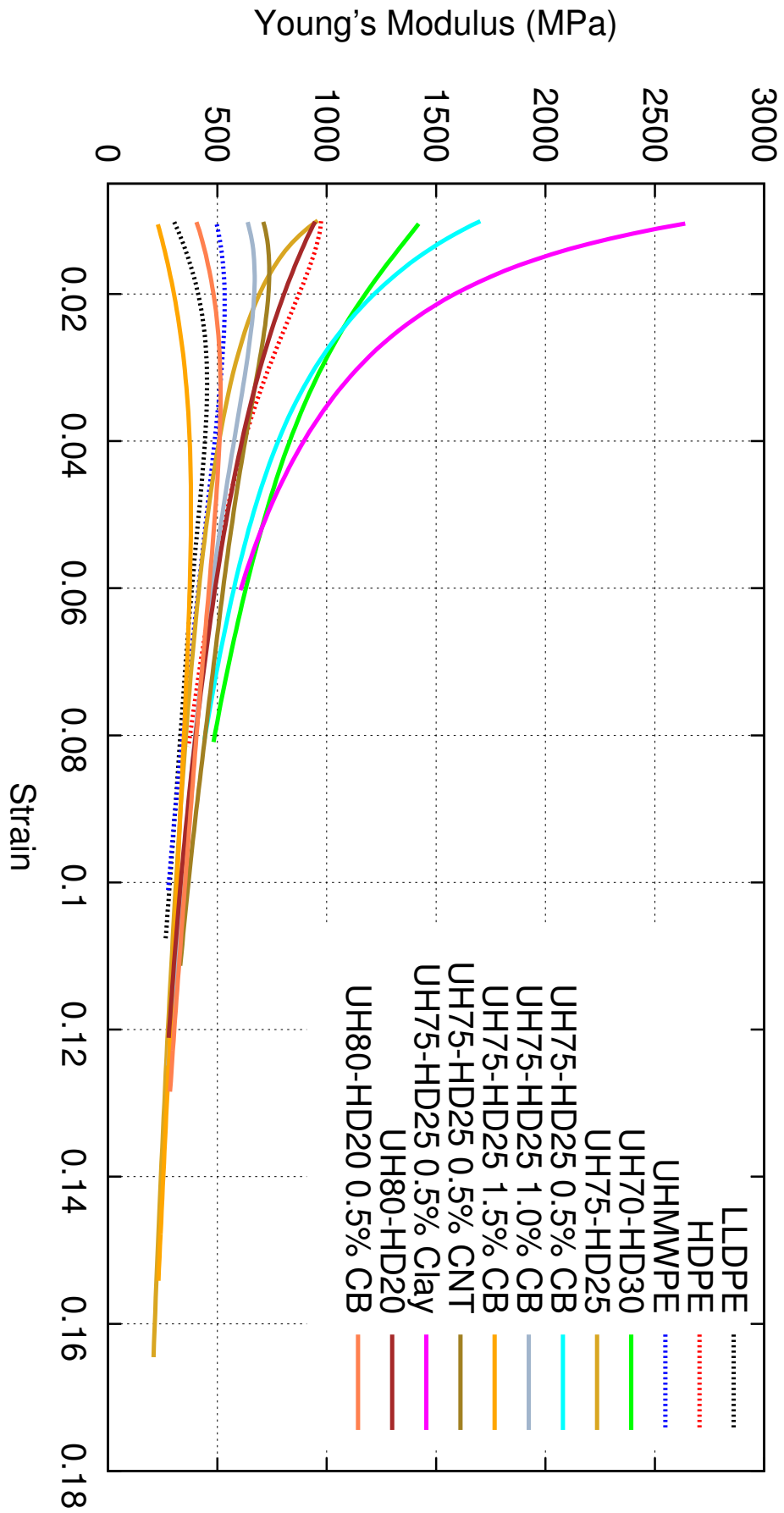


FIGURE L.29: ODW Young's modulus evolution for PE blends and nanocomposites.

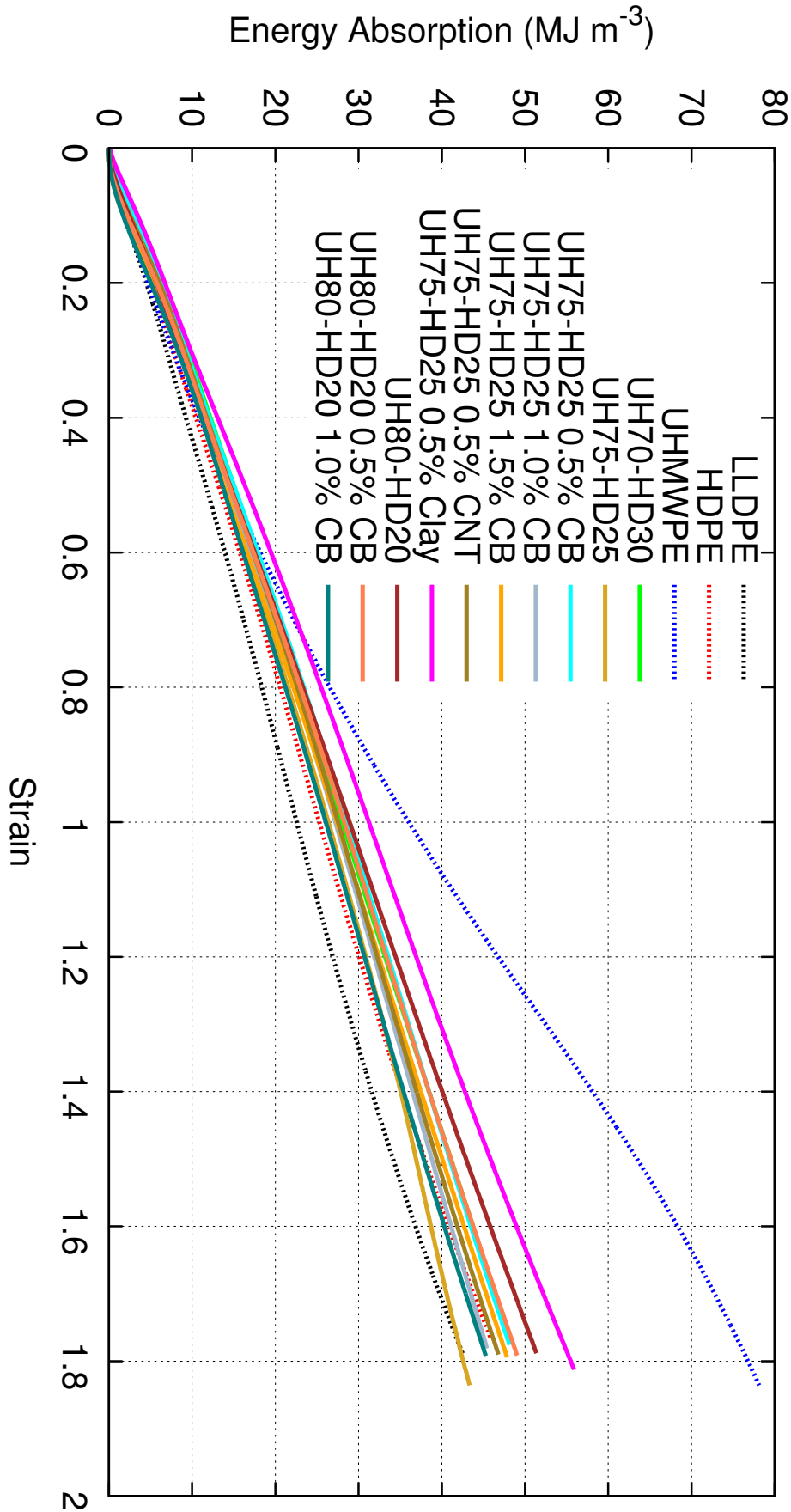


FIGURE L.30: *ODW* energy absorption for PE blends and nanocomposites.

Free Software

It is with care that the research detailed within this document has, wherever possible, been conducted using only computer software which is freely available without cost. It is the firm belief of the author that the overwhelming majority of scientific projects, no matter how complex, can be completed without the need to pay for software.

Following is a list of the software which has been used, its version, what it was used for, and Internet addresses from which more information may be obtained.

Kubuntu 11.10, 12.04 & 12.10 The operating system used on all of the computers used in the research for, and writing of this document.

<http://www.kubuntu.org/>

L^AT_EX2 ϵ Typesetting of this document.

<http://www.latex-project.org/>

Texmaker 3.2 Editing L^AT_EX documents.

<http://www.xmlmath.net/texmaker/>

JabRef 2.7b Organisation and management of the bibliography in this document.

<http://jabref.sourceforge.net/>

gcc 4.6.3 The GNU Compiler Collection, used for the compilation of all of the computer programs written for this project.

<http://gcc.gnu.org/>

Code::Blocks 10.05 Cross-platform integrated development environment used to edit all programming code.

<http://www.codeblocks.org/>

EasyBMP 1.06 A cross-platform bitmap image library for C++, used to manipulate images in programming code.

<http://easybmp.sourceforge.net/>

gnuplot 4.4 Plotting of all graphs.

<http://www.gnuplot.info/>

GNU Octave 3.2.4 Complex mathematical manipulation (e.g. low-pass filtering) of data.

<http://www.gnu.org/software/octave/>

LibreOffice 3 Fully integrated office suite including word processor, spreadsheet and drawing applications, used for general data manipulation and the production of all drawings in this document.

<http://www.libreoffice.org/>

GIMP 2.6.12 The GNU Image Manipulation Program, used to manipulate and convert graphical images and photographs.

<http://www.gimp.org/>

Inkscape 0.48 Fine tuning of the encapsulated postscript drawings created for this document.

<http://www.inkscape.org/>